UAF
NASA USRA ADP
Space Systems Engineering

WIreless Space Power ExpeRiment
Final Report
June 1993

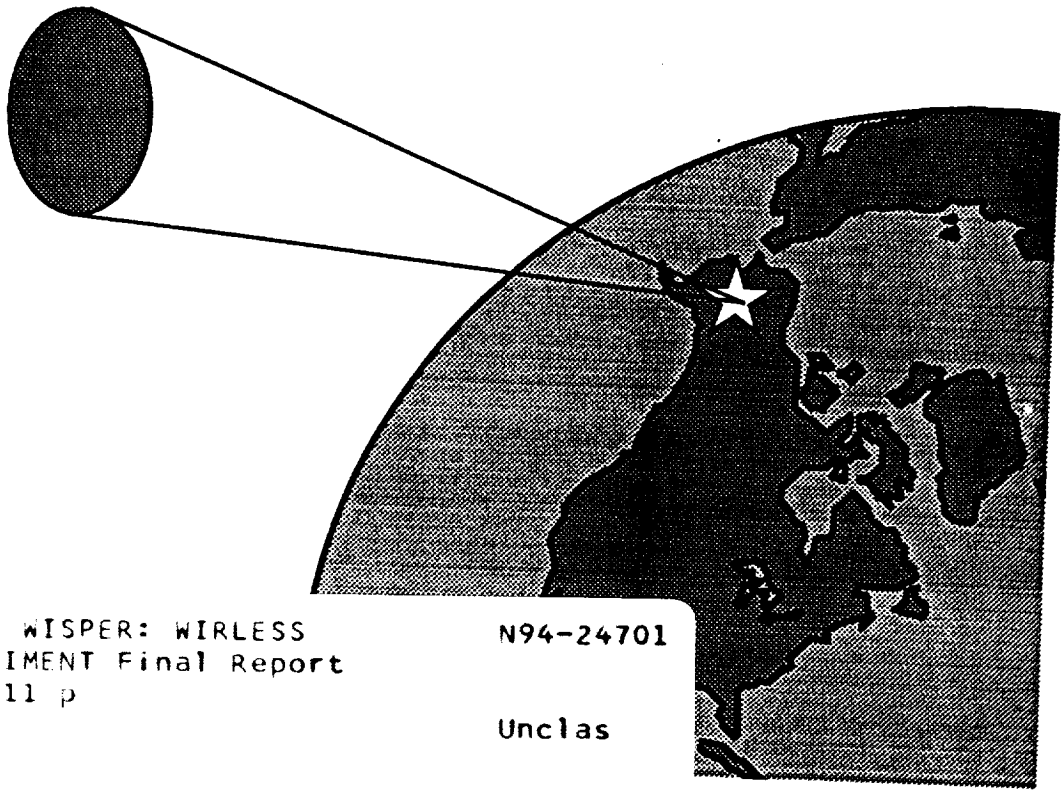

WISPER
WIRELESS SPACE POWER EXPERIMENT

University of Alaska Fairbanks
Departments of Electrical and Mechanical Engineering
Fairbanks, Alaska

Professor Joseph Hawkins

The 1993 Advanced Design Project at the University of Alaska Fairbanks was to design a spacecraft as a technology demonstration of wireless power transmission (WPT). With cost effectiveness as a design constraint, a microsatellite in low earth orbit (LEO) was chosen for the mission. Existing and near term technologies were analyzed and selected for the project. In addition to the conceptual design of the payload, support systems, and structure; the analysis included attention to safety, environmental impact, cost, and schedule for construction and operation.

Wireless power beaming is not a new concept. Experimental demonstrations and study efforts have continued since the early 1960's. With the latest progress in transmitter and receiver technology, the next natural step is to beam power from earth to space. This proposed flight demonstration will advance the science of power beaming and prove the viability of various applications of WPT in space.

Two methods of power beaming will be examined during the two separate phases of the spacecraft life. The first phase will demonstrate the technology and examine the theory of microwave power transmission at a high frequency. Special aspects of Phase I will include a highly accurate attitude control system and a 14 m inflatable parabolic antenna. The second phase will investigate the utilization of high intensity laser power using modified photovoltaic arrays. Special instrumentation on the spacecraft will measure the conversion efficiency from the received microwave or laser power to direct current power.

Table of Contents

List of Figures

List of Tables

UAF
NASA USRA ADP
Space Systems Engineering

WIreless Space Power ExpeRiment
Chapter 1
Introduction

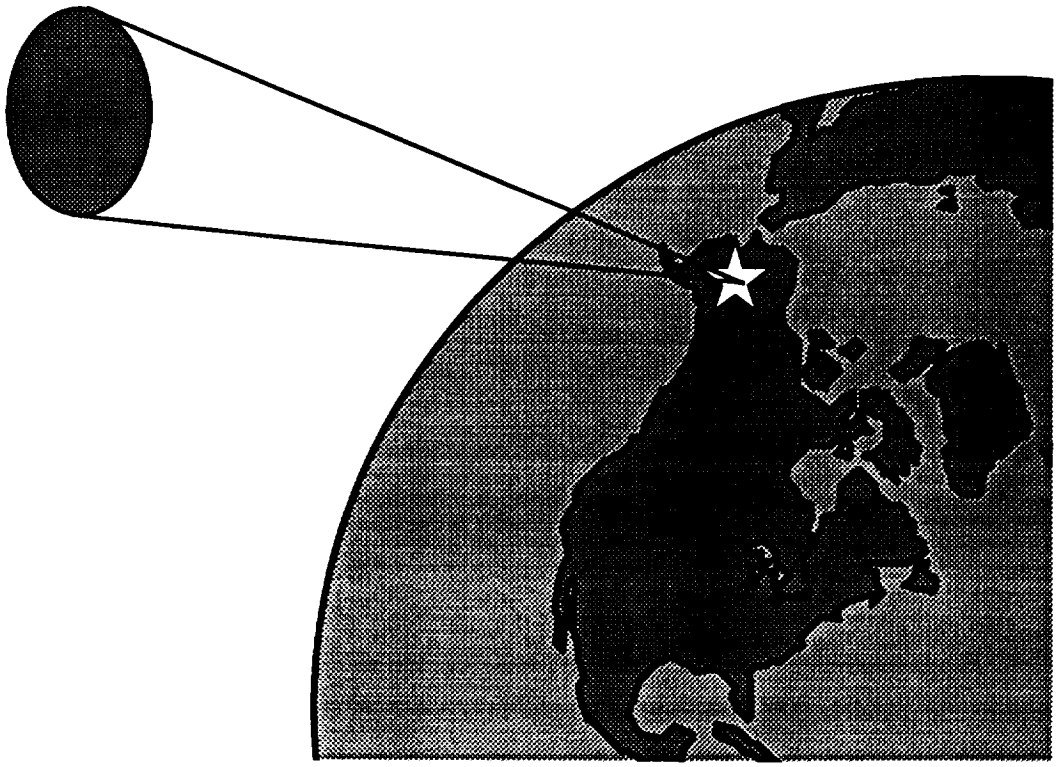

1.0 Introduction

Wireless power transmission (WPT) is simply the transfer of usable energy from one point to another without the use of wires or transmission lines. The energy is transmitted via electromagnetic waves at laser or microwave frequencies. This chapter is an introduction to the applications, history, and background for the WISPER project. It is not intended to serve as a complete survey of WPT. Rather, the chapter introduces the most significant applications, studies and concepts.

1.1 Potential Applications

A number of applications have been proposed using the new technology of WPT. These applications have been placed into four separate categories: Terrestrial and Airborne, Low Earth Orbit, Geosynchronous Orbit, and Moon and Mars Applications.

Terrestrial and Airborne. The terrestrial applications such as point to point transmissions for utility power are significantly limited because of the inherently low efficiencies and high cost of this developing technology. WPT would have to compete with conventional power sources such as hydrocarbon fueled generators, wind, hydroelectric, solar, batteries, and transmission lines. WPT becomes feasible under unique conditions where conventional power systems are not possible or prohibitively expensive. Several high power terrestrial demonstrations have been proposed. One example of a point to point system is proposed by the Alaska Energy Authority and Raytheon Company, where a net transfer of 50-1000 kW is received from the transmitting station 1- 15 miles away [1]. The unique power problems experienced by many remote areas in Alaska could be alleviated by WPT technology.

A second class of terrestrial application that has been proposed is the high altitude relay platform. A helicopter, balloon, or plane could be flown in the upper atmosphere for communication and monitoring. Utilizing WPT technology, such unmanned platforms could be kept aloft for long periods of time. The concept would compete with communication satellites in geosynchronous orbit, which typically cost between one and two hundred million dollars. The high altitude platforms could perform the same mission over a smaller area for a fraction of the cost.

William C. Brown of Raytheon Company examined the feasibility of using WPT to power an unmanned relay platform at high altitudes [2]. Both a microwave powered helicopter and dirigible were considered as the high altitude vehicles. Communications Canada has been working on the Stationary High Altitude Relay Platform (SHARP) program for over 10 years [3]-[9]. The concept proposes the use of an unmanned airplane circling 21 km in altitude for 6 months to a year with a 600 km diameter ground coverage. The 1000 kg aircraft would be reusable and cost about $20 million. Once operational, SHARP will be used for telecommunications, radar surveillance, environmental monitoring, remote sensing, and navigation.

Low Earth Orbit. One result of the International Space University Summer Conference in 1992 was a proposal for a technology demonstration of earth to low earth orbit (LEO) microwave power transfer. In this low cost demonstration, the 400 kW, 2.38 GHz, Arecibo radar and antenna would transmit power to a 10 m inflatable antenna launched from a Get Away Special Canister [10]. The total demonstration cost was estimated to be less than $10 million.

Manned or tended space stations in LEO require power at significantly higher levels than unmanned satellites. In low equatorial orbit the space station will be in the shadow of the earth for over 1/3 of the orbit and must rely on batteries. Geoffrey Landis proposed that a satellite be placed in sun synchronous polar orbit to gather solar energy and transmit microwave power to the space station [11]. The polar orbiting "power station" would be in a higher orbit where atmospheric drag on large solar panels is less of a problem as experienced in the lower orbit.

Arndt and Kerwin examined the applications of using microwave power between two co-orbiting satellites [12]. One specific application would be to generate power on a nuclear satellite and use WPT to transfer the energy from a safe distance to a space station. Power levels near 100 kW were discussed.

Geosynchronous Orbit. The geosynchronous orbit has been exploited by science and commercial applications such as communications satellites. As discussed earlier, the cost of a typical communication satellite including launch costs is $200 million. Such spacecraft can last as long as 10 years. One of the limiting factors in the life of a spacecraft is the decrease of power output from the solar arrays. Concentrated laser light from the earth focused on the photovoltaic arrays could prolong the life of the satellite by providing full or partial power to the spacecraft.

Similarly, lasers could be used to provide power to the satellite during the 70 minute eclipse time in the geosynchronous orbit. The maximum drain on the batteries occurs during this eclipse time which accounts for only 5% of the satellite orbit. Eliminating the need for power storage would result in a mass reduction of 10% [13].

WPT could be an enabling technology for a variety of renewable resources, primarily the sun. Terrestrial solar power systems are limited in that a large portion of the incoming solar flux is absorbed and reflected in the earth's atmosphere and in the diurnal cycle. Introduced by Dr. Peter E. Glaser in 1968, a Solar Power Satellite (SPS) could be situated in geosynchronous orbit where it could receive the sun's full flux over 99% of the time [14]. The energy could be converted into a single frequency electromagnetic wave and transmitted to earth where it would be received and tied into the existing power grid.

Constellations of satellites with applications utilizing WPT were examined in [15]. This paper analyzed four satellite constellation applications: space surveillance and tracking systems, spaced-based laser array, space-based radar, and boost surveillance and

tracking system. The SP-100 nuclear reactor system was examined as the beam power source. As the number of constellation satellite systems increase, WPT could become a viable power source for multiple spacecraft.

One of the proposed applications which has potential for large financial savings centers on the orbit transfer vehicle (OTV) concept. The OTV, pairing electric propulsion engines and WPT technologies, could operate as a tug between LEO and geosynchronous orbit. Using laser power beaming, earth to lunar orbit could be achieved. A microwave OTV was proposed by William Brown in [16] and a laser/electric OTV was proposed in [17]. Ion engine technology was evaluated for use in this project, and an analysis is given in Appendix C.

Moon And Mars Applications. The WPT could end up being an important technology as man further explores the solar system. Manned and unmanned missions to the moon and Mars create unique power challenges that WPT could solve. For example, the moon has a 354 hour night which necessitates large power storage systems. During the long lunar night, lasers from earth could be used to illuminate the solar arrays [18], [19]. Also proposed is power beaming from lunar orbiting solar power satellites to the surface using microwaves [20], [21]. Each of the alternative power systems show potential for significant mass savings over conventional solar power and storage systems. Similar studies have been done using mars orbiting microwave power transmission systems [22], [23].

Before a permanent lunar base or manned exploration of Mars, small unmanned probes or rovers will likely survey the surfaces. To save mass and eliminate multiple power sources, the rovers could be powered remotely using WPT. Systems have been proposed for both the moon [24] and Mars [25].

The WISPER project and study do not advocate any individual application listed above. Rather, the concept of WPT is the focus. The many applications, whether near or far term, indicate the possibilities of utilizing WPT as NASA and industry continue to explore the solar system, monitor the earth's environment, and commercialize space.

1.2 History

The WPT concept is not new, as both Heinrich Hertz and Nikola Tesla investigated it almost 100 years ago. However, technology was not sufficiently advanced until the 1960's when William Brown of Raytheon Company demonstrated the feasibility of the concept. Previously developed radar technology was married with the then new solid state technology, and thus, a new paradigm was introduced. Active research and development has continued as laser technology has advanced WPT to a new plane. Figure 1.2-1 shows a timeline of the major experiments, studies and demonstrations of WPT. The remaining portion of this section briefly describes each of the points on the timeline.

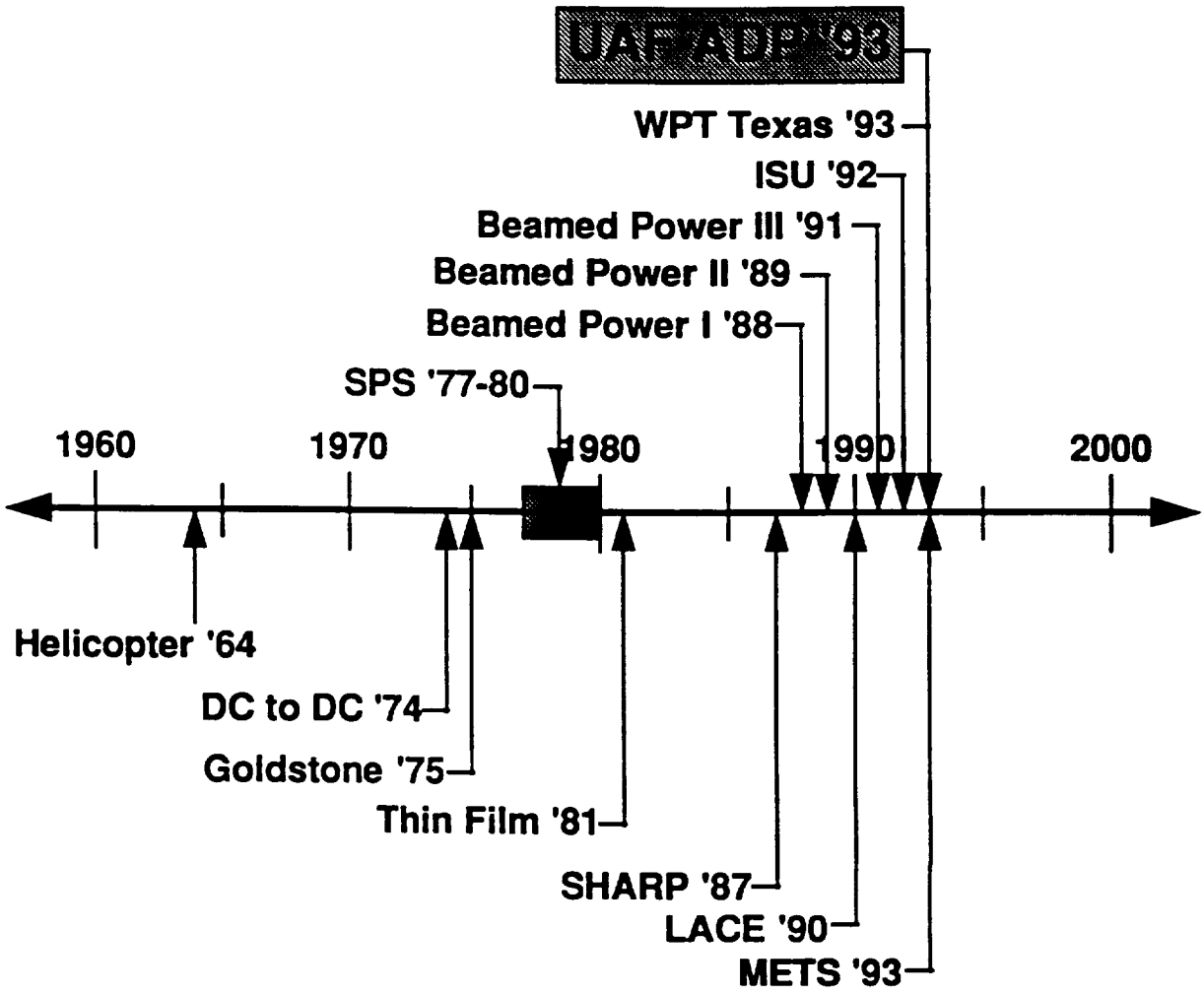

Figure 1.2-1. Wireless power transmission history.

Helicopter '64. In 1964 William C. Brown demonstrated a microwave powered helicopter, developed under contract to the Air Force. The platform was powered aloft for a period of 10 hours, tethered to an altitude of 50 ft. Raytheon later demonstrated a flight control system for a similar helicopter [26]. This system allowed the helicopter to automatically position itself over the center of the microwave beam and control its roll, pitch, and yaw attitudes with sensors that derived phase, polarization, and amplitude information from the beam itself. The publicity from these two developments generated great interest in adapting these technologies to various other applications.

DC to DC '74. In the 1970's WPT technology development was greatly accelerated. As part of the studies carried out to analyze this concept, a technology demonstration was performed in 1974. Quality assurance representatives from NASA's Jet Propulsion Laboratory (JPL) certified a Raytheon built WPT system to operate at a DC to DC efficiency of 54 $\pm$1% [27], [28]. The qualification of these results by JPL's Quality Assurance Department was significant as it validated earlier efficiency analyses previously believed by the scientific community to be unachievable. The report also projected an overall efficiency of 78% after a vigorous program of research and development.

Goldstone '75. The next demonstration teamed Raytheon and JPL together to further demonstrate the viability of this technology. At the Venus Site of JPL's Goldstone Facility, 30 kW of DC power was obtained from a 288 square foot rectenna array, with a 82% microwave to DC conversion efficiency [29] - [31]. The transmitting antenna was remotely located from the rectenna by the distance of one mile (1.54 km). This experiment demonstrated the capability for scaling of these technologies to significant power levels and significant distances. In addition, the reliable operation of the rectenna in the harsh desert environment testified to the robustness of the system.

SPS '77-80. Spurred by the oil embargo in 1973, the government created the Energy Research and Development Agency (ERDA) to charter the development of all energy sources to be used in the US. The ERDA created a task force to research Dr. Glaser's idea of a Solar Power Satellite (SPS) that included such companies as Raytheon, Boeing, North American Rockwell, and Grumman Aerospace. A three year study began in 1977 and was identified as the DOE/NASA Satellite Power System Concept. This study lead to a 670 page document summarizing the results [32]. Based on the current technology and research at the time, the operating frequency was chosen to be 2.45 GHz. This frequency was also selected due to the minimal attenuation through the earth's atmosphere. The overall system performance included 5 GW of power delivered from a 10 km diameter rectenna array. The power would be transmitted to earth from a 1 km diameter phased array located in geosynchronous orbit. One of the major discoveries from these studies involved the microwave source for the space based transmitting antenna. Microwave oven magnetrons, when combined with a passive directional device to enable them to be used as amplifiers, were very quiet and stable energy sources. A large active phased array of slotted waveguides could be produced that used low-cost magnetrons, and by controlling the phase between slotted waveguide subarrays, the microwave beam could be electronically steered. However, by 1980, the energy crisis had ended which made the $12 billion [33] SPS project economically unfeasible. Thus, the project never proceeded from the drawing board.

Thin Film '81. One of the criticisms of microwave WPT was the mass to power ratio of the rectenna receivers. In 1981, William Brown and James Triner developed the thin filmed rectenna [34]. The conventional rectenna was replaced by a rectenna array etched on one mil Kapton. The resulting circuit had a high conversion efficiency (85%) and a one watt per gram power to mass ratio. This configuration was a significant advance

because the resulting rectenna was much lighter and opened the door to the concept of etched or monolithic rectenna arrays at higher frequencies.

SHARP '87. The Canadian SHARP (Stationary High Altitude Relay Platform) program flew a one-eighth scale prototype solely powered by a microwave beam [3]-[9]. The SHARP-5 aircraft was flown in September, 1987 for 20 minutes at altitudes up to 150 meters. Further flights remained aloft for periods up to an hour. The airplane's wingspan was 4.5 meters and power was transmitted to the aircraft using a 4.5 m parabolic antenna that transmitted 10 kW of energy.

Beamed Power I - III. In 1988, 32 scientists, engineers, and administrators form NASA, industry and academia gathered at NASA Lewis Research Center in Cleveland, Ohio, for the first beamed power conference [35]. During this two day conference, research was presented and applications of this rapidly growing technology were discussed. The second conference was held at NASA Langley Research Center in 1989 [36]. This conference was larger with 54 participants and lasted 4 days. The third conference was held at Pasco, WA, in 1991 and was sponsored by the Pacific Northwest Laboratory [37]. With each conference, the interest in WPT grew and the power beaming community became more organized.

Lace '90. The history of laser power beaming is somewhat clouded. One of the major developers of the technology is the Strategic Defense Initiative Office. For obvious reasons, many of the experiments are difficult to find. One of the most important demonstrations that could be found was the Low Power Atmospheric Compensation (LACE) satellite [38]. The primary mission of the LACE satellite, launched on February 14, 1990, was to evaluate low power atmospheric techniques. The result of the experiment was a near diffraction limited laser beam bearing on the deployed booms.

ISU '92. During the summer session of the International Space University, the focus was the Space Solar Power Program [39]. The session held in Kitakyushu, Japan, examined the state-of-the-art and developing technology and described a development plan for space solar power. The result is a near and long term plan to promote the development of SPS technology in a cost effective manner.

METS '93. Japan's Institute of Space and Aeronautical Science (ISAS) has been investing in SPS related technologies for over a decade. In a manner characteristic of other Japanese technology programs, a consortium of government, industry, and academia is developing the technologies needed for an SPS. A series of small demonstrations of the technology have been held in the last 5 years, and more are planned for the near future. In 1983, a sounding rocket was launched into the ionosphere to study its interaction with a high power microwave beam, coined the Microwave Ionosphere Non -Linear Interaction Experiment (MINEX) [40]. The MINEX project was a precursor to Japan's interest in creating its own Solar Power Satellite. In 1992, a small microwave powered airplane was flown to verify a solid-state phased array transmitter.

In 1993, the Japanese launched the Microwave Energy Transmission in Space (METS) sounding rocket to again test the interaction of the ionosphere with a high power microwave beam operating at 2.41 GHz [41].

WPT '93. In February 1993 was the largest WPT conference to date [42]. It was held in San Antonio lasting for three days. The conference was sponsored by the NASA Center for Space Power and focused on the commercial potential of WPT technologies.

1.3 Project Introduction

It has been shown that there is a significant number of space applications for WPT technology. As mankind progresses in the exploration of the solar system, WPT will likely become an integral part of the space power infrastructure. A brief history of the progression of the technology was discussed. There is an obvious gap between the history of WPT and space applications. The history includes a beam powered helicopter and airplane. High efficiencies and high power transmissions have been demonstrated on earth. A sounding rocket has carried an experiment into the upper atmosphere. What is lacking is the next natural step, a demonstration of WPT in space. The Wireless Space Power Experiment takes that next step. The mission of the project is to demonstrate some of the technologies of WPT from earth to LEO in a cost effective manner. Simultaneously, the conceptual design will test some of the theories and models developed for high power transmissions through the atmosphere. The design difficulties and tradeoffs analyzed within this study will lay the foundation for the understanding of WPT on a larger scale. In accomplishing this mission, the project provides a springboard for the proposed applications and others yet to be conceived.

Although the project is both conceptual and academic, a cost effective design which achieves the mission is the ultimate goal. The mission constraints consist primarily of cost, schedule and availability of technology. Cost as a mission constraint is one of the most limiting to the design. For this reason, a microsatellite platform was selected for the mission. A complete description of the mission statement and mission constraints are available in appendices B and C, respectively.

1.4 Operations Overview

The mission will begin when the Pegasus booster is launched from the carrier aircraft at 41,000 ft (12,500 m). This mission will require the use of the optional HAPS stage (Hydrazine Auxiliary Propulsion System). 502 seconds after launch, the HAPS will place the spacecraft within 5.6 km of the 600 km target altitude. To reach this higher altitude, enhancements have to be made to the standard Pegasus motor. The spacecraft will automatically deploy the solar panels after separation from the HAPS. The onboard propulsion system may have to be used to adjust the inclination. Spacecraft systems will be checked, after which the satellite will begin the experimental phase of the mission.

The WISPER experiment will be divided into two separate phases; first is the microwave experiment. After the satellite has stabilized in its designated 600 km orbit, it will be allowed to reach temperature and pressure equilibrium before the 14 m inflatable microwave receiving dish will be deployed. The operations team will then prepare for the first pass over the ground site. WISPER will pass over the ground site approximately once per day and will pass directly over the ground site once every fifteen days. Before the spacecraft appears on the horizon, it will have oriented the receiving dish toward the ground site so that it can begin fine pointing adjustments when the signals from the interferometer attitude correction system begin to arrive. The spacecraft slews as a unit as it passes over the ground station. The ground transmitting antenna rotates using feedback signals from the monopulse receiver and maintains polarization using power density readings. The microwave ground site will be the NOAA satellite ground station near Fairbanks, Alaska. The first phase will gather as much data on microwave power beaming as possible over its 1 year duration. At the end of that period, the inflatable dish and microwave power conversion hardware will be separated from the spacecraft and allowed to reenter the atmosphere.

The second phase will involve the beaming of power by laser from a ground site at the White Sands Missile Range in New Mexico. The satellite will pass over the ground station once per day, however, there will be a twenty-four hour no contact period once every fifteen days. This is due to the lower latitude of the laser ground station. The second phase is designed to last a year, but additional funding will be sought to continue as long as useful experimentation can occur. The laser beam will impinge on special photovoltaic panels that are filtered to match the wavelength of the laser. The details of operation are covered in the sections that follow. Figure 1.4-1 shows an overview of the project operational life.

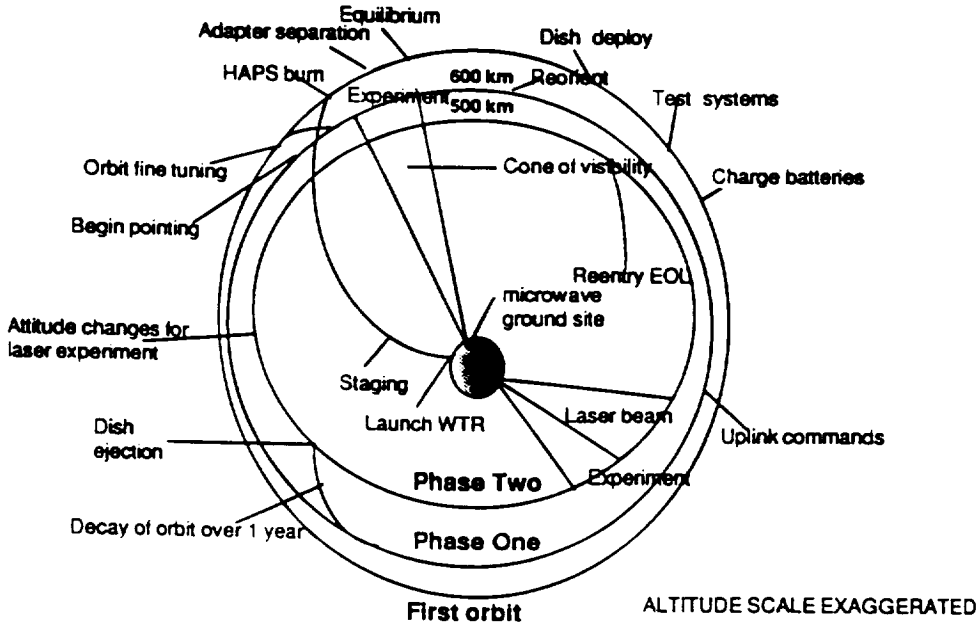

Figure 1.4-1. Operation overview.

UAF
NASA USRA ADP
Space Systems Engineering

WIreless Space Power ExpeRiment

Chapter 2

Microwave Power Experiments

Phase I

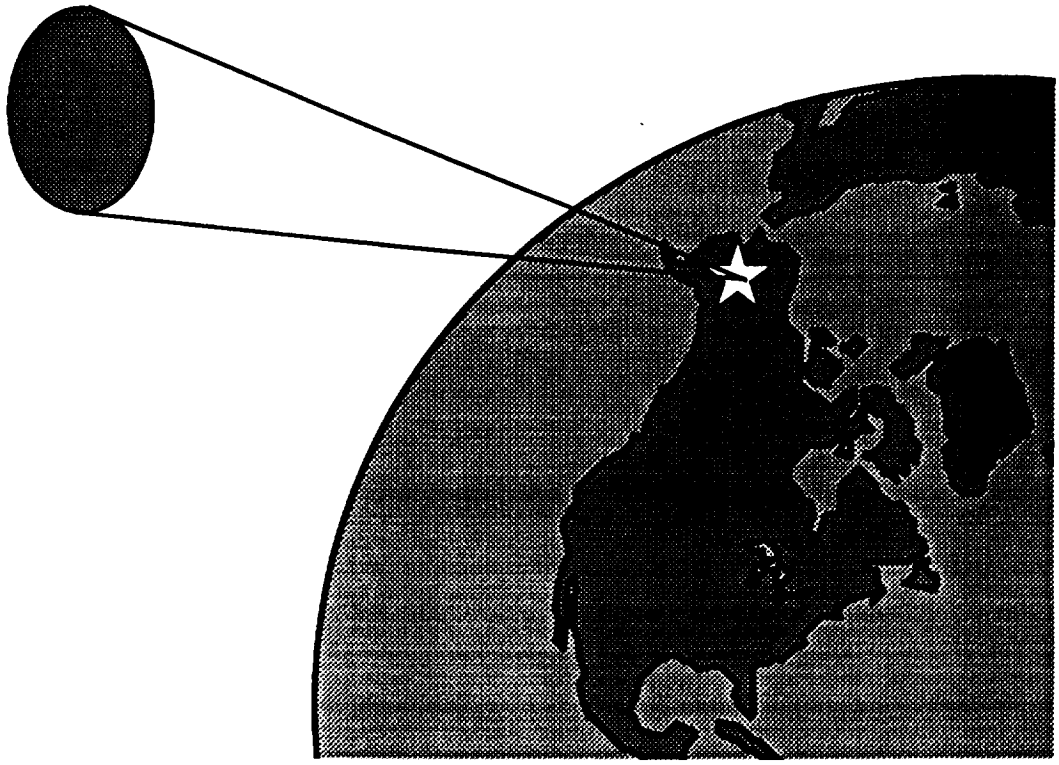

2.0 Microwave Power Experiment - Phase I

Microwave power transmission has developed into a mature technology for low operating frequencies. The operating frequency of 2.45 GHz has received the most attention due to its location in an Industrial, Scientific and Medical (ISM) research band and to its minimal attenuation through the atmosphere. A drawback to this technology is the large component sizes needed for efficient power transfer. Due to recent technology advancements at 35 GHz, the components are scaled down by a factor of nearly 14. Also, the transmission range is dramatically expanded by increasing the operating frequency to 35 GHz. This characteristic is valid when the transmitting antenna and power level are identical for both 2.45 and 35 GHz. However, the system components are less efficient and a complete system on a large scale has not been demonstrated. For the WISPER satellite, 35 GHz is selected because of the ability to focus power on the satellite at a large separation distance from a single transmitting antenna.

2.1 Microwave Experiment Overview

Microwave power transmission involves a system composed of a power source, transmitting antenna and rectenna. The power source converts direct current (DC) power into microwave power, the antenna radiates the microwave power, and the rectenna converts the microwave power back into DC power. An unique component of the WISPER satellite is the inflatable dish that reflects the microwave power onto the rectenna. The inflatable dish is discussed in detail in section 5.1.1. For the rectenna to perform efficiently in converting the microwave power into DC power, the incident power density must be high. The inflatable dish performs this feat by concentrating the microwave power onto the rectenna.

The major system components for Phase I consist of a 25 m antenna transmitting a 35 GHz power beam to the 14 m inflatable dish located on the WISPER satellite. The inflatable dish reflects the microwave power onto a 96 cm diameter rectenna array located at the focal point.

2.1.1 Operational Sequence

Microwave power beaming will begin after the WISPER satellite has achieved a stable polar orbit at 600 km. Gyrotron sources will generate approximately 400 kW of power at 35 GHz. A monopulse receiver at the transmitting antenna will track the satellite and align the transmitting antenna for power beaming. Figure 2.1-1 shows the operation sequence at an orbital altitude of 600 km.

When the satellite arrives at the ground station horizon, communication and tracking links will commence with receivers at the ground station. Allowing time for the WISPER satellite to align itself with the transmitting antenna, power transmission will nominally occur at angles between $\pm 40^{o}$ from zenith. The separation distance is 761 km at $\pm 40^{o}$. With a direct overhead pass, approximately 2 minutes will be allowed for power

beaming. At this altitude, a maximum of 105 W of DC power is expected from the rectenna under ideal weather conditions and perfect on-axis alignment between the transmitting antenna and inflatable dish.

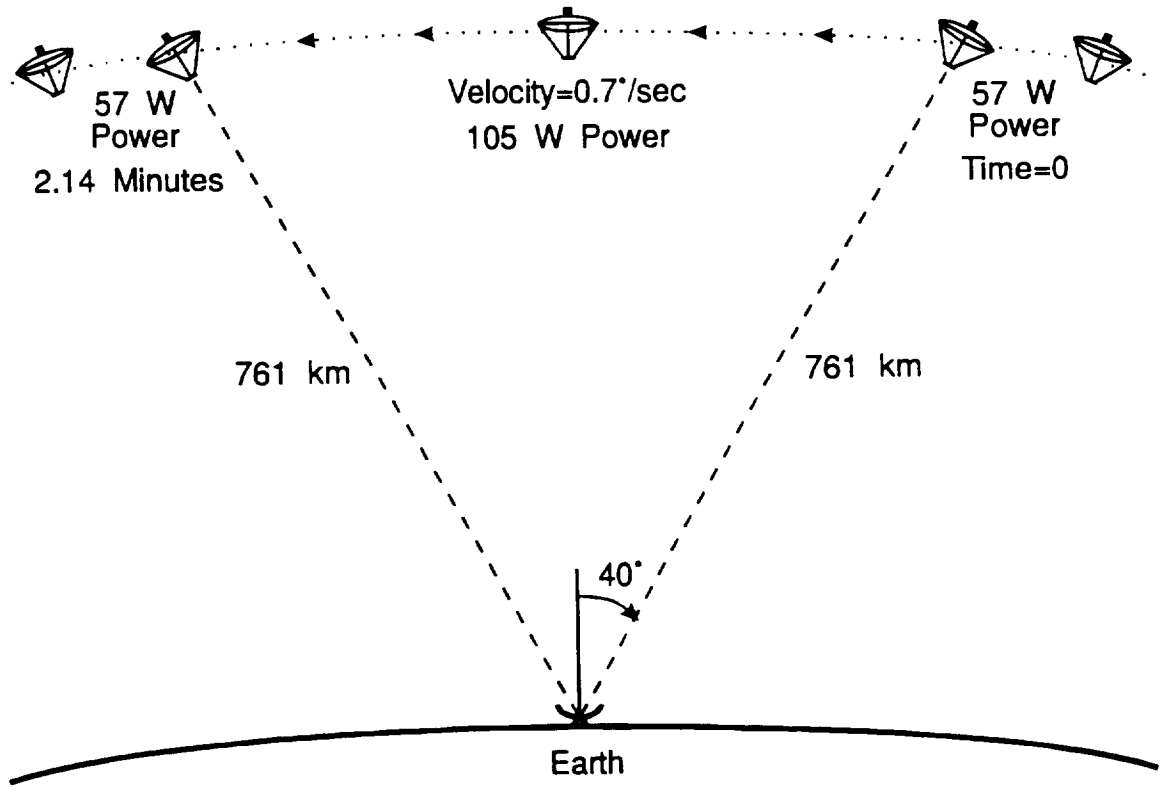

Figure 2.1-1. Operation sequence at an orbital altitude of 600 km.

Including atmospheric attenuation at 35 GHz on clear weather days and a transmitting antenna aperture efficiency of 50%, the power density of the microwave beam will be 3.22 W/m^2 at a zenith altitude of 600 km. Excluding atmospheric attenuation, the power density is determined from the Friis transmission formula given as [1]

$$S_r = \frac{P_t \pi r^2 \eta_{apt}}{\lambda^2 d^2} \left[\frac{W}{m^2}\right] \qquad (2.1\text{-}1)$$

where P_t is the transmitted power (W), r is the radius of the transmitting antenna (m), η_{apt} is the aperture efficiency of the transmitting antenna, λ is the wavelength (m) of the operating frequency, and d is the separation distance between the transmitting antenna and satellite (m). At ±40° from zenith, the power density decreases to 1.95 W/m^2 at the WISPER satellite.

The area ratio of the 14 m inflatable dish to the 96 cm rectenna is 213. The aperture efficiency of the inflatable antenna is 47%. Taking the area ratio and aperture

efficiency into account, the power density incident on the rectenna ranges from 208 W/m^2 at ±40° from zenith to 343 W/m^2 at zenith as shown in Figure 2.1-2.

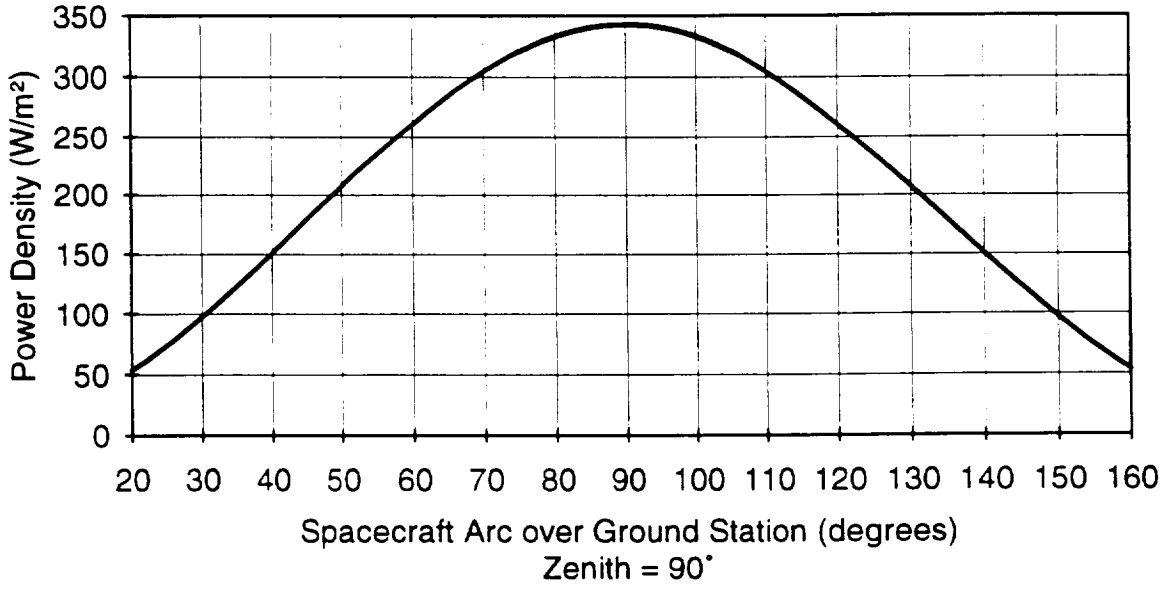

Figure 2.1-2. Incident power density on rectenna at an orbital altitude of 600 km.

The WISPER satellite will drift to a lower orbit due to the drag on the inflatable dish. The lower altitude limit for Phase I is set at 500 km. The operation sequence at 500 km is shown in Figure 2.1-3.

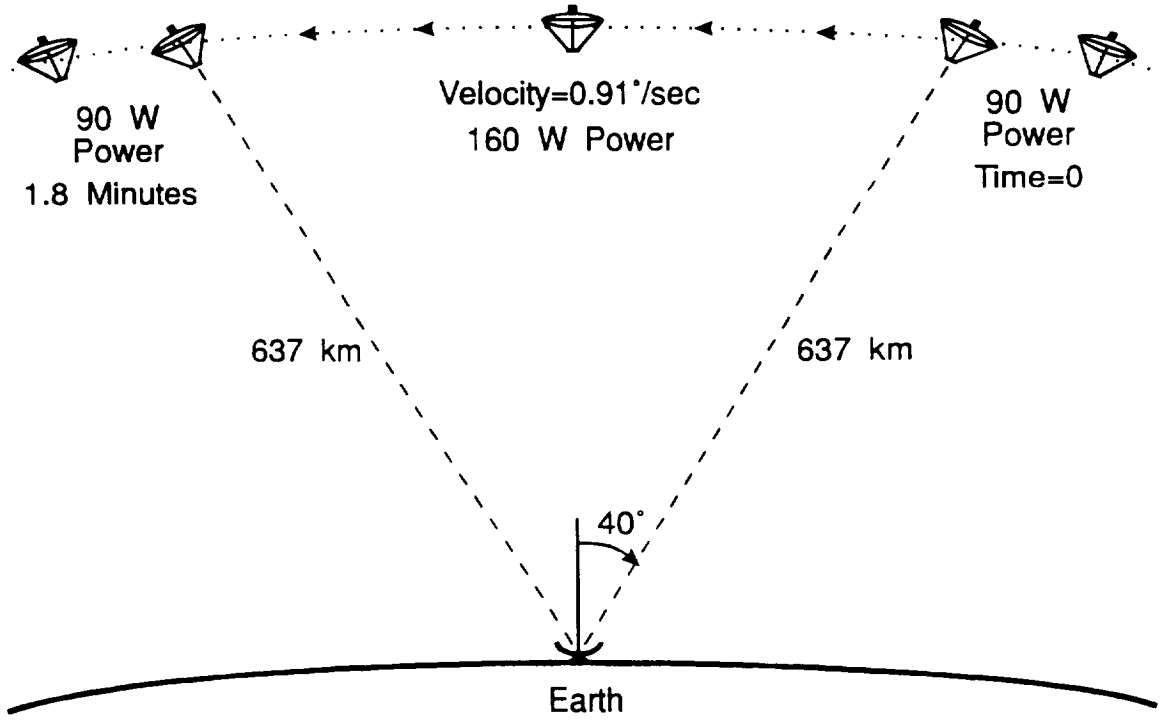

Figure 2.1-3. Operation sequence at an orbital altitude of 500 km.

Using the same assumptions of clear weather and perfect alignment between the transmitter and receiver, a maximum of 160 W of DC power is expected from the rectenna. Although the power delivered to the satellite is increased, the lower altitude results in a shorter power transmission period.

The incident power density will increase due to the lower orbital altitude. The power density will be 4.65 W/m^2 at zenith and decrease to 2.79 W/m^2 at $\pm 40^o$ from zenith. The separation distance at $\pm 40^o$ is 637 km. The power density incident to the rectenna ranges from 296 W/m^2 at $\pm 40^o$ from zenith to 494 W/m^2 at zenith as shown in Figure 2.1-4.

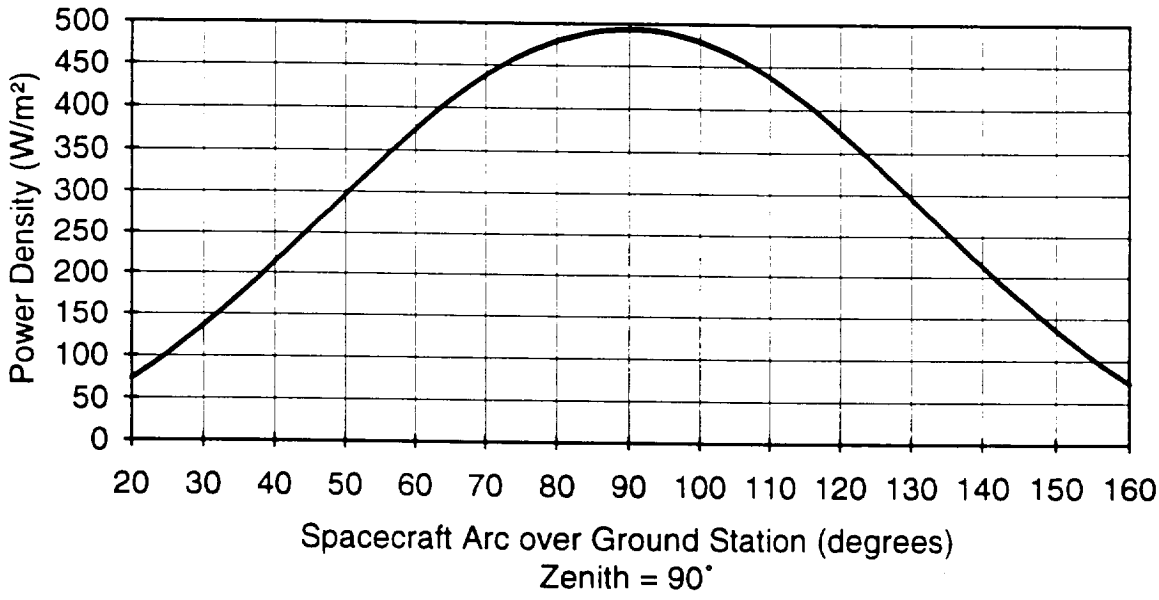

Figure 2.1-4. Incident power density on rectenna at an orbital altitude of 500 km.

The inflatable antenna will then be discarded to conduct laser power beaming experiments.

2.1.2 Experimental Objectives

Several experiments will be performed over the lifetime of the microwave power transmission phase. The main objective of this phase is to successfully receive microwave power and convert it to useful DC power. However, an assortment of secondary investigations deserve consideration.

Conversion efficiencies of the rectenna array will be determined and compared to theoretical calculations. The conversion efficiency can be measured by comparing the power density incident on the rectenna to the output DC power. The ability of the inflatable dish to focus the microwave power will be monitored. This focusing efficiency can be obtained by measuring the microwave power densities incident on the satellite and rectenna. These two efficiencies can also be measured at different power

densities by the constantly changing separation distance between the transmitter and satellite or by varying the output power from the transmitter.

Power patterns of the transmitting antenna can be determined by a microwave detection system on the spacecraft. The ground antenna will remain fixed as the spacecraft records the pattern passing overhead.

The ground station selected for the WISPER project is the National Oceanic and Atmospheric Administration (NOAA) satellite tracking station located in Fairbanks, Alaska. This ground station is ideal for microwave power beaming because it is located in a hill valley which isolates it from local inhabitants and power demands for the gyrotrons are available. Transmitting and receiving antennas are also available for satellite communication.

The effects of microwave power transmission at 35 GHz through a turbulent atmosphere can be analyzed. Using an existing water vapor radiometer at the NOAA tracking station, the amount of water vapor in the atmosphere can be measured. Thus, interactions of the power beam with clouds or inclement weather can be compared to clear weather transmissions and to existing attenuation models. Microwave beam propagation as a function of the ionospheric plasma density can be measured. Possible thresholds at which nonlinear effects occur in wave particle interactions with the microwave power beam may be determined where physical effects such as microwave defocusing or attenuation could occur [2]-[4].

Pointing accuracy of the ground station and spacecraft will be monitored. Data concerning the stability and structural integrity of the inflatable dish will also be gathered in the space environment.

2.1.3 Atmospheric Effects on Microwave Propagation

The effects of the atmosphere upon microwave power transmission can be divided into four categories according to the origin. These effects are breakdown, refraction, attenuation, and polarization rotation.

Atmospheric Breakdown. Atmospheric breakdown occurs when particles in the beam path are ionized by the electric field of the beam. Ionization then produces turbulence that disperses the beam. Air breakdown occurs at about 1.2×10^{10} W/m^2 for room air temperature and sea level pressure [5]. The power capacity of air increases as pressure increases. However, atmospheric pressure decreases with increasing altitudes to a point where ionization could arise. For the WISPER project the most probable chance of ionization to occur is located within the transmitting antenna. The maximum power produced by the microwave source will be 400 kW. Thus, the largest power density will be inside the waveguide feeding the transmitting antenna. One type of waveguide recommended for high power transmission is the oversized circular waveguide with a 10λ diameter [6]. Air breakdown in the waveguide feed is discussed further in Section 2.4.2.

Refraction. Refraction of a microwave beam is caused by gravitational and temperature variations in the atmosphere. This effect is independent of frequency and causes the beam to bend towards the earth. The average radius of curvature for a beam parallel to the earth is approximately four-thirds of the earth's radius [7]. Due to the beam angle not exceeding 30° from zenith, gravitational refraction will be minimal for this project. This effect is exaggerated in Figure 2.1-5.

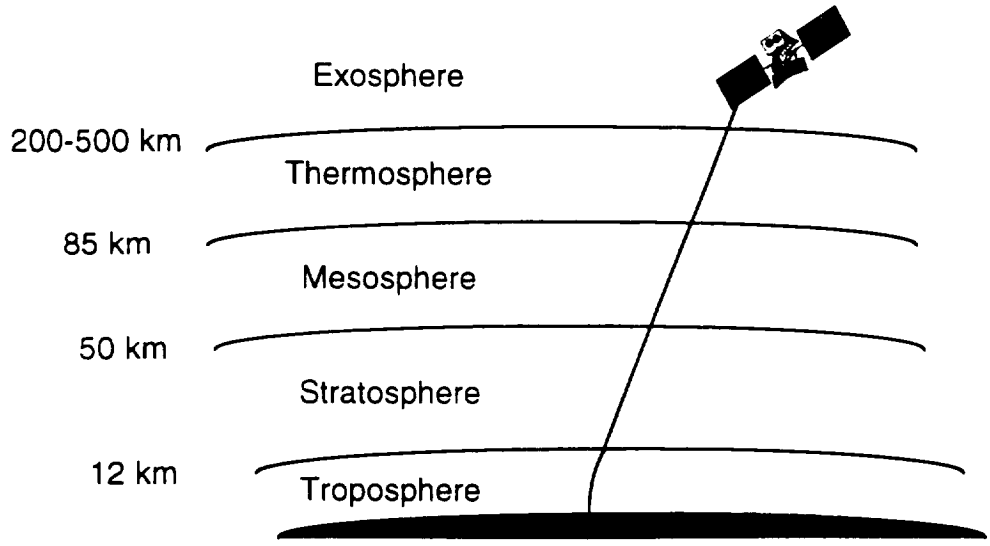

Figure 2.1-5 Gravitational refraction of a microwave beam.

Thermal refraction occurs when the beam travels in a medium with temperature variations. Differences in air temperature implies that they have different indices of refraction. The atmosphere can be modeled as a collection of air parcels where each has a different index of refraction. As the beam passes from one parcel to another, the beam is bent. Two types of thermal refraction, depending on the size of the air parcels relative to the beam pattern, are beam wander and turbulence.

If the parcels are large compared to the size of the beam pattern, beam wander can occur. The entire beam will be bent an equal amount and direction. This effect results in a beam that is coherent, but not located directly on the axis of transmission.

Turbulence is the movement of small air parcels within the atmosphere. The major effect of turbulence will be deformation of the phase pattern and variation of the beam amplitude. For the WISPER project, this effect will be minimized by using a rectenna array. Because each rectenna element has a diode, phase variation over the beam cross section is not detrimental.

Attenuation. Atmospheric attenuation is divided into absorption and scattering. Absorption occurs when molecules absorb radiation by changing vibrational and rotational energy states [8]. At 35 GHz absorption is caused chiefly by water vapor and oxygen. The amount of attenuation depends on the air temperature, relative humidity, and the amount of atmosphere that the beam traverses.

The scattering effect is a function of frequency, index of refraction and radius of the scattering particle. Scattering is generally subdivided into 3 categories according to particle size. Rayleigh Scattering results when the scattering particle is smaller than the wavelength. Mie Scattering results when the particle size is on the order of the wavelength. Nonselective scattering occurs when the particle is larger than the wavelength. At 35 GHz, the free space wavelength is 8.56 mm where scattering is primarily Rayleigh Scattering and caused by water droplets of clouds, fog, and rain.

The Crane Model is used to calculate the total attenuation due to rain at 35 GHz [9]. The model uses an effective height of the attenuating medium that depends on the type of rainfall event. This effective height corresponds to a variable isotherm height which is dependent on a rainfall probability. Table 2.1-1 shows the attenuation and the variables used to calculate the attenuation for the best and worst case rain conditions. The calculations are based on weather conditions at the NOAA tracking station under light rain for the best case (rain rate exceeded 2% of the time) and worst case conditions (rain rate exceeded 0.01% of the time). The best case scenario occurs at a path distance of zenith and the worst case occurs at 40° from zenith.

Table 2.1-1. Best and worst cases for rain attenuation at 35 GHz.

Variable	Best Case: Zenith	Worst Case: 40° off Zenith
Rain Rate R_p (mm/h)	1.2	19.0
Effective Path Distance D (km)	0	1.923
Attenuation A (dB)	**0.5**	9.492
b	(N/A)	1.39
c	(N/A)	-0.0623
d	(N/A)	2.033
u	(N/A)	0.1011
Slant Path Attenuation A_s (dB)	(N/A)	**12.424**

The path distance D through the effective atmosphere is given by

$$D = \frac{H(P) - H_g}{\tan\theta} \text{ [km]} \qquad (2.1\text{-}2)$$

where $H(P)$ is the 0° isotherm for a probability P of a rainfall event, H_g is the station height (295 m), and θ is the elevation angle from the horizon (50° worst case). The effective atmosphere is 2 km for the worst case.

For the best case at zenith, the total rain attenuation is given by

$$A = \left(H(P) - H_g\right)\alpha R_p^{\beta} \text{ [dB]} \qquad (2.1\text{-}3)$$

The specific attenuation parameters are $\alpha = 0.242$ and $\beta = 1.04$ for 35 GHz.

For angles relative to zenith, the total rain attenuation through the effective atmospheric distance is given by

$$A = \alpha R_p^{\beta} \frac{e^{u\beta D} - 1}{u\beta} \quad [\text{dB}] \tag{2.1-4}$$

where

$$b = 2.3 R_p^{-0.17} \tag{2.1-5}$$

$$c = 0.026 - 0.03 \ln(R_p) \tag{2.1-6}$$

$$d = 3.8 - 0.6 \ln(R_p) \tag{2.1-7}$$

$$u = \frac{\ln(b\, e^{cd})}{d} \tag{2.1-8}$$

For clear weather transmission, atmospheric attenuation is predicted by the CCIR (The International Radio Consultative Committee) Model [10]. Using local weather information from the NOAA tracking station, approximate conditions are used to predict the clear weather atmospheric attenuation.

Location:	NOAA/NESDIS Command and Data Acquisition Station, Fairbanks, AK
Elevation:	295 m
Mean Temperature:	21° C (maximum in June)
Relative Humidity:	60% (June, equal to a water vapor density of 11.1 g/m^3 at 21° C)

Specific attenuation due to oxygen at the surface for dry air (15° C) is given by

$$\gamma_o = \left[7.19 \times 10^{-3} + \frac{6.09}{f^2 + 0.227} + \frac{4.81}{(f-57)^2 + 1.5} \right] f^2 \times 10^{-3} \left[\frac{\text{dB}}{\text{km}} \right] \tag{2.1-9}$$

where f is the frequency (GHz).

Specific attenuation due to water vapor (15° C) is given by

$$\gamma_w = \left[0.067 + \frac{3}{(f-22.3)^2 + 7.3} + \frac{9}{(f-183.3)^2 + 6} + \frac{4.3}{(f-323.8)^2 + 10} \right] f^2 \rho_w \times 10^{-4} \left[\frac{\text{dB}}{\text{km}} \right] \tag{2.1-10}$$

where ρ_W is the water vapor density at the surface (g/m^3). These equations are accurate for water vapor densities less than 12 g/m^3.

Correction factors are given for changes in the temperature in the range of -20° C to 40° C as

$$\gamma_O = \gamma_O(15^oC)[1.0 - 0.01\,(T_O - 15)] \left[\frac{dB}{km}\right] \quad (2.1\text{-}11)$$

$$\gamma_W = \gamma_W(15^oC)[1.0 - 0.006\,(T_O - 15)] \left[\frac{dB}{km}\right] \quad (2.1\text{-}12)$$

where T_O is the surface temperature in degrees Celsius.

The equivalent heights for oxygen (h_O) and water vapor (h_W) are given as

$$h_O = 6 \text{ [km] for frequencies} < 57 \text{ GHz}$$

$$h_W = \left[2.2 + \frac{3}{(f-22.3)^2+3} + \frac{1}{(f-183.3)^2+1} + \frac{1}{(f-323.8)^2+1}\right] \text{[km]} \quad (2.1\text{-}13)$$

The total path gaseous attenuation through the atmosphere is found as

$$A_g = \frac{\gamma_O h_O e^{-\frac{H_g}{h_O}} + \gamma_W h_W}{\sin\theta} \text{ [dB]} \quad (2.1\text{-}14)$$

where H_g is the height of the ground station (km) and θ is the path elevation angle in degrees.

The ideal gas law used to convert relative humidity to water vapor density is given by

$$\rho_W = R.H.\frac{e_S}{R_W(T_O + 273.15)} \left[\frac{g}{m^3}\right] \quad (2.1\text{-}15)$$

where $R.H.$ = relative humidity
e_S = saturated partial pressure of water vapor corresponding to the surface temperature T_O (°C) given in N/m^2
R_W = 0.461 joule/(g K)

Figure 2.1-6 is used to obtain the saturated partial pressure in N/m^2 at a certain surface temperature [11].

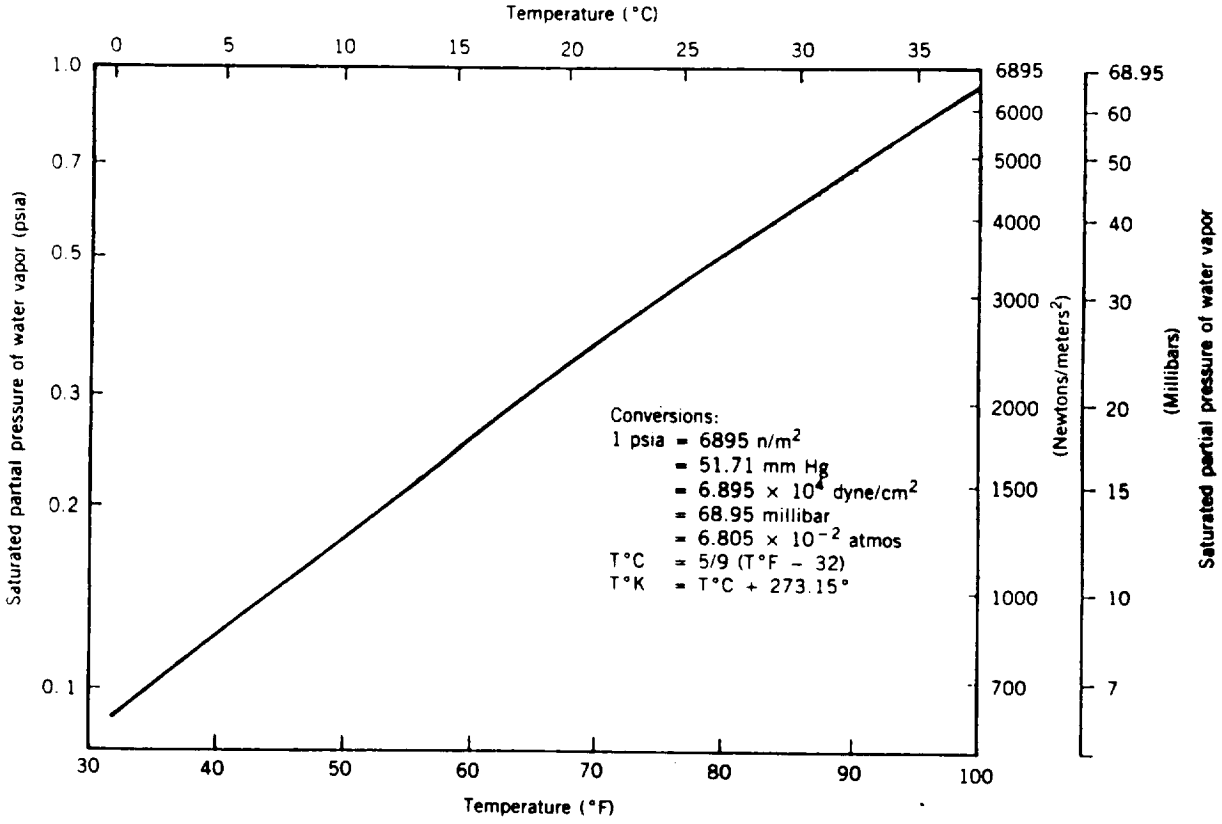

Figure 2.1-6. The saturated partial pressure of water vapor versus temperature [11].

Figure 2.1-7 shows the total atmospheric attenuation of the microwave beam versus look angle at 35 GHz. At zenith, the total power attenuation is 0.39 dB. At 40° from zenith (50° or 130° on figure), the attenuation is 0.51 dB.

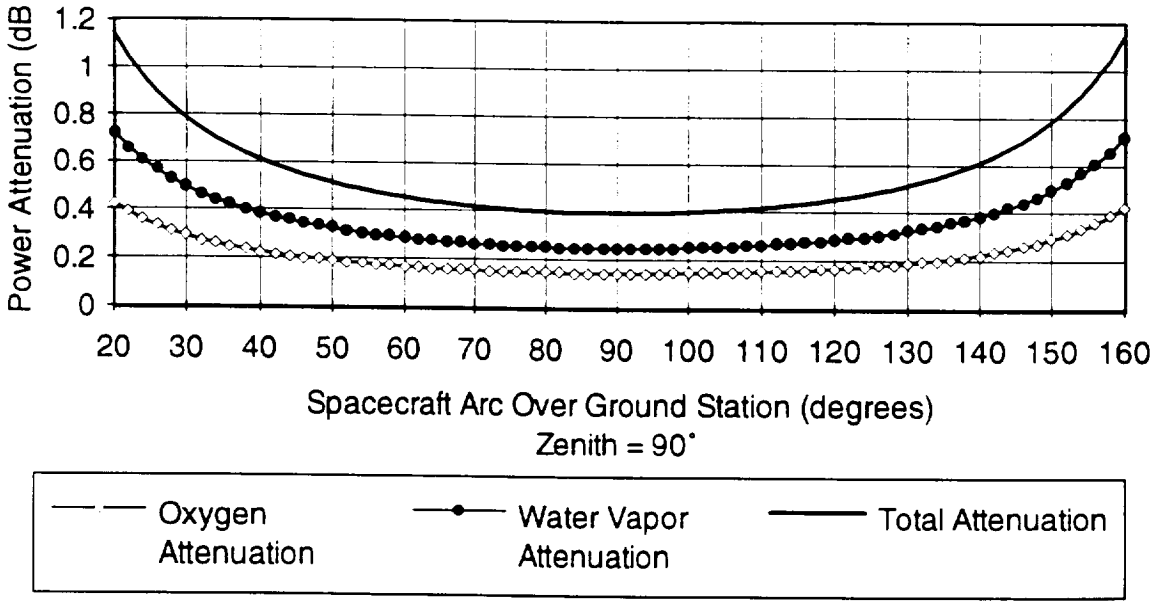

Figure 2.1-7. Total atmospheric attenuation at 35 GHz.

Polarization Rotation. In addition to scattering, the beam polarization will be rotated as it passes through water droplets in the air. Since the transmitting antenna and rectenna elements are linearly polarized, it is important that polarization of the two antennas be aligned. Therefore, instrumentation will be included to ensure polarization alignment.

2.2 Frequency Selection

The choice of operating frequency for microwave power transmission is driven by the separation distance between transmitter and rectenna, power density coverage over a certain area and the components to support the mission using existing technology. Because the pattern of a microwave beam diverges with distance, operating frequencies are increased to reduce component sizes and to sustain high power densities. The prime candidates for the operating frequency are 2.45 GHz, 5.8 GHz and 35 GHz. The first and second frequencies are selected based on operation in ISM bands and low attenuation through the atmosphere. As shown in Figure 2.2-1, 35 GHz is pursued by its location in a low atmospheric attenuation window [12]. Recent component developments have made power transmission at this frequency possible.

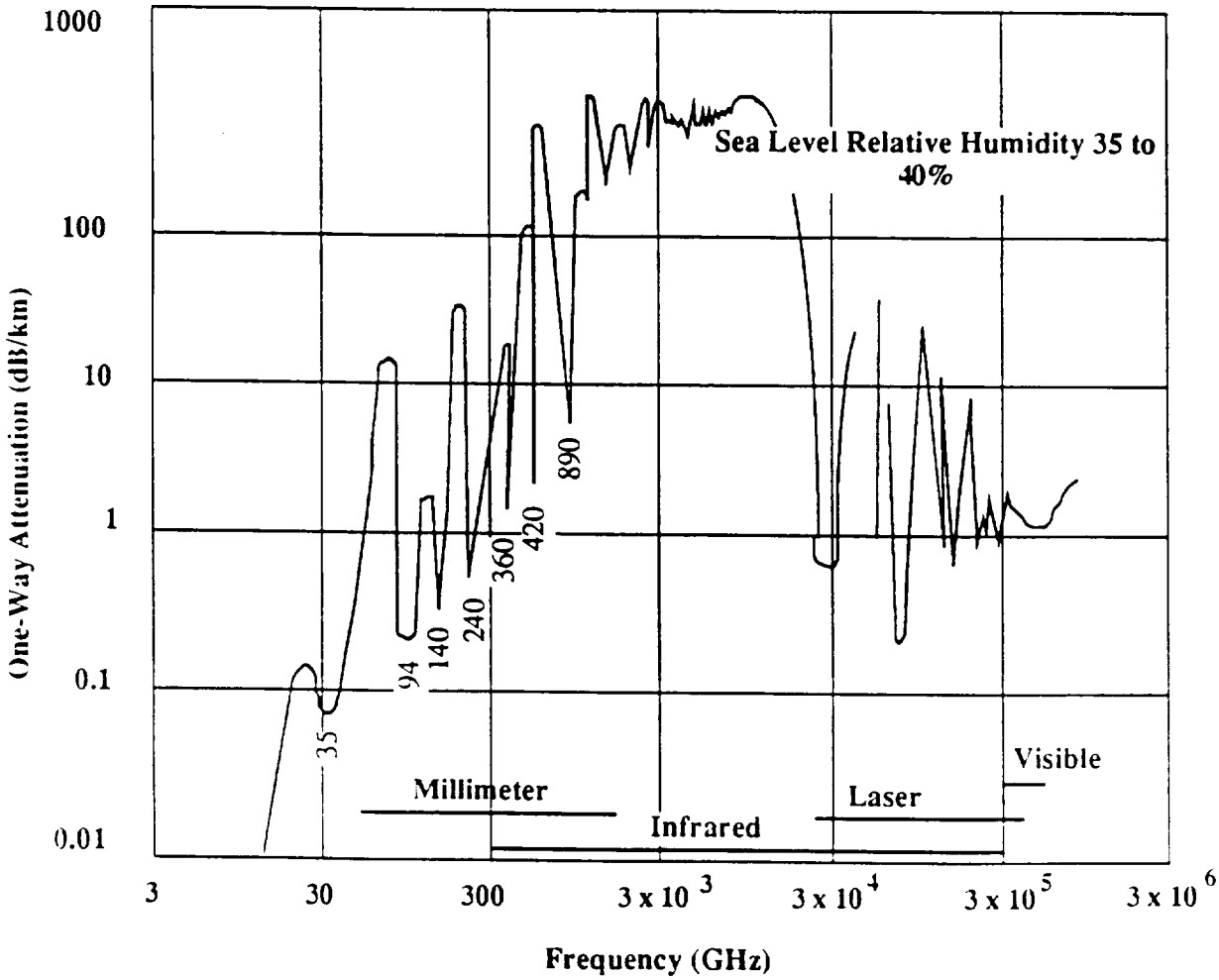

Figure 2.2-1. Atmospheric attenuation windows [12].

Figure 2.2-2 shows a frequency comparison of patterns generated by a 25 m diameter transmitting antenna at a distance of 600 km. The microwave power is more focused with increasing frequency.

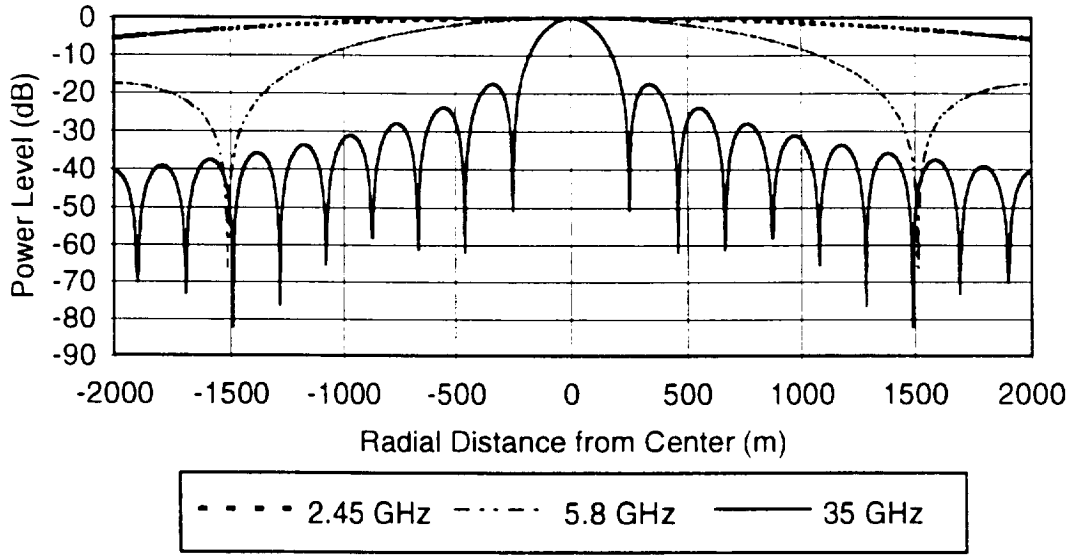

Figure 2.2-2. Power patterns of the different operating frequencies.

As the power density decreases by the inverse square of the distance, increasing the frequency can provide greater transmission distances for the same transmitting antenna. Figure 2.2-3 illustrates a scaled comparison of a constant power density of 3.22 W/m^2 as a function of the three operating frequencies. The number of rectenna elements also increases with frequency. The effective area for a rectenna element at 2.45 GHz is 50 cm^2 [13]. Thus, 135 rectenna elements could occupy the 96 cm diameter area. Scaling the effective rectenna element area to 5.8 GHz, 811 rectenna elements could reside inside the same area. Because the 2.45 GHz and 5.8 GHz rectenna efficiencies are higher and there is less atmospheric attenuation at these frequencies, the DC output power is greater than the 35 GHz rectenna for the same rectenna area and power density.

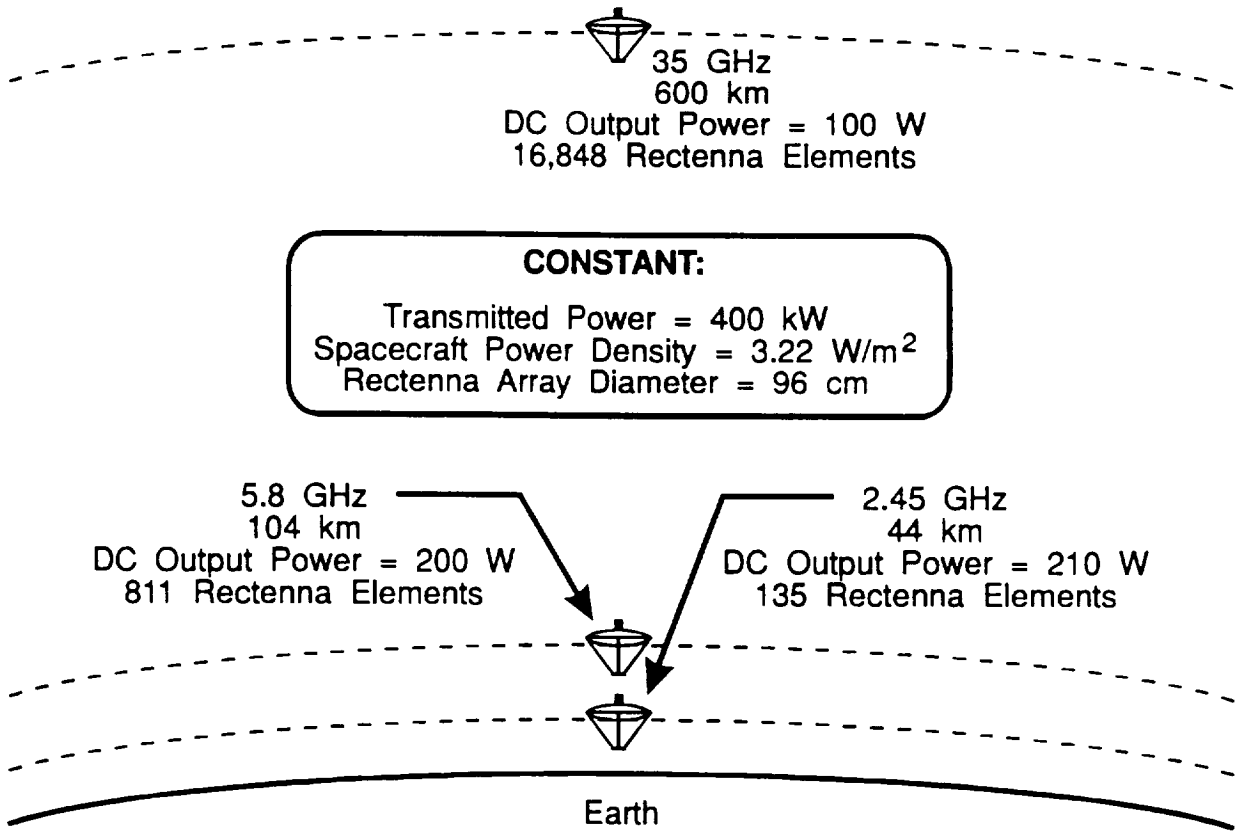

Figure 2.2-3. Scaled comparison of frequencies with a constant power density.

The operating frequency of 35 GHz is selected for this project due to the ability of focusing the microwave energy onto a small spacecraft.

2.3 Spacecraft Requirements

The spacecraft will carry many components to support the Phase I experiments. These components include the rectenna array, power density measurement components, monopulse beacon and antenna, and a communication antenna. These components will reside at the focal point of the inflatable dish as shown in Figure 2.3-1.

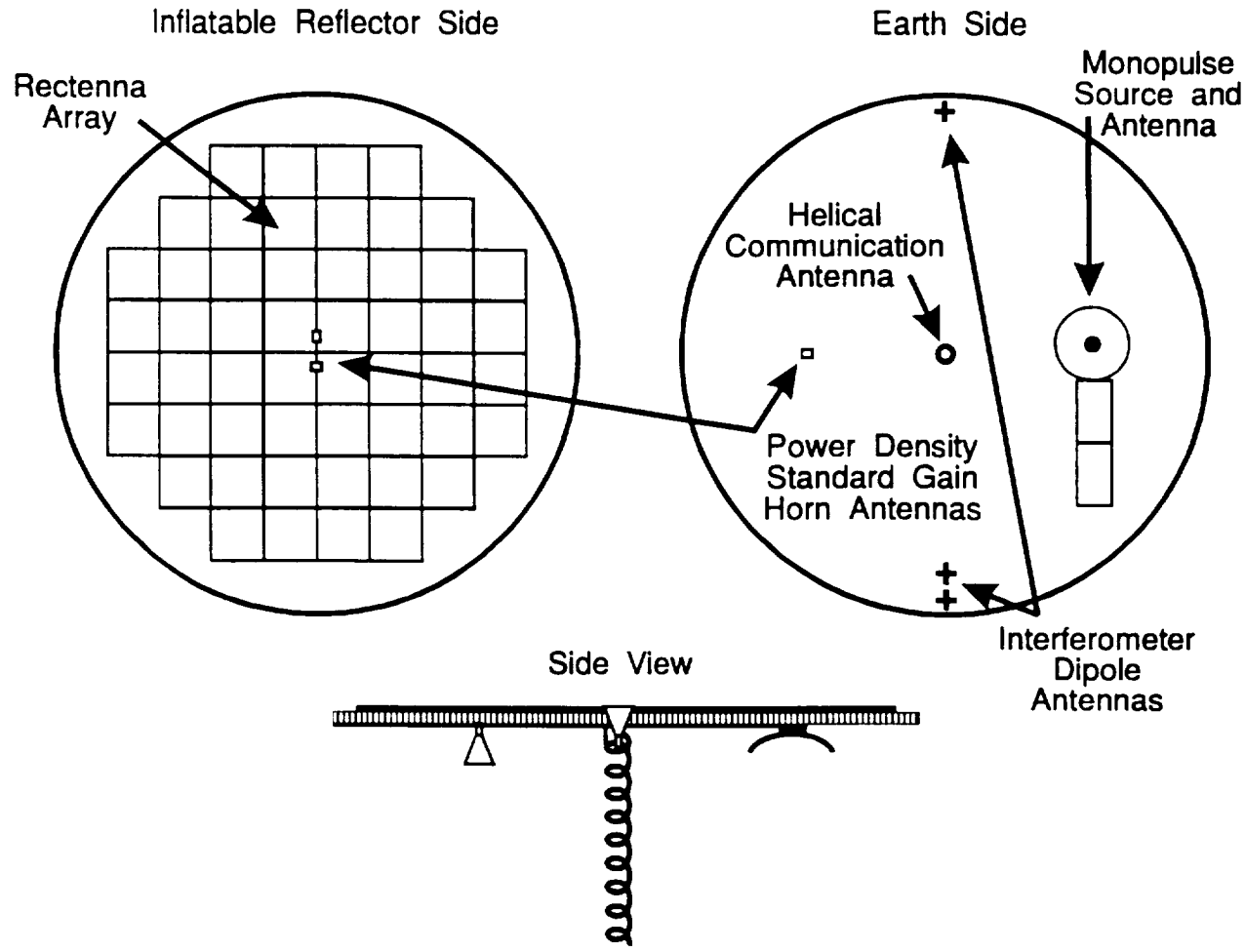

Figure 2.3-1. Focal point components.

2.3.1 35 GHz Rectenna

The rectenna is a receiving antenna that converts microwave power into DC power. The components of the rectenna consist of an antenna, filtering circuitry, and rectifying diode. The antenna is usually a dipole which feeds into a low pass filter. The low pass filter matches the antenna impedance to the diode, suppresses the harmonic radiation created by the diode, and acts as a tank circuit for the on and off cycles of the diode. The Schottky barrier diode is the crucial element in the circuit, for only an efficient diode will produce high conversion efficiencies. A second filter connects the diode to the DC bus lines. This output filter is used to resonate the diode's parasitic reactance and short circuit the microwave energy from passing to the DC bus line.

The 35 GHz rectenna array designed for the WISPER satellite is shown in Figure 2.3-2. The rectenna array consists of 16,848 elements which have their own filtering components and rectifying diode. Because the antenna on the rectenna is a printed

half-wave dipole, the polarization is linear. The total weight is approximately 1 kg and the total thickness is 2 mm. The rectenna array is modularized into 52 panels as suggested by the manufacturer, ARCO Power Technologies, Inc.

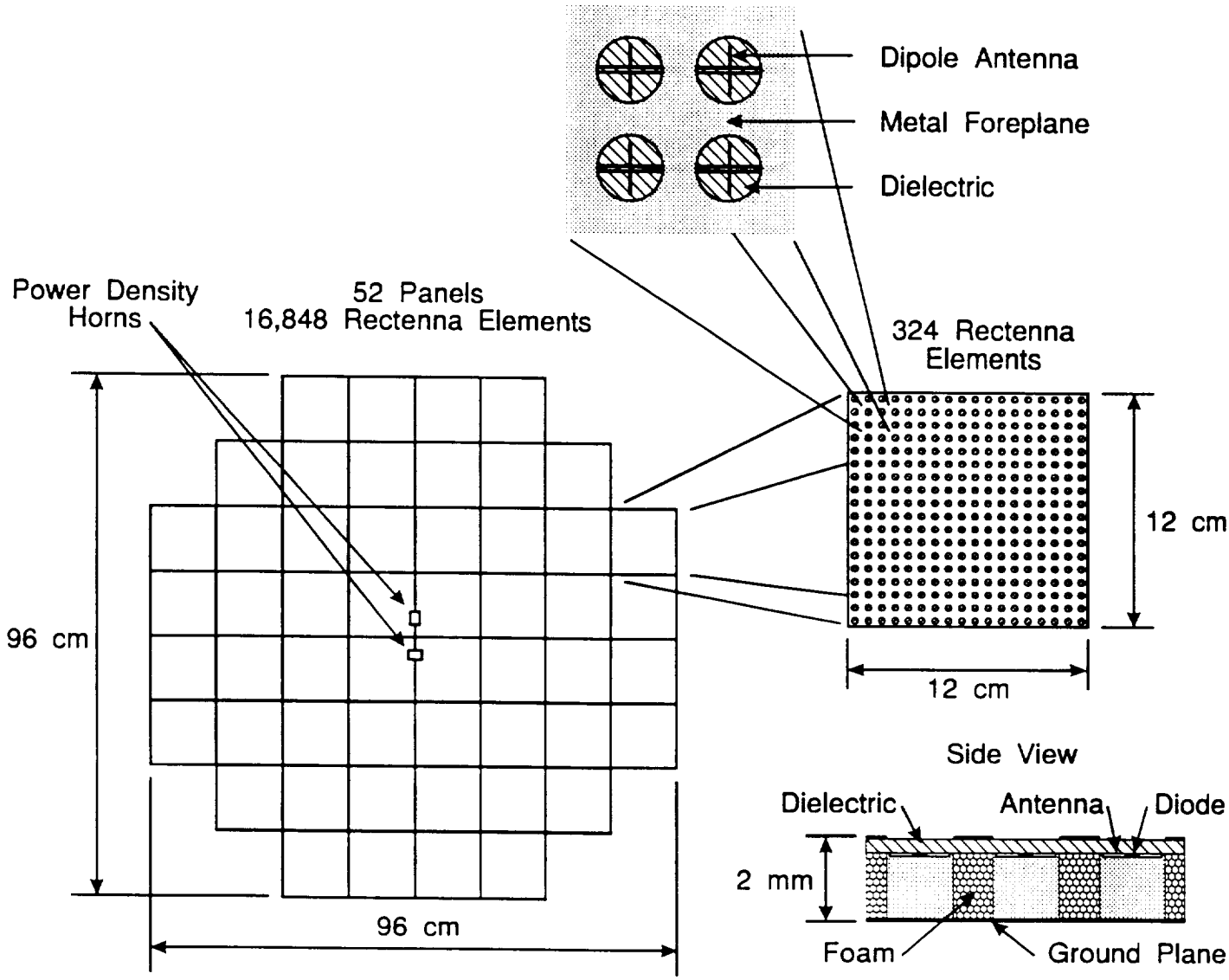

Figure 2.3-2. 35 GHz rectenna array designed for the WISPER satellite.

The performance of a 35 GHz rectenna element is shown in Figure 2.3-3 [14]. A 75% conversion efficiency for a rectenna element has been achieved by ARCO Power Technologies, Inc.

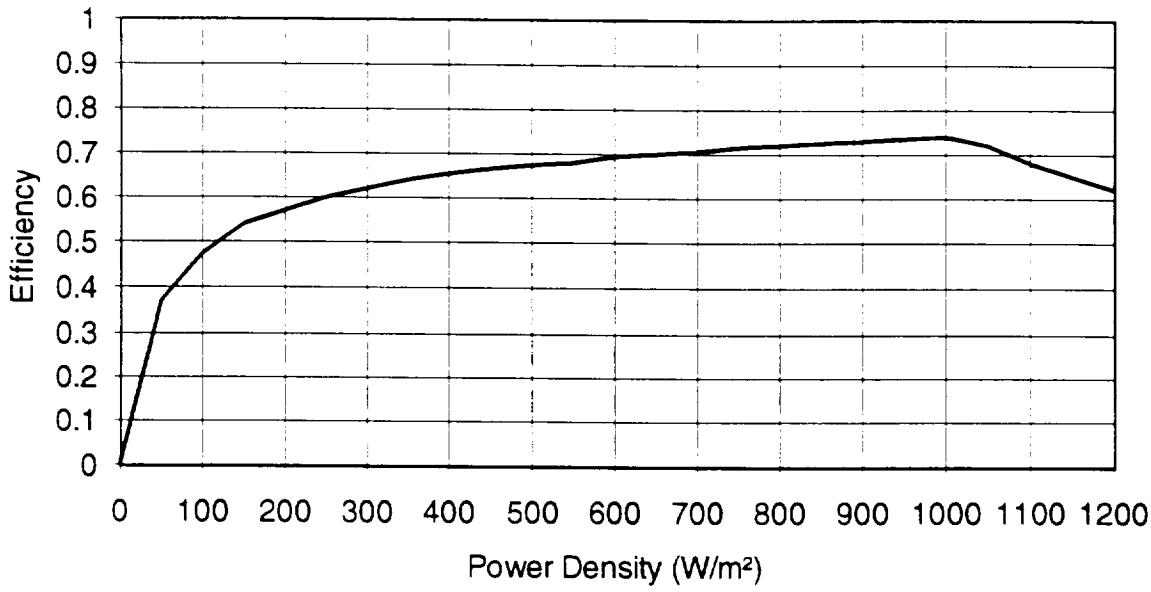

Figure 2.3-3. Rectenna element performance at 35 GHz [14].

However, the packing efficiency of the elements is not ideal due to the high frequency. Based on the manufactures advice, the maximum conversion efficiency of the rectenna array is 50%. Figure 2.3-4 shows the corrected performance curve for the proposed rectenna array.

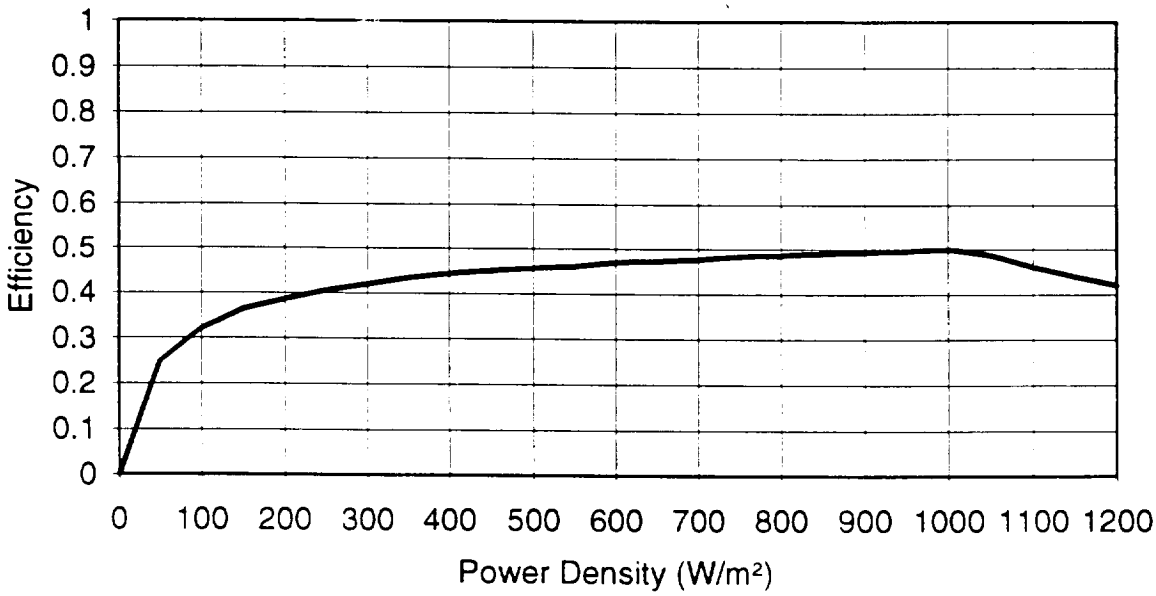

Figure 2.3-4. Corrected rectenna array efficiency at 35 GHz.

Applying the corrected efficiency to the 96 cm diameter array of Figure 2.3-2, the performance of the 35 GHz rectenna array is simulated in Figure 2.3-5.

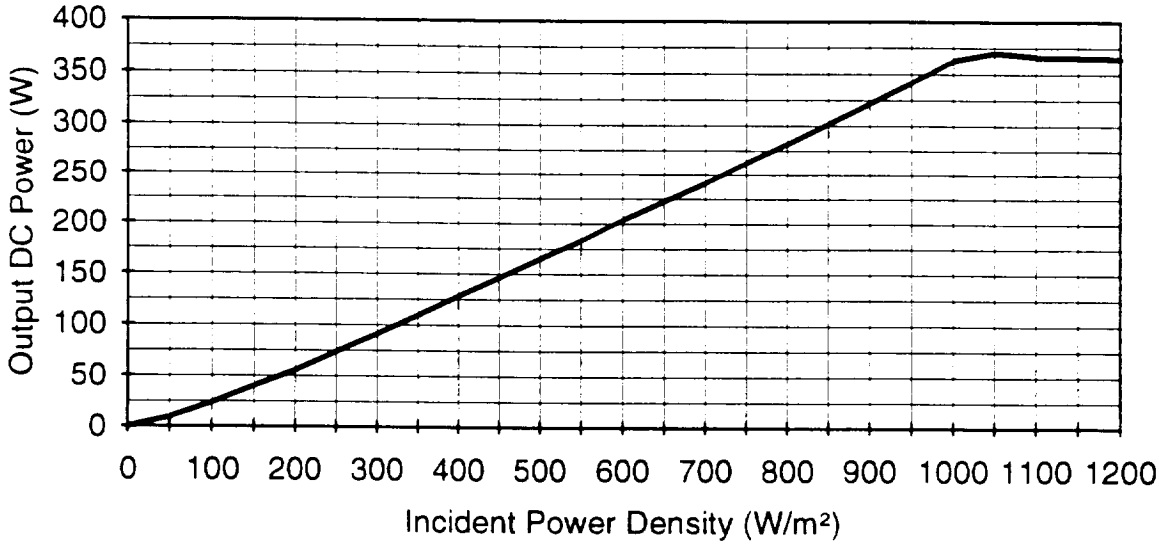

Figure 2.3-5. DC output power of the 35 GHz rectenna with a 96 cm diameter.

By comparing the graphs of figures 2.1-2 and 2.1-4 to Figure 2.3-5, the output DC power can be estimated.

2.3.2 Power Density Detection

The power density at the spacecraft will be detected in two ways. One Ka-band standard gain horn antenna will be placed on the underside of the focal point platform to face earth. The purpose of this antenna is to detect the incident power density to the spacecraft. Two Ka-band gain horns will be orthogonally placed on the frontside of the platform to detect the focused power density from the inflatable dish. Efficiency calculations and polarization tracking can be performed using the energy collected by these two horn antennas.

Because the rectenna is linearly polarized, detection of the incoming energy on the rectenna will dictate the rotation of the microwave feed at the ground station antenna. Polarization alignment is critical to ensure maximum reception by the rectenna.

The power signals from all three horns and the rectenna will be metered and sent to the A/D ports in the computer. From the computer, the information will be relayed to the ground station. The main power density components include the gain horns, attenuators, microwave sensors and power meters as shown in Figure 2.3-6. These components will have to be designed, fabricated, and tested for the space environment. Details of components are given in Table 2.3-1.

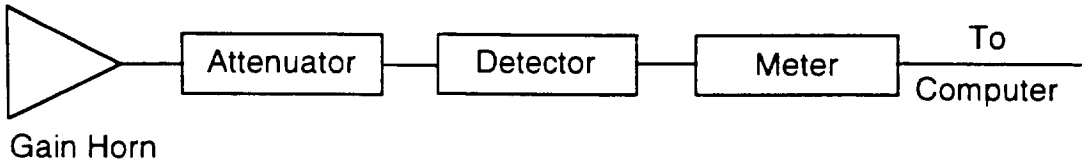

Figure 2.3-6. Microwave detection schematic diagram.

Table 2.3-1. Components for detecting microwave power density.

Component	Dimensions (cm)	Mass (kg)	Required Power (W)
Horn Antenna	4.5 x 2.5 x 2.0	0.05	0
Waveguide-Coax Transition	3.9 x 2.5 x 2.0	0.2	0
Attenuator	3.8 x 0.75 x 0.75	0.14	0
Sensor	9.4 x 3.8 x 3.8	0.14	0
Cable	2.4 mm type, 15 m	(N/A)	0
Microwave Power Meter	35.6 x 8.9 x 2.2	0.45	8
DC Power Meter	35.6 x 8.9 x 2.2	0.45	8

Note: Operating temperatures for all components are 0 - 50^{o}C.

2.3.3 Power Patterns and Pointing Accuracy of Inflatable Dish

A design tradeoff is required when deciding the diameter of the inflatable dish. To collect a large amount of the transmitted power, the dish diameter needs to be large. However, the pointing accuracy requirements also increase with diameter. Due to the large separation distance between the transmitter and satellite, the pointing accuracy of the inflatable dish is crucial. For the WISPER satellite, the power density is required to remain within 1 dB of the beam peak. Also, the pointing accuracy of the satellite is required not to fall below 0.01^{o}.

Power patterns of the inflatable dish were computed using a FORTRAN program. The program performs a Fourier-Bessel transform using a uniform taper across the aperture area to calculate the far field power pattern. As shown in Figure 2.3-7, the power pattern of the 14 m inflatable dish is given at 35 GHz and at 600 km. The 1 dB reference occurs at 112 m from the beam axis. Thus, a 0.01^{o} pointing accuracy is achieved.

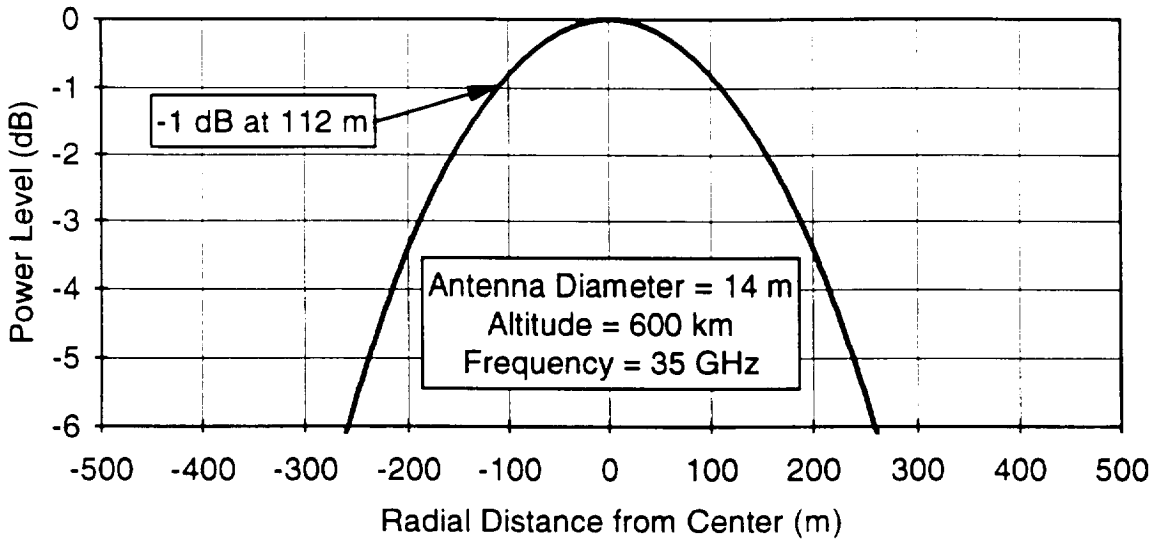

Figure 2.3-7. Far field power pattern of 14 m inflatable dish at 600 km.

For comparison, the pattern was computed at 500 km as shown in Figure 2.3-8. The 1 dB reference occurs at 93 m from the beam axis. Again, a 0.01^{o} pointing accuracy is required. With a 14 m dish, a 0.01^{o} pointing accuracy is needed at any distance in the far field.

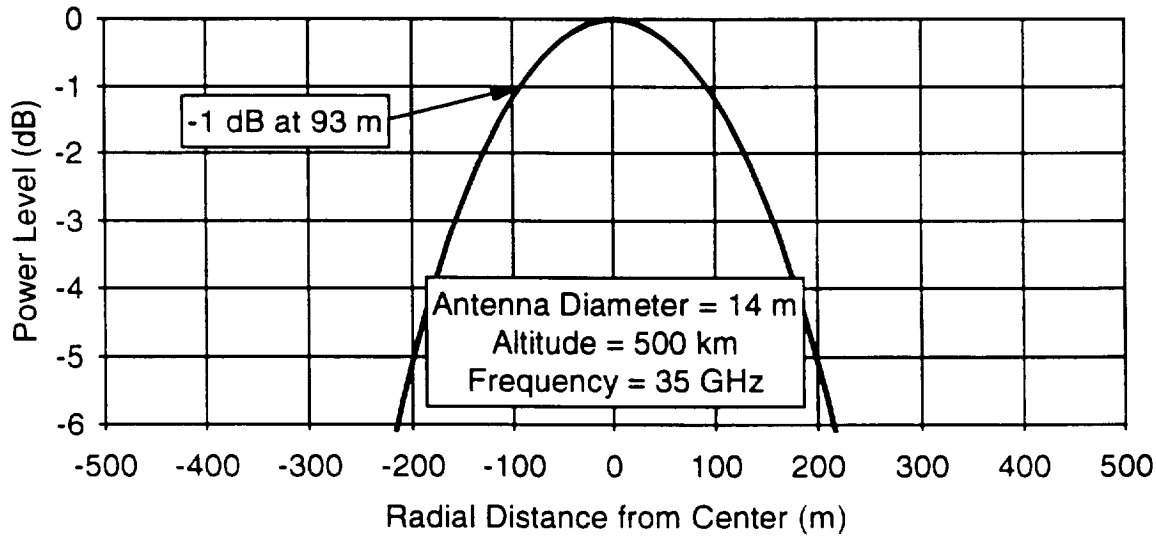

Figure 2.3-8. Far field power pattern of 14 m inflatable dish at 500 km.

Interferometer dipole sets operating in the C-band will provide pointing accuracy information for the satellite.

2.3.4 Monopulse Beacon

The other major component on the focal point pertains to the ground station pointing accuracy. A continuous wave (CW) and circular polarized signal at 12 GHz will be transmitted to the ground station at all times during the power beaming. The beacon consists of space qualified power supply and traveling-wave tube amplifier (TWTA), model 8522HC, made by Hughes Electron Dynamics Division. The output power of the beacon is 14 W. Table 2.3-2 lists physical and electrical characteristics of model 8522HC.

Table 2.3-2. Characteristics of 12 GHz beacon transmitter.

Component	Size (inches)	Weight (kg)	Efficiency (%)
Power Supply	8.0 x 3.2 x 3.8	1.85	>90
TWTA	12.7 x 2.6 x 2.4	0.7	55 - 58

The power supply requires a 4 minute warm-up before transmitting the microwave signal. The power supply will draw 22 W during the warm-up period and 35 W during the 12 GHz transmission.

2.4 Ground Station Requirements

The proposed ground station transmitter is shown in Figure 2.4-1. Two 200 kW gyrotrons will be used as sources to feed the 25 m antenna. A monopulse receiver will provide a pointing accuracy of 0.001^{o} to align the antenna with the WISPER satellite.

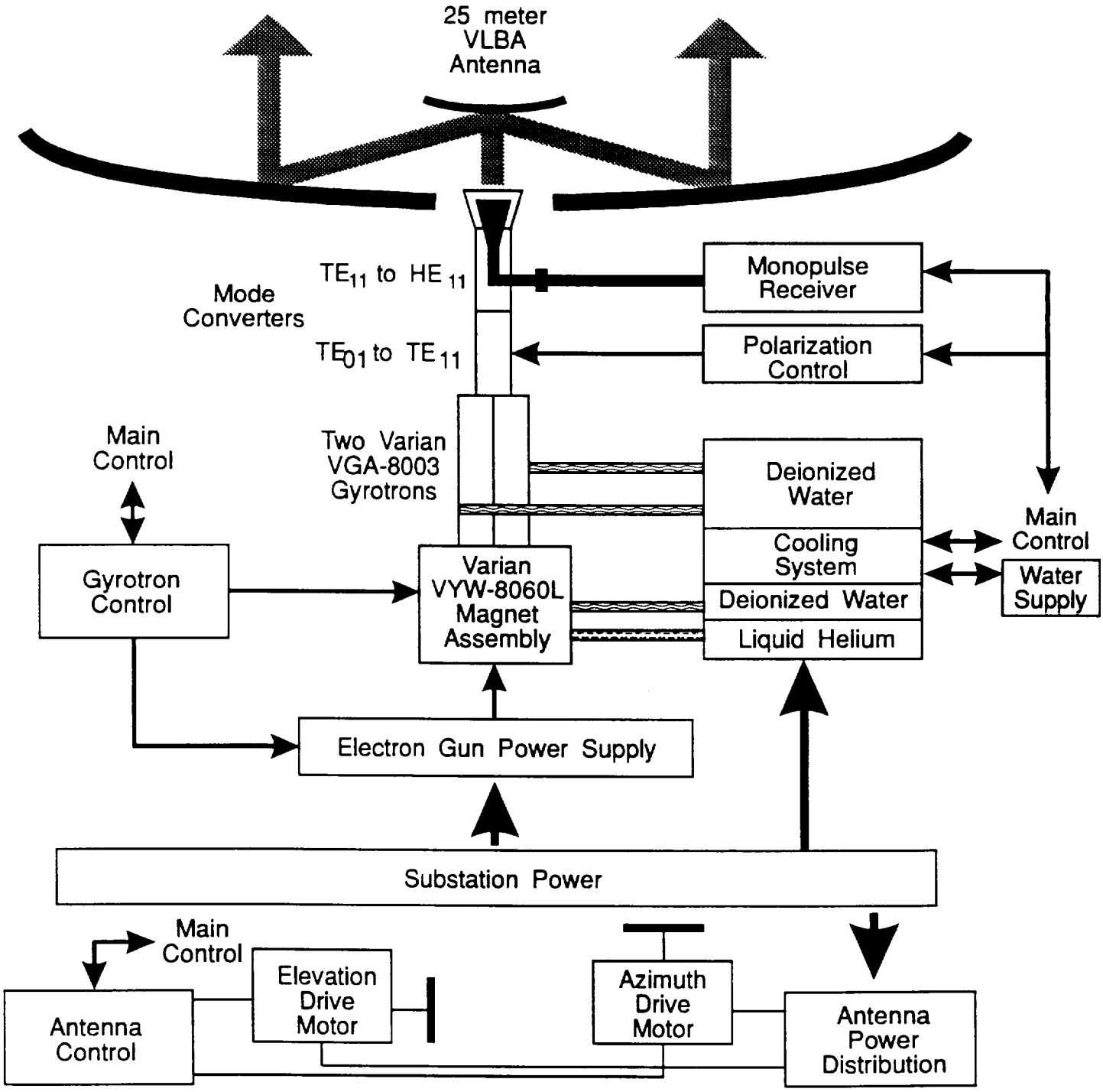

Figure 2.4-1 Ground station configuration.

2.4.1 Transmitting Antenna

A 25 m antenna with a high aperture efficiency is required for high frequency power beaming applications. The selection of the diameter is based on pointing accuracy

requirements and the availability of the antenna. As seen in Equation 2.1-1, aperture efficiency is important for power beaming applications because the total power transmitted is the product of the aperture efficiency and the power produced by the microwave power source.

An aperture efficiency of 50% at 35 GHz is achievable by the Very Long Baseline Array (VLBA) radio telescope antenna [15]. The VLBA, model 3250, is produced by Radiation Systems, Inc. located in Richardson, Texas. The VLBA has 200 AccuShape panels that provide a 0.46 mm root-sum-square (rss) surface tolerance ($\lambda/19$ at 35 GHz). The antenna has a Cassegrain feed system and a 20 ft x 20 ft x 10 ft hub directly under the main reflector. The hub is capable of holding 3,000 pounds of equipment. Cassegrain reflector configurations are mechanical steerable and can also be arrayed [16].

The VLBA is an elevation-over-azimuth mount. For a direct overhead pass by WISPER, the VLBA would be required to stop power beaming at 3^{o} from zenith and rotate 180^{o}. Power beaming would then commence after the antenna is correctly aligned with WISPER.

Power Pattern. Power patterns were also computed for the VLBA with uniform aperture illumination. As shown in Figure 2.4-2, the power pattern of the 25 m dish is given at 35 GHz and at 600 km. The 1 dB reference occurs at 63 m from the beam axis. Thus, a 0.006^{o} pointing accuracy is needed. As with the inflatable antenna, the same pointing accuracy is required at other transmission distances.

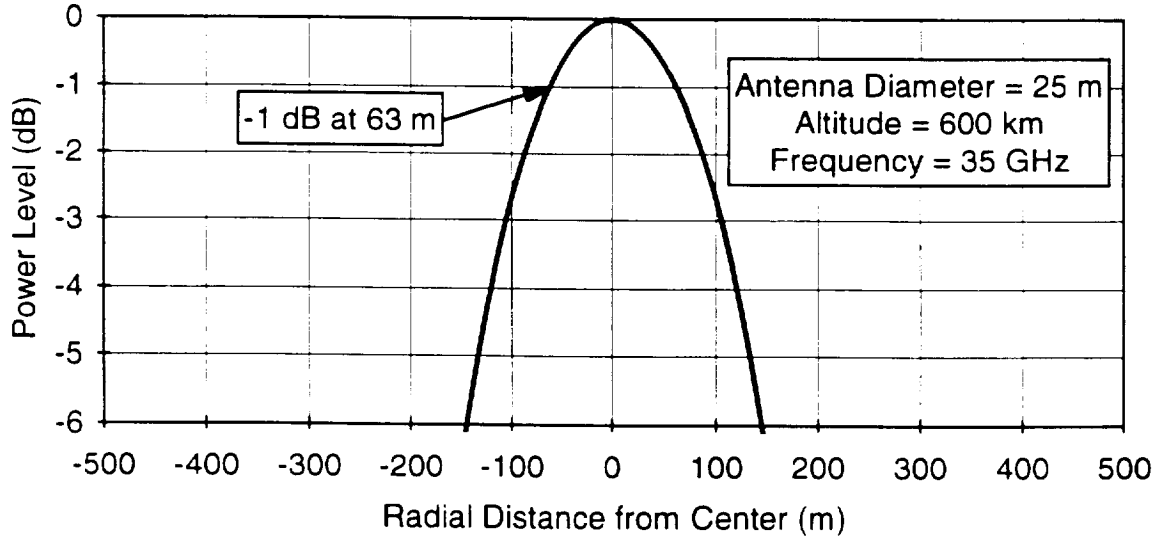

Figure 2.4-2. Far field power pattern of the transmitting antenna.

The pattern was computed with an uniform aperture distribution. In actual systems, a uniform distribution is not achievable. By having a non-uniform distribution, the antenna gain is reduced which relaxes the pointing requirements. The beam efficiency

is increased (i.e. lower sidelobes) with a non-uniform distribution. However, a high aperture efficiency is required for this application because it directly affects the amount of power transmitted in the main beam.

2.4.2 35 GHz Power Source

A goal for the Phase I experiments is an output of 100 W from the rectenna at an orbital altitude of 600 km. By setting this requirement, the ground station power source could be specified to obtain this goal. Varian Associates, Inc. manufactures a 35 GHz gyrotron, model number VGA-8003, that produces a 200 kW CW microwave beam [17]. Two gyrotrons will be needed to meet the rectenna output requirement,. The gyrotrons are synchronized together to produce 400 kW of power feeding the antenna.

At 35 GHz, gyrotron tubes have been invented to produce large amounts of power. Gyrotrons are a special breed of microwave tubes. The gyrotron is a microwave vacuum tube which operates on the basis of the interaction between an electron beam and microwave fields where coupling is achieved by the cyclotron resonance condition. This coupling allows the beam and microwave circuit dimensions to be larger than a wavelength. Thus the power density problems encountered in conventional traveling-wave tubes and klystrons at millimeter wavelengths are avoided in the gyrotron.

Gyro-devices require an electron beam where most of the electron energy is transverse to the axis of the tube. In linear beam tubes, such as klystrons and TWTs, energy parallel to the tube axis is used. Only electron energy transverse to the magnetic field axis can be used in a gyro-device. Gyro-devices have 100 times the output power capability of conventional tubes. Figure 2.4-3 shows a schematic diagram of a CW gyrotron oscillator. In this device the electrons are emitted from a narrow annular band on the inner element of the electron gun. The main magnet has two main windings which provide the cyclotron resonance field for the gyrotron and other windings for gun control and beam steering. The beam, which is compressed by the main magnet field, passes through the interaction cavity and continues into the collector region where it dissipates on the water-cooled walls of the collector. From the interaction cavity the RF follows the taper to the 63.5 mm (2.5 inch) output cylindrical waveguide.

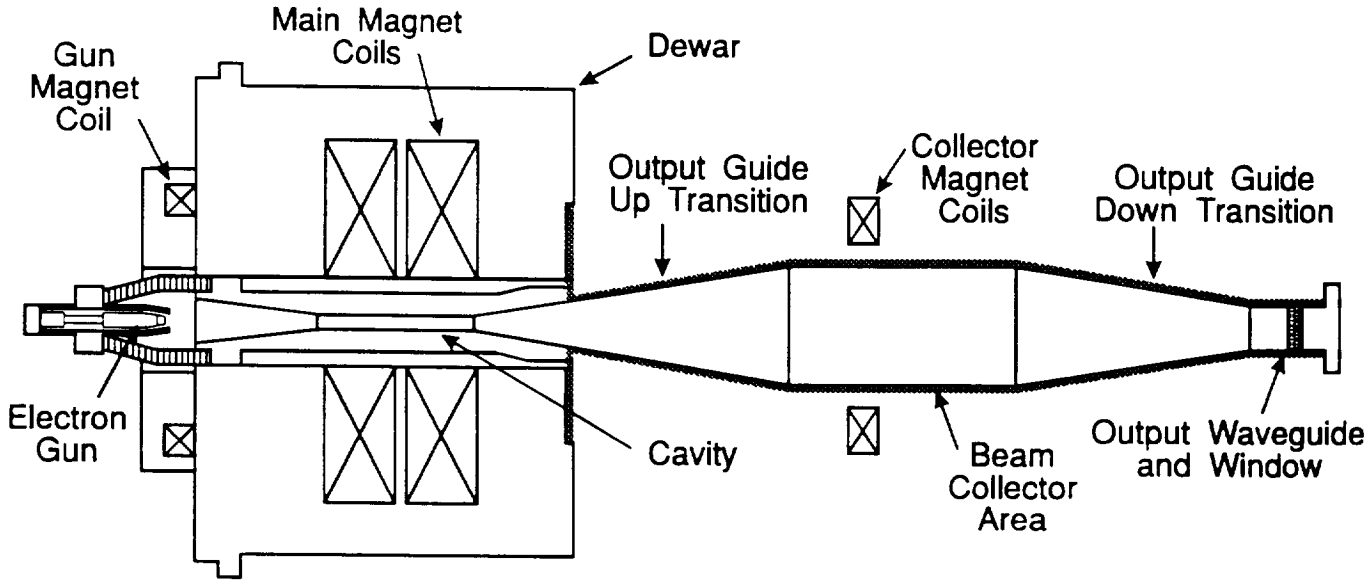

Figure 2.4-3. Schematic diagram of a gyrotron oscillator.

The electrical operating parameters of the VGA-8003 gyrotron are given in Table 2.4-1.

Table 2.4-1. Electrical operating parameters of the 35 GHz gyrotron.

Electrical Operating Parameters	Minimum	Maximum	Typical
Frequency (GHz)	34.5	35.5	35.0
Beam Voltage (kV)	70	90	85
Beam Current (A)	4	10	7
Collector Dissipation (kW)	-	700	595
Gun Control Anode (kV) (with respect to cathode)	14	30	26
Heater Voltage, AC (V)	6	15	8.5
Heater Current (A)	1	5	3.5
Heater Power (W)	10	75	30
Body Current (mA)	-	50	10
Gun Anode Current (mA)	-	10	2
Power Output, T_{01} mode (kW)	40	200	*
Efficiency (%) (at max. power output)	30	-	40

* The power can be varied in a smooth and reliable manner by variation of the gun anode voltage.

The gyrotron requires an average magnetic field of 13.5 kG with shaping of the field which can require peak fields as high as 20 kG for maximum gyrotron efficiency. The magnetic fields can be supplied by Varian magnet assembly VYW-8060L which produces a 35 kG maximum magnet field. This magnet assembly requires 115 VAC and 40 A. Thus, superconducting magnets are required for the gyrotron to achieve a high DC magnetic field. The superconducting coils require liquid helium to be supplied at a rate of 1 liter/hour and liquid nitrogen at a rate of 0.5 liter/hour. To profile the beam in the collector a large water-cooled coil is used. The coil requires 26 A at 125 VDC with 1-2 gpm of cooling water. In addition, two air-cooled coils are used. These coils require two separate power supplies rated at 3 A and 15 VDC.

The VGA-8003 gyrotron is approximately 105 inches long and 16 inches in diameter. The weight is approximately 500 pounds.

The VYW-8060L magnet assembly is 28.5 inches in diameter and extends 15 inches below the mounting plate and 18.5 inches above. The weight is approximately 600 pounds.

The output power from the gyrotron is delivered by a 63.5 mm (inner diameter) circular waveguide in the TE_{01} mode. The TE_{01} mode is appropriate for transmission through long runs of straight circular waveguide because the loss can be made small by using an overmoded guide [18]. However, the TE_{01} mode is unpolarized and produces a hollow conical radiation pattern with zero power along the waveguide axis [19]. High power microwave transmission requires an axi-symmetric, narrow, pencil-like beam with well-defined polarization. Therefore, a mode conversion is necessary.

The almost perfectly linearly polarized Gaussian HE_{11} hybrid mode that is radiated from an open-ended, circumferentially corrugated, oversized circular waveguide satisfies this condition. The HE_{11} mode can be generated from the TE_{01} gyrotron mode by a multi-step conversion sequence. This approach uses the TE_{11} mode as a polarized intermediate mode. Thus, the mode sequence is TE_{01} to TE_{11} to HE_{11}. This sequence has the advantage that the converters can be made without bends and allow an arbitrary choice and fast change of the polarization plane by rotating the TE_{01} to TE_{11} converter around its axis. This conversion process can be designed to be extremely efficient. The mode conversion efficiency can occur at 97% for each section. These mode converters have a smaller radius (20 mm) than the radius of the gyrotron output guide (31.75 mm). Therefore, a tapered circular waveguide section is placed at the output of the gyrotron to the input of the TE_{01} to TE_{11} section. The TE_{01} to TE_{11} converter is then connected to the TE_{11} to HE_{11} converter section. The power is then radiated from the tapered open-ended circular waveguide (63.5 mm diameter).

The power density received by the microwave detectors on WISPER will be processed and communicated to the VLBA. This information will dictate the rotation of the TE_{01} to TE_{11} converter to ensure correct polarization alignment between the VLBA and rectenna.

Because the power is contained within a circular waveguide, the threat of voltage breakdown or arcing within the waveguide walls becomes a concern. Using the minimum radius of 20 mm, the maximum power handling capacity can be computed. Voltage breakdown occurs at a field strength of about 3 x 10^6 V/m for room temperature air at sea level [20]. The dominant mode in a circular waveguide is the TE_{11} mode. The maximum average power carried by the TE_{11} mode is given by [21]

$$P_{max} = 3.97 \times 10^{-3} \sqrt{1 - \left(\frac{\lambda}{3.41\,a}\right)^2}\, a^2 E_{max}^2 \ [W] \qquad (2.4\text{-}1)$$

where a is the radius (m) and λ is the free space wavelength (m). At 35 GHz and a radius of 20 mm, the maximum power that can be transmitted down the guide before breakdown is about 14 MW. Good engineering practice should provide a safety factor of at least two, so the maximum power transmitted down the mode converters should be limited to 7 MW. The design for the ground station will have a maximum transmitted power of 400 kW, so breakdown in not an issue for these oversized circular waveguides.

2.4.3 Monopulse Receiver

The circular polarized 12 GHz beacon from the satellite is received by the VLBA and fed into the monopulse receiver. Radiation Systems, Inc. makes a monopulse receiver, model 133, that works in the autotrack mode. The autotrack mode will provide a pointing accuracy of 0.001^o. Isolation from the 35 GHz power beam is achieved by low pass filters in the waveguides that feed the monopulse receiver.

2.5 Microwave Safety

The health effects of microwave radiation have been studied for many years. The current ANSI recommendation is both a function of frequency and the time of exposure. At 35 GHz, the maximum safe radiation level is 5 mW/cm^2 (50 W/m^2) averaged over six minutes [22], [23]. However, the standard was determined from a questionable research database and with an eye toward leniency [24]. More recent research has indicated that long term effects may occur at much lower power densities [25]. However, conclusive evidence does not yet exist.

The WISPER project proposes to impose a high safety standard in anticipation of growing public concern and of forthcoming experimental data providing evidence of microwave radiation effects. The best way to protect the public and personnel from microwave radiation is to prevent them from entering the beam.

The two areas of concern are the airspace above the transmitter and the ground area near the antenna. In the airspace, the accidental interception of radiation by aircraft and birds is considered. Figure 2.5-1 shows the radiated near field pattern from the VLBA at an altitude of 12 km. The pattern shows the microwave power concentrated in

a 14 m diameter beam where commercial airplanes are flown. Thus, the accidental passage of an object through the beam will occur over a short period.

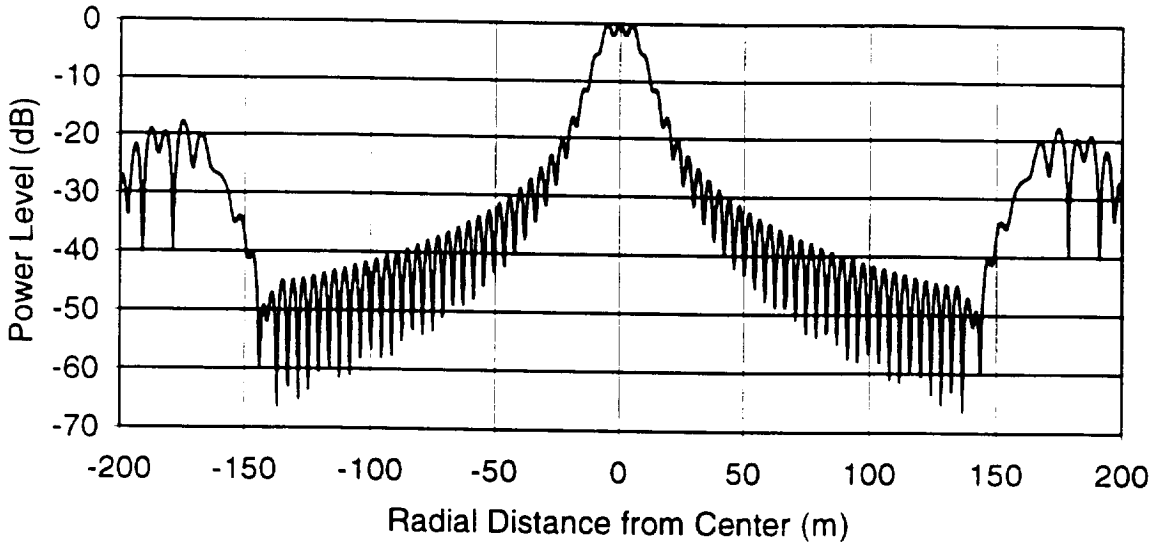

Figure 2.5-1. Near field pattern of the 25 m VLBA antenna at 35 GHz and a distance of 12 km.

Near field patterns were also computed at a distance of 1 km above the VLBA as shown in Figure 2.5-2. It is of interest to note that a null occurs on the beam axis at this distance.

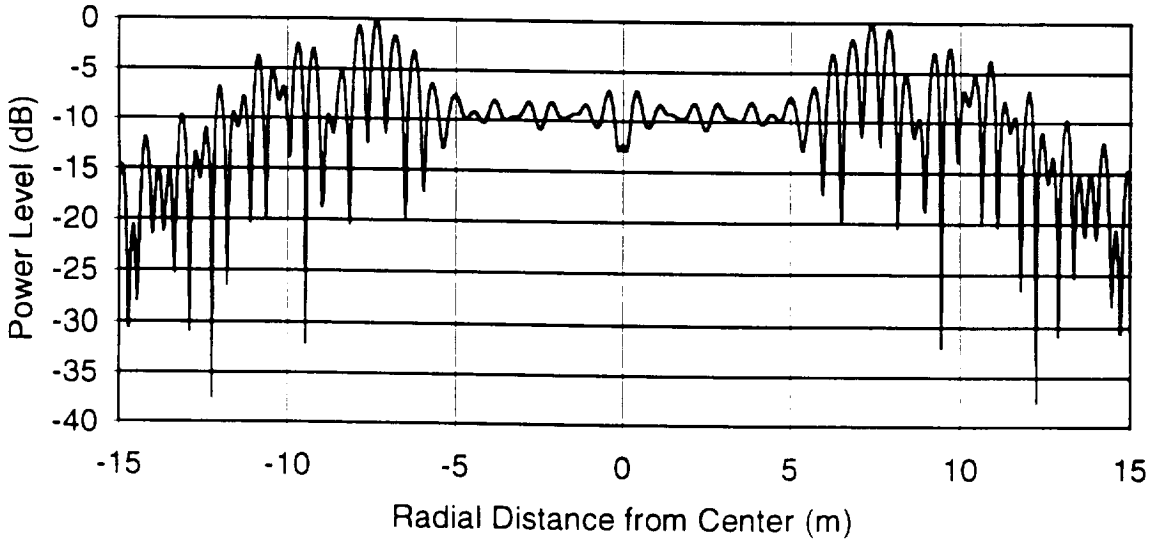

Figure 2.5-2. Near field pattern of the 25 m VLBA antenna at 35 GHz and a distance of 1 km.

The probability of thermal damage is low. Additionally, the microwave power beam will operate for approximately 2 minutes maximum, implying a fairly low probability of interception.

However, several precautionary measures may be required. First, a restricted airspace corridor around the beam will be created. As the power beam is swept across an arc of 80 to 100 degrees, this corridor will be large and therefore difficult to control. Furthermore, restricted airspace provides no protection to birds. Active tracking will be used to ensure a restricted corridor. Metallic objects as small as 1 cm^2 in cross sectional area can be tracked by installing a system at the ground station [26]. With such a system, the beam can be shut down if an object appears.

Two other methods have been proposed in the use of ground-to-ground microwave power transmission [27]. The first method implements a passive radar that detects microwave backscatter. Any metallic object entering the periphery of the beam will reflect energy toward the ground receiver and cause the transmitter to be shut down. The second method involves monitoring the received microwave power from the WISPER satellite. If the signal suddenly decreases, a communication signal will be sent to the ground station to shut down the power.

Similar methods can be used to protect people and/or wildlife on the ground. The best course of action is to prevent them from coming too close to the transmitter by restricting the nearby area. The exact size of such an area is determined by the power pattern measurements taken on the ground level. This area is dependent on the amount of power that is being transmitted. An additional measure of protection can be provided by active detection techniques. Personal microwave monitors, fixed site monitors, and hand held detectors can be installed at the ground station [22].

UAF
NASA USRA ADP
Space Systems Engineering

WIreless Space Power ExpeRiment

Chapter 3

Laser Power Experiments

Phase II

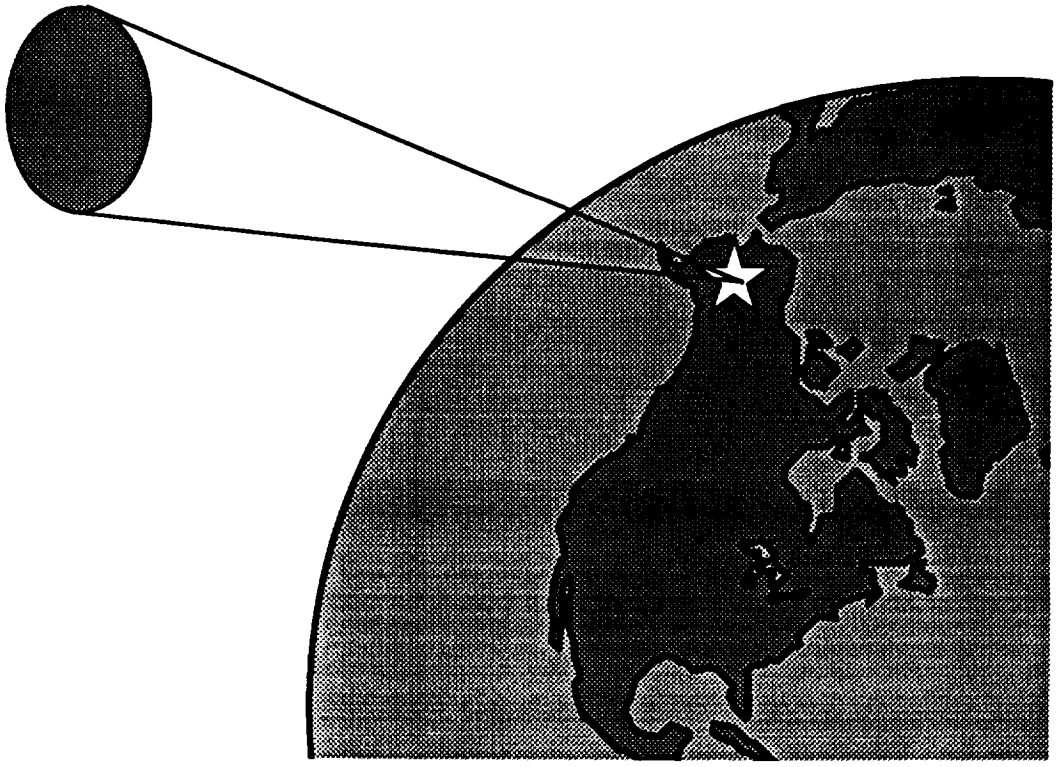

3.0 Laser Power Experiment - Phase II

Lasers are emerging as the future of power beaming. Technology advancements over the past several years, mainly sponsored by the Strategic Defense Initiative, have produced a state of the art that is capable of directing blocks of highly collimated laser power from the surface of the earth to lunar distance and beyond. The divergence of laser beams is minimal, and therefore they require much smaller transmitters and receivers which allows much greater power densities. At this stage laser technology is too inefficient and massive to be considered for space-to-space or space-to-earth applications, but it is realizable in the near-term for earth to space operations.

3.1 Laser Experiment Overview

The limited sources of power in space and the high cost of generating or storing that power make the Laser Power Beaming (LPB) concept attractive. Fuel and batteries for power generation and storage are important factors in determining the cost and lifetime of any spacecraft. When the satellite is in the earth's eclipse, the solar arrays are shadowed so the batteries must supply the necessary power. This cycle of charging and discharging shortens the life of the batteries. By beaming power to the satellite during the eclipse, the lifetime of the spacecraft can be increased by alleviating the load on the batteries.

3.1.1 Operational Sequence

By the time the microwave power Phase I experiments have been completed, the satellite's orbit will have decayed to an altitude of approximately 500 km. At this level, the laser beaming will take place. Two 2 kW lasers, one with a 0.85 μm wavelength and the other with a 1.06 μm wavelength, will be used. These two wavelengths are selected due to atmospheric attenuation windows. The satellite will be available to receive laser power when it is within 60 degrees from the ground station zenith. A direct overhead pass will allow 3.0 minutes of potential lasing time for power transfer. A schematic of the operational sequence is shown in Figure 3.1-1.

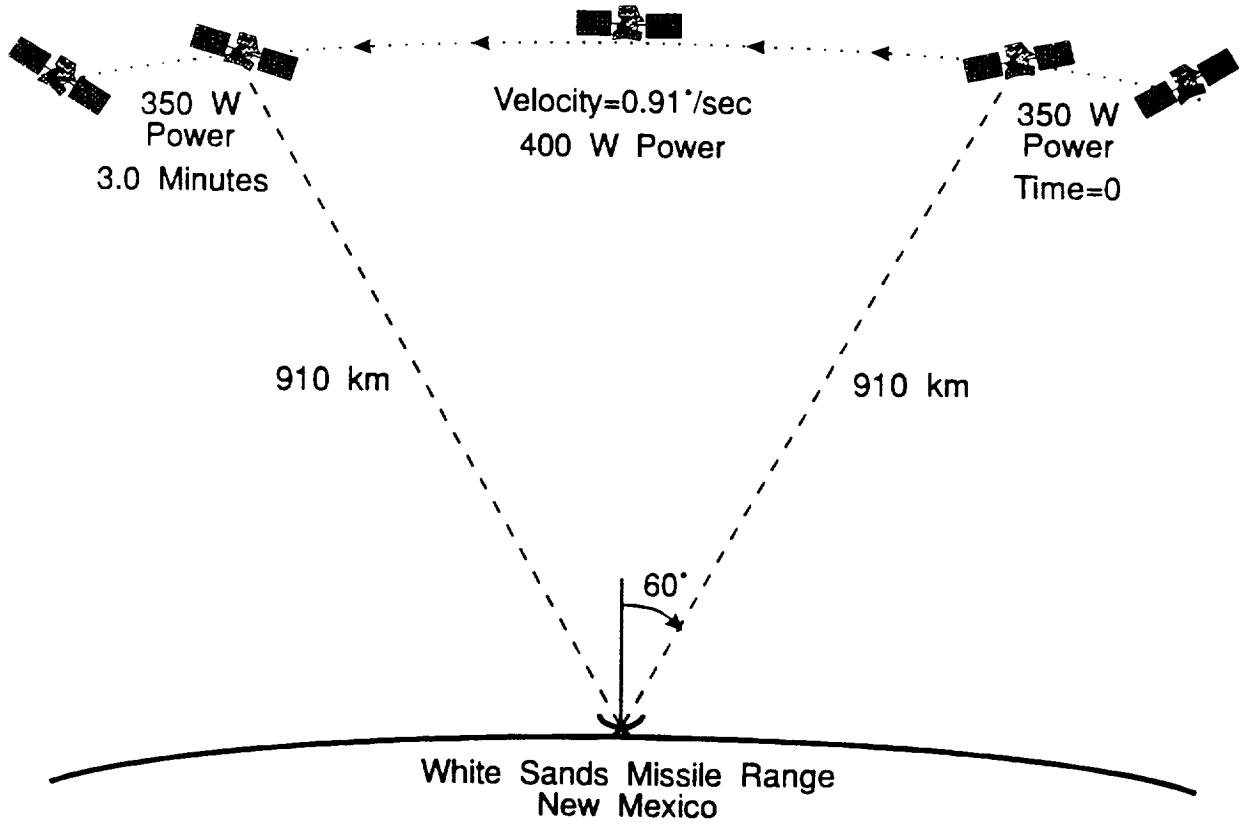

Figure 3.1-1. Laser power beaming operational sequence.

3.1.2 Experimental Objectives

After the microwave power experiments have been completed, the WISPER satellite will jettison its inflatable antenna in preparation for the laser power beaming experiments. A successful completion of the laser beaming program can be summarized in the following list of mission goals:

1. Successfully receive laser power from a ground station.
2. Determine the power conversion efficiencies of both Gallium Arsenide (GaAs) and Silicon (Si) photovoltaics.
3. Perform power density measurements of the transmitted beam.
4. Measure the incident laser spot diameter.
5. Analyze the laser transmission through the atmosphere.
6. Coordinate and maintain pointing accuracy of the ground station and spacecraft.

The efficiency degradation of both GaAs and Si photovoltaic arrays will be studied. The 0.85 μm wavelength laser can be directed first at the GaAs panel which has been optimized for this wavelength and then towards the Si panel. The power from each panel will be compared. Next, a similar experiment using a laser with a 1.06 μm

wavelength will be pointed at each panel. The Si panel is optimized for this wavelength. The laser power can also be varied in each of the cases mentioned.

3.1.3 Atmospheric Effects on Laser Power Beaming

A variety of atmospheric effects are significant when beaming power by laser: attenuation (also called extinction), thermal distortion, kinetic cooling, and bleaching.

Attenuation of laser radiation in the atmosphere is described by Beer's law as

$$\tau = e^{-\gamma z} \tag{3.1-1}$$

where τ is the transmittance percentage, γ is the attenuation coefficient (km^{-1}), and z is the path length (km). Attenuation can be divided into absorption and scattering. The attenuation coefficient is defined by

$$\begin{aligned} \gamma &= \alpha + \beta \\ &= \alpha_m + \beta_m + \alpha_a + \beta_a \left[km^{-1}\right] \end{aligned} \tag{3.1-2}$$

where α (km^{-1}) and β (km^{-1}) are the absorption and scattering coefficients while the m and a subscripts denote the molecular and aerosol processes, respectively.

At wavelengths of 0.85 and 1.06 μm, the principle atmospheric absorbers are: molecules of water, carbon dioxide, and ozone in that order. Although nitrogen and oxygen are the most common atmospheric gases, they do not exhibit molecular absorption because they do not possess an electric dipole moment.

In the absence of precipitation, the atmosphere contains finely dispersed solid and liquid particles (ice, dust, organic material, etc.). These particles vary in size from a few molecules up to 20 μm in radius. Such a colloidal system is known as an aerosol. The finite conductivity of these particles results in aerosol absorption.

While a precise calculation of the atmospheric absorption coefficients is extremely difficult, a simple model can be used [1]. The assumption is that variations in the absorption transmittance are due to changes in the water content of the air. In order to estimate the absorption transmittance, the following equations were developed:

$$\tau_{ai} = e^{-A_i\sqrt{\omega}} \quad \text{for } \omega < \omega_i \tag{3.1-3}$$

$$\tau_{ai} = K_i\left(\frac{\omega_i}{\omega}\right)^{\beta_i} \quad \text{for } \omega > \omega_i \tag{3.1-4}$$

where

$$\omega = 10^3 \rho z_p \tag{3.1-5}$$

and A_i, K_i, β_i, and ω_i are constants given for each transmittance window. The variable ρ is the density of water vapor (g/m^3), ω is the total precipitable water (mm), and z_p is the path length (km). At 0.85 μm the constants are: $A_i = 0.0305$, $K_i = 0.8$, $\beta_i = 0.112$, and $\omega_i = 54$. At 24^o C and a relative humidity of 75%, the predictable water content is calculated to be 0.0162 mm/m of path. Therefore a 5 km path would have $\tau_{ai} = 0.764$.

Rayleigh Scattering is due to the displacement of bound electrons by the incident electric field. The electrons act like an induced dipole which oscillates at the same frequency as the incident radiation and emits electromagnetic radiation. This re-radiated energy constitutes the scattered light. Due to the size of air molecules, Rayleigh Scattering is negligible for lasers with wavelengths above 0.6 μm.

Gustav Mie, a German meteorologist, developed a complex model of the scattering of electromagnetic waves by small dielectric spheres [1]. The model takes into account the size, shape, dielectric constant, and absorptivity of the particles. The difficulty with models based on Mie's theory is that all of these factors vary in the real atmosphere. Therefore, an attempt has been made to relate β_a to meteorological data. The formula which appears to provide the best relationship is

$$\beta_a = \frac{3.91}{V}\left(\frac{\lambda}{0.55}\right)^{-\delta} \qquad (3.1\text{-}6)$$

where V is the visual range (km), λ is the wavelength (μm), and δ is the aerosol constant. The aerosol constant has been found to be 1.3 ±0.3 depending on the humidity. This yields about $\beta_a = 0.06$ at 75% humidity.

Nonselective scattering is due to large atmospheric particles consisting of haze, fog, and rain. Nonselective scattering effects are frequency independent. An extensive study of this scattering has been done by Chu and Hogg [1]. Their results show that for light rain (2.0 mm/h) the transmittance is reduced by 8.9%/km and for heavy rain (19 mm/h) the transmittance is reduced by 19.2%/km.

Thermal distortion can be caused by blooming (conduction) or wind (convection). Thermal blooming occurs when the air molecules absorb laser photons and quickly release them as heat, causing the temperature of the air in the beam to rise. The hot air near the center of the beam axis expands rapidly outward at the speed of sound. This expansion causes a decrease in the mass density, which in turn lowers the index of refraction near the beam's axis. This expansion also causes the beam to defocus [1]. The bending is greatest near the center of the beam where the heat is concentrated. This causes a pattern with a stronger irradiance around the circumference of the beam as depicted in Figure 3.1-2.

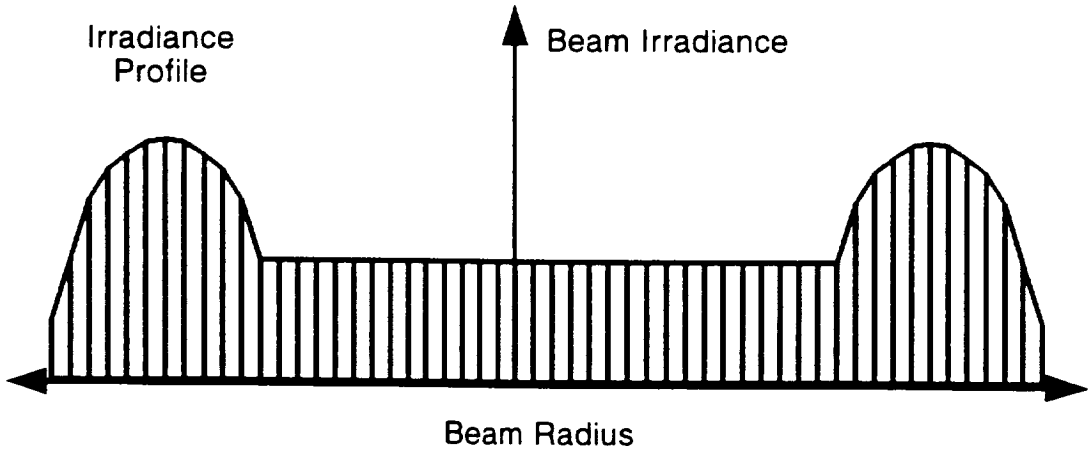

Figure 3.1-2. Conduction thermal blooming of a laser beam.

When wind transverses the laser beam, each molecule of air that crosses the beam is heated. This heating decreases the density and index of refraction. Since the index of refraction is higher on the windward side, the beam bends into the wind. As shown in Figure 3.1-3, the beam is bent more on the leeward side of the beam so the pattern becomes kidney shaped on the windward side [1]. Wind induced distortion is negligible when the wind is strong because the molecules of air do not have time to heat. In addition, the strong wind will also negate any conduction effects.

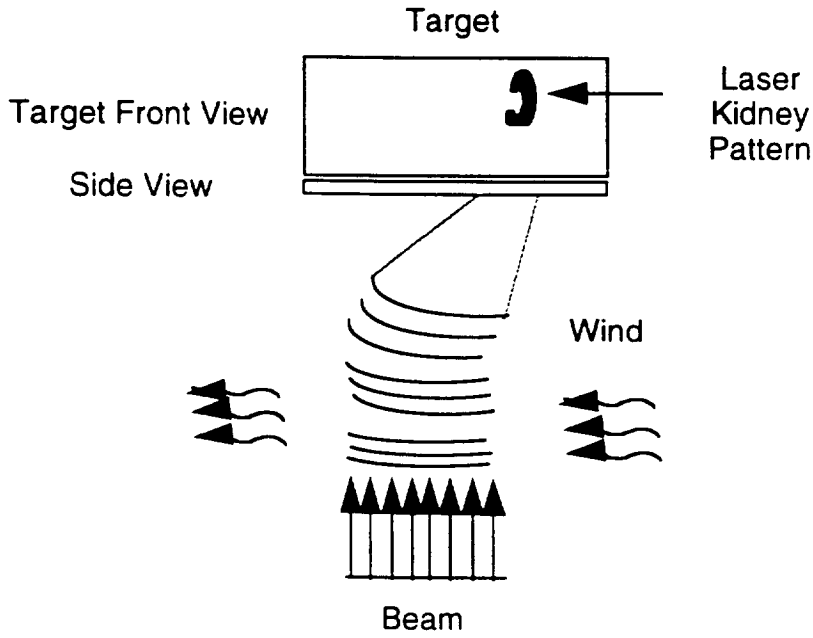

Figure 3.1-3. Convection blooming of a laser beam.

Kinetic cooling occurs when the absorbed beam energy is stalled in a series of energy transfers. Bleaching occurs when the absorption mechanism is saturated causing an

increase in the atmospheric transmissivity. These effects only occur when the laser is pulsed.

3.2 Wavelength and Laser Selection

The satellite is designed to receive power from a laser at wavelengths of both 0.85 and 1.06 μm. These wavelengths were determined by the available atmospheric transmission windows, as well as the efficiency curves of the monochromatically tuned photovoltaic receivers on the spacecraft. The criteria which determined the selection are shown in figures 3.2-1 and 3.2-2.

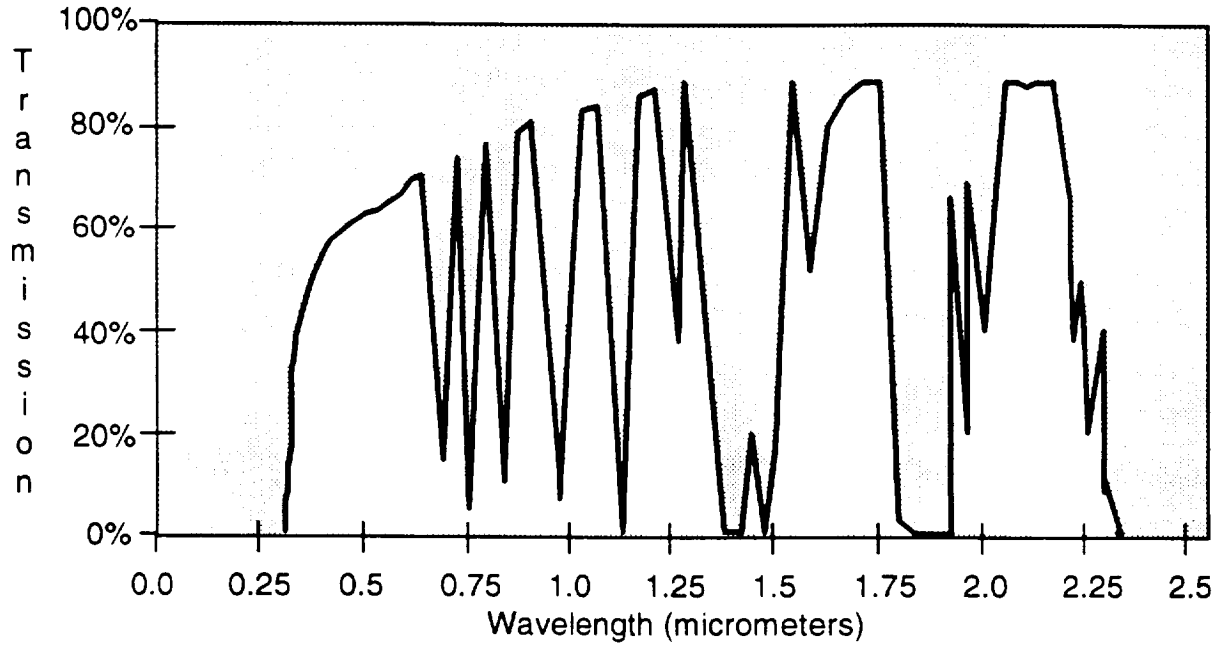

Figure 3.2-1. Laser atmospheric transmission windows with laser located 2 km above sea level.

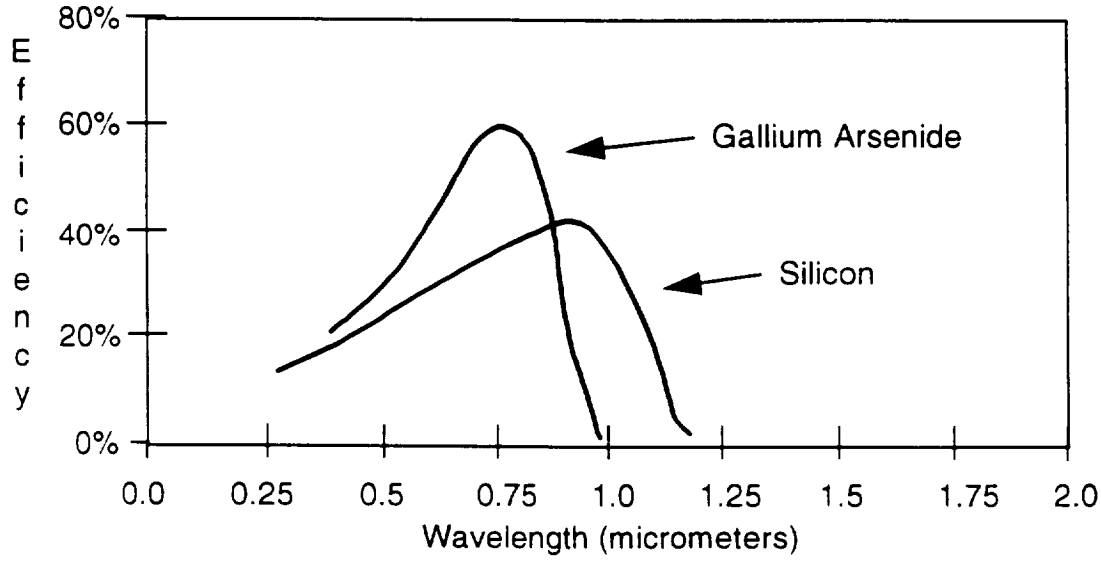

Figure 3.2-2. Photovoltaic compensated efficiencies.

The laser will operate in the visible spectrum where the atmosphere is nearly transparent. Laser windows exist between wavelengths of 350 nm and 1100 nm. Below 350 nm, the window is limited by atmospheric absorption. Above 1100 nm, the window is limited by photovoltaic cell technology [2].

There are only three laser types that are available for near-term demonstrations of LPB. These lasers are the neodynium YAG laser, the copper vapor laser, and the free electron laser (FEL). Of the three lasers mentioned, only the YAG laser has a CW format while the other two operate in pulsed mode.

The FEL is the prime candidate for LPB. The FEL meets two major requirements: 1) the FEL is one of the few lasers that can deliver the required high power and 2) the FEL is capable of operating in the wavelength range where the PV receivers are most efficient. Since the FEL is tunable to ±10% of its design frequency, a slight change in frequency will be possible for further experimentation.

The two types of FELs under consideration are the induction linac FEL (IL-FEL) and the radio frequency FEL (RF-FEL). The RF-FEL is better suited for this type of application because its pulse train is in the picosecond range which appears as a continuous wave to the photovoltaic receiver [3]. The IL-FEL only has nanosecond pulse separation.

Figure 3.2-3 shows the main components of an RF-FEL [4]. An RF linear accelerator provides a high-velocity beam of electrons. A magnet "wiggler" creates a periodic and vertical magnetic field. The resonator consists of two mirrors, one is a total reflector and the other is a partial reflector to allow the energy to escape. Beam-bending magnets direct the electron beam away from the laser beam to the electron beam dump.

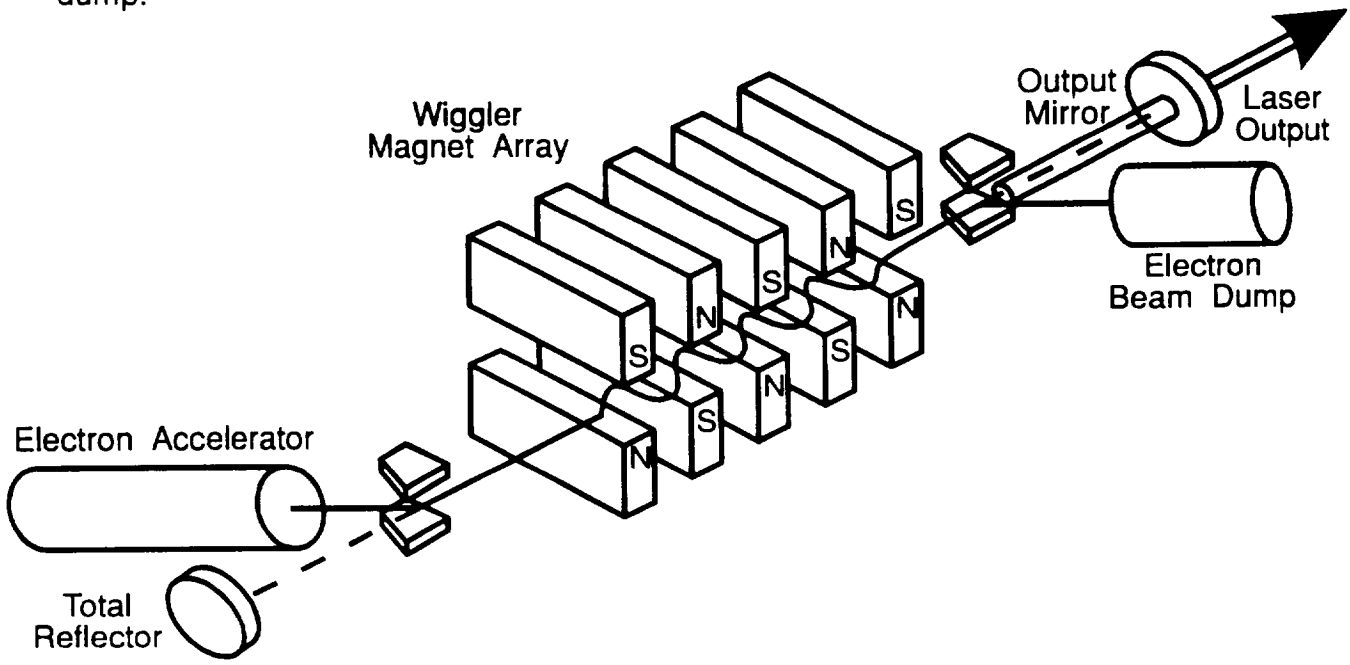

Figure 3.2-3. RF-FEL components.

3.3 Spacecraft Requirements

A less traditional application of photovoltaic cells is to act as a receiver for monochromatic light transmitted from a laser. Several advantages of using photovoltaic cells as a receiver include proven performance in space, a long history of operation, no moving parts, and a high conversion efficiency of monochromatic light into DC power at optimum wavelengths. Several laser power experiments have been performed on earth with a variety of solar cells, therefore the next step is proving laser power beaming in space.

Laser sensors will be arranged on the GaAs array to obtain an accurate measure of the incident beam intensity and the laser spot size. This information will not only be used to determine the efficiency of the photovoltaics, but also to analyze the atmospheric effects on the beam as well as the performance of the adaptive optics system.

3.3.1 Photovoltaic Receiver

The technology proposed for use with LPB is similar to existing photovoltaic science. The primary concern of the experiment is the availability of a cell that will provide a 50% conversion efficiency.

Of the four photovoltaic arrays onboard the spacecraft, two will be specially designed to efficiently receive the monochromatic laser beam. One panel will be composed of specialized GaAs cells that are designed to operate most efficiently at a wavelength of 0.85 μm. A conversion efficiency of 50% is anticipated with this design. The second laser panel will be composed of a tuned Si array with an expected conversion efficiency of 40%. The actual efficiency of the two arrays must account for operating temperature. This diversity will allow for a comparative analysis of the performance of each type of cell design.

3.3.2 Cell Technology

A primary concern in designing a photovoltaic laser receiver is the response of the cells to the laser illumination. It is unknown what effect the pulsed waveform will have on the receiver. Experiments announced at the 1992 Space Photovoltaic Research and Technology (SPRAT) conference showed that the response of cells to pulsed lasers is significantly different than the response to CW illumination, which is more like intense solar light. Previous experiments have shown difficulties with lasers using the FEL or copper-vapor formats, which have longer pulse periods. Few tests have been completed using the RF-FEL, and the results have been inconclusive about the response of photovoltaic cells to the picosecond micropulse structure of the laser [2].

One such experiment shows that the response of GaAs cells to a CW laser is close to 45%, but for a pulsed laser the number drops to between 1% and 3%. This drastic decrease is due to the extremely high peak currents (1000 to 3000 peak to average ratio) and the concomitant response capability of PV cells [5]. The next question is how

to correct for the pulsed format on the cell level. For many types of cells the electrical response time will be shorter than the pulse spacing, therefore the cell output will follow the laser peak power. This means that the cell must be designed to minimize series resistance. Additionally the effects involving the interaction of the short pulse with the inductance and capacitance of the cell must be compensated in the design [6].

The problems can be solved by either changing the laser pulse shape or by designing a solar cell to accept the pulsed input. Cell designs that may overcome this problem are a high efficiency, light trapping silicon cell, and a monolithic, low-inductance GaAs cell. Silicon has a minority carrier lifetime on the order of a thousand times longer than that of GaAs. The long lifetime means that the pulse can be stretched which reduces the peak current to a value where the series resistance is much less important. Efficiencies are comparable to that of GaAs cells by incorporating a light trapping structure. The light trapping structure allows the solar cell to be made thin without the loss of light generated current. These cells are also expected to be extremely radiation tolerant. A schematic of the cross grooved light trapping structure of the thin silicon solar cell is shown in Figure 3.3-1 [6].

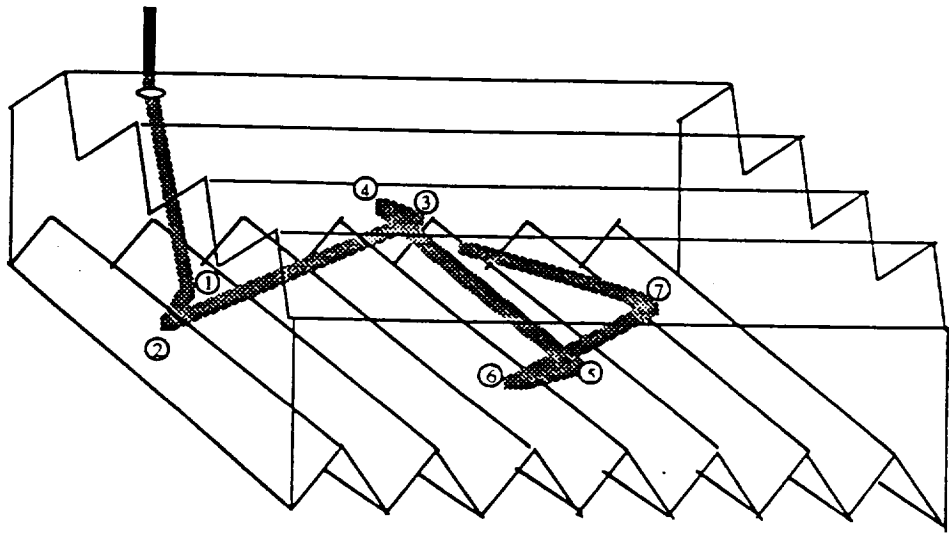

Figure 3.3-1. Silicon solar cell construction.

The other option is to use a monolithic voltage-adding GaAs cell and a power management circuit that is capable of accepting output with extremely high current spikes. This design implies that the cell structure must have low inductance and series resistance, as well as an output circuit with low inductance and a power management system which can tolerate high peak currents. Shown in Figure 3.3-2 are the important elements of a monolithic voltage-adding design for a GaAs cell, including the necessary blocking diode and integral capacitor [7].

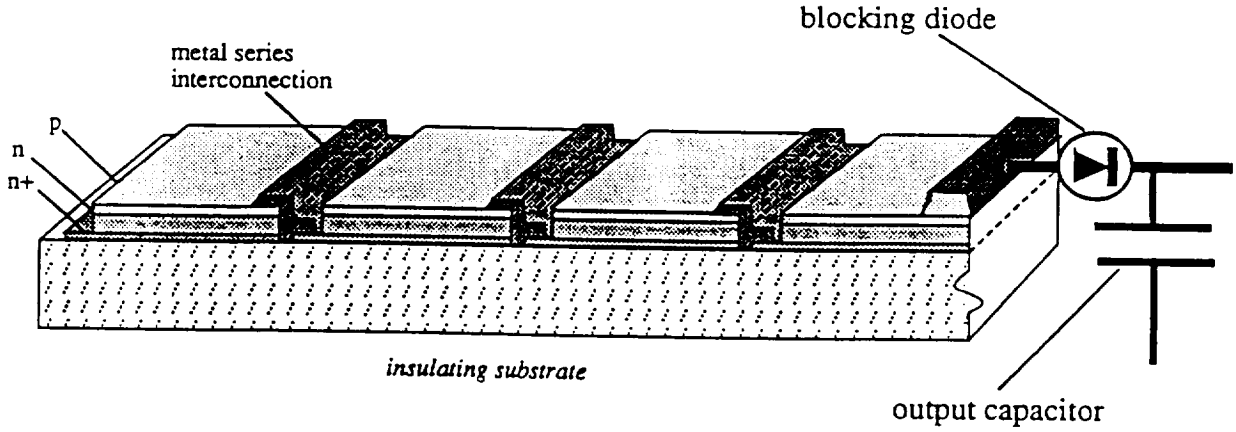

Figure 3.3-2. GaAs solar cell construction.

The specialized cell design alone will not be able to smooth the pulsed output from a laser. High intensities common from a pulsed format cause unique problems for photovoltaics, such as GaAs which are made from direct bandgap materials. Direct bandgap materials make these cells capable of tracking the illumination profile on a nanosecond time scale. This characteristic is important since all laser types, except the RF-FEL, have a pulse width in the nanosecond or longer range. RF-FELs have a much shorter pulse width typically between 10 to 20 picoseconds. This pulse width is significantly lower than the response of the photovoltaic cells. There has been some speculation about this time difference. Because the RF-FEL has such a short pulse width, many experts believe it cannot be tracked by the cells. The cells would recognize the monochromatic light as CW instead of pulsed. Conclusive research has not yet been completed on the topic of response time to the RF-FEL. But many authorities in the field believe that if a RF-FEL in the kilowatt to megawatt range can be developed, it would be compatible with existing photovoltaic technology and ideal for beaming laser power to space.

3.3.3 Spot Size

The size of the beam seen at the satellite can be calculated by [2]

$$r_{spot} = \frac{0.61\, d\, \lambda}{r_{lens}} \text{ [m]} \qquad (3.3\text{-}1)$$

where r_{lens} is the radius of the mirror used to focus the beam (m), d is the source to receiver distance (m) and λ is the wavelength (m).

The spot radius is defined as the first zero in the diffraction pattern, containing 84% of the energy. For the spacecraft at an altitude of 500 km, an operating wavelength of

0.85 μm for the GaAs panel, and a 5 m diameter transmitting mirror the spot size is calculated to have a 10.25 cm radius or 20.5 cm diameter. The Si panel has a similar altitude and transmitting mirror, but the optimum wavelength is 1.06 μm. Thus, the spot size radius is 12.9 cm or 25.8 cm diameter [6]. From the standpoint of the photovoltaics, calculation of the spot size is important for two reasons. First, it is important to have a target larger than the required spot size. Second, the spot size along with the incident power density must be known in order to address the issue of thermal management.

The first consideration should not cause problems due to the configuration of the WISPER satellite. The solar array is composed of four fold out panels, each 40.64 cm wide and 86.36 cm tall. For the GaAs panel, the spot size is half as wide and over one-fourth as tall which should fit neatly onto the panel. While the silicon spot size is slightly larger, once again there should not be a problem hitting the target panel. It should also be noted that the two panels were placed farthest away from the satellite body, so in either the GaAs or Si cases there is another panel of the same dimensions separating the photovoltaic receiver from the spacecraft. These panels should also absorb much of the 16% beam energy outside the spot area. The entire array can also be illuminated as well as all four arrays. The spot size is used to calculate the minimum size for thermal management considerations.

3.3.4 Receiver Array Format

Lasers require the same basic types of PV arrays as solar collection. The choices are between a flat-plate, thin film, or concentrator array. There are several advantages to a flat-plate array, such as projected efficiencies of over 50% for GaAs and 40% for Si [8]. Low pointing accuracy is needed, as cosine losses are small and thermal management is not required for power densities less than 2 kW/m^2 [8]. On the down side, the cell costs are high for large area arrays. Thin film arrays made of amorphous silicon, $CuInSe_2$, or CdTe are much cheaper and lighter but have correspondingly lower efficiencies (closer to 20%). It is also important to note that a majority of the thin film technology is still in the developmental stages.

On the WISPER satellite, due to the dual use of the laser receivers as solar collectors, flat plate array technology will be utilized. This is the most proven type of array, and would be the only cost effective design for the 0.35 m^2 area of the panel. It is important to note that the two panels that will be used for laser power beaming must be optimized for the specific type of cell that will be used in order to maximize power.

3.3.5 Thermal Management

The spot size and incident intensity of the laser beam is critical to designing a thermal management system. For the WISPER satellite with a spot diameter of 20.5 cm and power level of 400 W, the power density is calculated to be 12.125 kW/m^2. This power density exceeds the normal solar incident power of 1.358 kW/m^2 by a factor of almost 9.

Shown in Figure 3.3-3 are curves determined theoretically. They show the temperature response of both gallium arsenide and silicon photovoltaics to high incident power densities [9].

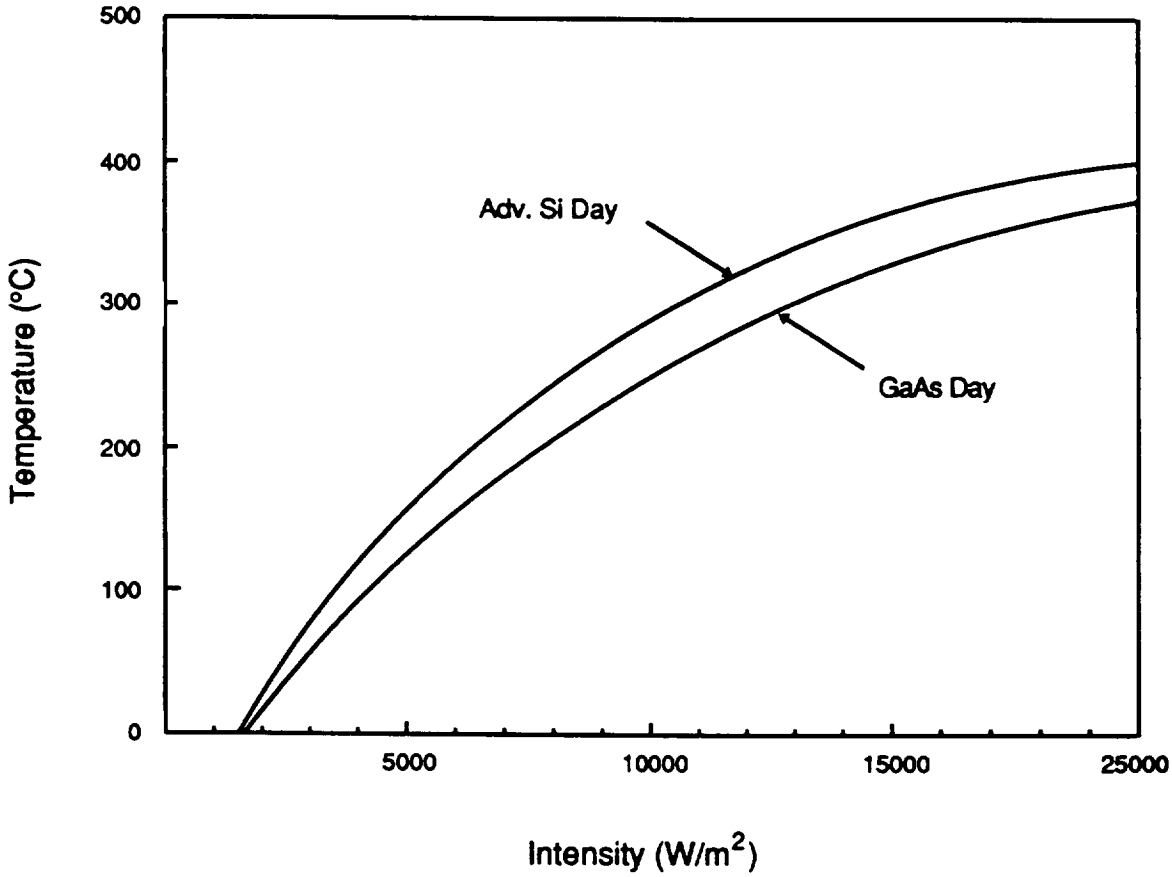

Figure 3.3-3. Theoretical operating temperatures of GaAs and Si PV cells in LEO.

Based on a projected power density of 12.125 kW/m^2 at the WISPER satellite, the GaAs panel will be heated to approximately 275^o C. The silicon array will be closer to 295^o C. These temperatures exceed the temperatures that the panels are normally exposed to. However, due to the short exposure period, the elevated temperatures should not harm the photovoltaic receiver.

3.3.6 Laser Sensors and Instrumentation

Based on the calculated incident laser spot size of 20.5 cm, an array of laser sensors will be positioned on the GaAs panel to provide an accurate dimension of the spot. The sensors are needed to verify the spot size and to determine the photovoltaic conversion efficiency.

The GaAs photovoltaic cells being used for the laser power beaming have an anticipated power conversion efficiency of approximately 50% at the proposed

wavelength of 0.85 μm [10]. This efficiency can be verified with the data collected by the laser sensors. Using both the value of incident power intensity and the measured spot size, the total incident power can be compared to the power supplied by each of the panels as measured by the onboard power meter.

Sensor Selection: An array of PIN silicon photodetector/filter combination sensors will be used to measure the incident laser beamed power. This type of sensor is available from a number of manufacturers, in various configurations. UDT Sensors of Hawthorne, CA, manufactures a line of these particular sensors which will be considered here as a typical representation of those currently available.

These photovoltaic detector/filter combinations combine a PIN silicon photodiode and a multiple element colored glass subtractive filter. The glass subtractive filter is computer designed to correct the detector spectral response to the desired spectral response. This correction is accomplished by cementing together several separately polished colored glass types and then individually mating this filter to a spectrally selected photodiode. With the glass filter element mounted in front of the detector, the spectral response curve of UTD's PIN-10DF is shown in Figure 3.3-4 [11]. The PIN-10DF produces a flat spectral response from wavelengths of 0.45 μm to 0.95 μm. This response would be appropriate to examine both the atmospheric attenuation and the photovoltaic efficiencies as the RF-FEL changes its frequency to ±10% of its base frequency.

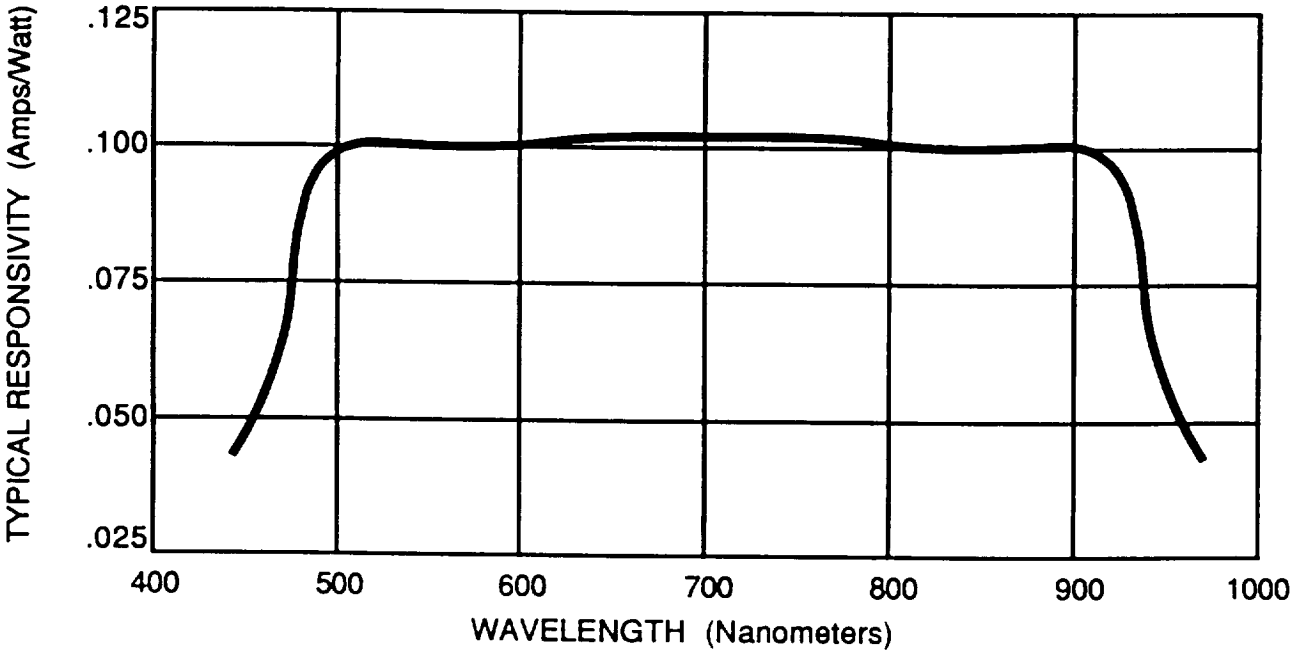

Figure 3.3-4. PIN-10DF spectral response curve.

A mechanical diagram of this particular photodiode model is shown in Figure 3.3-5 [11]. Rather than the space consumed by BNC connectors, it is possible to have this model custom built in a much smaller package with solderable leads. Some of the specifications for the PIN-10DF are listed in Table 3.3-1.

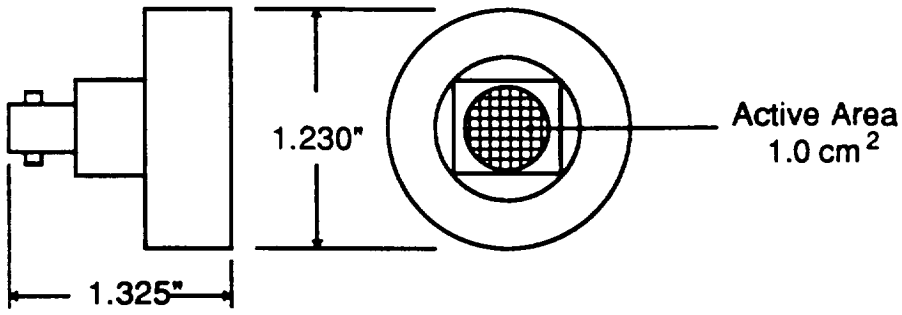

Figure 3.3-5. PIN-10DF mechanical detail.

Table 3.3-1. PIN-10DF specifications (typical at 22° C).

Active Area (cm^2)	Responsivity (A/W)	Capacitance (nF)	Rise Time (μs)	Shunt Resistance
1.0	1.0	10.0	1.0	5 MΩ

Sensor Operation: To accurately measure the laser intensity these detectors will be operating in a photovoltaic mode rather than the more common photoconductive mode. Figure 3.3-6 shows the internal construction of a photovoltaic photodiode.

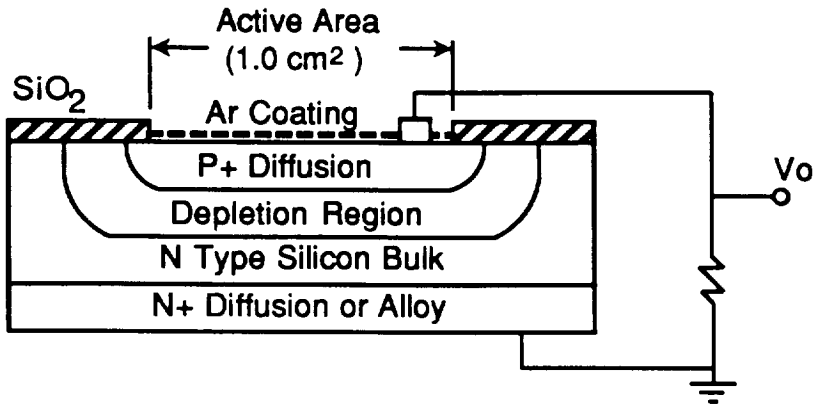

Figure 3.3-6. Photovoltaic photosensor construction.

Figure 3.3-7 suggests an appropriate amplifier circuit for this type of operation [11]. The electronic circuit elements can be integrated in the sensor package as a hybrid photodetector/amplifier for this custom application.

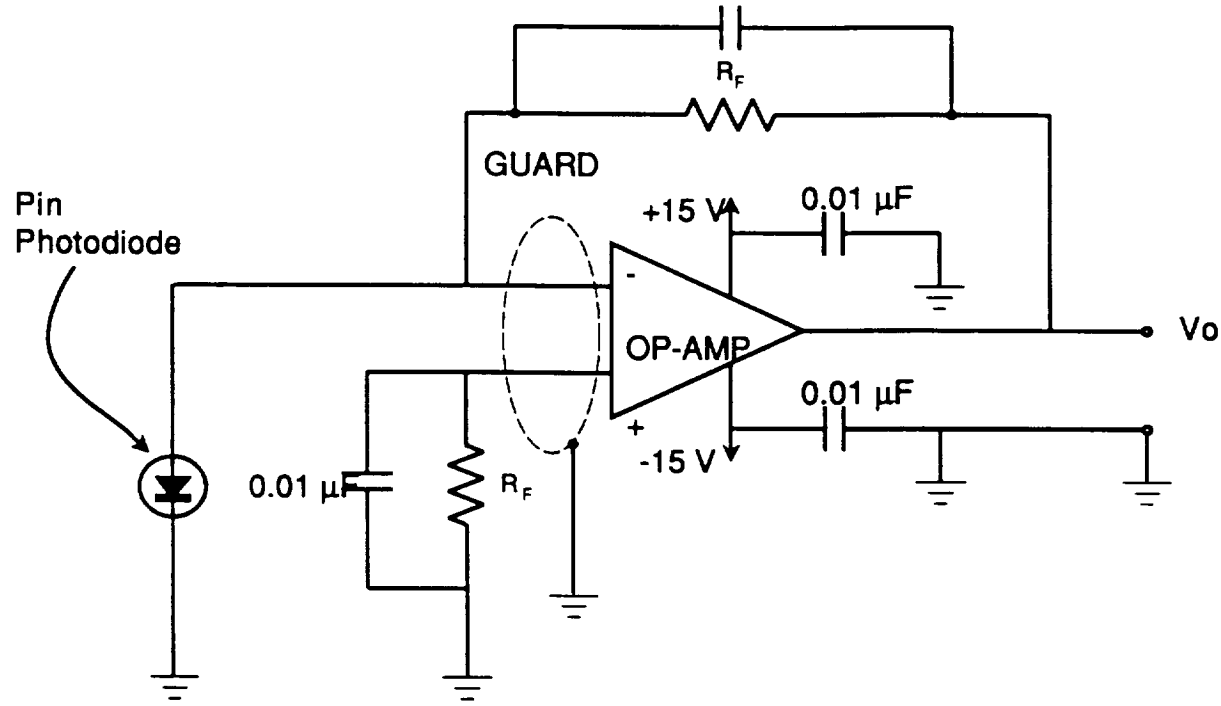

Figure 3.3-7. Internal current amplification circuitry in photovoltaic mode.

Sensor Positioning: A number of these detectors will be arranged on the GaAs photovoltaic panel to determine the position and size of the incident laser spot. A possible arrangement is shown in Figure 3.3-8. The intent of this geometric configuration is to assure that a minimum of three sensors will be within the 20.5 cm spot when it is entirely incident upon the PV panel. The information from this sensor array may then be used to help center the beam directly in the center of the panel. This configuration allows an accurate spot diameter measurement without using an unnecessarily large number of sensors. Any sensor in the main laser spot will have the capability of providing the incident power density information. If several sensors detect the laser power, the readings will be averaged to account for beam inconsistencies or sensor variations.

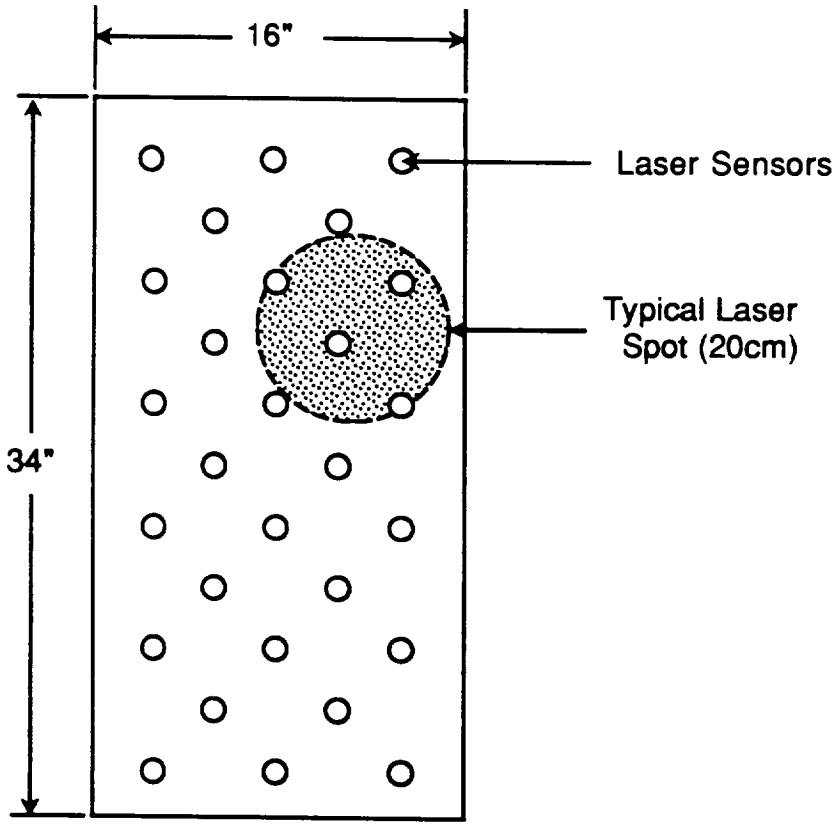

Figure 3.3-8. Laser sensor configuration.

This simple array of laser sensors will be used to collect the pertinent experimental data during Phase II of the WISPER project. The intent of the sensors is to determine the incident beamed power density and the laser spot size, which can then be used to calculate the efficiency of the GaAs photovoltaic cells. These PIN silicon laser sensor/filter/amplifier hybrids will be operated in an active photovoltaic mode to effectively collect and convey this information to the onboard computer system for further analysis.

Data Transfer: The power output of the photovoltaic sensors during the actual laser power beaming will be monitored by the satellite's CPU through a series of analog to digital converters. This data can then be stored in the computer for future evaluation or down linked through the TDRSS communication system to the ground station to confirm accurate target tracking and effective power delivery.

3.4 Ground Station Requirements

The ground site chosen for the WISPER project is the White Sands Missile Range, NM. In the near term, the availability of a 1 to 5 kW RF-FEL laser for laser power beaming

purposes is anticipated. Adaptive optics will be used to compensate for the atmospheric disturbance of the beam. However, turbulence, extinction and thermal blooming will attenuate the laser beam by a finite amount. A tracking telescope at the ground site will provide information on the position of the WISPER satellite for pointing the laser beam.

3.4.1 Adaptive Optics

A tracking system is needed for the laser to have high pointing accuracy. A limiting factor on the spot size is the atmospheric turbulence. Atmospheric turbulence limits the resolution of an astronomical telescope to about 4 microradians. At a 500 km target distance, the turbulence contributes about 2 m to the spot diameter. This problem can be resolved by the adaptive optics technique.

The principle of adaptive optics involves a light source beacon at the target above the atmosphere that transmits a beam towards the earth station. The beacon source could be a distant star. As the beam propagates through the atmosphere it experiences atmospheric distortion. The incoming beam can be detected by the wavefront sensor at the ground station. The wavefront sensor constructs a phase map of the beam. The conjugate of the distortion (i.e. the phase map of the incoming wave) is applied to the outgoing laser beam by a deformable mirror. When the predistorted beam travels through the atmosphere and picks up the atmospheric distortion, it leaves the atmosphere almost diffraction limited. This sequence is possible since the time scale of the atmospheric turbulence is much slower than the time it takes the beacon to get to the ground station plus the time of the deformable mirror to react.

Many methods utilizing adaptive optics exist. One method is to implement the deformable array in the path of the beam before it reaches the mirror, as illustrated in Figure 3.4-1.

Another option is to implement the deformable array on the mirror itself as shown in Figure 3.4-2. This method is known as the Phased Array Mirror, Expandable Large Aperture (PAMELA) [12]. Figure 3.4-3 shows the PAMELA concept in detail.

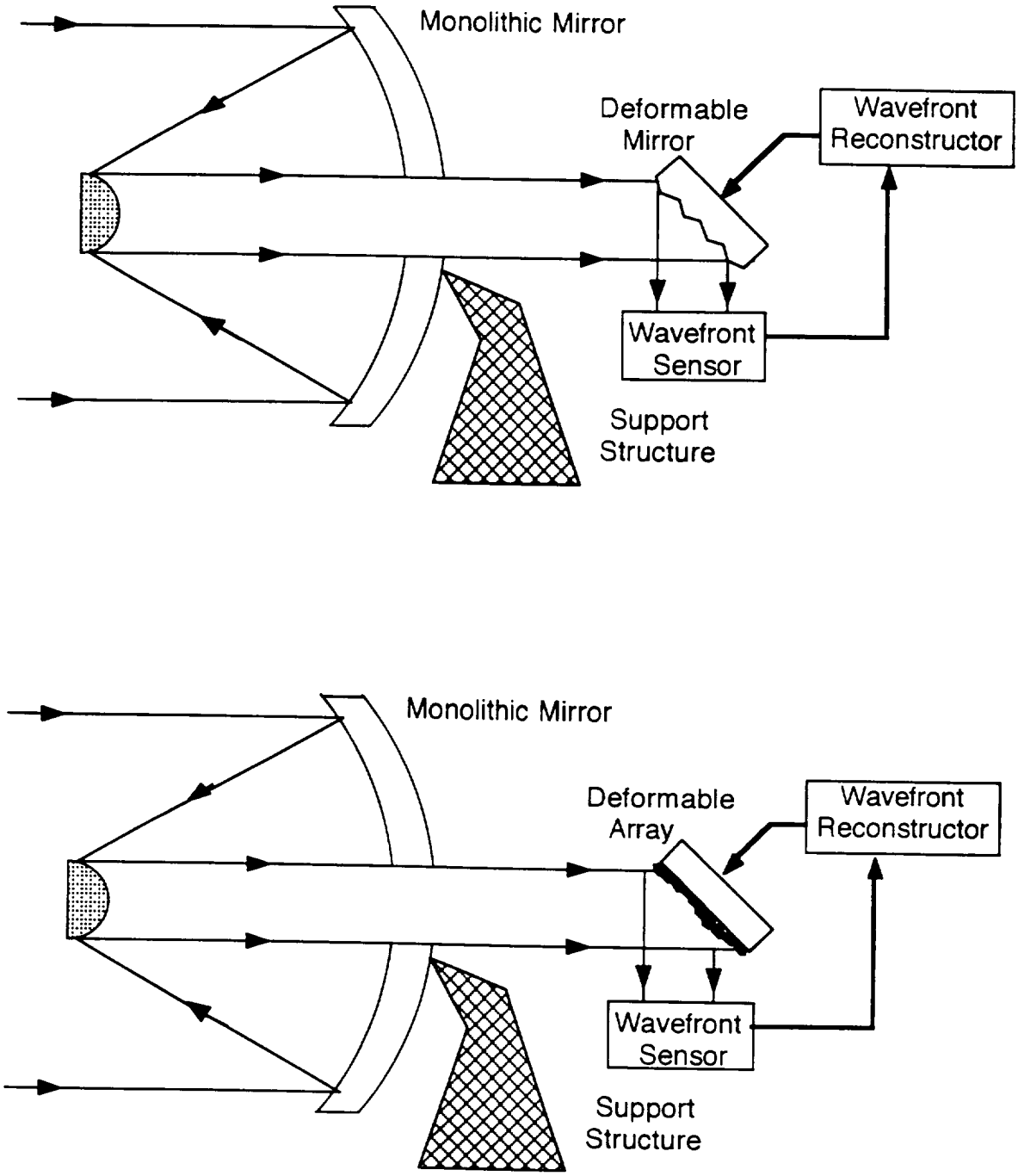

Figure 3.4-1. Adaptive optics using a deformable array in the beam path.

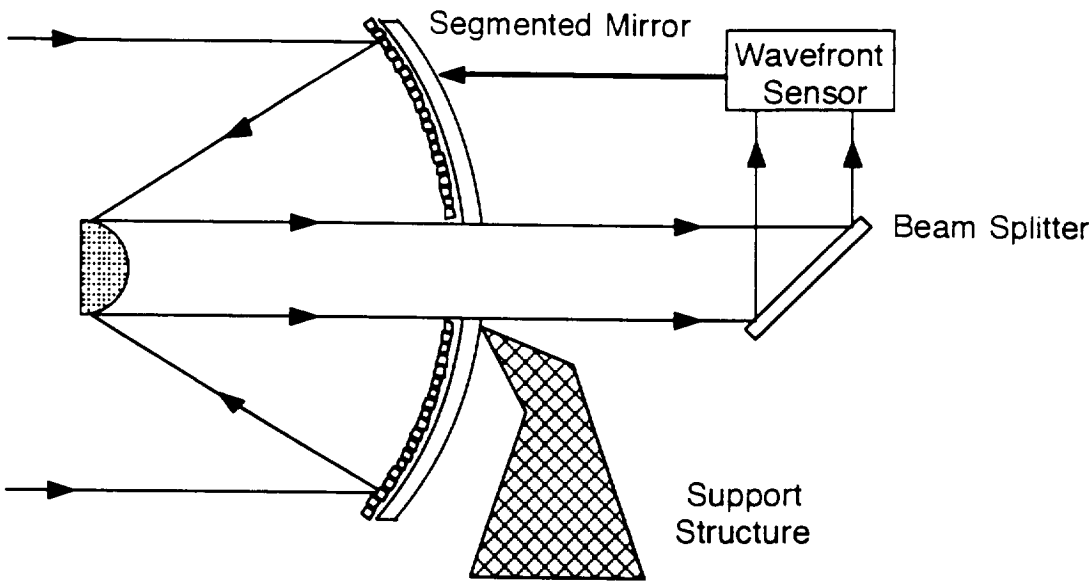

Figure 3.4-2. Adaptive optics using a deformable mirror.

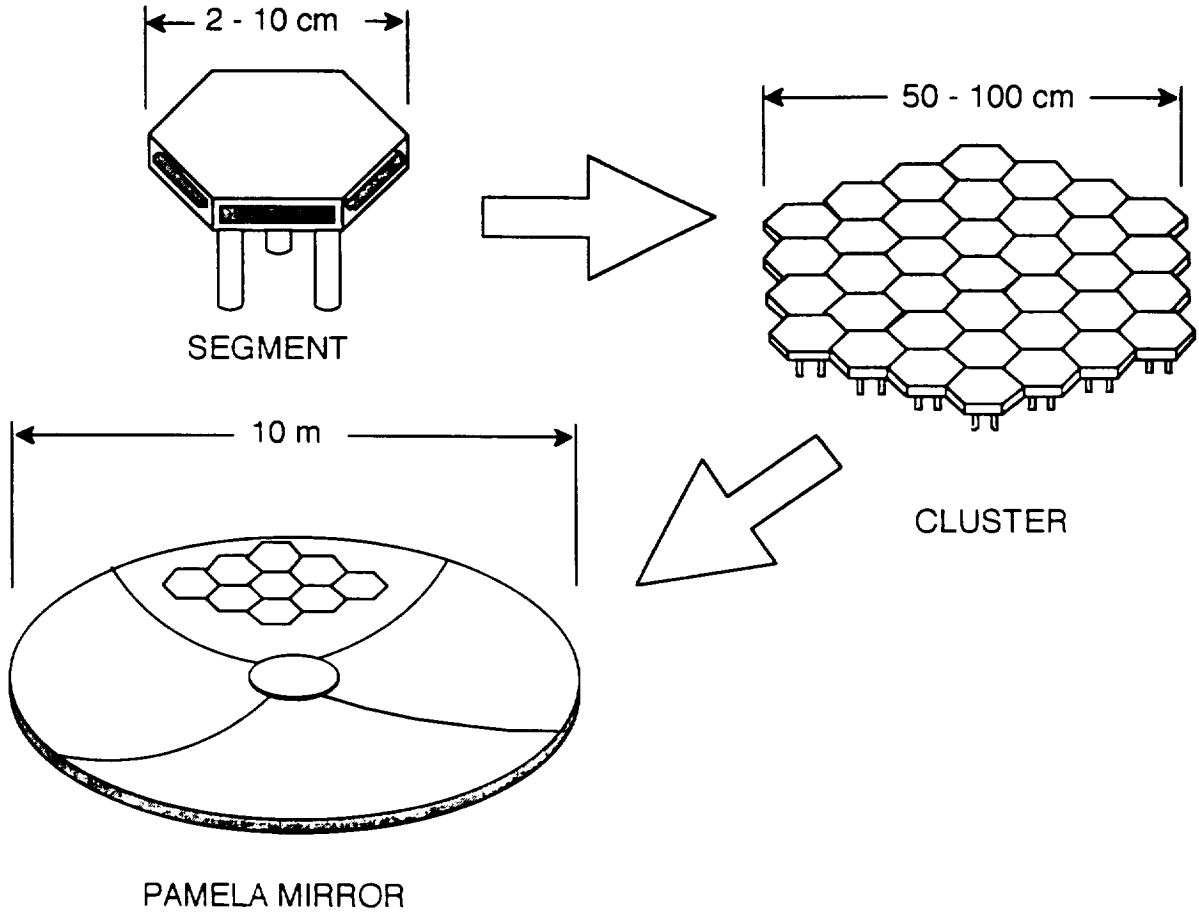

Figure 3.4-3. PAMELA adaptive optics concept.

Since the pathlength through the atmosphere is a function of zenith angle, and because of adaptive optics limitations with long pathlengths through the atmosphere, a limit is set for the angle off zenith to 60 degrees. The beacon must be separated from the target by a distance of *2 t v* (m) where *t* is the one way travel time (s) and *v* is the velocity (m/s) of the target in relation to the motion of earth at the ground station.

This requirement comes from the need to point at the atmosphere ahead of the satellite to know the distortion that the beam will be facing. The point ahead angle is *2v/c* where *c* is the speed of light [13]. This configuration is shown in Figure 3.4-4.

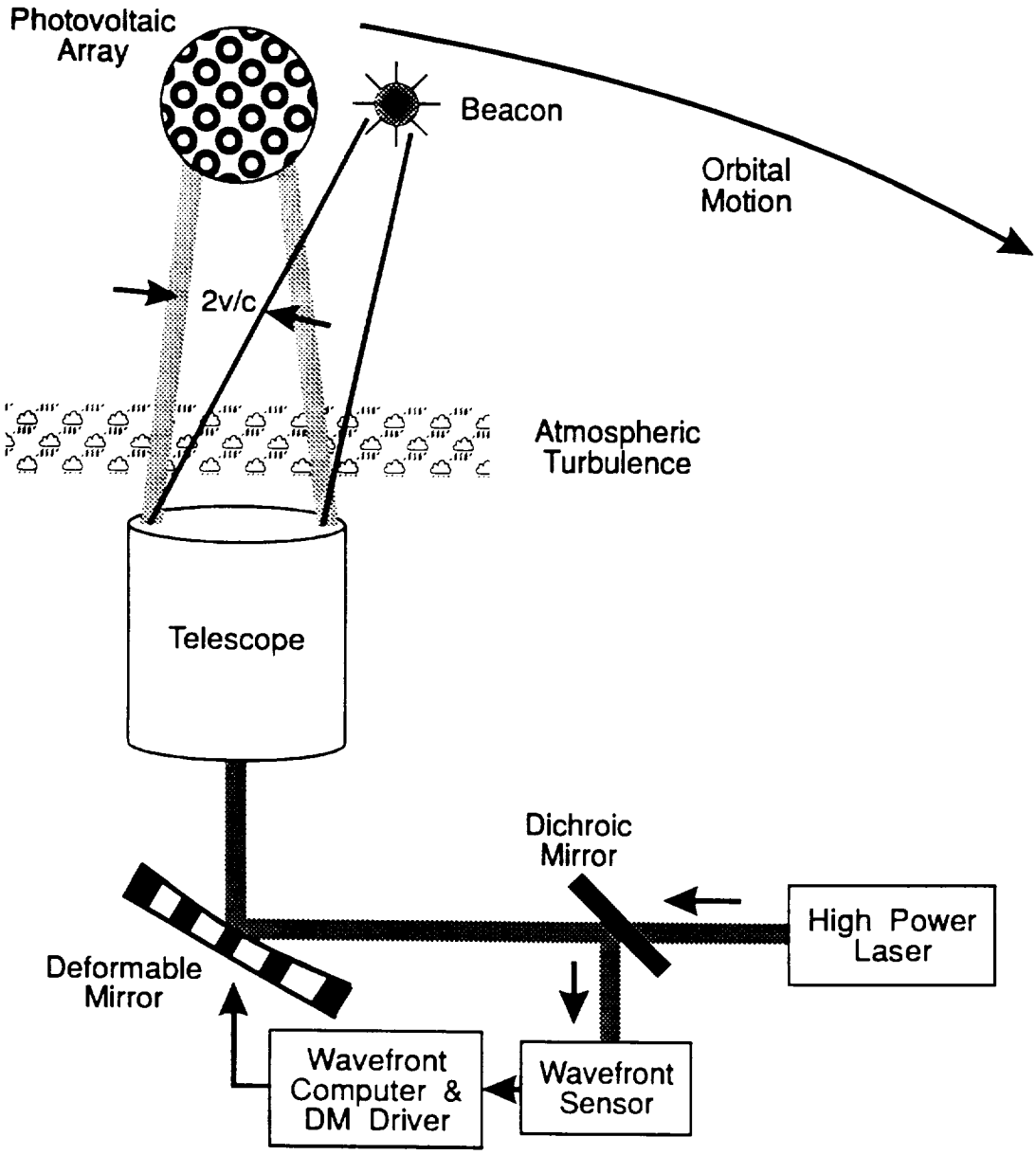

Figure 3.4-4. Laser beam guidance system using a tracking lead angle.

For low earth orbit, the distance that is separating the beacon from the satellite is large and the beacon cannot be located on the satellite. Synthetic beacons can overcome this problem where a different laser beam in wavelength and power is propagated up in the atmosphere as shown in Figure 3.4-5.

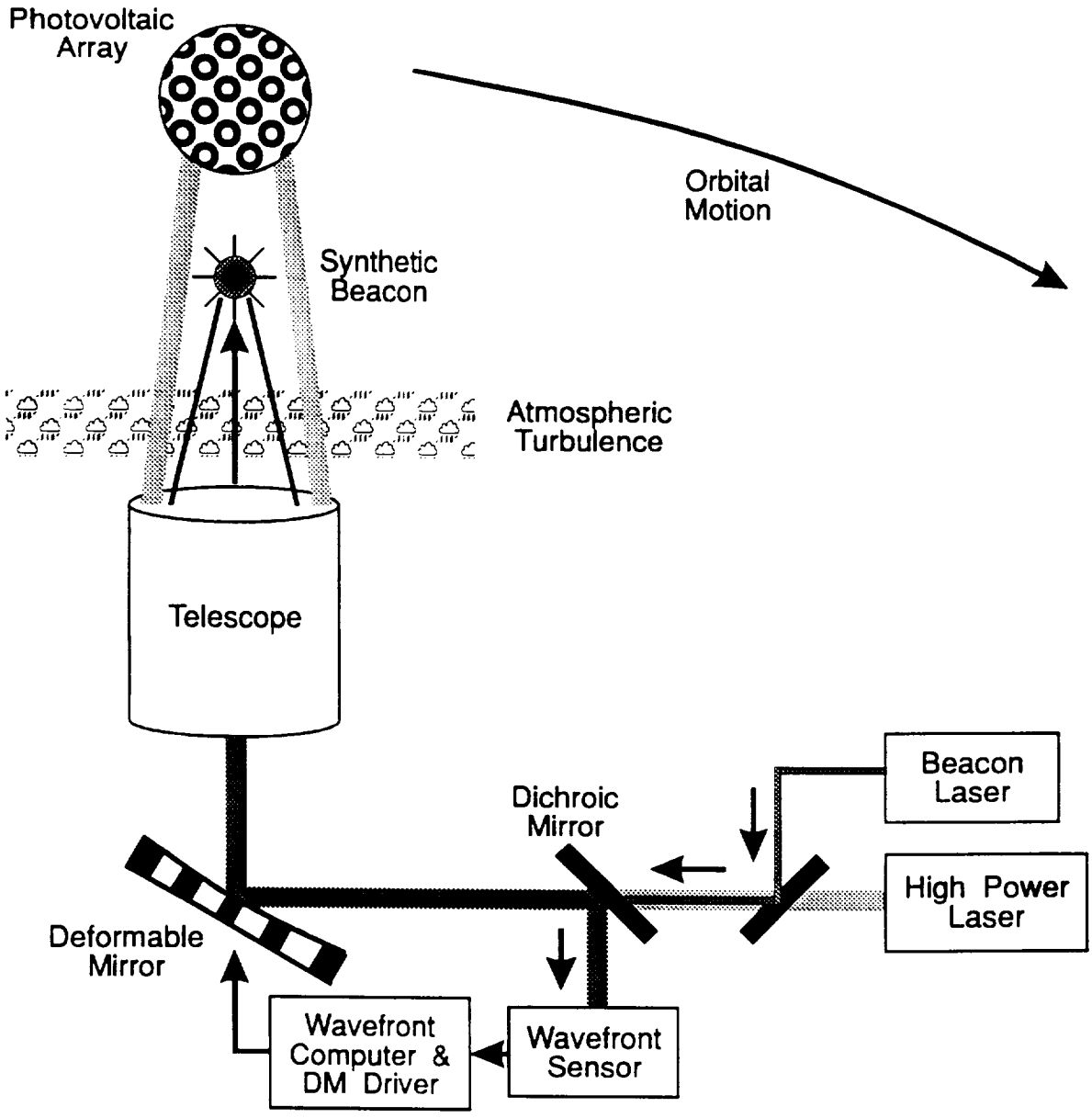

Figure 3.4-5. Synthetic beacon configuration.

The ground station for the laser power beaming will use the synthetic beacon approach. A beacon signal will be transmitted from the ground station to the WISPER satellite. A portion of the beacon will be reflected and received at the ground station. Distortion through the atmosphere will be processed to guide the laser beam.

3.5 Laser Power Measurements

Information regarding the incident power density will be collected to confirm the expected operational parameters and spot size. This information will also be used to monitor the performance of the GaAs photovoltaic array and the power transfer to the onboard power system, as well as the tracking ability of the ground station. An array of photovoltaic laser sensors will be positioned among the PV cells on the GaAs panel to provide this information.

3.5.1 Incident Power Density

Figure 3.5-1 shows the anticipated laser power density incident upon the satellite at an altitude of 500 km. Experiments will be conducted on clear days, with no precipitation or visible clouds, to allow an expected transmittance through the atmosphere of approximately 80% to 90%. With a 2 kW RF-FEL located at the 3 km altitude White Sands facility, approximately 38% of the laser power will reach the photovoltaic panel. This estimation results from a number of different tests performed on the various components involved as well as from some theoretical calculations [14], [15]. In order to validate the expected transmission efficiency, accurate laser sensors will be used to measure the incident power density.

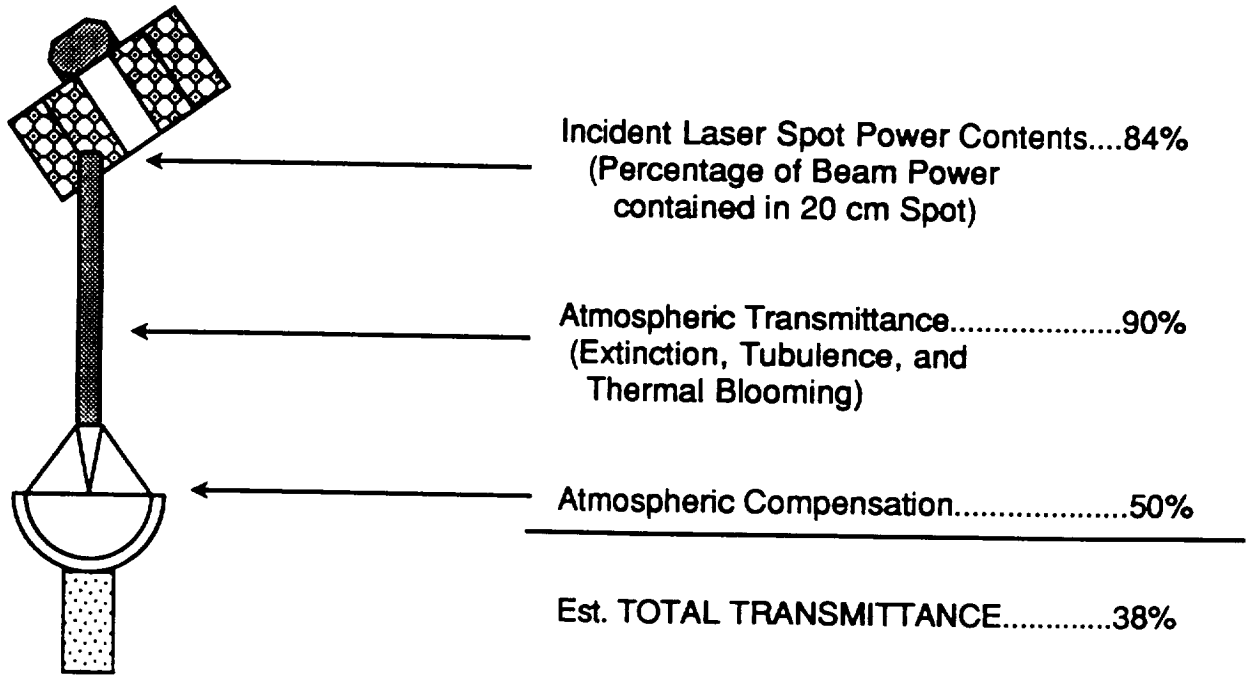

Figure 3.5-1. Laser transmission efficiency from the 3 km altitude ground station.

Taking into consideration that the PV conversion efficiency of monochromatic light is 50%, the spot power distribution is 84%, and the required atmospheric compensation loss is 50%, an overall transmission efficiency from the laser to the satellite is expected to be approximately 20%. Thus, approximately 400 W will be received from a 2 kW RF-FEL.

Demonstrations to prove the feasibility of LPB, such as this one, will be valuable to all industries and scientists investigating laser power beaming for future of space exploration applications. The size and orbit of the WISPER satellite make it possible to do experiments with available laser technology and transmitters using adaptive optics.

3.6 Laser Beam Safety

For the SELENE project, the US Army Corps of Engineers wrote an environmental impact statement concerning the White Sands facility [16]. The report stated that the laser beam will operate at a frequency which is not eyesafe the strength of the beam may induce thermal effects. The report also determined that the beam will be focused and dangerous in low earth orbit. Therefore, three separate effects must be considered: 1) the hazards to eyes of ground station personnel and the local population due to backscatter and reflections, 2) the hazards to the eyes of pilots and their passengers, and 3) the effects on other satellites.

The reflection and backscattering effects are potentially dangerous within a 1 km radius of the site. The Corps of Engineers recommend this area be maintained as a keep out zone. Additionally, ground sensors could be used in offsite areas to watch for coherent radiation. Finally, both ends of the power beam can be monitored to insure sudden power level drops do not occur. If the power level drops, the laser beaming will be discontinued.

Airplanes and birds must be kept out of the beam's operating zone. At the White Sands facility, this zone consists of a cone with a beamwidth of 120 degrees. Similarly sized airspace have been controlled during shuttle launches [3]. As backup protection, radar can be used to detect metallic objects with a cross sectional area larger than 1 cm^2. When such an object enters the zone, the laser beam can be shut off within a millisecond [14].

The final hazard of the laser power beam is the hazard to other satellites. Although thermal damage is unlikely, various satellites have sensitive instruments which may be damaged by even brief exposure. Furthermore, accidental laser illumination of satellites is an internationally sensitive area and may have political ramifications. To avoid this situation, tracking radar can be used through coordination with NASA's Laser Clearinghouse. The Clearinghouse coordinates any laser transmissions from Earth which may affect orbiting satellites.

UAF
NASA USRA ADP
Space Systems Engineering

WIreless Space Power ExpeRiment

Chapter 4
Mission Analysis

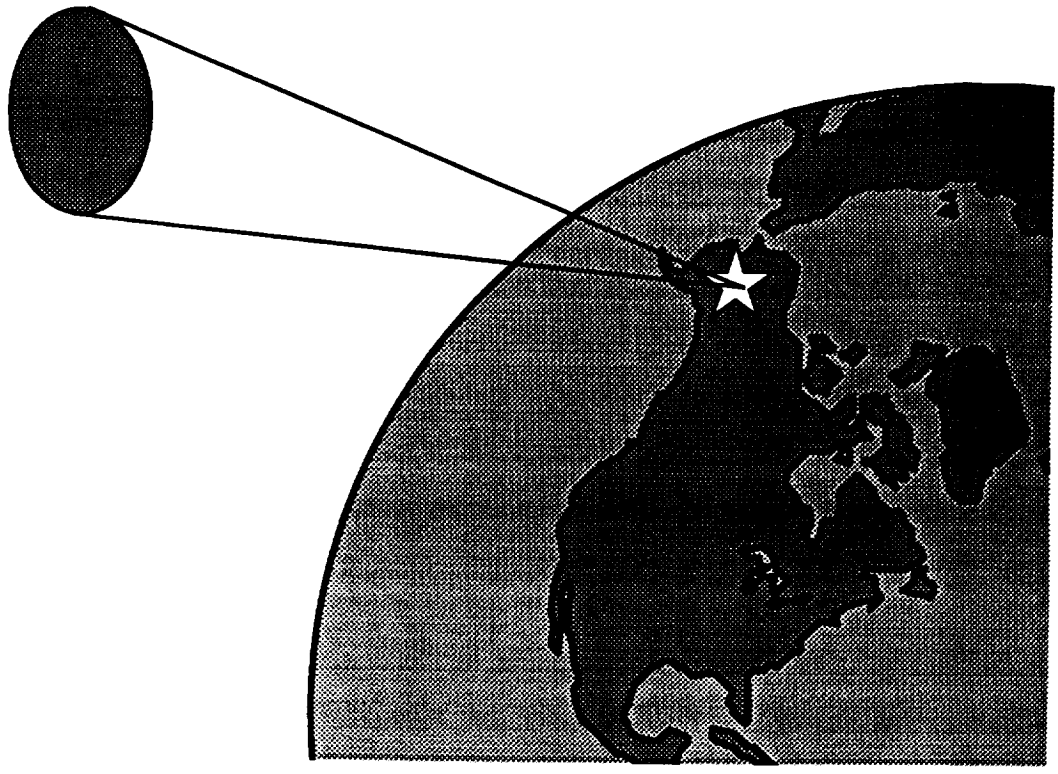

4.0 Mission Analysis

Mission analysis is the process of turning the mission statement goals into the best combination of components, guided by the operational constraints and optimizing criteria. The goals of this mission are the demonstration of power beaming technology, a short completion time, and the collection of data for comparison to power beaming theory. The operational constraints are; the requirements of the experiment, the cost, the availability of technology currently under development, the computer and communications limits, the demands of the space environment, the launcher capability (mass and volume limits), political support, federal regulations, and the health and safety of everyone. The optimizing criteria are to maximize experimental data, reliability, and utility. A secondary goal is to use Alaskan resources wherever it is feasible or cost effective in order to promote aerospace development within the state. The flowchart in Figure 4.0-1 shows the mission analysis process.

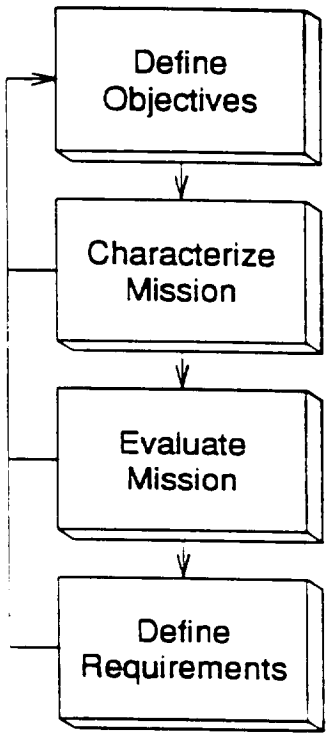

Figure 4.0-1. Flowchart of mission analysis process.

4.1 Orbital Selection

An essential aspect of the WISPER design is the selection of a proper orbit. This involves a complex set of calculations and tradeoffs. This section will detail the procedures used and decisions made to determine WISPER's orbital profile.

4.1.1 Orbit Description

In performing the orbital selection and analysis for WISPER, a list was generated of parameters that have some dependency on the orbit. This list was then prioritized in accordance with each parameter's overall mission importance. Table 4.1.1-1 contains a summary of the orbital selection requirements and the "best case" solution for each requirement.

Table 4.1.1-1. Orbital selection requirements.

Requirement	Best Case
Power Density	Low Altitude
Mission Life	High Altitude
Launch Cost	Low Altitude, Low Inclination
Power Availability	Sun-synchronous
Experiment Time	High Altitude
Contact Frequency	Inclination Equal to Ground Station

Though this table is not entirely comprehensive, it shows the major concerns involved in selecting the orbit. The orbital profile was determined using these guidelines. Since WISPER will perform essentially two separate missions, the orbital profile was split into two separate sections. It has been decided that the satellite will have no orbital maintenance capabilities. Therefore, the satellite will need to be placed in an orbit above the optimum and then allowed to decay through to the optimum altitude. The orbit has been defined as follows:

Orbital Profile:

Phase I. Microwave Experiment

Initial Altitude:	600 km
Final Altitude:	500 km
Decay Time	~370 days
Inclination:	97.59°

Phase II.

Laser Experiment

Initial Altitude:	500 km
Final Altitude:	400 km
Decay Time	>4 years
Inclination:	97.59°

The following sections will provide an in-depth analysis of the orbital profile and the individual details of the selection process.

4.1.2 Power Density

A critical aspect of the Phase I orbit design is the received microwave power density. The power density is directly related to the amount of power available from the rectenna. The rectenna requires a high microwave density in order to maintain a high level of efficiency. For a particular size of transmitter, the Principle Investigation (PI) team has specified that the mean power density should remain at 3 W/m^2. This results in an altitude between 500 to 600 km as discussed previously in section 2.1.1. In addition, the altitude also affects the visibility of the satellite to the ground station on each passover. During much of the passover time, WISPER will be low on the horizon.

The power density is less critical for Phase II than it is for Phase I. This circumstance is primarily due to the nature of laser power beaming compared to microwave. The second phase will be at a lower altitude, because the spacecraft will be allowed to decay in altitude. The laser beam, when focused by adaptive optics system, produces a smaller beam than the microwave transmitting antenna. Both of these factors allow more of the original power to strike the receiver.

4.1.3 Mission Life

The second most important aspect of orbit selection is the consideration of how the chosen orbit will affect the length of the mission. The PI team has suggested a mission lifetime of two years. The atmospheric density and the ballistic coefficient of the spacecraft have been used to calculate the mean orbital drag. Given the spacecraft's configuration, the orbital decay during the initial phase of the mission is rather substantial. The calculations are given as [1].

configuration, the orbital decay during the initial phase of the mission is rather substantial. The calculations are given as [1].

Ballistic Coefficient B:

$$B=\frac{AC_D}{m} \quad [m^2/kg] \qquad (4.1.3\text{-}1)$$

Mean Orbital Decay ΔD:

$$\Delta D=-2\pi B\rho\frac{r^2}{P} \quad [10^3 \text{ km/yr}] \qquad (4.1.3\text{-}2)$$

Variables:

A	Satellite cross sectional area (m^2)	C_D	Drag coefficient
m	Satellite mass (kg)	P	Orbit period (yr)
r	Orbit radius (km)		
ρ	Atmospheric density, values obtained from the mass spectrometer incoherent scatter (MSIS) atmospheric mode, using solar activity index F10.7 (kg/m^3)		

Using the above calculations, the orbital decay time for Phase I was determined to be about 370 days. This value is approximate due to the nature of the factors involved (i.e., the solar index and the drag coefficient).

For Phase II, the large inflatable antenna is jettisoned. It is assumed that the jettisoned antenna will not have a negative dynamic affect on the satellite, and that the springs will push the dish out of the area where it could interfere with operations. This change in cross-section greatly reduces the atmospheric drag. For this configuration, the orbital decay time was calculated to be 50 km over four years. This result more than meets the design specifications. The overall atmospheric drag on the satellite can be reduced by launching it during a solar minimum. Then the satellite would reenter during the next

4.1.4 Launch Cost

The launch cost of the spacecraft is related to the orbit selected because higher altitudes, or higher inclinations require more performance capability from the booster. The launch site's geographical latitude and longitude determine the amount of energy required by the booster to attain a particular orbital inclination. It has been requested that the ground station and possibly the launch site be located in Alaska. The NOAA site has a suitable communications antennas and meets the hardware power requirements. Under these assumptions, an inclination equal to the launch site latitude will provide the highest mass to orbit. Below in Figure 4.1.4-1 is a graph comparing the payload mass and volume of several possible launch systems. The amount of mass boosted to orbit is given for a polar orbit at 185 km, but is proportionally the same as what it would be for a 600 km orbit [2].

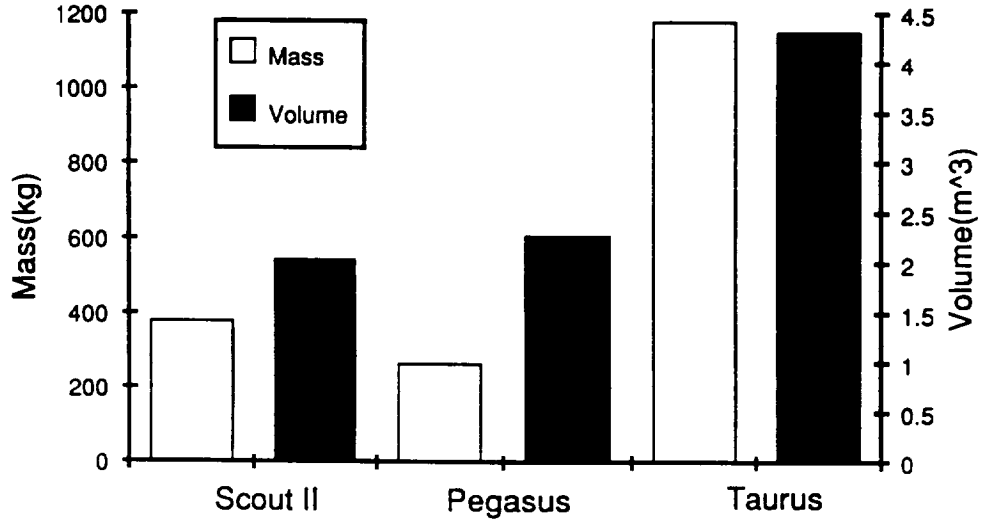

Figure 4.1.4-1. Launch cost bar chart.

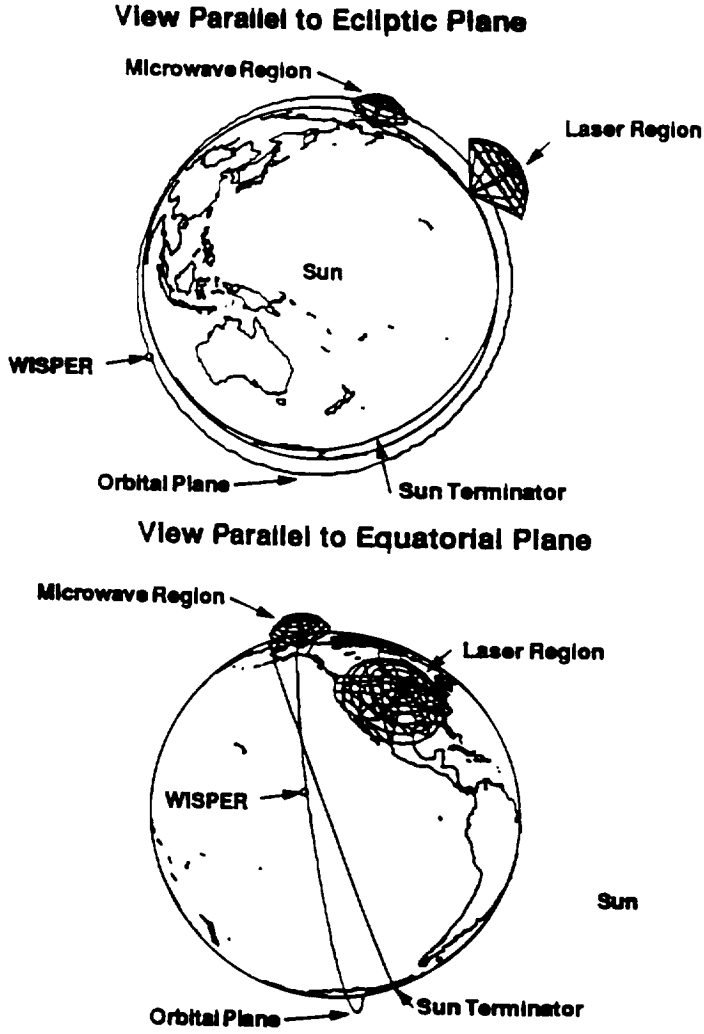

Figure 4.1.5-1. Views of proposed orbit and ground site locations [4].

4.1.5 Power Availability

In Figure 4.1.5-1. the proposed orbit is depicted and the position of the orbit relative to the ground sites is shown. The spacecraft operating power requirement demands that the satellite achieve maximum available energy from the solar arrays. This is achieved by utilizing a sun-synchronous orbit. The inclination, i, of a sun-synchronous orbit is calculated using the following formula [2],

$$i = a\cos(4.77348\times10^{-15}r^{\frac{7}{2}}) \quad \text{[degrees]} \qquad (4.1.5\text{-}1)$$

where r is the radius of the orbit (km) and a is a dimensionless constant that represents the effect of the earth's oblateness. The ascending node is oriented such that the orbital plane remains nearly perpendicular to the solar radiation as the earth revolves.

However, since the satellite does not have orbital inclination maintenance capabilities, it will be launched into a sun-synchronous orbit to a 600 km altitude. The inclination for the 600 km sun-synchronous orbit is 97.59 degrees. Since the true inclination deviates a maximum of 0.1947 degrees, the effect on the solar radiation angle can be treated as a negligible perturbation. The sun-synchronous inclination was chosen in order to help alleviate the effect of solar cell degradation. The maximum radiation angle due to this perturbation is less than 15 degrees. This yields a value 96.6% of the amount of power received when the radiation impingement is perpendicular. This number represents the minimum power reduction due to this affect when the ascension node is placed at 45 degrees.

The precession of the orbit is another affect that must be considered. During the first year there will be a loss of 6 degrees between the spacing of the orbital plane and the solar radiation vector; which in turn translates into a 21 degree angle to the maximum radiation. Fortunately, this lag will help matters once the orbit falls below 550 km, since the node precession will change the orbital angle faster than the earth's angle changes relative to the sun. Once the 500 km orbit is reached the orbit plane will be 9 degrees ahead of the solar normal. This lead coupled with the previous 6 degrees lag yields a 3 degree total lead and a maximum solar radiation angle of 18 degrees [2].

4.1.6 Experiment Time

The amount of time available on each pass to conduct the experiments is related to both the altitude and the minimum elevation angle of the transmitting stations. For Phase I the PI team has specified a maximum distance from transmitter to receiver as 1000 km. Therefore the antenna elevation is always more than 30 degrees above the horizon. The maximum experiment time is obtained when the satellite passes directly overhead. Using the following equations, the maximum experiment time for Phase I was found to be 4 minutes (for beaming to 30 degrees above the horizon). Using a similar approach for Phase II yields a maximum experiment time of 3 minutes. This difference is due to the lower altitude of the second phase.

Maximum Time in View:

$$t=\frac{P\lambda_{max}}{180} \quad \text{[minutes]} \qquad (4.1.6\text{-}1)$$

Maximum Earth Central Angle:

$$\lambda_{max}=90-\epsilon-\eta \quad \text{[degrees]} \qquad (4.1.6\text{-}2)$$

Nadir Angle:

$$\eta = a\ \sin(\cos(\epsilon)-\sin(\rho)) \quad \text{[degrees]} \qquad (4.1.6\text{-}3)$$

Earth's Angular Radius:

$$\rho = a\ \sin(\frac{R_E}{r}) \quad \text{[degrees]} \qquad (4.1.6\text{-}4)$$

Variables:

P	Orbit period (min)	ϵ	Minimum antenna elevation (degrees)
η	Maximum nadir angle (degrees)	ρ	Earth angular radius (degrees)
r	Orbit radius (km)	a	Oblateness factor
R_E	Earth radius (km)		

4.1.7 Contact Frequency

The number of contacts received by the ground station over a particular period is highly dependent on the initial conditions of the orbit. Simulations of the chosen orbits were performed on PC SOAP [3], an orbital analysis package. During Phase I, the satellite was found to be within range of the ground station at least once per day. The majority of these contacts were at the outer edge of the experimental envelope, with high elevation passes occurring approximately fifteen days apart. The Figure 4.1.7-1 shows the contact period as a function of the instantaneous ascension node, relative to the earth's inertial frame.

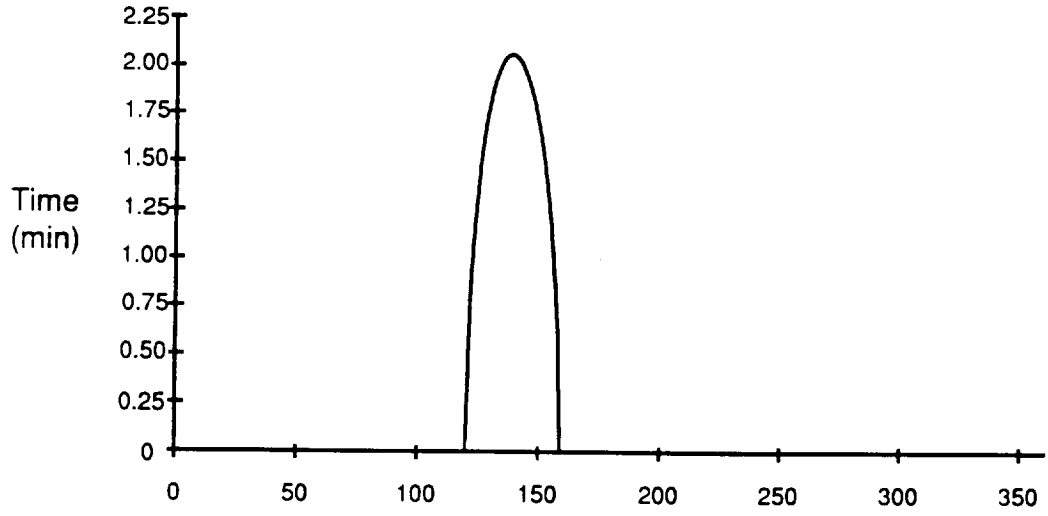

Figure 4.1.7-1. Contact time versus ascending node, Phase I [3].

For Phase II, fewer contacts are made. The satellite passes through a 24 hour no-contact zone once every fifteen days. This is due to the lower latitude of the laser ground station. Despite this, the maximum experiment time of the overhead passes will not be affected and the satellite will still pass overhead every 15 days. Figure 4.1.7-2 shows the contact period relationship for Phase II.

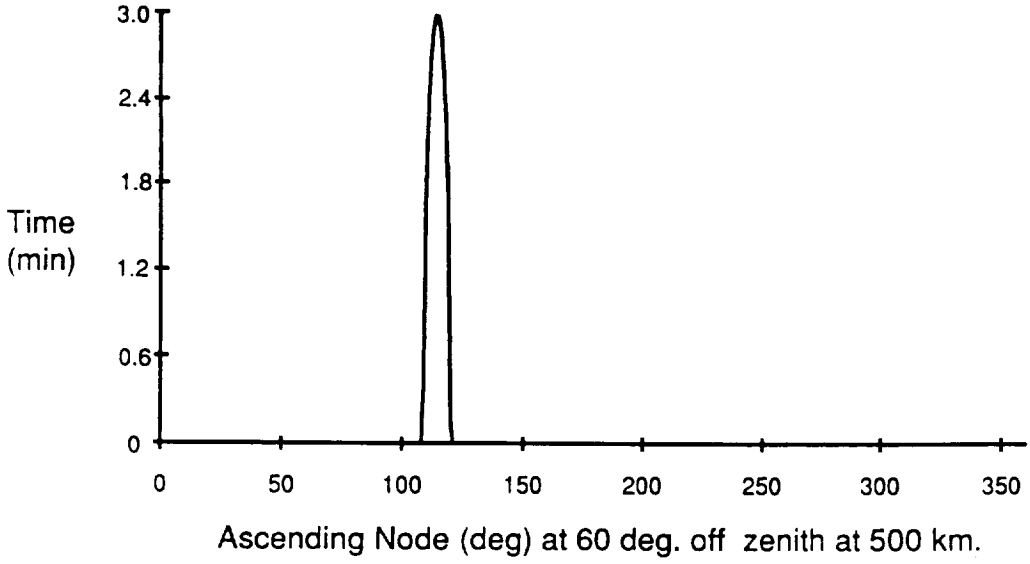

Figure 4.1.7-2. Contact time versus ascending node, Phase II [3].

4.1.8 Orbit Selection Summary

Several considerations and compromises were involved in selecting the orbit for WISPER. The orbital profile has been optimized to yield the best possible experiment time and power density for each of the mission phases. In addition, the orbit has been selected to reduce the size of the solar array to a minimum and to remain within the funding constraints for the booster selection.

4.2 Launch Vehicle Selection

It was decided by the Mission Analysis team to design the best spacecraft possible within the constraints of the University Explorer Program and then to find a booster to meet its needs. A theoretical spacecraft mass estimation was used to size the booster for the first iteration. In the initial analysis, the total mass for this spacecraft was thought to be approximately 300 lb (136 kg). Based on this figure, research was done to determine the suitability of using a USRA Spartan derivative, because it would have met the boost requirements. However, after contact with the manufacturer of the inflatable dish, the weight estimate suddenly jumped to 900 lb (410 kg) due to misinformation on the mass of the antenna. There is currently only one booster in this class, the Taurus, which seemed infeasible because it is still under development and prohibitively expensive. This forced the designers to examine possible mass reductions. The current estimated weight is 560 lb (254 kg).

The booster selection and payload maximum mass have been fixed in order to allow the detailed design of the mechanical systems to proceed. The Pegasus launch vehicle was chosen based on its mass and altitude capabilities and its state of development. There are more suitable boosters in development, but the information for those unlaunched boosters is not detailed enough to allow a realistic mechanical design. The designed systems must able to withstand the booster's acceleration, acoustic, and vibration environment which will be unknown until they are flight tested. It will be possible to reconfigure the spacecraft for launch on the Scout II or Taurus if the Pegasus cannot be used for some reason.

The spacecraft design and the launch vehicle selection involved various tradeoffs. The experiment demanded that the distance covered by the power beam not exceed 600 km when WISPER is directly overhead, and that there be as many passes as possible. In order for the spacecraft to fulfill all of its functions, a certain amount of mass and volume was required to be boosted. Also, the power system required sun synchronization to reduce the solar panel area. The launch vehicle has to meet those requirements. On the other hand, the choice of the booster limited the spacecraft design to the limits of its altitude and inclination, as well as the shroud volume and adapter specifications. The launch vehicle determines the environment of the payload from earth to orbit and this is the most demanding dynamic environment. Another factor that affects both the payload design and the booster selection is the location of the launch site. This selection is a

result of the orbital inclination choice and booster selected. For the sake of upgrading the Alaskan launch capability, it would be desirable to launch the Pegasus from Eielson AFB which is near Fairbanks and use the Poker Flat Research Range impact zones. However, higher launch costs would result. The launch site will probably be the Western Test Range (Vandenberg AFB, California). This would satisfy both the inclination requirements and the needs of Orbital Sciences Corporation, the builders of the Pegasus, for integration and launch support facilities. Launcher selection is the result of the iterative process of compromise between the experiment, the payload mechanical structure, the launch site, and the booster capabilities.

The Pegasus is launched from an aircraft flying at 41,000 ft (12,500 m) at a speed of 0.8 Mach [4]. All of the payload umbilical activity can take place in flight from consoles aboard the launching aircraft. There is a wing on the 1st stage of the Pegasus and its initial flight is similar to an airplane as the first stage burns (the X-15 design was utilized). By the time the first stage has burnt out, the lift from the wing is no longer significant and the second and third stages are finless solid motors. After 8 minutes the spacecraft is ready for the Hydrazine Auxiliary Propulsion (HAPS) motor to burn, which will place it within 5.6 km of the target altitude. The HAPS is an optional module that increases the insertion reliability to 99%. The Pegasus stages would be lengthened to increase their altitude performance. A special adapter will mate with the standard payload adapter. This special adapter will protect the stowed inflatable dish and rectenna until it is ejected at the deployment of the microwave receiving dish.

The Pegasus has a command destruct system that will destroy the rocket and payload in the event of a dangerous deviation from the flight plan. In addition to this, NASA requires standard safety plans to be written that ensure the highest standards of safety for the launch personnel and the general public. The expended stages will fall into uninhabited, reserved, and cleared impact zones. The following figures detail the flight profile (Figure 4.2-1), the Pegasus breakdown (Figure 4.2-2), and the comparison of the different vehicles being proposed (Figure 4.2-3).

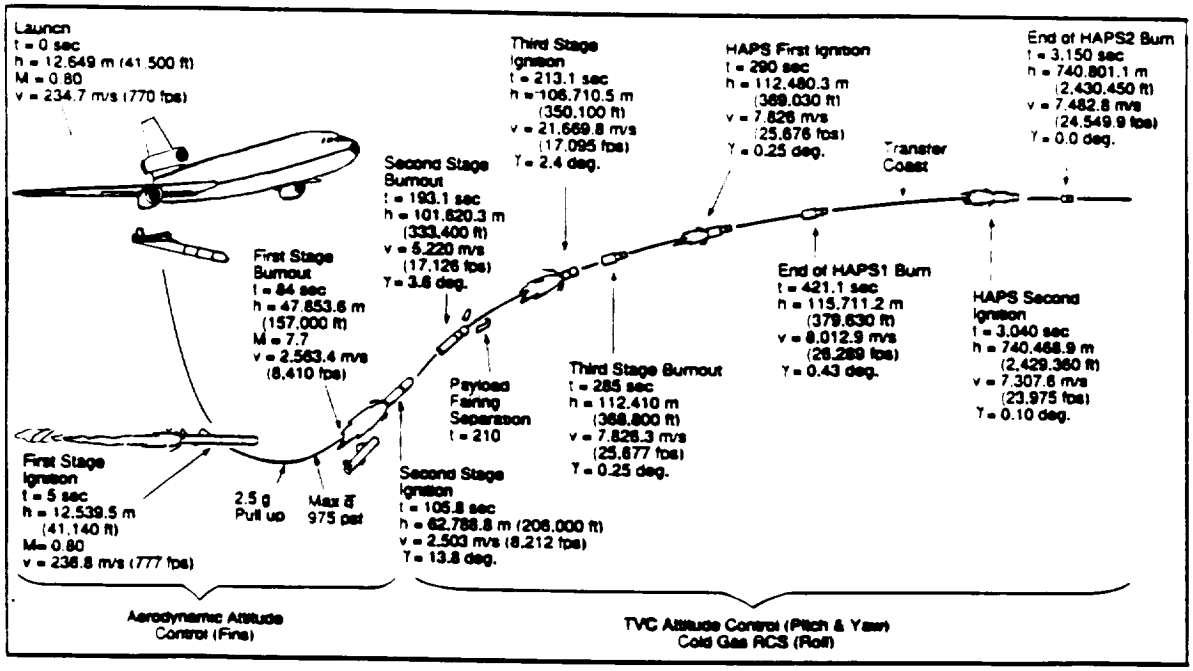

Figure 4.2-1. Pegasus flight profile [4].

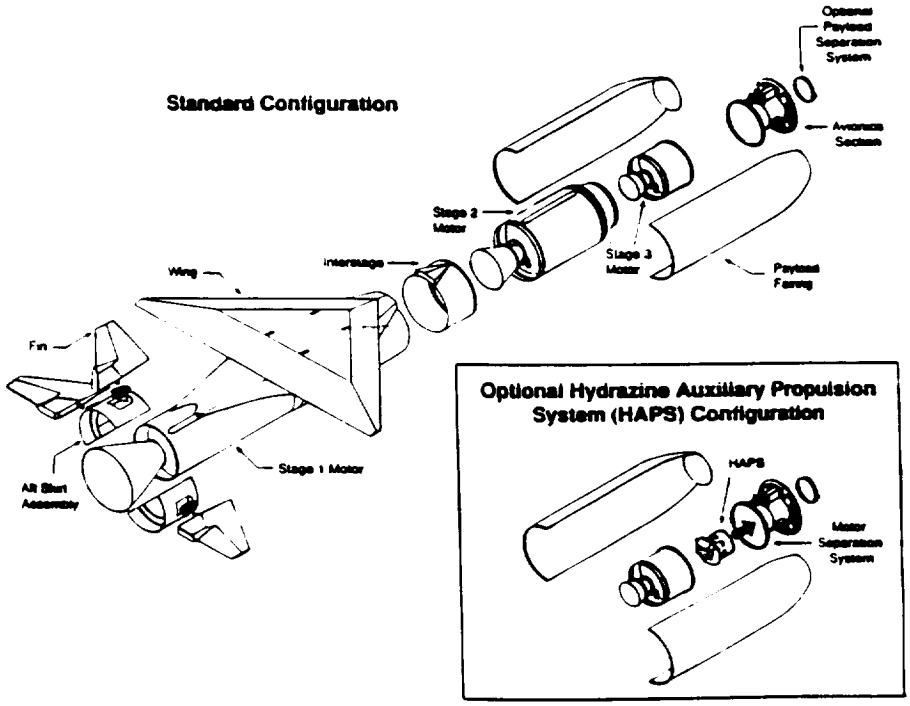

Figure 4.2-2. Pegasus configuration breakdown diagram [4].

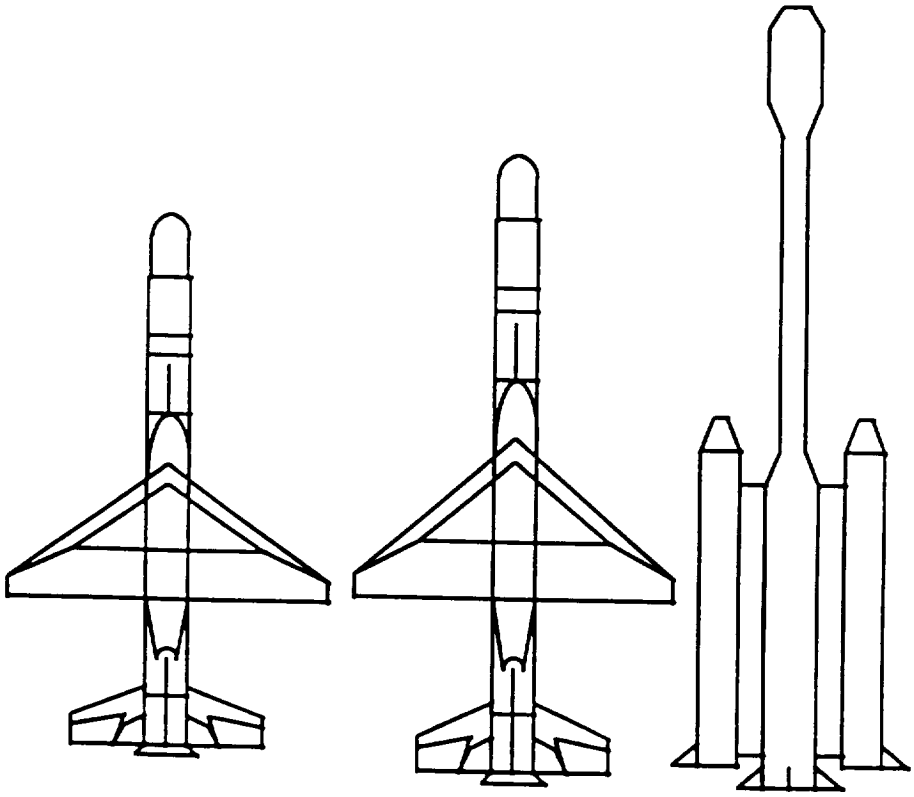

Figure 4.2-3. Launch vehicle proportional comparison [4].

UAF
NASA USRA ADP
Space Systems Engineering

WIreless Space Power ExpeRiment

Chapter 5
Spacecraft Design Considerations and Specifications

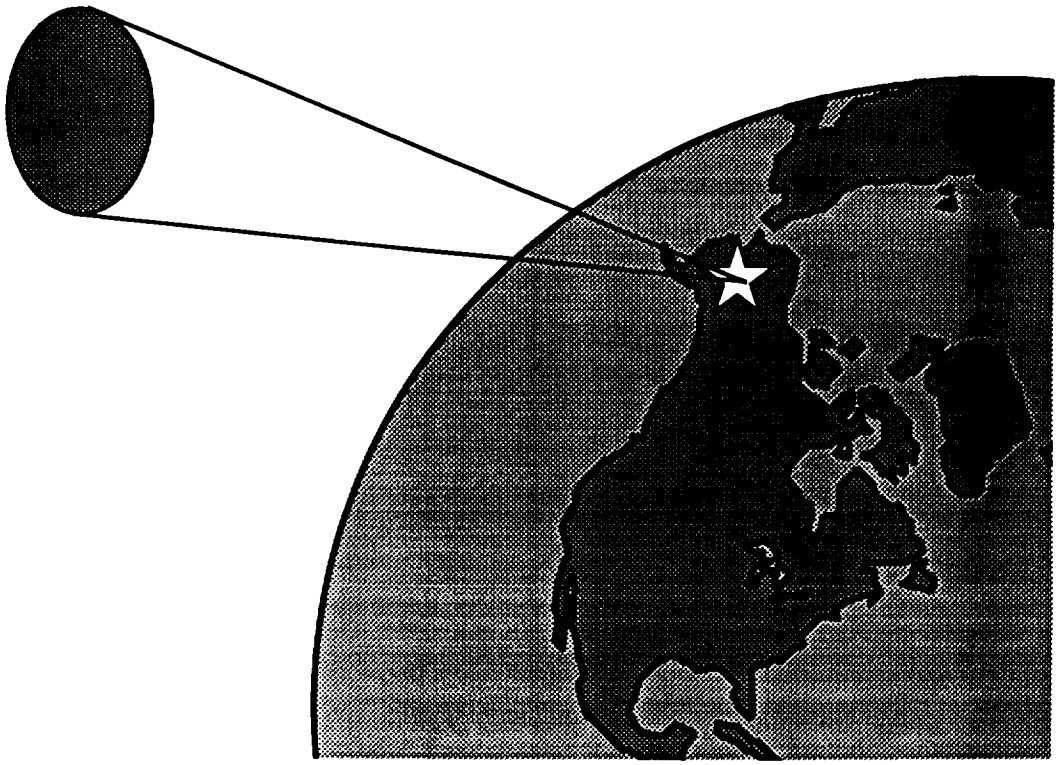

5.0 Spacecraft Design Considerations and Specifications

5.1 General Spacecraft Configuration

5.1.1 Inflatable Antenna

Background. Large aperture parabolic reflectors for space applications are significantly different from terrestrial antennas of similar size. Terrestrial antennas with 10 m to 50 m diameters are extremely massive. To put a similar structure into earth orbit would be prohibitively expensive. Antennas are also limited by the volume of the launch vehicle such as the shuttle bay or a rocket fairing. With limited budgets, alternative technologies have been proposed to allow larger apertures that are both lighter and have greater packing densities.

One such technology utilizes inflatable structures. Inflatables have significant advantages in mass and volume, and therefore cost, over conventional systems. This innovative technology also allows space structures of a scale not previously realizable. A near term application of this technology is large aperture antennas.

System Advantages. For the WISPER demonstration, a microsatellite was selected to minimize the cost of the demonstration. The only technology feasible for implementing the required large aperture reflector on such a small payload is an inflatable antenna.

Inflatable antennas have significant advantages in mass and volume over more traditional technologies. Large aperture antennas on earth are constructed to withstand the immense gravity and wind loads. Once removed from the majority of the gravity and atmosphere of the earth, antenna designs change significantly. Inflatable space structures utilize the different conditions to the fullest. In microgravity and near vacuum conditions, it is the nature of an inflatable structure to form curved surfaces such as a paraboloid. This allows relatively high surface accuracies with minimum antenna structure. Also, the system mass and packaged volume are considerably less than traditional mechanical systems. Comparisons of mass and volume for space antenna systems are shown in figures 5.1.1-1 and 5.1.1-2. The figures also show the system weight and volume versus antenna diameter for competing systems [1]. The curves on the figure are for inflatable designs with focal length to diameter ratios (F/D) from 3/8 to 2. The system weight includes the entire support structure, deployment mechanism and inflatant for a ten year mission. The data was shown for inflatable antennas with surface accuracies less than 1.0 mm rms. Smaller tolerances are possible with heavier designs.

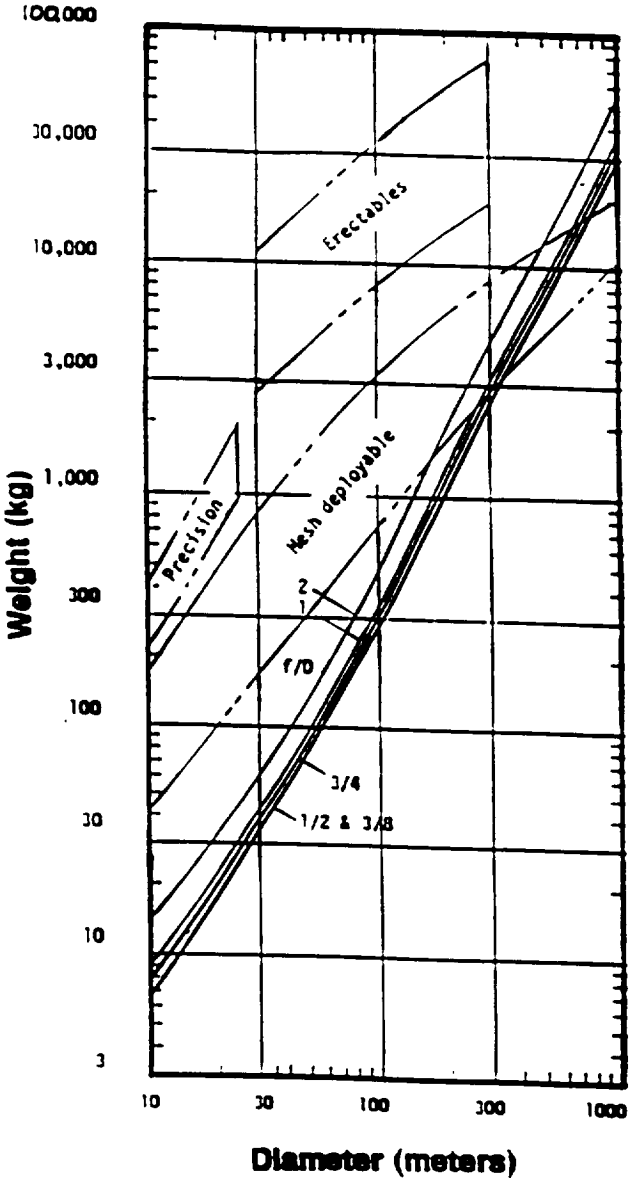

Figure 5.1.1-1. Antenna system mass comparison [1].

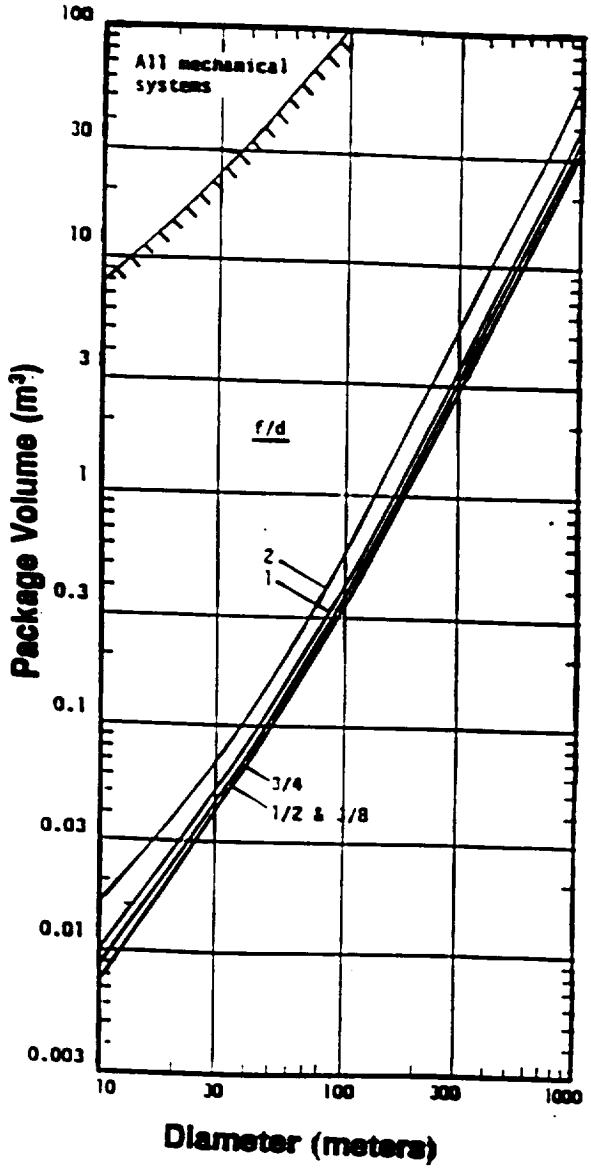

Figure 5.1.1-2. Antenna system volume comparison [1].

Inflatable Antenna Structure. The antenna consists of a self rigidizing torus, a thin film metalized surface as the reflector, a frequency transparent canopy, and the inflation system. Internal pressure holds the parabolic shape, and the structural torus carries the load. A similar design and demonstration was proposed for launch from a STS GAS Canister in [2]. The general configuration for the inflated antenna is shown in Figure 5.1.1-3. Not included in the drawing are inflatable struts from the spacecraft body to the structural torus. L'Garde Inc., a manufacturer of inflatable structures for space, indicated that the struts are necessary to avoid deformation of the reflector surface while the spacecraft is slewed [3].

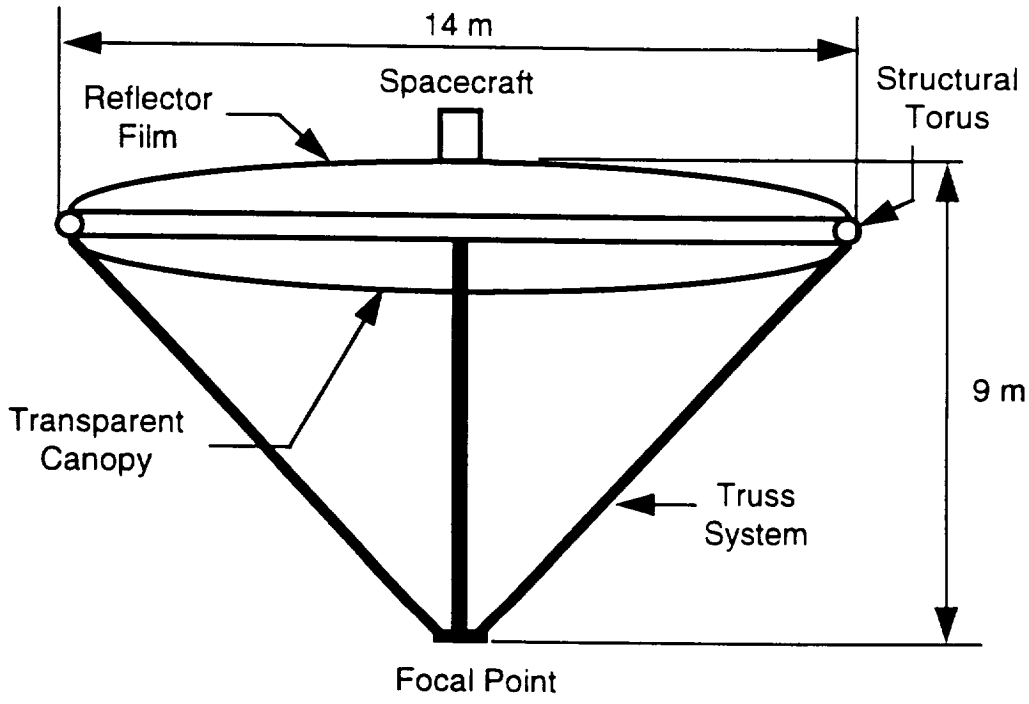

Figure 5.1.1-3. Inflatable antenna configuration.

The torus is a composite of aluminum, polyester and heat-activated adhesive. During deployment the torus is inflated to the yield strength of the aluminum using $C0_2$ gas. After the inflation process, internal pressure is no longer necessary. The torus is "rigidized" and will support the space loads. Figure 5.1.1-4 shows the self rigidizing torus composite [4].

The paraboloid and radome are constructed of triangular gores. The reflector surface is metalized with a thin film of aluminum. The number of gores is optimally designed for the size and pressure of the antenna. The gore films are connected by a tape on the seam along the back of the reflector. This is a difficult process because the seams effect the surface tolerance of the reflector. Figure 5.1.1-5 shows the layout and connection process for two gores [5].

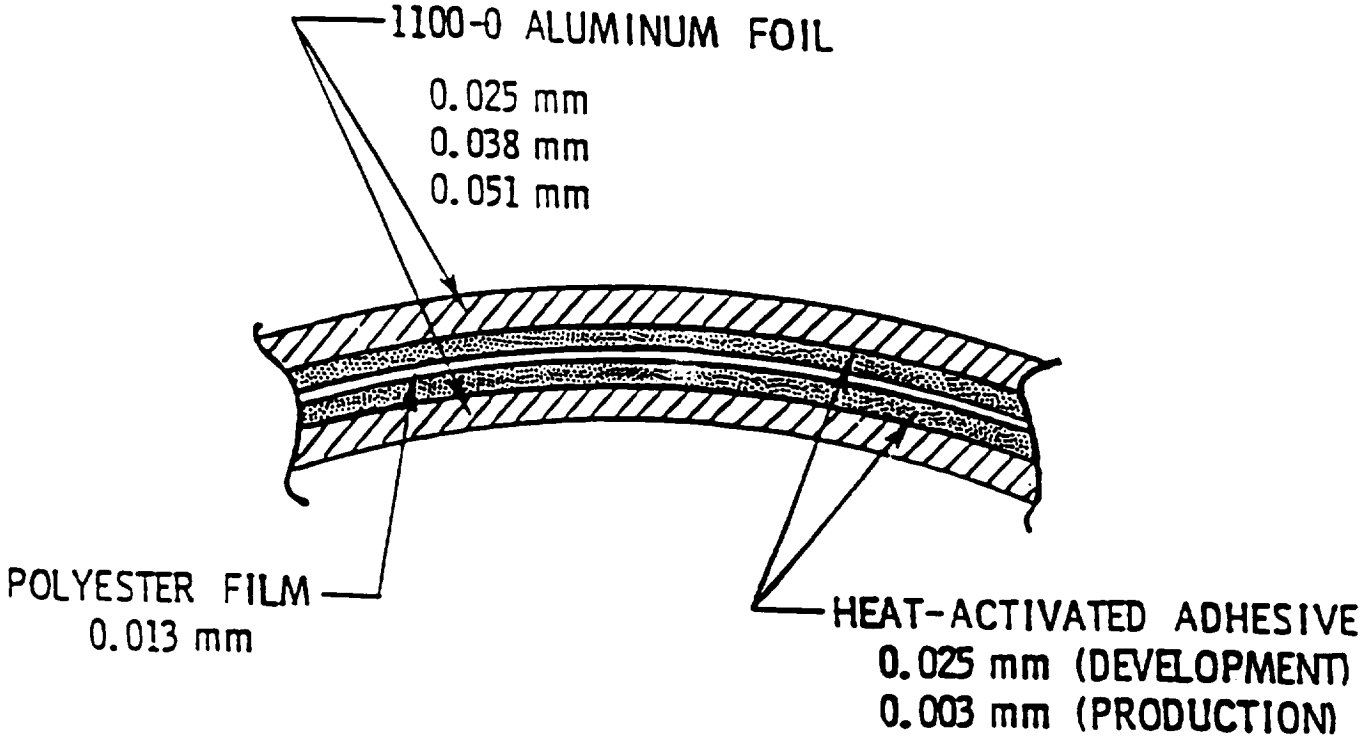

Figure 5.1.1-4 Torus composite [4].

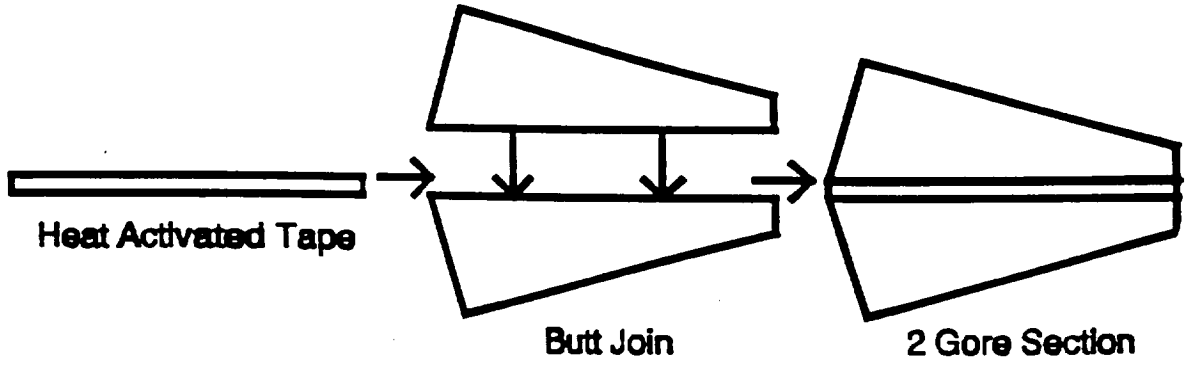

Figure 5.1.1-5 Connection of two thin filmed gores [5].

Surface Accuracy. This specific application requires an aperture efficiency near 50%. One of the determining factors in aperture efficiency is the surface accuracy of the antenna. The surface accuracy specified is 0.5 mm rms. The surface tolerance is equivalent to $\lambda/17$ at 35 GHz. The frequency for maximum gain (in Hz) for the antenna is specified by

$$f_{max\ gain} = \frac{c}{4\pi\delta'} \qquad (5.1.1\text{-}1)$$

where δ' is 0.5 mm and c is the speed of light. This corresponds to a frequency of 47.7 GHz. To show the effect of surface deviation on the gain of the antenna, Equation 5.1.1-2 was plotted in Figure 5.1.1-6. The equation shows the maximum gain possible for the given surface deviation (i.e. all other efficiencies = 1, [6]) and D is the antenna diameter (14 m) and λ is the wavelength. The surface accuracy efficiency is approximately 55%. The overall aperture efficiency specified, 47%, requires all other antenna efficiencies to be approximately 86%.

$$G = 10\ Log_{10}\ [\cos^2(4\pi\delta'/\lambda)\ (\pi D/\lambda)^2] \qquad (5.1.1\text{-}2)$$

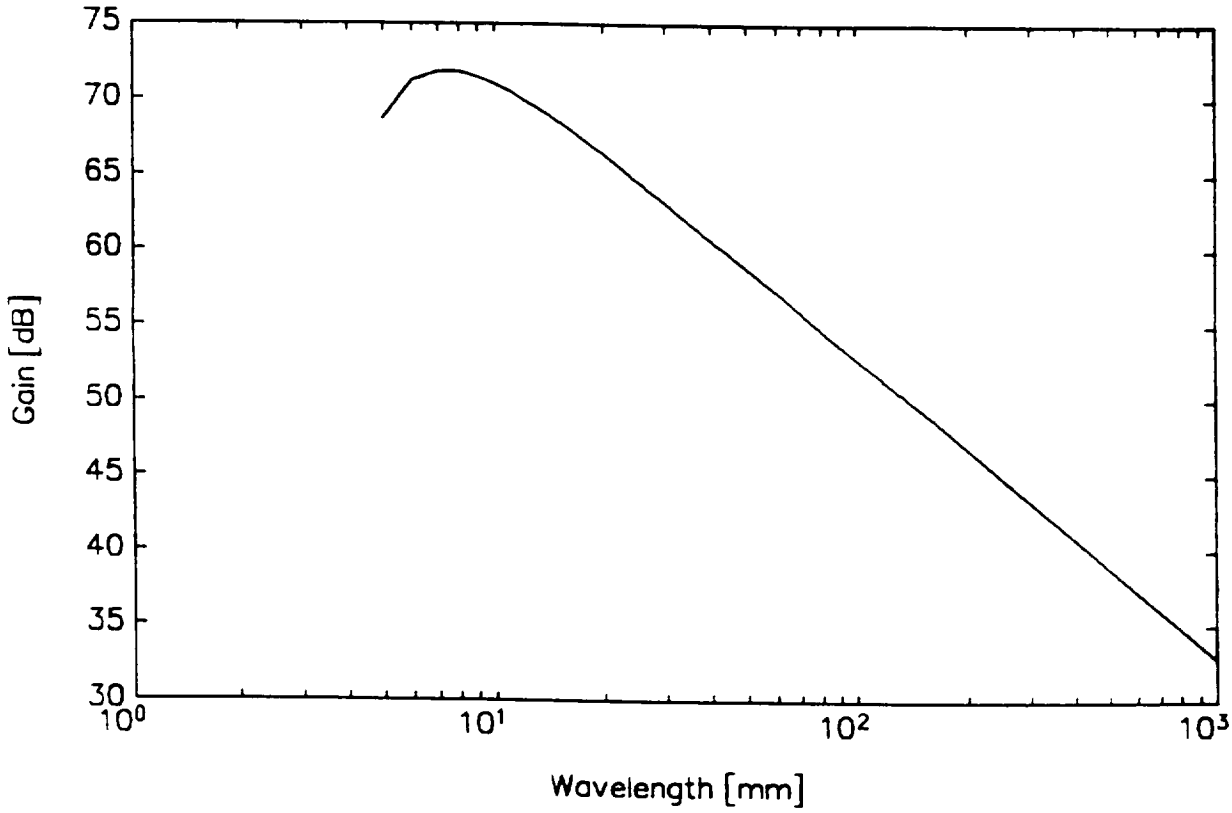

Figure 5.1.1-6. Maximum gain calculation as a function of wavelength.

Paraboloid Geometry. The paraboloid geometry is shown in Figure 5.1.1-7, where D is the diameter of the antenna, 14 m, L is the focal length, 9.1 m, and the F/D ratio is 0.65. Given the F/D ratio, x_1 is calculated in Equation 5.1.1-3, and the half-opening angle θ_1 in Equation 5.1.1-4. The feed of the antenna is a rectenna 96 cm in diameter. The entire rectenna was placed slightly in front of the focal point to allow all of the rectenna to be illuminated. By similar triangles, the length x_2 was found to be 53.1 cm.

$$X_1 = \frac{D^2}{16L} = 1.35 \quad [\text{m}] \tag{5.1.1-3}$$

$$\theta_1 = \tan^{-1}\left(\frac{D/2}{L-X_1}\right) = 42.1° \tag{5.1.1-4}$$

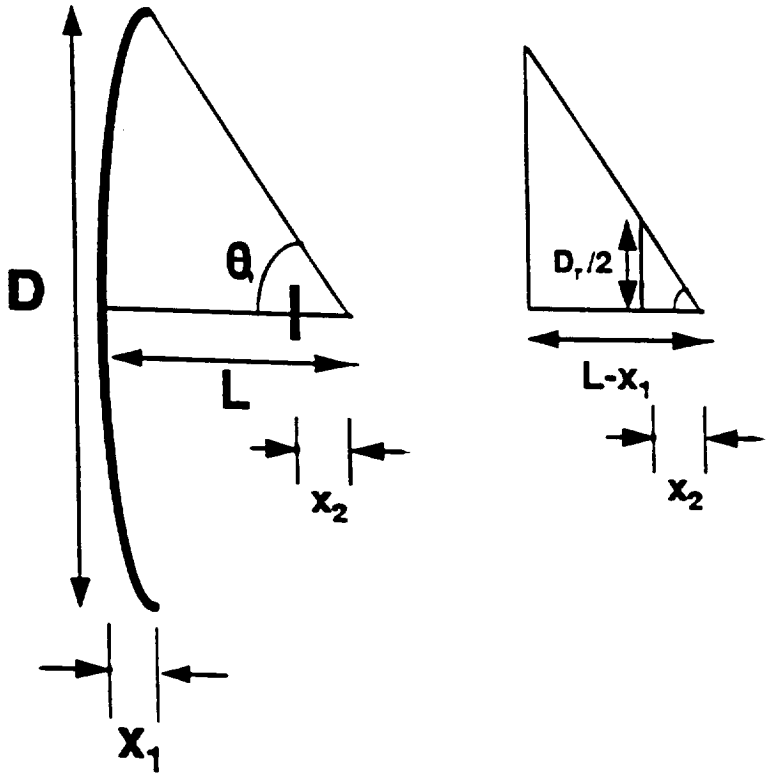

Figure 5.1.1-7. Paraboloid geometry.

Mass and Volume Specifications. Given an F/D ratio of 0.65, a mass and volume specification of the system could be determined. To estimate the system mass and volume, Figures 5.1.1-1 and 5.1.1-2 were used. However, the data shown in the figures was for inflatable antennas with surface accuracies of 1.0 mm rms. The antenna for the application has a specified surface accuracy of 0.5 mm rms. The tighter constraints correspond to a heavier and larger torus and paraboloid. To determine the system mass and volume, a multiplier of 4.5 was used for mass, and 10 was used for volume. These are conservative numbers. A mass percentage breakdown was determined using the nomograms in [1], which contains the system descriptions for inflatable antennas 10, 100 and 1000 meters in diameter. The data was interpolated for a 14 m antenna and slightly adjusted for the new surface accuracy. The results are shown in Table 5.1.1-1.

Table 5.1.1-1. Inflatable antenna system mass breakdown.

System	Mass (kg)	% Total
Inflatable Antenna	68	100
Paraboloid	35	51.5
Torus and Truss	23	33.8
Inflation System	7	10.3
H_2O Inflatant	2.8	4.1
CO_2 Inflatant	0.2	0.3

Micrometeoroids. Micrometeoroids and orbiting space debris pose a threat to thin filmed and inflatable structures. However, the potential danger is less than one might imagine for two reasons. The first is that there are fewer micrometeoroids than was originally estimated. Thomas states, "The meteoroid flux in space was not well known, and estimates of the fluxes of meteoroids were too high by almost three orders of magnitude." [7]. The second reason is that the inflation pressure is low enough that the holes created by collisions with micrometeoroids do not greatly effect the internal pressure. The low internal pressure can be easily maintained with replacement gas. The higher pressure struts and torus would be affected by even small holes. For this reason the structures were rigidized, eliminating the need for internal pressure. If necessary, the entire paraboloid could be made rigid eliminating the need for replacement gas. However, such a design reduces the surface accuracy of the antenna.

The effect of the micrometeoroids depend upon the type of meteoroid. If it is "solid", then two holes will be created, one on each side of the paraboloid. If the meteoroid is "soft" the first impact could cause the meteoroid to break apart resulting many small holes or dents on the second surface. Test results showed that, typically, the resulting holes were approximately 1.5 times larger than the diameter of the projectile [8]. This, over time, can have an effect upon the surface tolerance of the reflector and inflation pressure of the system. For low inflation pressures, the extra inflatant needed for a ten year mission would be less than 10% of the initial system weight.

Antenna Deployment. Once the platform has reached the required orbit the deployment sequence can begin. There is a relatively small number of moving parts in the deployment mechanism. Timing may be more critical for proper deployment. However, the overall reliability of the inflatable antenna should be higher than the mechanical systems described earlier. The following lists the inflation sequence [1].

1. A small amount of water (<0.5 grams for a 14 m antenna) is released into the antenna to erect the system.

2. The CO_2 is then released into the torus and struts to the yield stress of the material, removing packaging wrinkles and rigidizing the torus.

3. Simultaneously, additional water is released into the paraboloid to remove packaging wrinkles on the reflector surface.

4. Once fully erect, the antenna and torus are vented to space until the operational pressure is achieved.

Inflatable Antenna Summary. This section examined the large aperture inflatable antenna technologies for space. Pressurized inflatable antennas have many characteristics which are attractive for space applications. The greatest of these traits is the inherently low mass and volume. At the same time, long mission lifetimes on the order of five to ten years are achievable.

An ongoing research and development program within NASA and industry has advanced the state of the art of inflatables for space. A variety of rigidization techniques are being studied, and the surface accuracies are increasing. Environmental effects such as meteoroids, radiation, oxygen degradation, and thermal distortions have been examined and designs compensated.

L'Garde Inc., in Tusten, CA, has manufactured several inflatable reflectors for aerospace applications. When contacted, L'Garde indicated that they could develop and test an inflatable antenna to meet the specifications described in this section. The cost to develop, manufacture, and test the specified inflatable antenna within two years is $2 million.

5.1.2 Structural Design

Material Selection. Materials are selected on the basis of strength, stiffness, density, thermal conductivity, thermal expansion, fabrication advantages, and compatibility with the orbit environment. Materials offering higher strength to weight ratios are preferred to conventional materials for spacecraft applications. Aluminum alloys are the most common structural materials in aerospace applications [9].

Aluminum alloys have a high strength to weight ratio. They are easy to fabricate and inexpensive. Since aluminum is a space tested material, development costs of structures made of aluminum are less, making it an ideal material for a low cost mission [10]. Hence aluminum was selected as the structural material for WISPER.

Primary Structure. The spacecraft structure was designed to fit in the payload envelope of the Pegasus launch vehicle. The structure is an octagonal shell, 1.016 m in diameter and a height of 0.558 m. A thickness of 2.75 mm made of 7075 Aluminum will provide sufficient strength, stability, and rigidity. The structure was developed from the analysis of the worst case scenario which occurs during launch.

A unique feature of the Pegasus launch vehicle is that it will be launched from a B-52 aircraft. This means the structure will experience loading on 2 axes. Table 5.1.2-1 displays the payload acceleration environment in the Cartesian coordinate system for the Pegasus.

Table 5.1.2-1. Payload acceleration environment.

Type	X Axis	Y Axis	Z Axis
Aerodynamic pull up	-4 g	± 0.5 g	+2.85 g
Stage 1 Burnout	-7.5 g	± 0.2 g	± 0.2 g
Stage 2 Burnout	-3.75 g	± 0.2 g	± 0.2 g
Stage 3 Burnout	-3.0 g	± 0.2 g	± 0.2 g
Flight Design Limit	- -	- -	6 g

In order for the structure to survive the ride into orbit it must be able to withstand the maximum loads, and the worst case shock scenario of 200 g in the frequency range from 1000 to 10000 Hz [9].

Sizing for Strength. Various methods can be used to predict the distribution of internal loads on the structure depending on its complexity and scope of analysis. Since satellite structures are statically indeterminate, finite element analysis is generally the preferred way of calculating the stresses [11]. Preliminary calculations can be done on a statically determinate model that is fixed and its base has an axial load working on it.

The external structure of the satellite is assumed to be a cylindrical shell. This shell is under the worst case loading. The combined load is represented by P_{eq} which is comprised of the axial force P_{axial} and the bending moment M about the vertical Z axis. The maximum axial load and the maximum bending moment were calculated to be 19,500 N and 2,125 Nm, respectively. The combined load is given by

$$P_{eq} = P_{axial} + \frac{2M}{R} \quad [\text{N}] \tag{5.1.2-1}$$

where R (m) represents the radius of the circle circumscribing the satellite structure. This gives an equivalent load of 25,000 N. The stress σ is given by

$$\sigma = \frac{P}{A} \quad [\text{MPa}] \tag{5.1.2-2}$$

where A represents the cross sectional area of the satellite (m^2). The stress should be less than the allowable tensile strength of aluminum (524 MPa). According to Equation 5.1.2-2, the minimum area required is approximately 53.4 mm^2.

Stability. The allowable buckling stress must be less than the compressive yield stress for the structure to be stable. The equation for the theoretical cylinder buckling stress, σ_{cr}, is

$$\sigma_{cr} = 0.6\gamma\frac{Et}{R} \quad [\text{MPa}] \tag{5.1.2-3}$$

where γ is a reduction factor used to correlate theory to test results. In Equation 5.1.2-3) t represents the thickness of the cylinder (m) and R the radius (m). E is the modulus of elasticity (MPa) and is characteristic of the material used to fabricate the shell. Thin shell buckling is sensitive to minor imperfections in shape, so γ can be as low as 0.15 [11]. The reduction factor depends on a geometric parameter, ϕ, for cylinders.

$$\phi = \frac{1}{16}\sqrt{\frac{R}{t}} \tag{5.1.2-4}$$

MS in Equation 5.1.2-5 stands for the Margin of Safety, the value of which is greater than

$$S = \frac{\textit{Allowable Stress}}{\textit{Applied Stress}} - 1.0 \qquad (5.1.2\text{-}5)$$

value of 0.4 for *MS* (which gives a factor of safety of 1.4)
ess, σ_{cr}, is calculated for buckling. The applied stress is
-4. The value of the allowable stress can be modified by
radius of the shell. The minimum thickness needed for
romagnetic radiation is 2.75 mm (see section 5.9). The
ents are smaller. Thus, a shell thickness of 2.75 mm was

n and Packaging

o an initial 600 km orbit. The Pegasus vehicle will be able
m) into orbit. After many iterations and by reducing the size
m components, WISPER could fit into the Pegasus. Figure
nfiguration with the satellite assembled within the Pegasus

.3-2, will last for approximately one year as the orbit decays

satellite has decayed to a 500 km orbit. Orbital decay is
drag on the inflatable antenna. To increase the lifetime of
ve antenna and its components will be jettisoned following
re 5.1.3-3 shows the satellite as envisioned in Phase II.

onfiguration is a function of other variables in the satellite
nass, total volume, booster requirements, thermal control,
ntal shocks, etc. [9].

e a 546.1 mm tall octagon cylinder which can be inscribed
r circle as shown in Figure 5.1.3-4. This satellite "bus" is
all module at its base which contains the inflatable microwave

of the inflatable microwave dish, it was the most difficult item
. Originally, the microwave dish was mounted on top of the
panded upward. However, this configuration shielded the
initial polar orbit) from the sun, resulting in a power shortage
ving the dish to the bottom of the satellite and expanding it
cs maintain full illumination from the sun at all times except
g experiments.

5-12

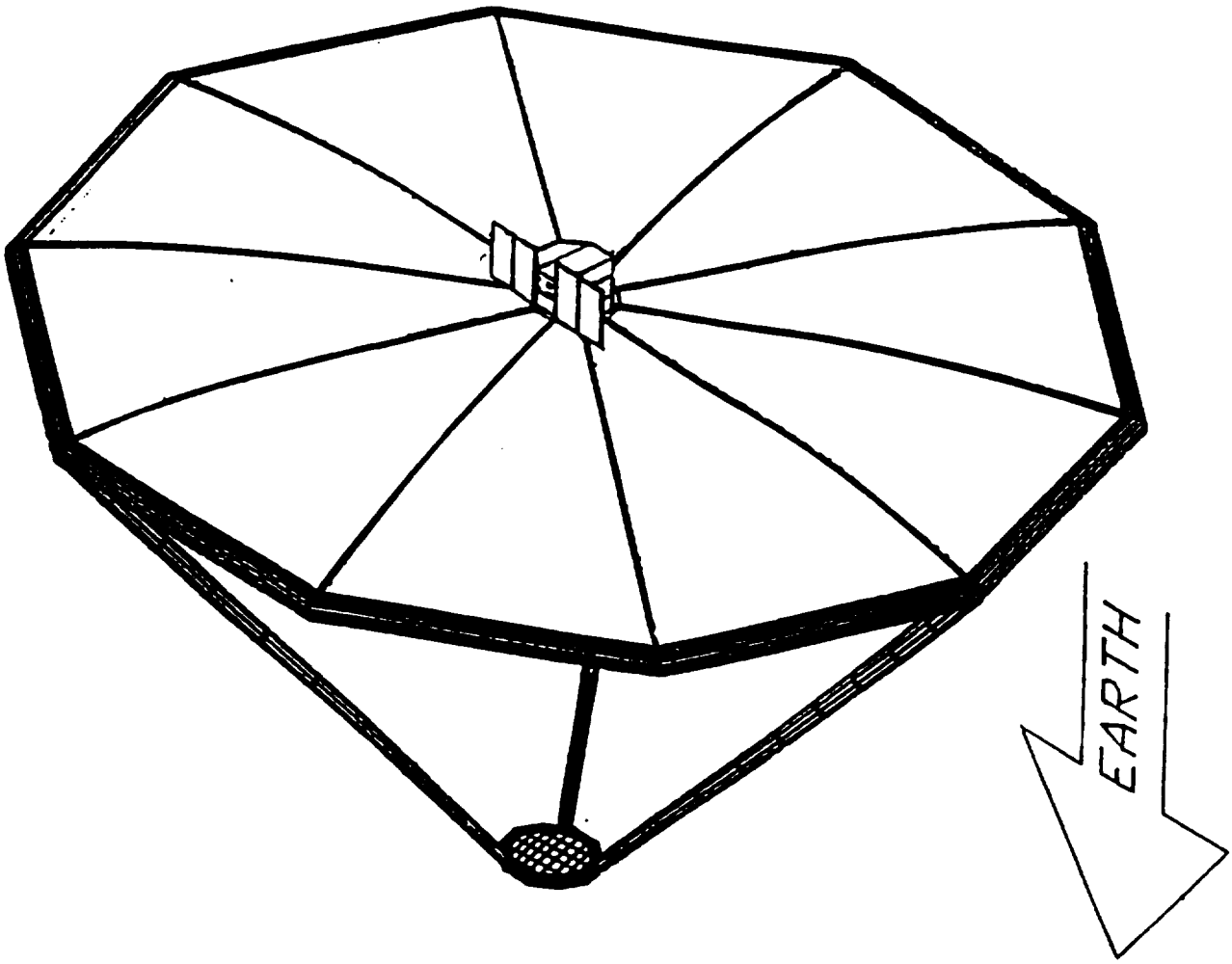

Figure 5.1.3-2. Phase I WISPER configuration.

C-2.

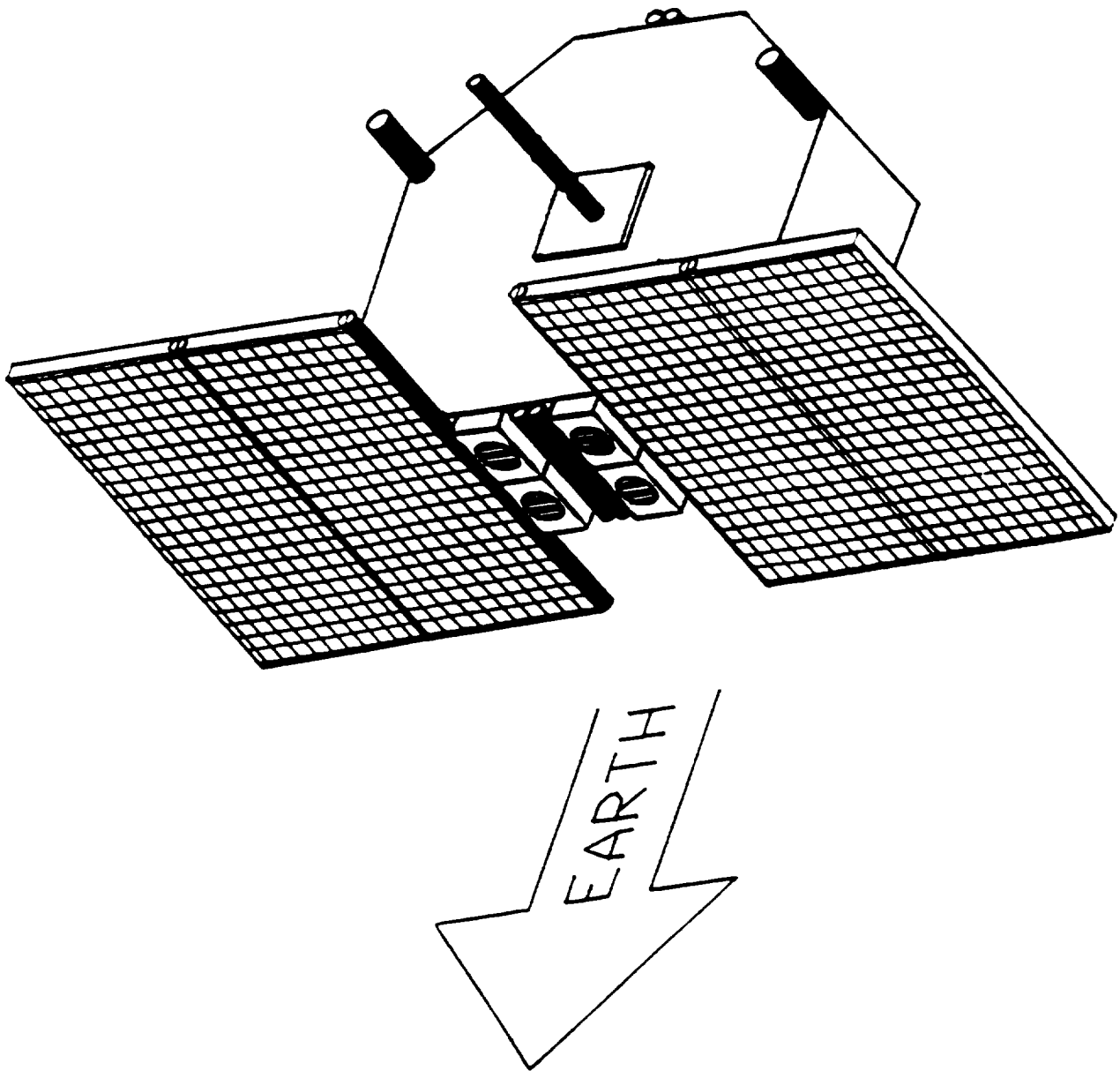

Figure 5.1.3-3. Phase II WISPER configuration.

Unfortunately, positioning the dish at the base of the satellite excluded the use of a standard payload adapter. The payload adapter is the mechanical connection between the spacecraft and the launch vehicle. The standard adapter supplied by Orbital Sciences for the Pegasus mounts to the satellite with a 590.6 mm (23.25 in) diameter ring. There are no structural mounts on the horizontal surface of the satellite base. Therefore, all loads must be transferred directly to the outer structural shell of the spacecraft. This required the design of a special payload adapter.

Another problem of having the dish inflated at the base is that the satellite cannot "see" the earth. Without reverting to long booms, communications from satellite to earth could not take place directly. The obvious solution was to place the necessary communications antennas on the bottom of the rectenna. Design trade-offs involve increased complexity, mass, volume, and cost to the microwave dish assembly.

Internal packaging of components depends on a number of factors including thermal management, mass distribution, vibration, and available internal volume. An assembly diagram of the major spacecraft components is shown in Figure 5.1.3-5.

The microwave dish occupies nearly 70% of the internal satellite volume. This large volume and the special requirement that it be jettisoned from the rest of the satellite at the end of Phase I dictated that it requires its own module. Components requiring clear view of the earth are located on the bottom of the rectenna. These components will not be needed for Phase II of the experiment and are lost when the microwave module is jettisoned at the end of Phase I.

The primary heat transfer mode in space is radiation [11]. Excluding the microwave module, most of the components are mounted on the walls of the main satellite bus. Those components requiring heating are mounted on the sun facing side. Conversely, components that must be kept relatively cool are located on the deep space side of the bus.

Conduction heat transfer occurs within the satellite structure. To avoid extra heating of the solar arrays, the arrays are mounted with low thermal conductivity hinges.

The majority of the components onboard are electrically powered and require data transmission lines. The components are connected by a wiring harness in the center of the main bus.

Plumbing of fuel lines is required by the thruster system. Two fuel tanks, serving 4 small hydrazine thrusters, are located in the center of the main bus to minimize the length of plumbing lines. The plumbing required for the inflatable microwave dish is an integral part of the microwave dish module.

The Pegasus launch vehicle has strict center of gravity (CG) requirements. The CG must

be less than 1092 mm above the payload interface plane and within ±25.4 mm of the vehicle's axial centerline. The current design does not take these requirements into strict account.

Most components have specific dynamic operating limits. As the various subsystems are clearly defined and this data becomes available, the component packaging can be reevaluated in light of the expected shock and vibration environments at each component location. Not only will more specific information be required on the components, but a more detailed vibration analysis will have to be performed. The current analysis do not indicate the different dynamic environments at different positions on the satellite, but assumes constant behavior throughout the structure.

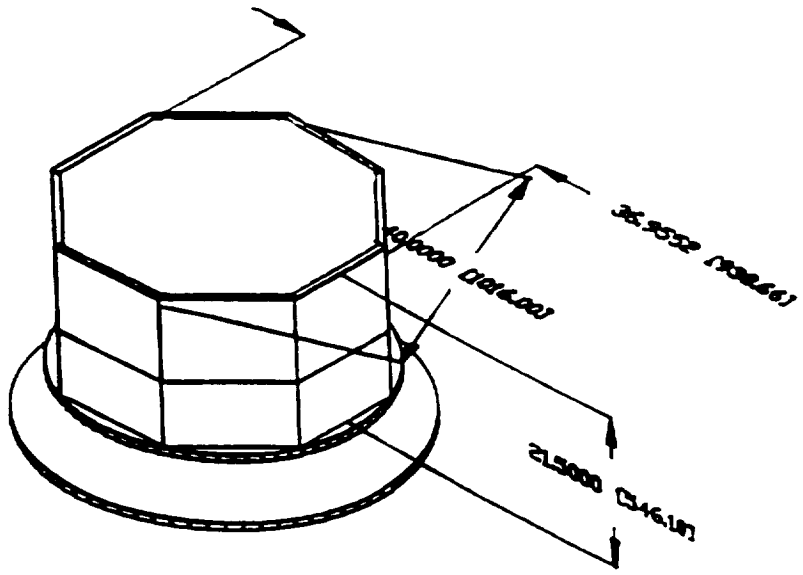

Figure 5.1.3-4. Critical dimensions.

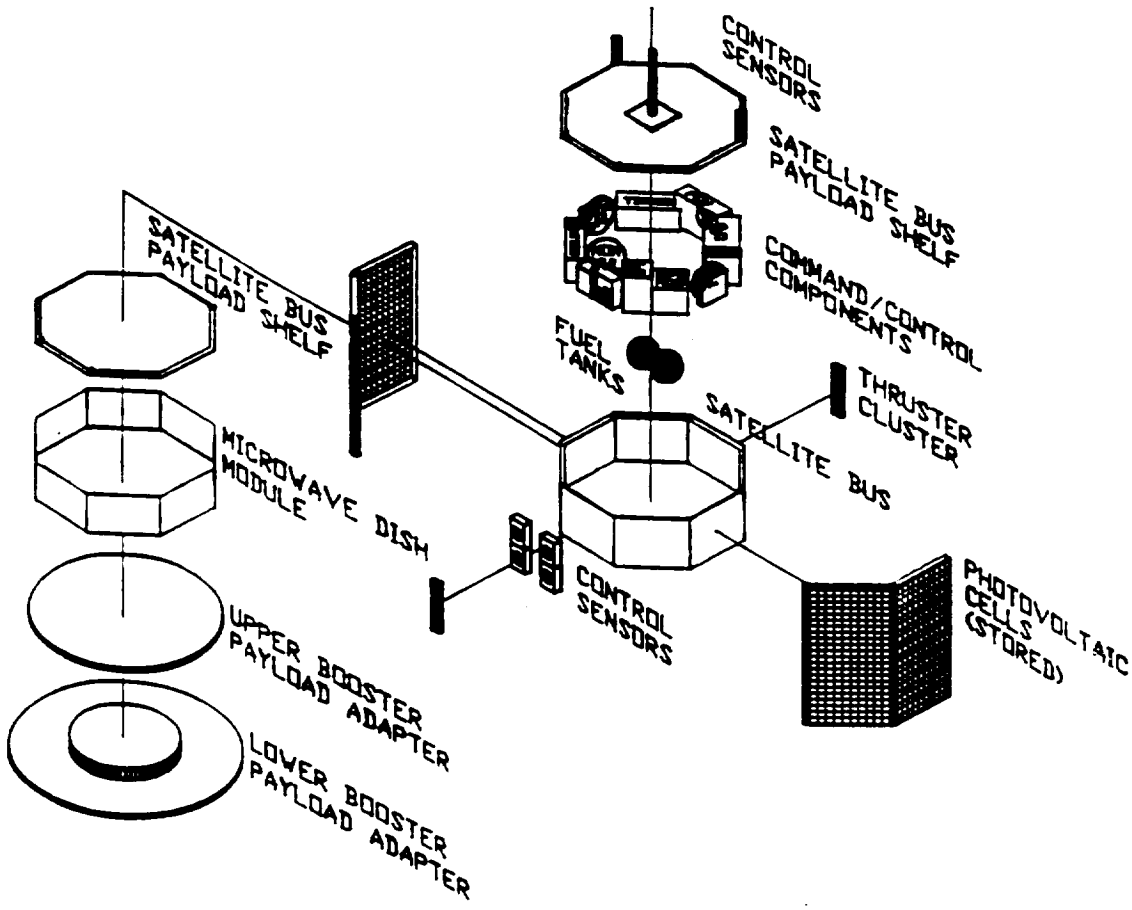

Figure 5.1.3-5. Assembly diagram.

5.1.4 Vibration

The vibration environment of a satellite is most severe at launch. Vibration comes from many sources. Acoustically induced vibration is engine noise that is reflected from the ground back to the booster. Aerodynamic effects on the booster payload fairing cause vibration at speeds around Mach 1. The engines are a constant source of vibration. At staging high g forces and short duration shocks are encountered [11].

Vibrations are transferred from the rocket to the satellite through the booster adapter. Typically the top and sides of the satellite are not rigidly attached to the booster. As a result, the satellite itself will tend to oscillate at some frequency induced by the forcing functions at its base. If this base frequency approaches the natural frequency of the satellite, the satellite may impact the fairing. Subsystem components are designed to operate within specific frequency, shock, and mechanical loading ranges. The satellite must be analyzed to avoid frequencies that would damage components. Booster vibration and loading characteristics are generally provided by the manufacturer and can be used

for a preliminary analysis.

Pegasus has a relatively low lateral natural frequency of about 12 Hz. The spacecraft should have a lateral natural frequency above 12 Hz to avoid resonance. Orbital Sciences recommends that a design minimum value of 2 Hz be used to account for variations in the Pegasus natural frequency for various configurations and payloads.

At 41,000 ft the launch vehicle is dropped from the wing of the carrier aircraft. This vertical drop (with the rocket in a horizontal position) is where the natural frequency of the booster and payload is most likely to occur. The vibration analysis of the payload must include a lateral natural frequency estimation to determine whether damage to the spacecraft is likely. Potential spacecraft are placed on a shaker table and excited at their natural frequency to evaluate their vibration performance [12]. Another common test is to vibrate the spacecraft at its natural frequency at the force of 0.037 N for the Pegasus environment [9].

It is necessary to know the minimum skin thickness required to meet 20 Hz lateral natural frequency requirement. To obtain these values a computerized mathematical model of the structure in Mathcad was developed. Figures 5.1.4-1a and 5.1.4-1b show the structural configuration and the cantilevered beam used to represent the satellite.

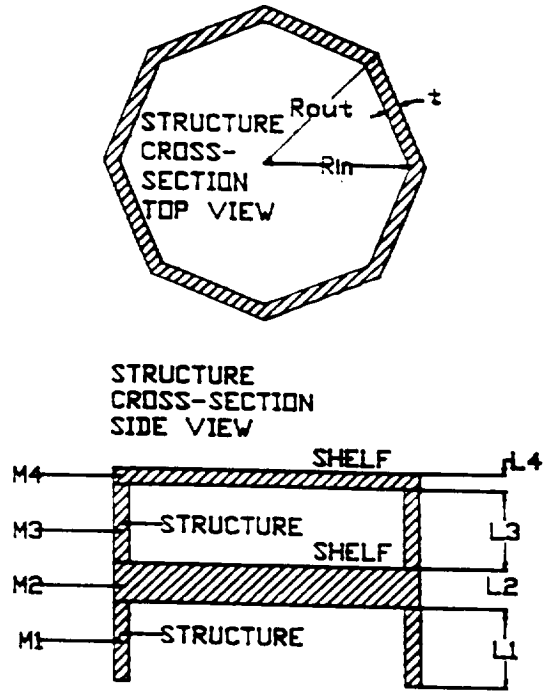

Figure 5.1.4-1a. WISPER structural configuration model.

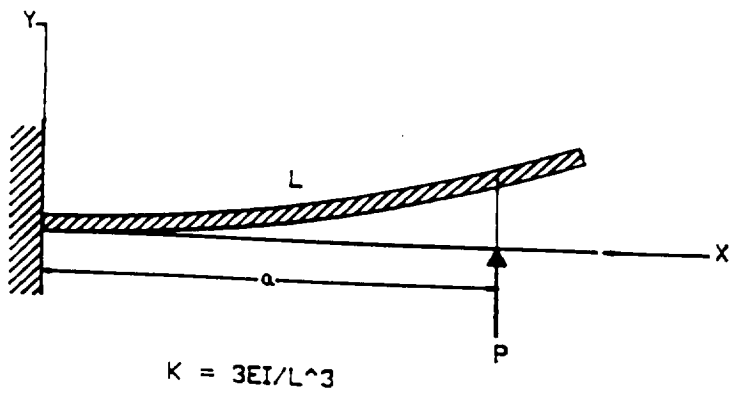

Figure 5.1.4-1b. Cantilever beam model.

As shown in the following mathematical model, the natural frequencies of the satellite are well above the 20 Hz minimum value required for the Pegasus [12]. The lateral natural frequency of the WISPER satellite is about 1000 Hz. Dynamic coupling will not be a problem with a lower natural axial frequency of approximately 340 Hz.

The amount of structural response to input loads and displacements is determined by the use of transmissibility relationships. These relationships are plotted for a range of damping ratios, with a damping ratio of 0.05 being typical for satellite structures [13]. The transmissibility graphs (figures 5.1.4-2 and 5.1.4-3) indicate that components onboard the spacecraft will experience an amplitude about 10 times greater than those input at the base of the satellite.

The magnification graphs (figures 5.1.4-3, 5.1.4-4 and 5.1.4-5) give an idea of the displacement magnification which the components will experience when the loads are suddenly applied to the satellite.

Although the vibration analysis seems to indicates that the spacecraft will not encounter vibration induced damage, extensive vibration testing will be required to verify the structure and component vibration resistance.

VIBRATION ANALYSIS:
UAF/USRA/NASA "WISPER" SPACECRAFT

This analysis models the spacecraft as a lumped mass beam with an octagon cross-section monocoque. The model utilizes 4 seperate descrete mass sections which correspond to the 4 structural sections of the spacecraft. This results in a total of 4 degrees-of-freedom. To insure that the spacecraft will not be damaged by vibration during launch it should have a fundamental lateral frequency greater than 20 Hz.

I. CONSTANTS:

E = modulus of elasticity (N/mm^2) $E := 71 \cdot 10^3 \cdot \frac{newton}{mm^2}$

ρ = density (kg/mm^3) $\rho := 2.8 \cdot 10^{-6} \cdot \frac{kg}{mm^3}$

t = skin thickness of structure (mm) $t := 2.75 \cdot mm$

N = number of sides on structure $N := 8$

II. CALCULATE THE AREA MOMENT OF INERTIA OF THE SATELLITE STRUCTURE:

A.

CIRCUMSCRIBED RADIUS OF STRUCTURE $R_{out} := 508 \cdot mm$

INSCRIBED RADIUS OF STRUCTURE $R_{in} := R_{out} - \frac{t}{\cos\left(\frac{180}{N} \cdot deg\right)}$

$R_{in} = 505.02 \cdot mm$

B.

SIDE LENGTH OF EXTERNAL POLYGON $L_{side.o} := 2 \cdot R_{out} \sin\left(\frac{180}{N} \cdot deg\right)$

$L_{side.o} = 388.81 \cdot mm$

SIDE LENGTH OF INTERNAL POLYGON $L_{side.i} := 2 \cdot R_{in} \sin\left(\frac{180}{N} \cdot deg\right)$

$L_{side.i} = 386.53 \cdot mm$

C.

AREA OF INTERNAL POLYGON $A_{out} := \frac{N \cdot R_{out}^2 \sin\left(\frac{360}{N} \cdot deg\right)}{2}$

$A_{out} = 7.3 \cdot 10^5 \cdot mm^2$

AREA OF INTERNAL POLYGON $A_{in} := \frac{N \cdot R_{in}^2 \sin\left(\frac{360}{N} \cdot deg\right)}{2}$

$A_{in} = 7.21 \cdot 10^5 \cdot mm^2$

D.

MOMENT OF INERTIA OF EXTERNAL POLYGON $I_{out} := \frac{A_{out}\left(6 \cdot R_{out}^2 - L_{side.o}^2\right)}{24}$

$I_{out} = 4.25 \cdot 10^{10} \cdot mm^4$

MOMENT OF INERTIA OF INTERNAL POLYGON $I_{in} := \frac{A_{in}\left(6 \cdot R_{in}^2 - L_{side.i}^2\right)}{24}$

$I_{in} = 4.15 \cdot 10^{10} \cdot mm^4$

E.

MOMENT OF INERTIA OF VERTICAL STRUCTURE $I_{oct} := I_{out} - I_{in}$

$I_{oct} = 9.87 \cdot 10^8 \cdot mm^4$

MOMENT OF INERTIA OF HORIZONTAL SHELVES $I_{shelf} := I_{out}$

$I_{shelf} = 4.25 \cdot 10^{10} \cdot mm^4$

III. CALCULATE THE LATERAL AND AXIAL SPRING CONSTANTS FOR EACH SECTION OF THE SATELLITE USING A CANTILEVERED BEAM MODEL:

A.

LENGTH MATRIX - LENGTH OF EACH SECTION:

$L := \begin{bmatrix} 228.6 \\ 5.08 \\ 309.88 \\ 2.54 \end{bmatrix} mm$

$n := 1 .. 4$

$L_{T_1} := 0 \cdot mm$

$L_{T_{n+1}} := L_{T_n} + L_n$

$L_{ttl} := L_{T_5}$

$L_{ttl} = 546.1 \cdot mm$

$L_T = \begin{bmatrix} 0 \\ 228.6 \\ 233.68 \\ 543.56 \\ 546.1 \end{bmatrix} \cdot mm$

B.

MOMENT OF INERTIA MATRIX - MOMENTS OF INERTIA OF EACH SECTION:

$I_{strct} := \begin{bmatrix} I_{oct} \\ I_{shelf} \\ I_{oct} \\ I_{shelf} \end{bmatrix}$

$I_{strct} = \begin{bmatrix} 9.87 \cdot 10^8 \\ 4.25 \cdot 10^{10} \\ 9.87 \cdot 10^8 \\ 4.25 \cdot 10^{10} \end{bmatrix} \cdot mm^4$

C.

LATERAL SPRING CONSTANT

$k_n := \frac{3 E \cdot I_{strct_n}}{(L_n)^3}$

$k = \begin{bmatrix} 1.76 \cdot 10^7 \\ 6.9 \cdot 10^{13} \\ 7.07 \cdot 10^6 \\ 5.52 \cdot 10^{14} \end{bmatrix} \cdot \frac{newton}{mm}$

D.

AXIAL SPRING CONSTANT:

$k_{axial} := \frac{(A_{out} - A_{in}) E}{L_{ttl}}$

$k_{axial} = 1.11 \cdot 10^6 \cdot \frac{newton}{mm}$

IV. CALCULATE THE LATERAL STIFFNESS MATRIX FOR THE STRUCTURE:

BANDED LATERAL STIFFNESS MATRIX:

$k_0 := 0 \frac{newton}{mm}$

$K := \begin{bmatrix} k_1 + k_2 & -k_2 & k_0 & k_0 \\ -k_2 & k_2 + k_3 & -k_3 & k_0 \\ k_0 & -k_3 & k_3 + k_4 & -k_4 \\ k_0 & k_0 & -k_4 & k_4 \end{bmatrix}$

$K = \begin{bmatrix} 6.9 \cdot 10^{13} & -6.9 \cdot 10^{13} & 0 & 0 \\ -6.9 \cdot 10^{13} & 6.9 \cdot 10^{13} & -7.07 \cdot 10^6 & 0 \\ 0 & -7.07 \cdot 10^6 & 5.52 \cdot 10^{14} & -5.52 \cdot 10^{14} \\ 0 & 0 & -5.52 \cdot 10^{14} & 5.52 \cdot 10^{14} \end{bmatrix} \cdot \frac{newton}{mm}$

V. DETERMINE THE MASS MATRIX FOR THE SYSTEM:

A.

STRUCTURAL MASSES

$m_{struct_1} := L_1 \cdot \rho \cdot (A_{out} - A_{in})$

$m_{struct_3} := L_3 \cdot \rho \cdot (A_{out} - A_{in})$

$m_{struct_2} := L_2 \cdot \rho \cdot A_{out}$

$m_{struct_4} := L_4 \cdot \rho \cdot A_{out}$

COMPONENT MASSES:

$m_{comp_1} := 75.95 \cdot kg$

$m_{comp_3} := 99.5 \cdot kg$

$m_{comp_2} := 39.75 \cdot kg$

$m_{comp_4} := 2.81 \cdot kg$

B.

STRUCTURAL MASS MATRIX

$m_{struct} = \begin{bmatrix} 5.46 \\ 10.38 \\ 7.4 \\ 5.19 \end{bmatrix} \cdot kg$

$\Sigma m_{struct} = 28.43 \cdot kg$

COMPONENT MASS MATRIX

$m_{comp} = \begin{bmatrix} 75.95 \\ 39.75 \\ 99.5 \\ 2.81 \end{bmatrix} \cdot kg$

$\Sigma m_{comp} = 218.01 \cdot kg$

C.

TOTAL MASS MATRIX X IDENTITY MATRIX

$m_0 := 0 \cdot kg$

$m := m_{struct} + m_{comp}$

$m_{ttl} := \sum m$

$m_{ttl} = 246.44 \cdot kg$

$$MI := \begin{bmatrix} m_1 & m_0 & m_0 & m_0 \\ m_0 & m_2 & m_0 & m_0 \\ m_0 & m_0 & m_3 & m_0 \\ m_0 & m_0 & m_0 & m_4 \end{bmatrix} \qquad MI = \begin{bmatrix} 81.41 & 0 & 0 & 0 \\ 0 & 50.13 & 0 & 0 \\ 0 & 0 & 106.9 & 0 \\ 0 & 0 & 0 & 8 \end{bmatrix} \cdot kg$$

VI. CALCULATE THE NATURAL FREQUENCIES OF THE STRUCTURE:

A.

CALCULATE THE DYNAMIC MATRIX:

$D := K \cdot MI^{-1}$

$$D = \begin{bmatrix} 8.48 \cdot 10^{14} & -1.38 \cdot 10^{15} & 0 & 0 \\ -8.48 \cdot 10^{14} & 1.38 \cdot 10^{15} & -6.61 \cdot 10^{7} & 0 \\ 0 & -1.41 \cdot 10^{8} & 5.17 \cdot 10^{15} & -6.9 \cdot 10^{16} \\ 0 & 0 & -5.17 \cdot 10^{15} & 6.9 \cdot 10^{16} \end{bmatrix} \cdot sec^{-2}$$

B.

SET D TO ZERO AND SOLVE FOR THE EIGENVALUES (λ):

$\lambda_n := eigenvals(D)_n$

$$\lambda = \begin{bmatrix} 2.23 \cdot 10^{15} \\ 2.1 \cdot 10^{8} \\ 3.92 \cdot 10^{7} \\ 7.42 \cdot 10^{16} \end{bmatrix} \cdot sec^{-2}$$

C.

LATERAL NATURAL FREQUENCIES:

$\omega_n := \sqrt{\lambda_n}$

$$\omega = \begin{bmatrix} 4.72 \cdot 10^{7} \\ 1.45 \cdot 10^{4} \\ 6262.98 \\ 2.72 \cdot 10^{8} \end{bmatrix} \cdot sec^{-1} \qquad f := \frac{\omega}{2 \cdot \pi} \qquad f = \begin{bmatrix} 7.51 \cdot 10^{6} \\ 2305.36 \\ 996.78 \\ 4.34 \cdot 10^{7} \end{bmatrix} \cdot hz$$

D.

FUNDAMENTAL LATERAL FREQUENCY:

$\omega_{nat} := \omega_3$

$\omega_{nat} = 6262.98 \cdot sec^{-1}$

$f_{nat} := f_3$

$f_{nat} = 996.78 \cdot hz$

E.

AXIAL NATURAL FREQUENCIES:

$$\omega_{axial} := \sqrt{\frac{k_{axial}}{\sum m}}$$

$\omega_{axial} = 2121.17 \cdot sec^{-1}$

$$f_{axial} := \frac{\omega_{axial}}{2 \cdot \pi}$$

$f_{axial} = 337.6 \cdot hz$

The fundamental axial and lateral frequencies are considerably different. Therefore coupling effects will be minimal.

VII. CALCULATE THE LATERAL TRANSMISSIBILITY OF THE SYSTEM FOR BASE EXCITATION AND RESPONCE ASSUMED CONSTANT THROUGHOUT THE STRUCTURE:

COUNTER VARIABLES:

$i := 1..300$

$j := 1..6$

INPUT FREQUENCIES:

$f_{in_i} := i \cdot 10 \cdot hz$

FREQUENCY RATIO:

$r_i := \frac{f_{in_i}}{f_{nat}}$

DAMPING COEFFICIENTS:

$\zeta_j := \frac{j+2}{100}$

$\zeta = \begin{bmatrix} 0.03 \\ 0.04 \\ 0.05 \\ 0.06 \\ 0.07 \\ 0.08 \end{bmatrix}$

TRANSMISSIBILITY:

$$TR_{i,j} := \frac{\sqrt{1+\left(2\cdot\zeta_j\cdot r_i\right)^2}}{\sqrt{\left[\left[1-\left(r_i\right)^2\right]^2+\left(2\cdot\zeta_j\cdot r_i\right)^2\right]}}$$

MAXIMUM TRANSMISSIBILITY:

$\max(TR) = 16.55$

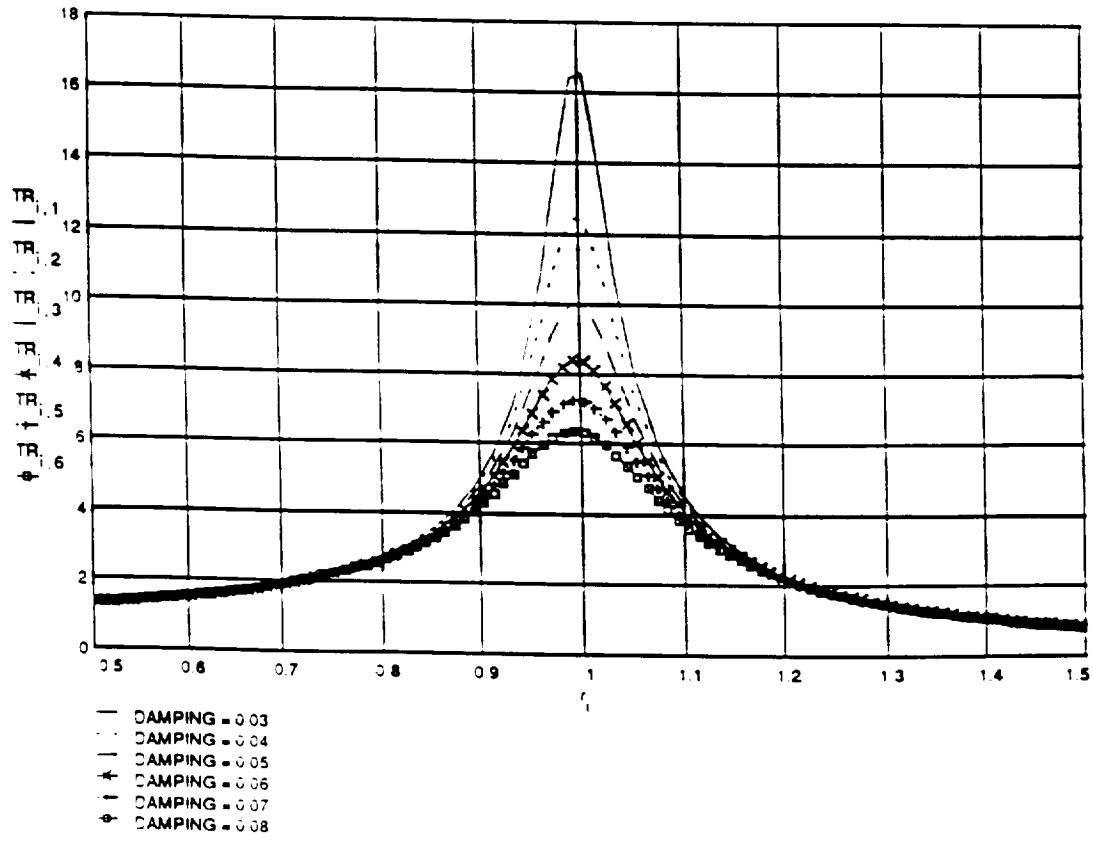

Figure 5.1.4-2. Lateral transmissibility versus frequency ratio.

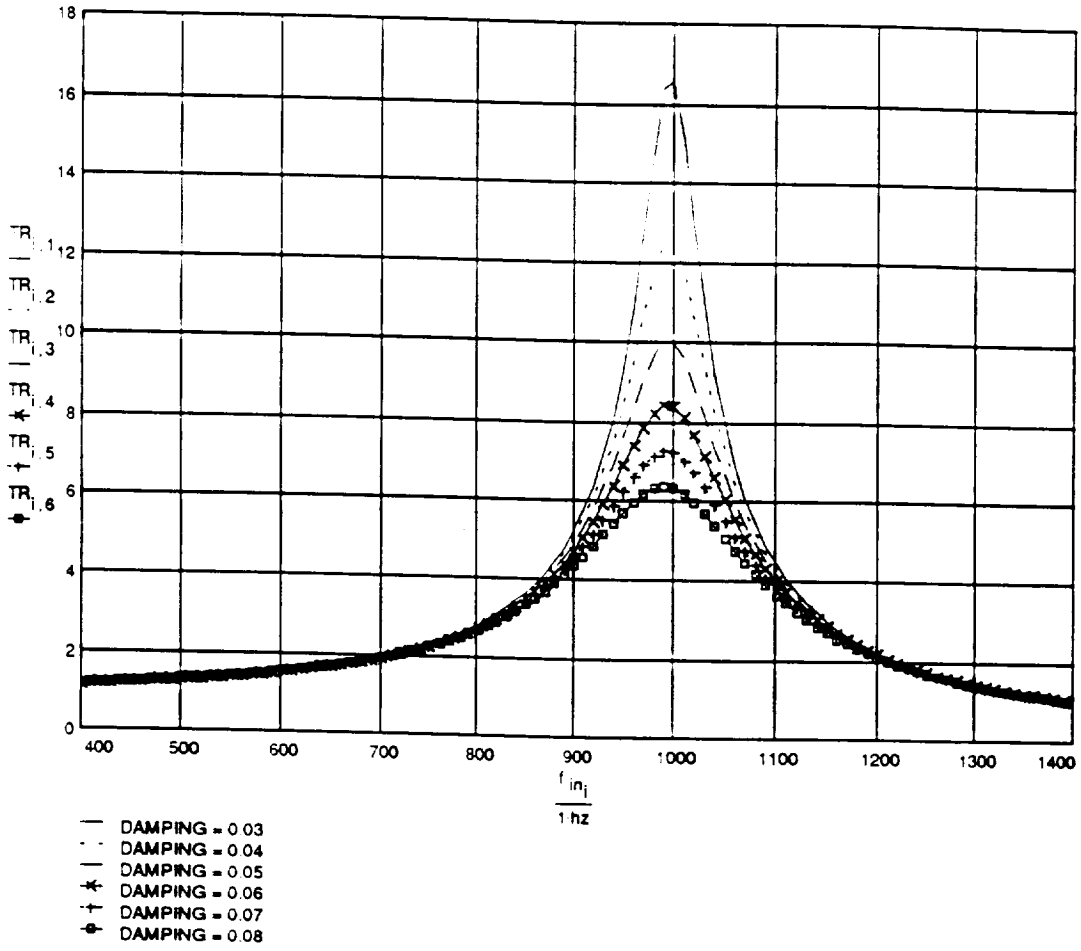

Figure 5.1.4-3. Lateral transmissibility versus input frequency.

VIII. CALCULATE STEADY STATE AND TRANSIENT VIBRATION RESPONSES (MAGNIFICATION FACTORS) OF THE SYSTEM FOR BASE EXCITATION AND RESPONCE ASSUMED CONSTANT THROUGHOUT THE STRUCTURE:

A.

STEADY STATE RESPONCE TO HARMONIC EXCITATION:

$$MF_{i,j} := \frac{1}{\sqrt{\left[1-(r_j)^2\right]^2+\left(2\cdot\zeta_j\cdot r_j\right)^2}}$$

MAXIMUM MAGNIFICATION: max(MF) = 16.52

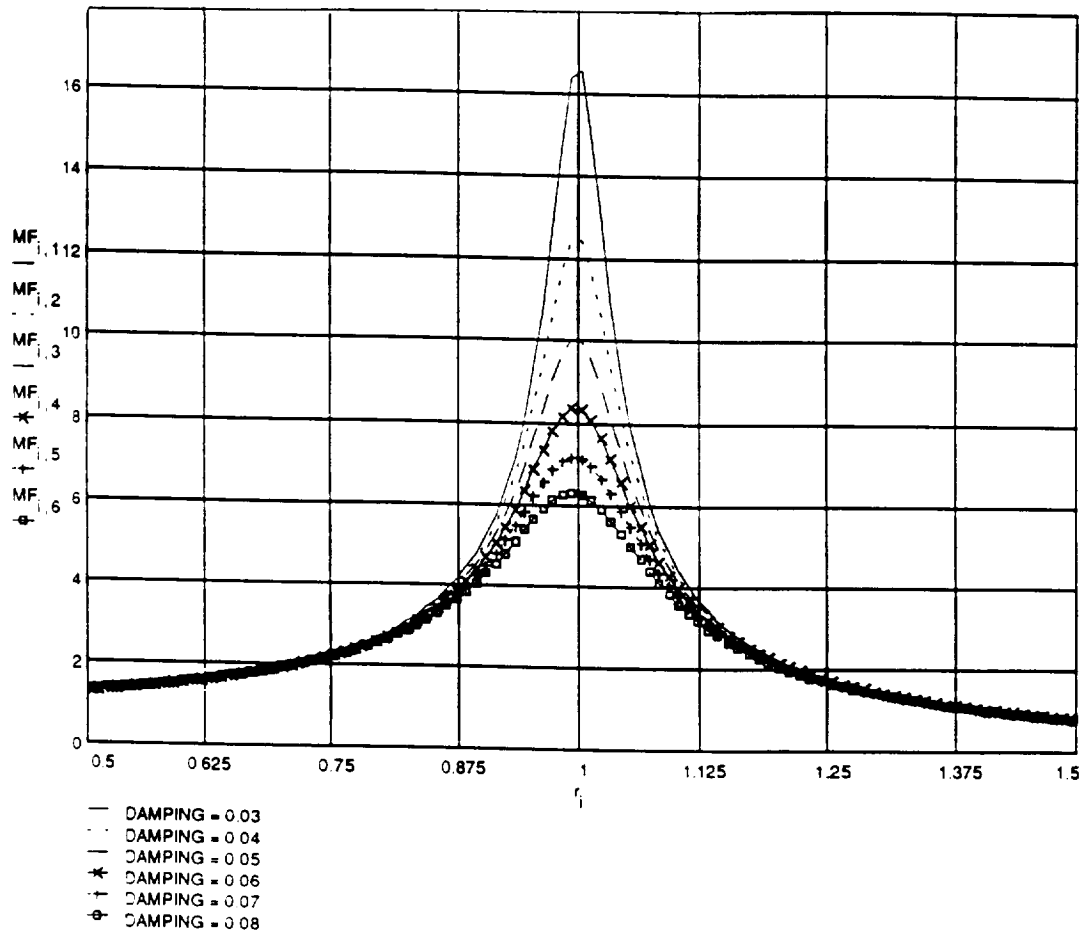

Figure 5.1.4-4. Steady state magnification factor versus frequency ratio.

B.

TRANSIENT RESPONSE TO STEP LOAD FUNCTION WITH DURATION t:

FUNDAMENTAL PERIOD: $T_{nat} := \frac{1}{f_{nat}}$ $T_{nat} = 0.001 \cdot sec$

$\omega_{d_j} := \omega_{nat}\sqrt{1-(\zeta_j)^2}$ $i := 1..201$ $t_i := \frac{(i-1)}{10000} \cdot sec$ TIME RATIO: $tr_i := \frac{t_i}{T_{nat}}$

$$MF_{i,j} := 1 - e^{-\zeta_j \cdot \omega_{nat} \cdot t_i}\left[\cos\left(\omega_{d_j} \cdot t_i\right) + \frac{\zeta_j}{\sqrt{1-(\zeta_j)^2}} \cdot \sin\left(\omega_{d_j} \cdot t_i\right)\right]$$

MAXIMUM MAGNIFICATION: $\max(MF) = 1.91$

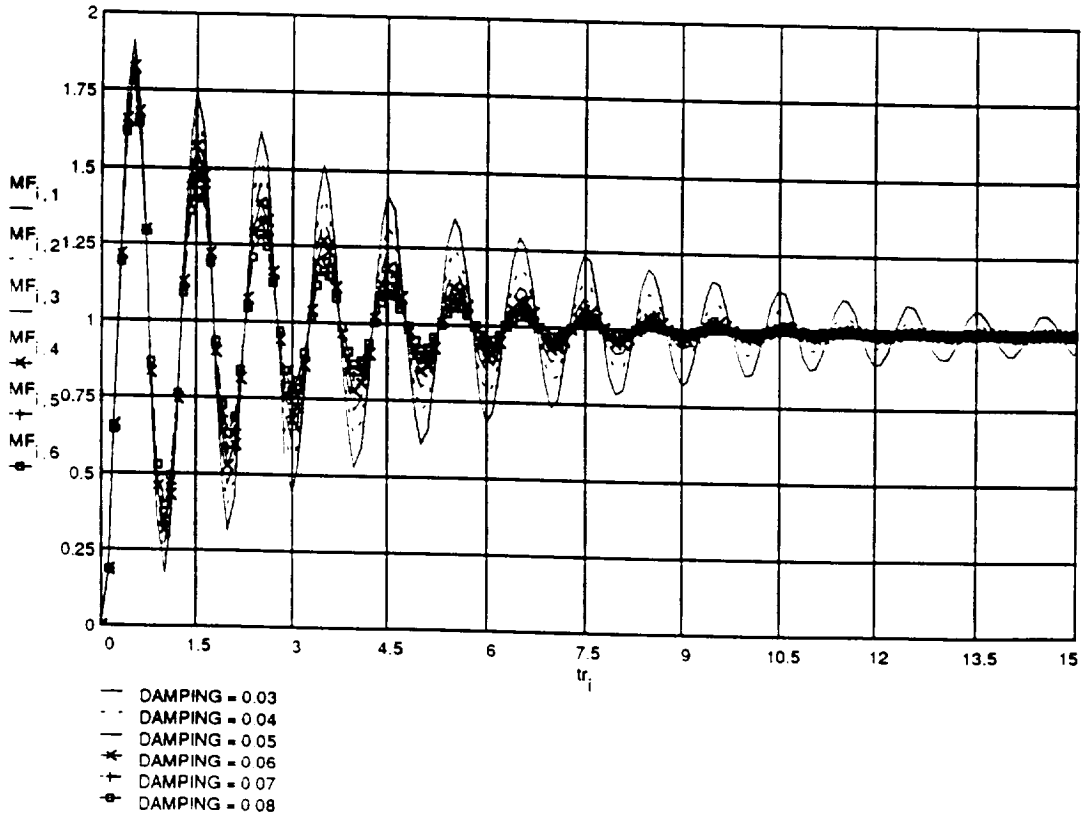

Figure 5.1.4-5. Transient magnification factor versus time ratio.

C.

TRANSIENT RESPONSE TO STEP LOAD FUNCTION WITH RISE TIME t_r AND ZERO DAMPING.

$i = 1 \ldots 100 \qquad t_i = \frac{i}{20000} \cdot sec$

$$MF_{max_i} = 1 + \frac{\tau_{nat}}{\pi \cdot t_i} \cdot \left| \sin\left(\frac{\pi \cdot t_i}{\tau_{nat}}\right) \right| \qquad tr_i = \frac{t_i}{\tau_{nat}}$$

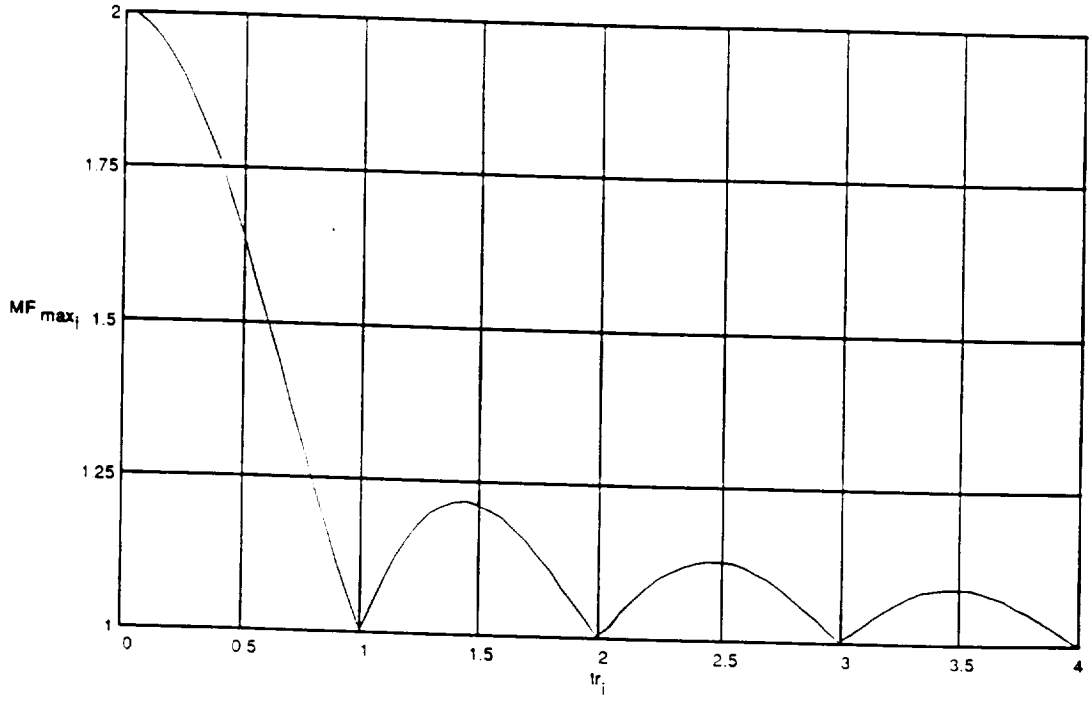

Figure 5.1.4-6. Maximum magnification factor versus time ratio.

5.2 Electrical Power Requirement

5.2.1 Power Demand

The design of the power subsystem is based on the expected power consumption of the mission equipment and satellite subsystems. The power estimation for each subsystem presented in Table 5.2.1-1 illustrates the extent to which the satellite is currently defined. Using data from Table 5.2.1-1, a power profile for each phase of the mission was constructed to indicate when peak loads occur, their magnitude, and duration. The power profile consists of a set of curves that represent various power parameters with respect to time. This curve consists of the sum of the power input and power output. Phase I and Phase II do not include the input from the microwave and laser power beaming. Notice the PV output falling off to zero as the satellite rotates to face earth. Table 5.2.1-1 shows the peak and average power demands for phases I and II. The power demand profile for both Phase I and II are shown in figures 5.2.1-1 and 5.2.1-2, respectively.

Table 5.2.1-1. WISPER power demand.

System	Activity Level			
	Phase I		Phase II	
	High	Low	High	Low
Reaction Wheels (norm)	20	20	0	0
Reaction Wheels (peak)	40	20	40	0
Beacon	40	0	0	0
Horizon Sensors	10	10	10	10
Sun Sensors	5	5	5	5
GPS	5	5	5	5
Instrumentation	18	18	18	18
Computer	35	35	35	35
Communications	37	7	37	7
PMAD	10	10	10	10
Unknown	15	15	15	15
TOTAL (norm)	155	125	135	105
TOTAL (peak)	215	125	215	105

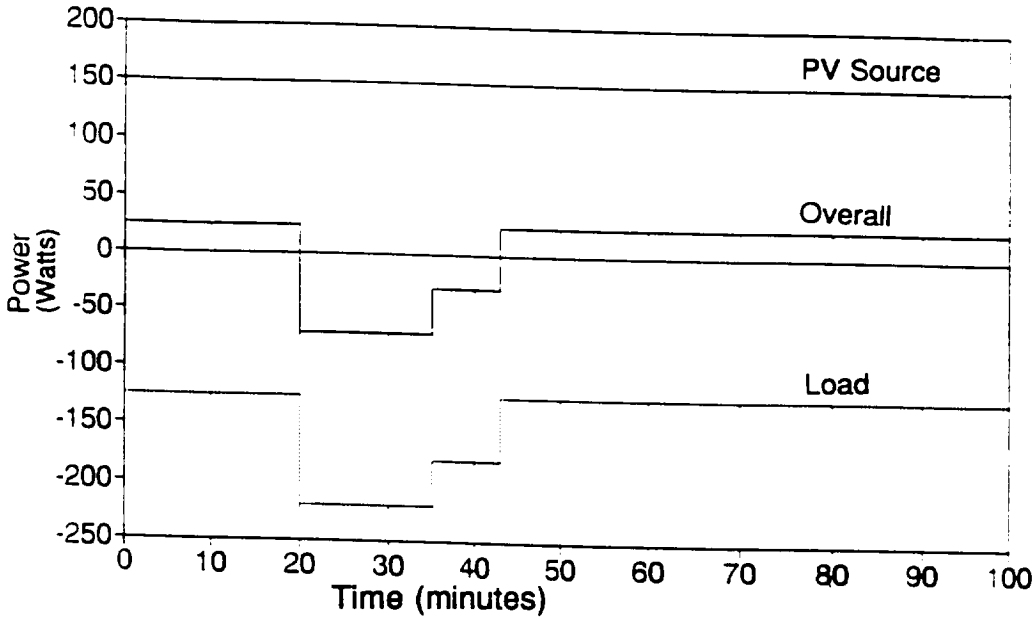

Figure 5.2.1-1. Phase I power profile.

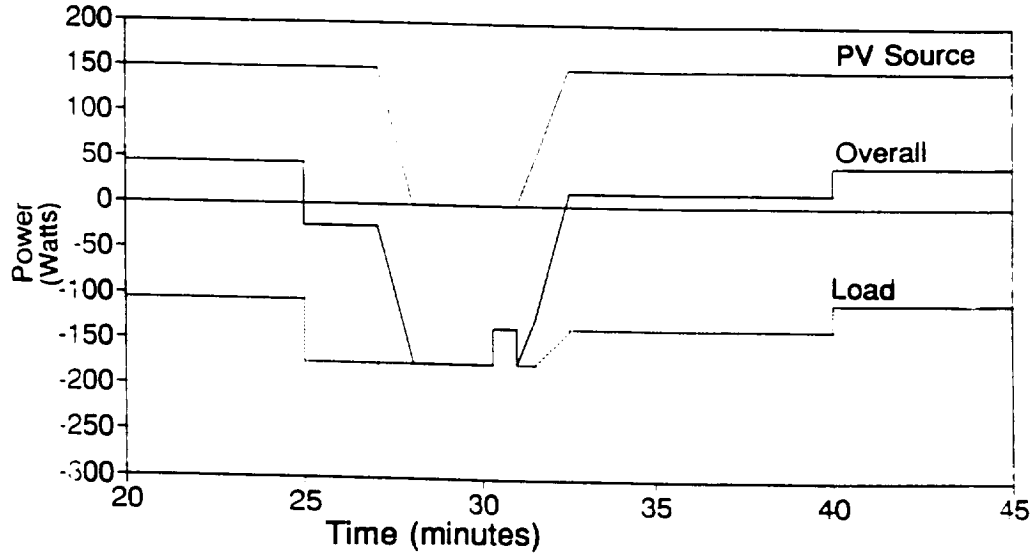

Figure 5.2.1-2. Phase II power profile.

5.2.2 Power Storage

The power storage system was sized by reviewing the power profile diagram, and setting a battery capacity level such that the greatest power demand on the batteries would not exceed a 40% depth of discharge (DOD) [14]. Through an iterative process, a battery capacity of approximately 140 W-hr was reached. This value is confirmed by estimating the required capacity of the batteries given by [11]

$$C_r \quad \frac{P_e T_e}{DOD(Nn)} \quad \text{[W-hr]} \qquad (5.2.2\text{-}1)$$

where:

C_r = Required capacity (W-hr)
P_e = Average eclipse load (W)
T_e = Maximum eclipse time (hr)
DOD = Depth of discharge , typically .2 to .4
N = Number of batteries (non - redundant)
n = Transmission efficiency between battery and load

The primary power storage unit is a bank of 24, 1.2 volt, 5 Ah cells, rated at 140 W-hr, with a minimum lifetime of 4 years assuming a 40% average DOD [15]. The cells are sealed fibrous Nickel Cadmium (NiCd) construction which does not outgas. Given the 2 year mission life, it has been decided that a fully redundant power storage system is not necessary. The satellite will utilize a single bank of high reliability batteries (failure rate = 0.3×10^{-7}), manufactured by either Eagle Pischer or SAFT. To improve reliability, the system allows up to 4 random cells to fail. This is accomplished by using bypass diodes for individual open circuit protection, thus preserving the current path for the remaining cells. This configuration is shown in Figure 5.2.2-1. NiCd batteries were chosen over Nickel Hydrogen (NiH_2) since no source of 5 Ah NiH_2 batteries could be found. To this date, the smallest NiH_2 cells are in the neighborhood of 20 to 30 Ah. The critical specifications regarding the batteries are as follows:

Quantity	- 24 cells
Cell voltage	- 1.2 volts, nominal
Capacity	- 5 Ah
Battery Voltage	- 28.2 volts, nominal
	- 31.7 full charge
Cell dimensions	
height	- 3.17 in (8.05 cm)
width	- 2.14 in (5.44 cm)
thick	- 0.82 in (2.08 cm)
mass	- 221 gm (0.47 lb)

Battery dimensions (including mounting hardware)

height	- 3.17 in (8.05 cm)
width	- 4.91 in (12.45 cm)
thick	- 11.72 in (29.76 cm)
mass	- 7.12 kg (15.67 lbs)

Life Expectancy

LEO 40% DOD - > 4 yrs

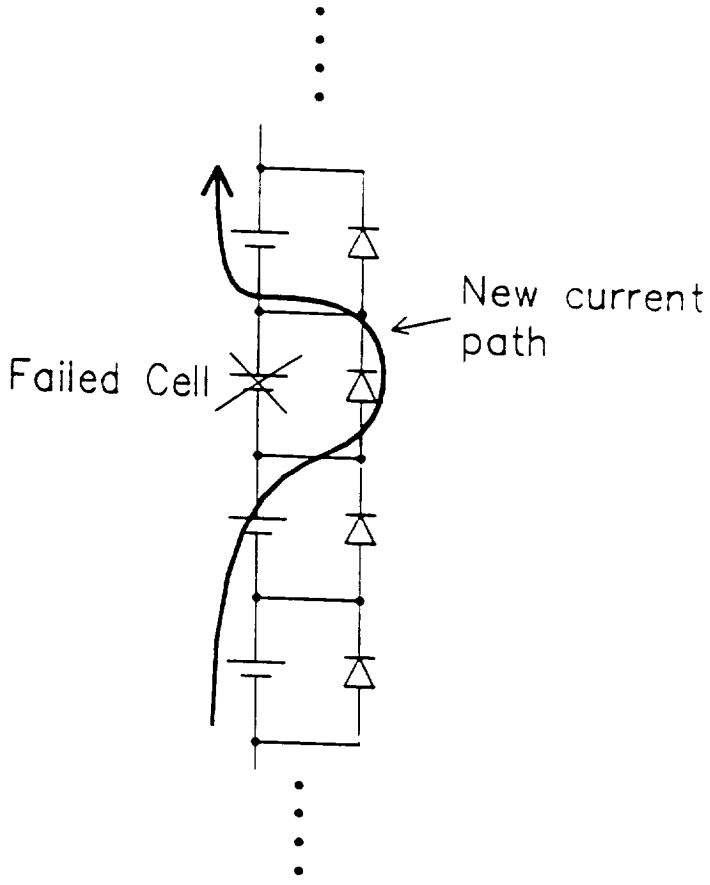

Figure 5.2.2-1. Failed cell bypass circuitry.

During the power beaming experiments, the output of the rectenna will be connected to the battery, thus providing a load for the rectenna. Similarly, during Phase II of the mission, the output of the PVs will be connected to the battery. These inputs were not represented in the power profile figures shown previously (figures 5.2.1-1 and 5.2.1-1).

5.2.3 Power Generation

Primary power for the spacecraft will be supplied by three GaAs photovoltaic arrays and a single Si array. Size limitations of the WISPER satellite require high power production from a small area, therefore GaAs cells were chosen for their proven ability in space and significant specific power. The space hardened GaAs cells chosen have demonstrated an average Beginning Of Life (BOL) efficiency of 18.5%.

Two solar panels will be deployed on either side of the satellite body. The PV array is shown in both the stowed and deployed positions in Figure 5.2.3-1. This area of 1.4 square meters will provide the satellite with 150 continuous watts of power. When calculating the necessary area of the array, factors such as normal lifetime degradation, thermal degradation, packing density and shading from other sections of the array itself have been taken into consideration.

5.2.4 Power Routing and Conditioning

Power routing will be controlled by the FS386 onboard computer. A high speed 8 bit serial line from the FS386 will connect to a decoder inside the control unit. Multiple output lines from the decoder will provide control of each of the switches. The control unit will be designed specifically for the satellite. Controlled power lines are provided for safety purposes only. The lines isolate a subsystem from the bus in case the subsystem fails and presents a short circuit to the bus. The switches are sealed mechanical relays and are controlled by a single serial line from the onboard computer. If a source of reliable solid state switches becomes available, then the mechanical relays could be replaced. A block diagram of the controller is shown in Figure 5.2.4-1. The controller dimensions are approximately 10 cm x 20 cm x 25 cm, and its mass is approximately 4 - 5 kg. Control lines, the quantity of which are shown in parenthesis, will be supplied to the following sub-systems:

Photovoltaics (5)
Rectenna (1)
Communications (2)
GPS (1)
Horizon Sensors (1)
Sun Sensors (2)
Instrumentation (2)
Reaction Wheels (4)
Magnetic Torque rods (16)

Thrusters (4)
Monopulse Beacon (1)

Although the orbit is sun-synchronous, the batteries will be cycled similar to a typical LEO cycle. This process is adopted in lieu of some other form of regulation and has the advantage of minimizing mass and maximizing simplicity. When the battery is fully charged, the PVs will be disconnected. The spacecraft will draw power from the battery until the battery reaches a 40% DOD. For Phase I, this requires the battery to operate as a 40 W power source for approximately 25 minutes. The photovoltaics are then reconnected, and the battery recharged, taking about 140 minutes. Therefore, one complete cycle takes 165 minutes, resulting in about 3200 cycles per year. Compared to the 5000 cycles per year encountered in a typical LEO orbit, this provides an easy life for the battery, and it should last in excess of 4 years. A plot of the proposed cycle is shown in Figure 5.2.4-2.

This system requires that each subsystem contain its own regulators. The bus is guaranteed to be 28 ±7 VDC, which is within the tolerance of all other subsystems in the satellite.

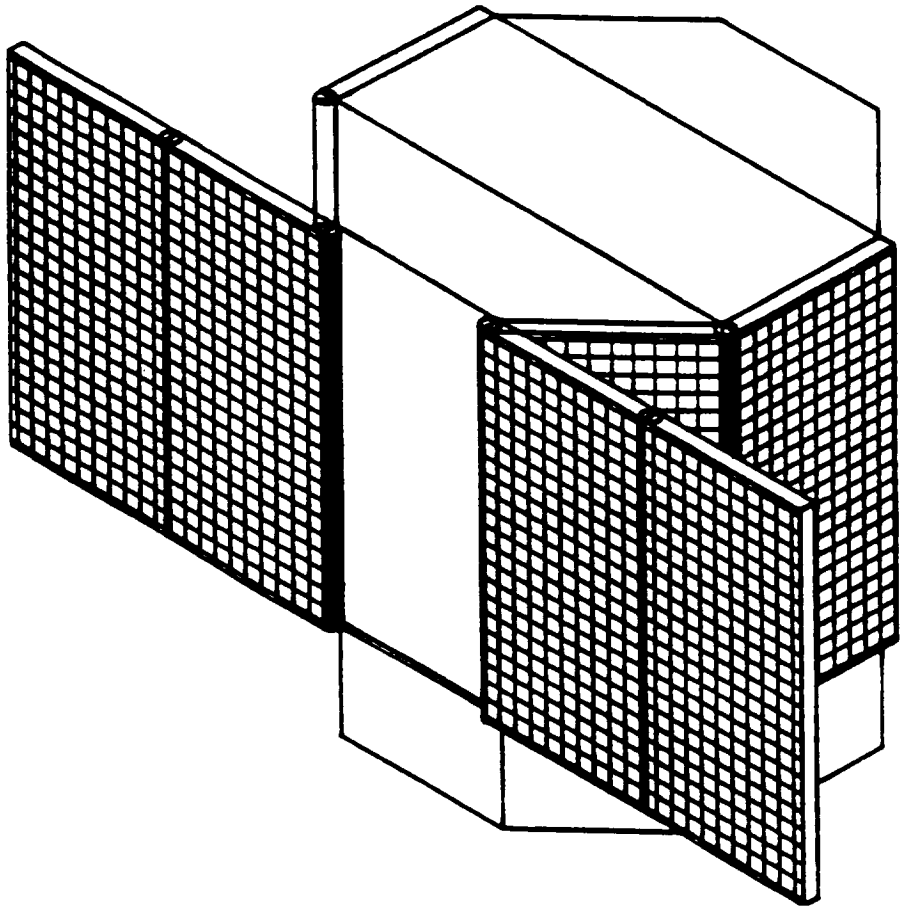

Figure 5.2.3-1. Photovoltaic array (shown in both stowed and deployed positions).

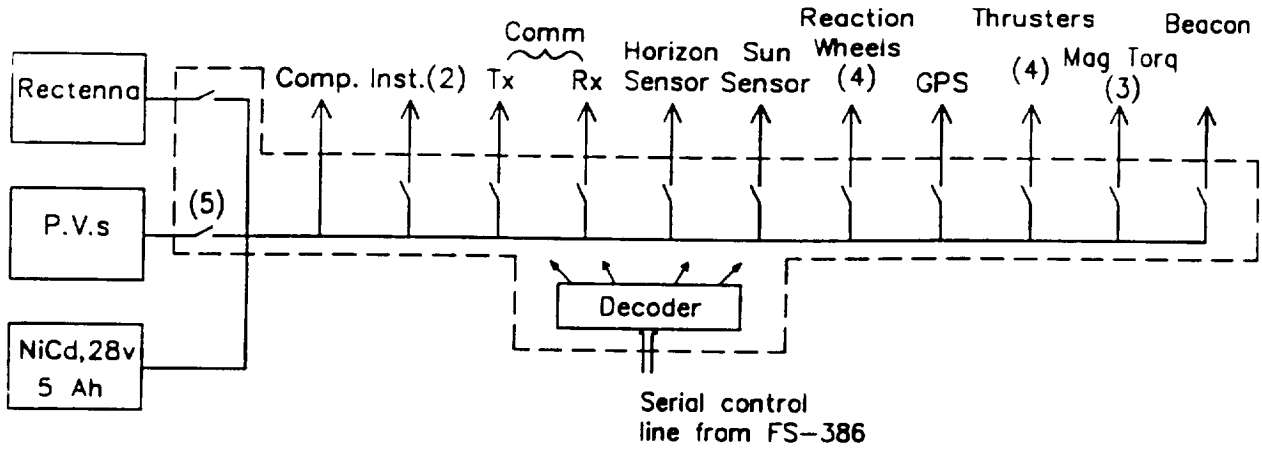

Figure 5.2.4-1. Block diagram for power control unit.

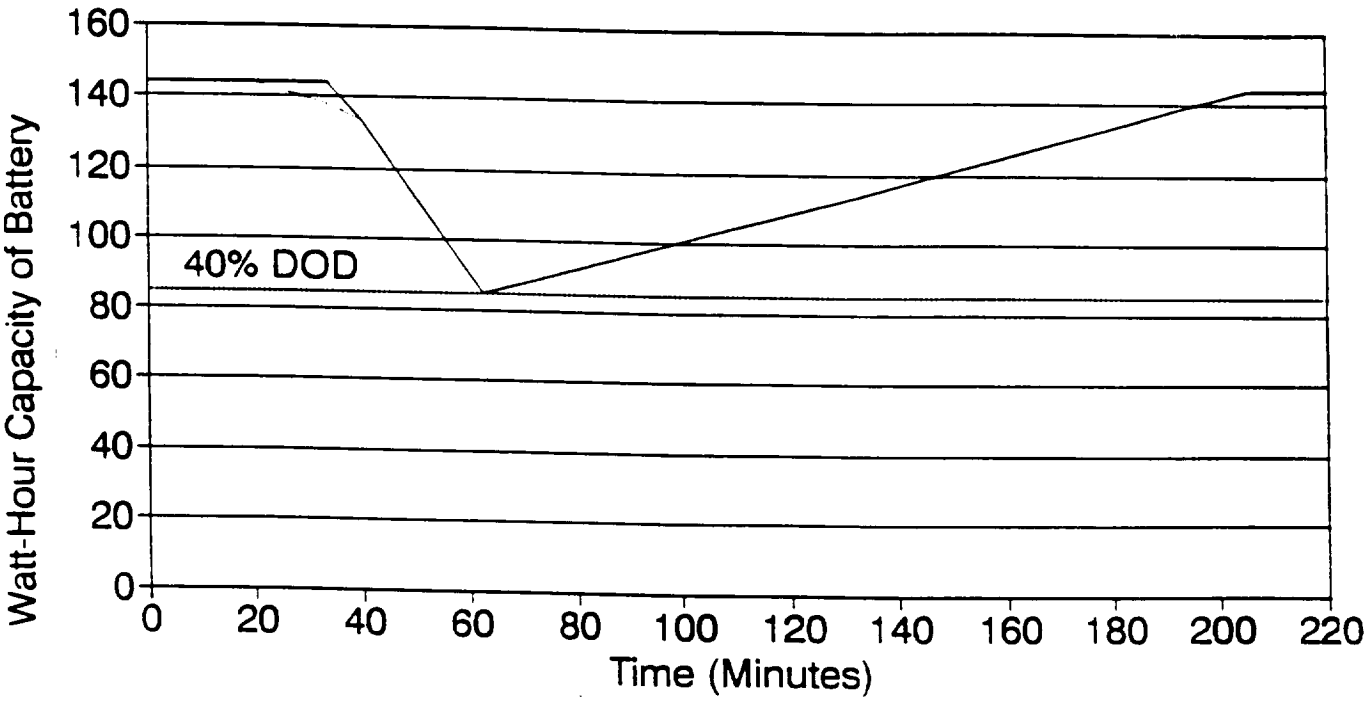

Figure 5.2.4-2. Battery maintenance proposal.

5.3 Attitude Determination and Control

5.3.1 Attitude Determination

The attitude determination and control system for the WISPER satellite must conform to the following constraints: the pointing accuracy must be within 0.01° of nominal, the spacecraft will have moderate and predictable slew rates, and the spacecraft control configuration is expected to change when the inflatable microwave antenna is jettisoned. The spacecraft is in a sun synchronous low earth orbit at an initial altitude of 600 km. The spacecraft's main body is attached to a 14 m inflatable dish that points towards the earth and blocks the view of the earth as seen from the main satellite body. Given these constraints the following sensors will be utilized in conjunction with a FS386 onboard computer to determine the attitude.

There will be two digital sun sensors of 0.01° accuracy mounted orthogonal to each other on the sun pointing side of the spacecraft and one digital sun sensor off axis to the first two sun sensors to provide redundancy. The three sensors will pinpoint the sun's position relative to the satellite and will be the primary attitude reference. A magnetometer is included for two reasons; to aid in attitude determination and control, and to provide magnetic field information which will control the system by setting the magnetic torque rods to the correct values. The output of the magnetometer will provide a three axis attitude with some ambiguity due to the random fluctuations of the earth's magnetic field. The magnetometer output combined with the output from the sun sensor and the GPS receiver will yield an initial attitude accurate to within 0.03°.

This pointing accuracy is less than the necessary accuracy for Phase I, so an interferometer is used to obtain better pointing. Mounted at the focal point of the antenna facing earth, there will be three half wave dipoles sized for a frequency in the 6-7 GHz range. Two of the dipoles will be approximately 20 wavelengths apart, with the third dipole being more than one wavelength distant from one of the other two dipoles. This dipole set will serve as a reference antenna. The signals from these three antennas will be fed through matched coaxial cable to an interferometer mounted on the focal point platform. The interferometer has a pointing accuracy of less than 0.018°. Modern systems are likely to be more accurate than the system flown on the ATS-6 spacecraft in 1974 [16]. Using a higher frequency reference signal will increase the accuracy of the interferometer. The ATS-6 interferometer is capable of maintaining 0.0004° pointing accuracy, however the reference signals must be available during Phase I.

WISPER will jettison the 14 m inflatable antenna at the end of Phase I to accommodate the laser experimentation. During laser power beaming, the satellite will be reoriented with the solar arrays pointing towards the earth. For this orientation, the digital sun sensors will be unavailable for attitude determination. One analog sun sensor will be placed on the side of the spacecraft that is facing the sun during the laser power beaming experiments. Therefore three digital sun sensors, one analog sun sensor, one

magnetometer and a radio interferometer will provide acceptable attitude determination with enough redundancy to maintain a highly reliable system.

5.3.2 Orbit Determination Using the Global Position System (GPS)

The GPS signal beamwidths extend approximately 3000 km beyond the earth's limb to enable an earth orbiter below that altitude to receive continuous three-dimensional coverage [17]. With the GPS constellation almost complete, continuous three-dimensional coverage of a space vehicle is now a reality.

WISPER's orbit is between 400 and 600 km, which invariably makes the GPS an ideal instrument for accurate orbit determination. The recommended unit for this application is the Rockwell space-based 5-channel Standard Positioning Service (SPS) GPS receiver. This receiver is configured under firmware control to track either the L1 (C/A or P code) or L2 (P code) signals when P code is available (i.e. Anti-Spoofing (A/S) is turned off). Although both the L1 and L2 codes are needed for ionospheric correction, at lower altitudes (<1000 km) single frequency ionosphere calibration and a reduced dynamic differential solution can yield real time orbit accuracies of about 1 m [17]. Further information concerning the GPS specifications used onboard WISPER is in Appendix D.

Figure 5.3.2-1 summarizes the performance that can be achieved as a function of altitude for both real time and after-the-fact differential GPS orbit determination. The curves reflect the optimal estimation strategy for each case. These curves are approximates, as actual performance will depend on specifics of the GPS tracking configuration and satellite dynamics [17].

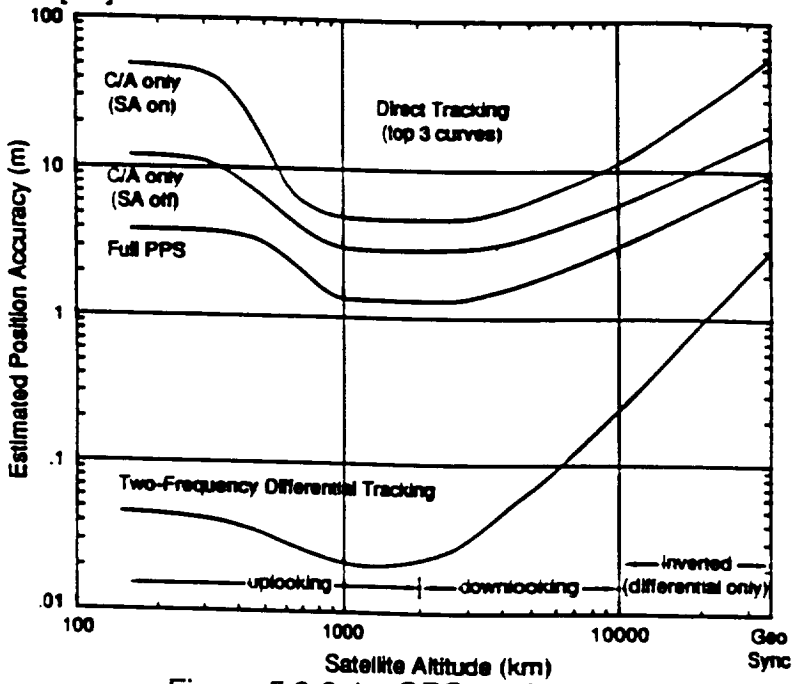

Figure 5.3.2-1. GPS performance.

5.3.3 Attitude Control

Spacecraft attitude control will be accomplished by a Kalman filter or a fuzzy logic based control algorithm implemented by the FS386 based onboard computer. The control algorithm must be adaptive and capable of easily changing reference data as different sets of sensors are used during the various phases of the satellite's mission. A fuzzy logic control algorithm is preferable as it is easier to implement the complex control law needed for the WISPER satellite and is inherently more stable than a Kalman filter if programmed correctly. The control actuators consist of three torque rods, four momentum wheels and three hydrazine thrusters. The primary control actuators are the momentum wheels which were chosen because of the tight pointing requirements for this mission. Momentum wheels have smooth control curves and are the all around best choice for primary control actuators. The torque rods will be used primarily to dump excess momentum from the momentum wheels. The torque rods will also be used to overcome small secular or periodic torque and for initial orbit despin and three axis acquisition.

WISPER has a 3 axis attitude control system. To facilitate this a combination of reaction wheels and magnetic torque rods are used.

The system chosen for the WISPER is called a zero momentum system and has a reaction wheel on each axis. The reaction wheels respond to disturbances on the vehicle. For example, during maneuvering a wheel is made to speed up or slow down. This creates a reaction torque which accelerates the satellite to the desired angle. Since the torque requirements for WISPER are mostly cyclic, the wheel may not reach saturation speed at all. Secular disturbances caused by solar drag and other effects, however, cause the wheel to drift toward saturation. An external torque should be applied with the magnetic torque to de-saturate the wheel. This process is called momentum dumping and can be done automatically or by command from the ground.

During orbit insertion, short term spin stability is achieved by spinning the momentum wheels perpendicular to the vertical axis. Once on station, the wheel speed is brought back to zero by onboard magnetic torque rods.

When sizing wheels, it is important to distinguish between cyclic and secular disturbances. For WISPER, the angular momentum capacity of the reaction wheels was sized to handle the cyclic storage during an orbit (when the satellite is maneuvered to meet pointing requirements) without needing frequent momentum dumping.

The torque capability of the wheels is influenced by slew requirements and pointing accuracy. For three axis control, at least three wheels are required on three different axis. A redundant fourth wheel, not orthogonal to any of the other three is provided as a fallback in case one of the primaries fail.

The external disturbances are due to the gravity gradient, solar radiation, aerodynamic drag, and magnetic field of the earth. Of these, the first three are secular in nature, whereas the unbalance due to the magnetic field is cyclic. For WISPER, the unbalance due to the secular torques is small in magnitude and can be dumped with the help of the magnetic torque rods whenever needed.

The torque capability of the wheels is a function of the slew rate as well as the accuracy of the pointing requirements. It has been sized taking into account these considerations.

The specifications for the momentum wheels are given in Table 5.3.3-1:

Table 5.3.3-1. Momentum wheel specifications.

Speed Range (rpm)	0 to ± 6000
Angular Momentum Capacity (N-m-s)	135
Reaction Torque (N-m)	1.04
Weight: Wheel Assembly	(A) Two wheels each of 12 kg and two of 5 kg (B) Two wheels each of 5 kg and two of 1.5 kg
Dimensions:	(A) Two wheels of diameter 300 mm and thickness of 7.5 mm (B) Two wheels of diameter 212 mm and thickness of 4.4 mm
Static Imbalance (gm-cm) Worst Case for (A)	4
Maximum Power Consumption (W)	40
Dynamic Imbalance ($gm\text{-}cm^2$) Worst Case for (A)	96

Calculations for Selecting a Attitude Determination and Control System (ADCS) Hardware:

Reaction wheels are essentially torque motors with high inertia rotors. They can spin in either direction, and provide one axis control for each wheel.
For any spacecraft the reaction wheels have two primary functions:
a) Provide required slew rate necessary to meet pointing requirements.
b) Provide stability against external disturbing torques.

What follows is an estimation of the sizing of the wheels required to meet the above requirements for WISPER.

The reaction wheels have been designed to take care of secular torques caused by the gravity gradient, the earth's magnetic field, and the unbalance due to the solar and aerodynamic drag.

Disturbance due to Gravity Gradient

Let R be the radius of the orbit in meters.
Let Ix, Iy, Iz represent the Moment of Inertia about the X, Y, Z axis in Kg-sq met
Let u represent the earth's gravity constant
Let Tg represent the unbalance due to the gravity gradient in N-m

$$I_x := \frac{4\cdot(350\cdot 25)^2 + \left[50\cdot(30\cdot 25)^2 + 150\cdot(25\cdot 22)^2\right]}{1000^2\cdot 20}$$

$$I_x = 18.9875$$

$$I_z := \frac{0.5\cdot\pi\cdot 7^2\cdot 1\cdot 50}{2}$$

$$I_z = 1.92\cdot 10^3$$

$$R := (6378 + 500)\cdot 1000$$

$$\mu := 3.986\cdot 10^{14}$$

$$T_g := \frac{3\cdot\mu}{2\cdot R^3}\cdot\left(I_z - I_x\right)\cdot\sin(2\cdot\mathrm{deg})$$

$$T_g = 1.22183\cdot 10^{-4} \text{ N-m.}$$

Unbalance due to Solar Radiation:

The basic assumptions made are :
1) Solar flux acts on a cross sectional area of 625 mm by 750 mm.
2) The distance between the center of solar pressure and the center of mass is assumed 0.4 meters, (calculated by taking into account the fact that the center of mass of the satellite, with the dish inflated is 380 mm away from the center of the satellite before the inflation)
Let Tsp represent the torque due to the solar drag.

$$T_{sp} := \frac{1358\cdot(20\cdot25)\cdot(30\cdot25)\cdot0.4\cdot(1+0.6)\cdot\cos(0)}{3\cdot10^{8}}\cdot10^{-3}$$

$T_{sp} = 0.00109$ N-m.

Unbalance due to Earth's Magnetic field:

For a spacecraft magnetic dipole of 1 A sq m and a worst case polar magnetic field ,

$$M := 2\cdot\frac{7.96\cdot10^{15}}{\left(7.198\cdot10^{6}\right)^{3}}$$

The torque due to the magnetic field is calculated as:

$T_m := 1\cdot M$ N-m.

$T_m = 4.26882\cdot10^{-5}$ N-m.

Unbalance due to Aerodynamic Drag:

Since the satellite is symmetric, about the vertical plane, there would be no drag along the vertical axis. Additionally, there would be no drag in a direction perpendicular to the plane of motion
The areodynamic drag creates a torque Ta which tends to turn the satellite in the plane of motion

$T_a := 3\cdot10^{-4}$

The total torque due to the external factors could be in the worst case an addition of the above four torques.

$T := T_g + T_{sp} + T_m + T_a$

$T = 0.00155$ N-m.

Cyclic Variation of torque:
The cyclic variation in the torque occurs when the satellite is manevoured to point at a particular location on the earth. The reaction wheels need to be spun with increased angular velocity during the first half of the pointing phase, and despun at the same rate during the second half

.
The maximum angular acceleration (alpha) during the pointing phase was calculated by numerically diffrentiating the velocity at atleast 10 points in the orbit.

The maximum rate of change of the slew rate determines the sizing of the wheels and was calculated to be 1.8 deg/ sec^2. From this the torque requirement (Tc) for achieving the slew rate is determined.

$\alpha := 1.8 \cdot deg$

$T_c := I_x \cdot \alpha \cdot \sqrt{2}$

$T := T + T_c$

$T_c = 0.84359$

$T = 0.84514$ N-m

This is the worst case torque requirements for the reaction wheels. One Reaction wheel and the redundant reaction wheel will have to be capable of exerting this torque and are sized accordingly.
In normal practice, the momentum wheels are sized several times the maximum required torque, to achieve pointing accuracy
To calcualte the angular momentum capacity we use the following formula

$$H := T \cdot 15 \cdot \frac{60}{4} \cdot 0.637$$

$H = 121.13022$ N-m-s

5.4 Propulsion Subsystem

5.4.1 Mission Profile

To design the propulsion system, a nominal orbital insertion trajectory was estimated for the Pegasus launch vehicle. The required velocity change, ΔV, and the propellant mass are needed to determine the required propulsion. At an altitude of 600 km, the atmospheric drag is a significant problem. Drag acts opposite to the velocity vector and removes the kinetic energy of the spacecraft. This causes the orbit to decay. Figure 5.4.1-1 shows altitude decay versus time. The altitude decays from 600 km to 500 km in about 370 days. Microwave power beaming experiments will be conducted during this period.

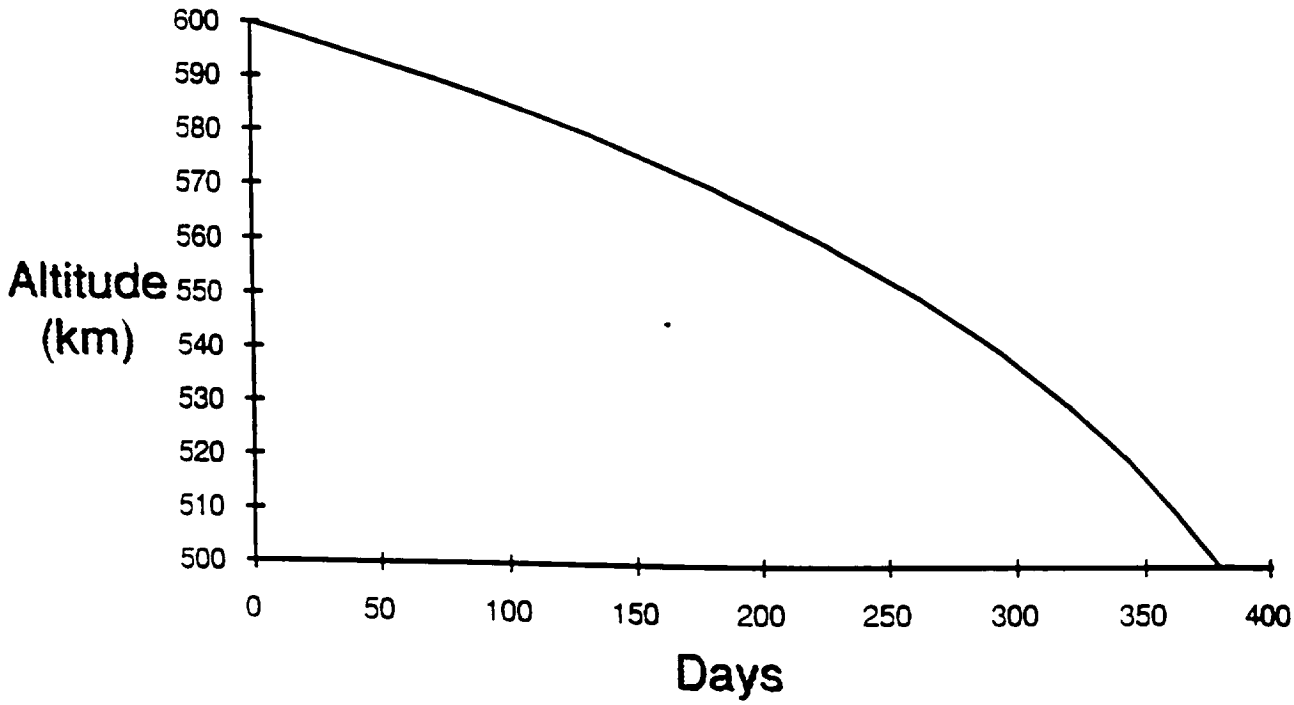

Figure 5.4.1-1. Phase I orbit decay.

When the satellite reaches at an altitude of 500 km the microwave antenna will be jettisoned, and the second stage of the mission will commence. Figure 5.4.1-2 shows the altitude versus the decay time during the descent from 500 km to 400 km. The drag cross-sectional area will be smaller after the antenna is jettisoned. Therefore, the satellite's orbit will decay more slowly. The time for the satellite to fall to 400 km is adequate for the laser experiments and eliminates the need to reboost the satellite.

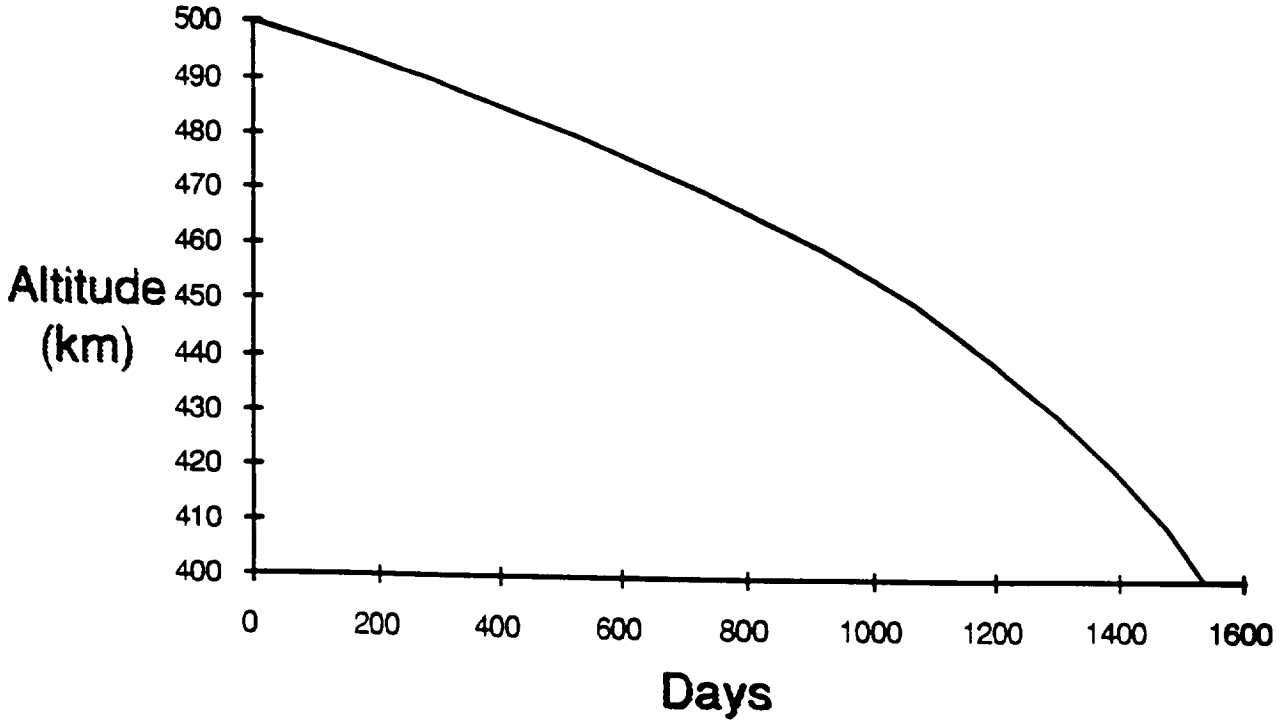

Figure 5.4.1-2. Phase II orbit decay.

Four thrusters will be provided to correct the orbit injection errors. Two of the thrusters are redundant. These thrusters will be located on the side of the satellite.

5.4.2 Propulsion System

With the ΔV and mission requirements defined, it was possible to the proceed with the hardware selection process. A liquid propulsion system was chosen for WISPER. A mono-propellant or simple hydrazine system was selected and will be able to accomplish all aspects of the mission. The budget of the propulsion system is shown in Table 5.4.2-1.

Table 5.4.2-1. Propulsion subsystem budget.

Mass of Fuel (kg)	3.15	Tank Quantity	2
Mass of Tank (kg)	0.8	Tank Radius (m)	0.083
Total Mass (kg)	5.75	Tank Volume (m^3)	0.00234

The attitude control subsystem will control all aspects of firing the thrusters. Data management will monitor the temperature and pressure of the hydrazine tanks.

5.5 Computer and Instrumentation Subsystems

5.5.1 Interface and Instrumentation

The instrumentation subsystem is an interface between the computer and the systems which comprise the WISPER satellite. The computer monitors the instrumentation system's sensors and transducers and processes the accumulated data from them. Table 5.5.1-1 shows all the subsystems, their components and the parameters that will be monitored, as well as command lines that are needed for the proper operation of the subsystem.

Table 5.5.1-1. Telemetry and command lines.

Subsystem	No. Digital Lines	No. Analog Lines	No. Command Lines	Sampling Rate Range
Propulsion	4	5	4	1-2 Hz
AD&C	7	25	22	1-200 Hz
Power	1	15	1	1-2 Hz
Thermal	---	3	---	1 Hz
TT&C	6	10	2	1 Hz
Miscellaneous	5	11	3	2-1000 Hz
Total	23	70	33	—

All operations on the WISPER spacecraft will be monitored. There will be analog and digital signals coming from the various systems. All digital channels will be multiplexed into serial digital channels. Figure 5.5.1-1 shows the number of analog and serial digital lines for each system to the computer. The number going into or out of a block represents the quantity of lines at that point in the system.

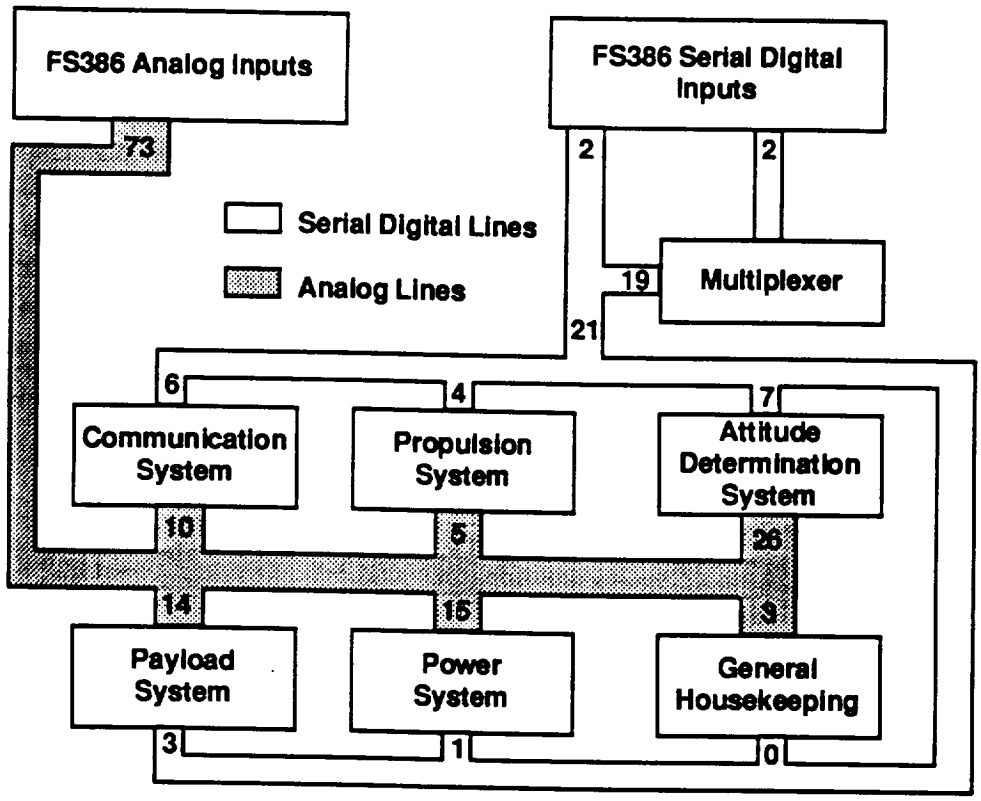

Figure 5.5.1-1. Data line breakdown.

Command lines are connected from the computer to the satellite components that require data in order to operate. The FS386 computer has 33 command lines available and Figure 5.5.1-2 shows a breakdown of how the lines are used.

To prevent errors, the command lines will activate functions through use of a digital word. Potentially hazardous functions, such as the antenna release, will make use of a redundant error detection and correction system to ensure the command was issued correctly.

It is necessary to design several instrumentation circuits. A list of these circuits is provided along with an explanation for their use.

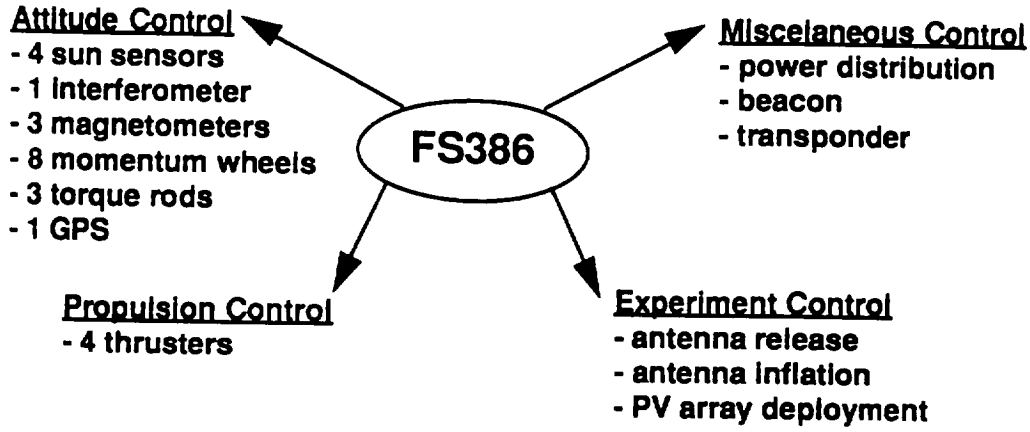

Figure 5.5.1-2. Command line utilization.

Payload power sensors. During the experiment it is desirable to know what kind of power the payload is receiving. Circuits will be required for the rectenna, and one for each of the PV arrays. The circuit will measure the voltage and current across a small in-line resistor to determine the power output.

Multiplexer circuits. The status of many components are monitored and represented as a digital one or zero. Instead of running a line for each status point, up to 16 status points will be multiplexed into a single serial digital line.

Vibration sensor. Vibrations of the satellite will be of interest throughout the mission. During launch, vibrations can be up to 2000 Hz. During the mission, the resonance frequency of the satellite should be around 20 Hz. These frequencies determine the Nyquist sampling speed of the instrument. The vibrational effects of inflating and ejecting the antenna will also be examined. This vibration information can tell if anything is making unwanted contact with the satellite, such as the jettisoned antenna. A Fourier analysis of the signal, with a uniform sampling period , will yield the necessary information. The sensing circuit will be constructed from a piezoelectric accelerometer.

PV diodes instrumentation. There are 28 photovoltaic diodes that are being used for monitoring the laser experiment. With so many sensors it is desirable to preprocess the information. During Phase II, the information going to the computer will be the location and diameter of the laser spot size. The power of the effected diodes will also be monitored.

Strain gages instrumentation. Determination of when the antenna has completed inflation will be determined by strain gages. This information will be processed into a single line which will have information concerning the overall tension exerted by the antenna.

Housekeeping instrumentation. Some of the manufacturers do not include the housekeeping functions that are necessary to the WISPER satellite. It is necessary to identify the excluded circuits so they can be custom designed and built. All instrumentation circuits will be built with space tested, off the shelf materials whenever possible.

5.5.2 Processor and Memory Requirements

In order to estimate the software size and throughput requirements of the WISPER command and data handling computer system, it is necessary to separate the functions of the computer into two areas: the onboard applications and the operating system.

Applications. Table 5.5.2-1 lists the general categories of application software and their estimated size and throughput [11]. The communications software include the capability of processing external commands and collecting internal data for transmission through the TDRSS/STDN telemetry link. Since the WISPER satellite must operate autonomously when not in direct contact with the ground station, both the size and throughput of the system are quite large. Closely linked with autonomy, the fault detection function monitors the onboard equipment for failures and the correction is introduced through large tables of prestored procedures that require considerable data. The power management function controls the battery charge and discharge and monitors the power bus.

Table 5.5.2-1. Onboard applications estimates.

Application	Code & Data Size (Kwords)	Throughput (KIPS)
Communications: -Command Processing	5.0	7.0
-Telemetry Processing	3.5	3.0
Complex Autonomy	25.0	20.0
Fault Detection: -Monitors	5.0	15.0
-Fault Correction	12.0	5.0
Kalman Filter	9.0	80.0
Power Management	1.7	5.0
Applications Total	61.20	135.00

Operating System. The next set of functions to be evaluated includes the functions shown in Table 5.5.2-2. The local executive is the code that manages all of the computer system functions. These functions include providing interrupt services, tasks based on timers, and controlling the resources and memory of the computer. The executive also corrects single event upsets and detects memory faults. It is estimated that as many as 400 tasks per second must be supported by this system. This is twice the typical value [11] for most computer subsystems and is used to allow for a margin of safety in the estimate.

The run-time kernel supports higher level languages in interfacing with other devices, program languages, and packaging data. The BIT (Built-In Test) and diagnostics software affords various levels of testing but also identification and recovery of faults.

To control the flow of data through the processor and the peripheral devices for the I/O handlers, it is necessary to calculate the worst case scenario of data handled per second. This was done by assuming that during a pass over the ground station every telemetry line coming into the computer had to be addressed at the data rates designated in the interface inventory above. The resulting calculation is shown below:

$$A+2B+4C+15D+100E+200F+400G+1000H = 9.256*10^3 \quad [\text{Hz}] \qquad (5.5.2\text{-}1)$$

A = 20 = no. of lines sampled at 1 Hz
B = 47 = no. of lines sampled at 2 Hz
C = 3 = no. of lines sampled at 4 Hz
D = 2 = no. of lines sampled at 15 Hz
E = 1= no. of lines sampled at 100 Hz
F = 3 = no. of lines sampled at 200 Hz
G = 1 = no. of lines sampled at 400 Hz
H = 8 = no. of lines sampled at 1 kHz

Table 5.5.2-2. Operating system estimates.

System	Code & Data Size (Kwords)	Throughput (KIPS)
Executive	5.5	0.3x(400)
Run-Time Kernel	12.0	Included in functions
I/O Device Handlers	2.7	0.05x(9.256*10^3)
Built-In Test & Diagnostics	1.1	0.5
Operating Systems Total	21.30	583.30

Margin Requirements Calculations. With the estimates gathered at this point, the margins needed to compensate for uncertainty in the requirements and an on-orbit spare have been calculated in Table 5.5.2-3. Without any operating system components that are off-the-shelf, the compensation works out to be the same size as the total for the onboard applications. However, the on-orbit spare was found to be a combination of the totals of the applications, operating system, and the uncertainty compensation.

Table 5.5.2-3. Margin requirements.

	Code & Data Size (Kwords)	Throughput (KIPS)
Requirement Uncertainty Compensation	61.2	135.0
On-Orbit Spare	143.7	853.3
Margin Total	204.90	988.30

Total Processor and Memory Requirements. The total computer requirements are then a calculation of the total margin and total software size and throughput estimates as shown in Table 5.5.2-4.

Table 5.5.2-4. Total computer requirements.

	Code & Data Size (Kwords)	Throughput (KIPS)
Margin Total	204.9	988.3
Operating Systems Total	21.3	583.3
Applications Total	61.2	135.0
Total Size & Throughput	287.40	1,706.60

Since attitude and control requires such extreme pointing accuracy and continuous onboard processing of the ephemeris and control law, it has been determined to allocate this system 3 Mwords of memory and an entire processor to accomplish this task.

5.5.3 FS386 Configuration

The computer subsystem is an FS386 computer that consists of two 32-bit processors, one memory circuit card assembly (CCA), two telemetry and command CCAs, a transponder CCA, and a power convertor, all of which are connected via a multi-layer backplane. This computer will be used in a centralized architecture which uses the computer as the central node of a network of peripherals. The architecture is very

reliable in that a failure on one point to point interface cannot affect any other interface.

As noted earlier, one processor will be dedicated to attitude, control, and pointing, while the other is primarily responsible for command and data handling (CDH). When possible there may be overlap of functions between the two processors. During a pass the basic operation of the processor will be to "pipeline" data from the experiment to the ground station through the TDRSS (Tracking and Data Relay Satellite System)/STDN (Spaceflight Telemetry and Data Network) telemetry link. While not in a pass, any data that was stored in memory would then be processed, and/or transmitted to Earth when the telemetry link becomes available. The CDH processor will regulate the power throughout the WISPER satellite by monitoring its power levels and providing the power management and distribution (PMAD) subsystem with the necessary control data to bring various systems on and off-line. The WISPER structural systems that will be controlled through the FS386 computer are as follows: deployment, release, and inflation of inflatable antenna and deployment of photovoltaic arrays. Due to a completely passive thermal management system the only operation required of the central processing unit (CPU) is that of monitoring the thermal conditions of all of the WISPER onboard equipment. The propulsion system will primarily be under the charge of the attitude and control (AC) processor, and will monitor the signals from the thrusters for their operation. Meanwhile the CDH processor will acquire data as to the pressure of the hydrazine fuel tanks.

Each processor has 512 Kbytes of static RAM (SRAM) that is essentially single event upset (SEU) immune, and is reserved for executing application code as well as necessary work space. For program and boot purposes there are 384 Kbytes of EEPROM. A 32 MHz clock rate generates 2.4 MIPS with a backplane timer to force rebooting as a part of the fault recovery system.

The memory circuit card assembly will allow for 6.6 Mwords of SRAM for user space with extra memory allocated to the 7-bit error detection and correction (EDAC) operation. This EDAC functions in a single correction, double detection scheme. The memory not allocated to the attitude and control processor will be used as intermediate storage until it can be directly downloaded.

The telemetry and command (T&C) cards serve as the primary data gathering and command generation interface element between the other subsystems, sensors, and processors. It provides the following command channels: two analog, 32 serial digital, and 128 discrete (64 logic & 64 relay drivers). The T&C cards also provide 128 input telemetry channels each of which may be configured in any of the following ways: active or passive analog, and serial or discrete digital. The interface configuration for each card is described in Section 5.5.1.

The power converter is a DC to DC converter which will receive 28 V from the power bus and convert it into 5 V (regular CCAs) and $\pm$15 volts (T&C CCAs). It also provides a low current standby power (+5 V @ 1 A) to the SRAM memory card and presents a 10 MΩ

input to output isolation as well as an overcurrent protection of 125%.

The transponder CCA provides command and telemetry link interfaces to two redundant transponders for communication to the ground station. The telemetry link can handle up to 6 Mbps and the command link can vary from 100 Mbps to 200 kbps. It also supports command authentication, decryption, and has a command bypass detection function for critical commands. This system can be made compatible with the requisite TDRSS and STDN systems.

If further storage capacity is required or a third telemetry and command card is necessary for the system, it is possible to expand the current configuration by the addition of the necessary CCA in the extra slot in the FS386.

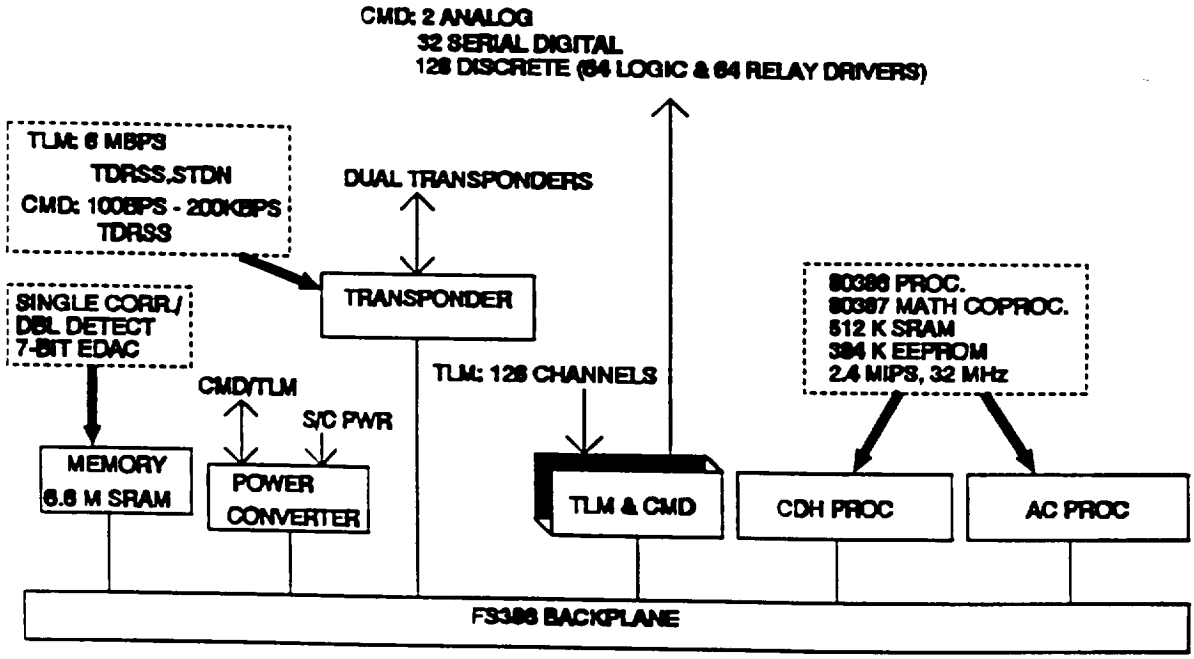

Figure 5.5.3-1. FS386 block diagram.

5.5.4 Telemetry Format

The telemetry format consists of the format shown in Figure 5.5.4-1.

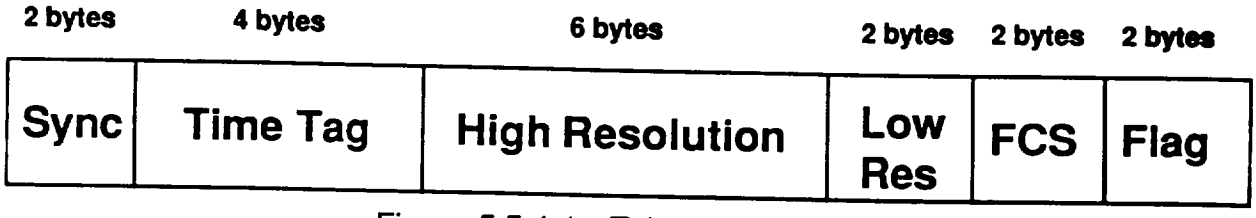

Figure 5.5.4-1. Telemetry format.

Each frame will consist of 9 16-bit words. The first 2 bytes are the synchronization bytes. This word is shown in Figure 5.5.4-2.

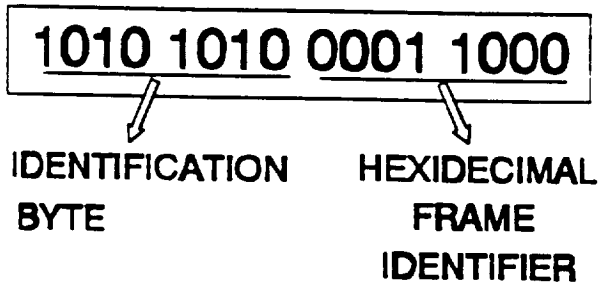

Figure 5.5.4-2. Sync bytes.

The first 8 bits consist of the predetermined pattern shown above. This pattern will let the ground station know that a new sub-frame is starting. The second 8 bits will contain a hexadecimal number indicating which of the 200 sub-frame is being sent. This data will let the ground station know what specific data is contained in the high and low resolution bytes.

The second portion of the frame consists of a time tag. These 2 bytes will keep track of the time that the sub-frame data was formed. Timing information will be done in a modulo counter fashion. These 32 bytes will keep track of time, accurate to the millisecond.

The next two sections of the frame consist of the data. There are 3 high resolution bytes and 1 low resolution byte of data. There are 200 different subframes of data which are possible. The main design constraint was the sampling speed needed for an operation. The Nyquist sampling frequency must be met. The payload experiment requires sampling at 1000 Hz to meet this requirement. The vibration sensor requires 4000 Hz at launch but only 100 Hz for the rest of the mission. The next highest sampling requirement is 180 Hz from the interferometer. Since the experiments sampling speed is only for a short period of time the frames were designed around the interferometer requirements. The 3 bytes of high resolution data will contain the 3-axis information from the interferometer. The last byte will consist of all the low resolution data. The highest requirement in this byte will be the vibration measurements. The frames would be executed in a predetermined order with the vibration subframe inserted every other subframe because the Fourier analysis of vibrations require a periodic sampling interval. These sub-frames will occur every 5 milliseconds.

During experiment modes the needs of telemetry change. The microwave experiment requires the highest sampling rate. Same length frames are desirable at the ground station, so extending the number of bytes in a sub-frame was undesirable. To meet our sampling speed requirements it will be necessary to increase the sub-frame occurrence to every millisecond. Interferometer data and rectenna power will be monitored in the

third byte of high resolution data. The 5 high resolution data sub-frames will be repeated. The low resolution data will be taken similar to the normal operations mode.

During Phase II, the requirements are similar. Frame speed will be 1 millisecond per frame with all attitude control data in the low resolution byte. Interferometer data and PV array power will be inserted every 10 frames. All high resolution data will be dedicated for laser experiment data, which will repeat every 2 frames.

During launch the effects on the satellite will be examined. The sub-frame rate will be increased to 1 millisecond with vibration data during launch.

The next byte is know as a cyclic redundancy check, which will be used for error detection. Given a k-bit frame, the transmitter will generate an n-bit sequence. This frame check sequence consisting of k+n bits will be exactly divisible by some predetermined number. The receiver then divides the incoming frame by the same number, and if there is no remainder, it assumes there was no error [18]. Figure 5.5.4-3 shows the flag bytes.

1100110011001100

Figure 5.5.4-3. Flag bytes.

These bytes will always have the same pattern shown above. It will let the ground station know that a sub-frame has ended.

5.6 Communications Subsystem

5.6.1 Uplink and Downlink Requirements

The WISPER communication subsystem was designed to conform with the requirements set forth by the PI team for both phases of the mission.

During the microwave experiment the PI team stated that it was necessary to obtain a real time link during the power beaming experiments. The attitude and control system also required a link during portions of the orbit not in the horizon mask of the mission ground station.

It was determined by the PI team that a real time link was not essential during the laser power beaming portion of the mission. A store and forward type of communication link would suffice for Phase II.

5.6.2 Antenna and Transmitter Selection

In order to provide a real time link during Phase I, the communication ground station must

be at the NOAA power beaming earth station near Fairbanks, Alaska. The NOAA ground station consists of, in part, a 26 meter receiving antenna and a 6 meter transmitting antenna [19]. The 26 m and 6 m antennas can be tied together in a master-slave configuration with the power beaming antenna for communication purposes.

Also on site at NOAA is NASA STDN operational equipment. Through the use of the STDN equipment, precise ranging and carrier Doppler measurements can be made. The STDN equipment operates at a receive frequency of 2287.5000 MHz, with a transmit frequency of 2106.4106 MHz. The transmitting frequency is precisely 221/240 time the receiving frequency; this transmission versus reception frequency relationship is a requirement for STDN operations.

Using these frequencies and Equation 5.6.2-1 [11], the gains of the antennas were calculated as

$$G=\frac{(\pi * D)^2 * \eta}{\left(\frac{c}{f}\right)^2} \qquad (5.6.2\text{-}1)$$

where f is the operating frequency (GHz), G is the antenna gain over an isotropic radiator, D is the antenna diameter (m), η is the aperture efficiency (estimated at 0.55), and c is the speed of light, 2.99792 x 10^8 m/s. The resulting calculations were converted to decibels, 10 times the logarithm, and are displayed in Table 5.6.2-1.

The half power (or 3 dB) beamwidth of the antennas were calculated using Equation 5.6.2-2 [11]

$$\theta_{3dB}=\frac{21}{f * D} \quad \text{[degrees]} \qquad (5.6.2\text{-}2)$$

where θ_{3dB} is the half power beamwidth (degrees) and D is the antenna diameter (m). The θ_{3dB} values for both antennas at the NOAA site are also displayed in Table 5.6.2-1.

Table 5.6.2-1. NOAA antenna characteristics.

Antenna Diameter (m)	Gain (dBi)	θ_{3dB} (degrees)
26	53.33	0.35
6	38.84	1.7

In order to link with the WISPER satellite beyond the horizon mask of the experiment

ground station, it was necessary to design the communication subsystem using one or more relay satellites. The NASA TDRSS was chosen because of the flexibility it offers for satellites in low earth orbit. There are two TDRS satellites in geosynchronous orbit, with Goddard Space Flight Center as the ground terminal, TDRS east and TDRS west. Using the TDRS system and the antennas, to be discussed later in this section, the WISPER satellite will be able to contact at least one of the satellites during the beaming experiment orbits.

The transponder used onboard the WISPER spacecraft must conform to requirements set by both STDN and TDRSS protocols.

First, the transponder must acquire and track the suppressed carrier and demodulate the non-return-to-zero phase shift key (NRZ-PSK) command data when receiving a forward link signal from a TDR satellite. It must also be able to reject false acquisitions due to multipath reflections, provide hard command data decisions, and reconstruct bit time to the spacecraft command system. Finally, it must allow coherent turnaround capability to the TDR satellite that is transmitting [20].

The transponder must transmit at a frequency 240/221 times the receiver frequency and have a coherent turnaround capability which allows for Doppler tracking. It must also have a noncoherent capability that allows the transponder to secure a carrier that is approximately 240/221 times the receiver frequency. The latter mode is not conducive to the ranging process. The transponder must also transmit specific spectrum spreading codes in accordance with the TDRSS return link parameters [20].

To conform with the STDN requirements the transponder must be able to receive and track an unspread residual carrier signal from an STDN station and track and demodulate command data from a 16 kHz subcarrier in a NRZ-PSK format. It must also perform the same turnaround frequency reference as required by the TDRSS functional requirements, including a coherent or noncoherent transmit carrier 240/221 times the receive frequency. Likewise the transponder must provide a direct hard line interface for command data decisions and recovered bit timing via a 16 kHz subcarrier [20].

The transponder should also allow the mounting of a remote diplexer and/or a low noise preamplifier without influencing the performance or the system in excess of the effects caused by the cables and mismatch. The transponder must provide redundant control command interfaces and either a parallel or serial format interface to the spacecraft's telemetry system.

The transponder chosen for the WISPER communications subsystem satisfies all the requirements of TDRSS, STDN, and the mission vehicle command and telemetry systems. It is the NASA standard second generation TDRSS User Transponder. The transponder provides many options to be specified by the user upon ordering the device. These options include choices such as a 2.5 W or 5.0 W power amplifier, the first of

which was chosen for this mission, a TDRSS telemetry data interface of 50, 1000, or 5000 Ω nominal impedance, and a temperature sensor for telemetry purposes. There are also programming options to be specified by the user. Some options include a power-up command rate and a pseudorandom noise (PN) code address. Appendix G contains a work sheet in which the many manufacturing and programming options are listed, and those chosen for the WISPER satellite are marked.

The use of both TDRSS and STDN calls for the use of two antennas, one on the top of the satellite facing away from earth, and the other on the bottom of the satellite.

The antennas chosen were helical with an operational range of 2.1 GHz to 2.5 GHz. Using equations 5.6.2-3 and 5.6.2-4 [11] the antenna gain and half power beamwidth was determined. C is the circumference (π times the diameter), L is the length of the antenna, and λ is the wavelength (c/f). Table 5.6.2-2 shows the calculated values for both gain and beamwidth at both the transmit and receive frequencies.

$$G_{dB}=10.3+10\log\frac{C^2*L}{\lambda^3} \quad \text{[dB]} \qquad (5.6.2\text{-}3)$$

$$\theta_{3dB}=\frac{52}{\frac{\sqrt{C^2*L}}{\sqrt{\lambda^3}}} \quad \text{[degrees]} \qquad (5.6.2\text{-}4)$$

The design of this communication system is based on the assumption that the helical antennas used on the TDRSS satellites exhibit the same characteristics as those used on the WISPER satellite.

Table 5.6.2-2. Helical antenna characteristics.

	2106.4106 MHz	2287.500 MHz
Gain (dBi)	11.98	13.06
Beamwidth (degrees)	42.85	37.86

A diplexer allows a transponder to use the same antenna for simultaneous transmission and reception. The diplexer, which is specified upon ordering the transponder, will allow the transponder to switch to the necessary antenna, whether it be the STDN antenna or the TDRSS antenna. This would mean a two line out diplexer. As a note, the TDRSS transponder automatically switches to the appropriate antenna upon detecting either a STDN or TDRSS signal.

There are three basic types of transponder interfaces: antenna, power control, and command and telemetry. The antenna interface is accomplished using female N-type connecters at both the antenna and diplexer ends of the cable. There will be minimum cable loss from the TDRSS antenna to the diplexer due to the short length involved. However, the cable loss for the STDN antenna to transponder connection will be more significant. This is largely due to the longer length of line (10 m) and the high frequency. The nominal impedance of both antennas is 50 Ω, as are the interfaces to the command and telemetry unit. The command and telemetry unit interfaces with the TDRSS transponder via several RS232 type cables and connectors. The power control unit of the satellite is governed by the satellite's CPU and interfaces with the transponder via two cables. The first connection is made directly with the transponder's receiver which will typically be left on but could conceivably be programmed, through the CPU to switch off. The second cable connects the power control unit to the transmitter of the transponder. This second connection is switched off and on by the CPU as demand warrants. Figure 5.6.2-1 displays a block diagram of the communication subsystem onboard the satellite.

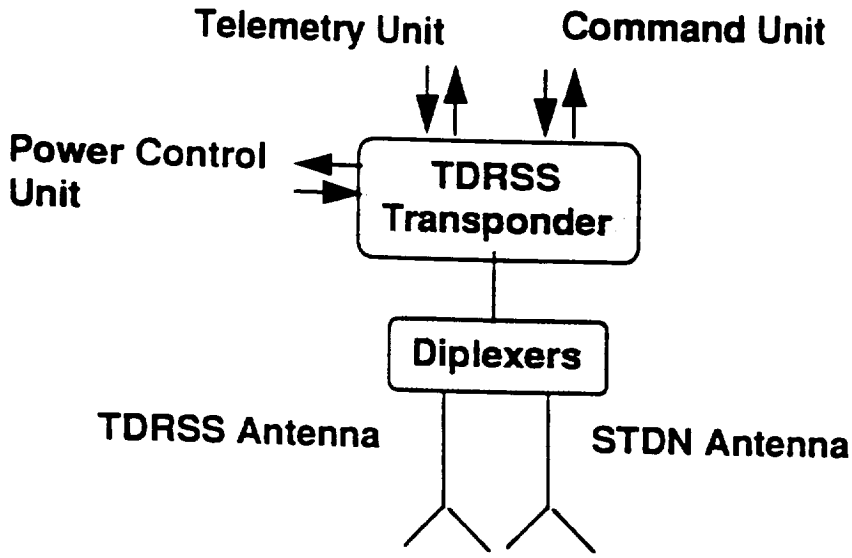

Figure 5.6.2-1. WISPER satellite communications subsystem block diagram.

5.6.3 Link Budgets

Atmospheric loss, L_a, is a function of frequency. At frequencies under 10 GHz these effects tend to be relatively small. Figure 5.6.3-1 displays atmospheric attenuation versus frequency at various ground station altitudes [11]. From the figure the atmospheric losses for the STDN to WISPER link were estimated at 1 dB each way.

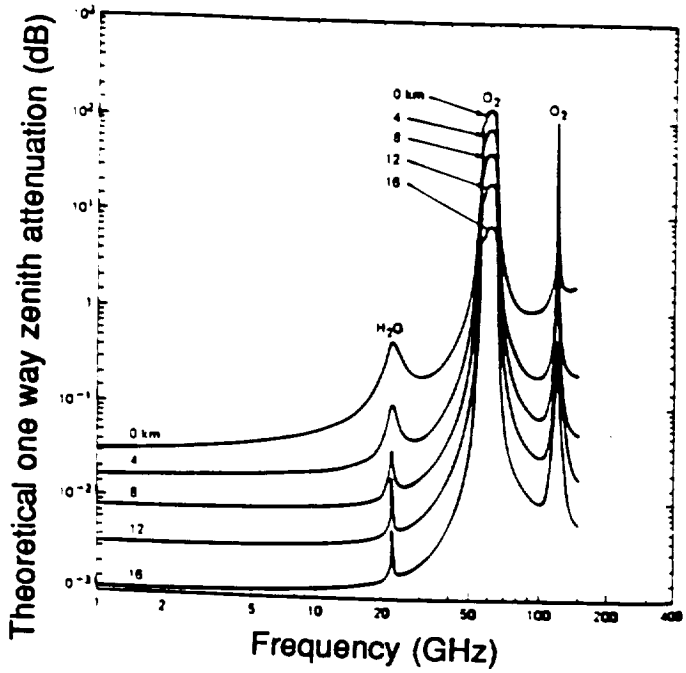

Figure 5.6.3-1. Theoretical vertical one-way attenuation from specified height to the top of the atmosphere.

The rain loss for frequencies below 10 GHz is also relatively low when compared to those higher [21]. For the STDN to WISPER link a worst case rain loss of 1 dB was assumed.

Free space loss, L_s, is a function of frequency and distance. Equation 5.6.3-1 displays the equation used to calculate the free space loss for the various links in the communication system [11]

$$L_s=\left(\frac{c}{4*\pi*S*f}\right)^2 \quad \text{[dB]} \qquad (5.6.3\text{-}1)$$

where c is the speed of light (m/s), S is the distance (m), and f is the frequency. The figure of merit for a communication link is the fade margin. For the two links in the WISPER communication system this was determined by subtracting the required energy per bit to noise density ratio, E_b/N_o, by the incident E_b/N_o on the receiver.

$$\frac{E_b}{N_o}=\frac{P*L_l*G_t*L_s*L_a*G_r}{k*T_s*R} \quad \text{[dB-Hz]} \qquad (5.6.3\text{-}2)$$

In Equation 5.6.3-2 [11], the terms that have yet to be introduced are P the transmitted power (W), G_t the transmitting antenna gain, G_r the receiving antenna gain, k Boltzmann's constant (J/K), T_s the system noise temperature (K), and R the data rate (bps). The following pages include calculations of the telemetry and command links for both TDRSS and STDN communications. Following the calculations, the link budget is provided in Table 5.6.3-1. The fade margins, of particular interest in link budgets, are at the bottom of Table 5.6.3-1 and are adequate for communications links with both the relay satellites and the ground station.

A monopulse beacon is to be used in the tracking system for the microwave beaming. The link budget calculations (following the communications link calculations) show a 20.12 dB fade margin. This fade margin is achievable without the use of and low noise amplifiers at the receiving antenna. If rain attenuation becomes a factor for the beacon link, LNAs may be added to the ground station beacon receiver system.

TDRSS Command Link Calculations

$f1 := 2106.4106 \cdot 10^6$ MHz — Frequency

$c := 2.99792 \cdot 10^8$ — Speed of Light

$P := 100$ W — Transmitted Power

$PdB := 10 \cdot \log(P)$

$PdB = 20$ dBW

$GtdB := 19.0$ dBi $Gt := 17.4328$ — Transmit Antenna Gain

$LldB := -1$ dB $Ll := 1.25893$ — Line Loss

$EIRP := GtdB + PdB + LldB$

$EIRP = 38$ dBW — Effective Isostropic Radiated Power

$S := 35786 \cdot 10^3$ m

$$Ls := \left(\frac{c}{4 \cdot \pi \cdot S \cdot f1}\right)^2$$

$LsdB := 10 \cdot \log(Ls)$

$LsdB = -189.993$ dB — Free Space Loss

$Gr := 15.7761$

$GrdB := 10 \cdot \log(Gr)$

$GrdB := 11.98$ dBi — ReceiveAntenna Gain

$RIP := EIRP + LsdB + GrdB$

$RIP = -140.013$ dBW — ReceivedIsotropic Power

$Ts := 552$ K — System Temperature

$R := 1000$ bps — Data Rate

$k := 13.8 \cdot 10^{-24}$ — Bolztmans Constant

$Eb := P \cdot Ll \cdot Gt \cdot Ls \cdot Gr$ — Energy per Bit

$No := k \cdot Ts \cdot R$ — Noise Density

$$X := 10 \cdot \log\left(\frac{Eb}{No}\right) \quad \text{dB} - \text{Hz}$$

$X = 26.583$ dB – Hz — Energy per Bit to Noise Density Ratio

$Y := 21.99$ dB – Hz — Required Energy per Bit to Noise Density Ratio

$FM := X - Y$

$FM = 4.593$ dB — Fade Margin

TDRSS Telemetry Link Calculations

$f1 := 2287.5000 \cdot 10^6 MHz$ — Frequency

$c := 2.99792 \cdot 10^8 \frac{m}{s}$ — Speed of Light

$P := 5 \quad W$

$PdB := 10 \cdot \log(P)$

$PdB = 6.99 \quad dBW$ — Transmitted Power

$GtdB := 13.06 dBi \quad Gt := 20.2302$ — Transmit Antenna Gain

$LldB := -1 \quad dB \quad Ll := 1.25893$ — Line Loss

$EIRP := GtdB + PdB + LldB$

$EIRP = 19.05 \, dBW$ — Effective Isostropic Radiated Power

$S := 35786 \cdot 10^3 \, m$

$$Ls := \left(\frac{c}{4 \cdot \pi \cdot S \cdot f1}\right)^2$$

$LsdB := 10 \cdot \log(Ls)$

$LsdB = -190.709 dB$ — Free Space Loss

$Gr := 17.4328$

$GrdB := 10 \cdot \log(Gr)$

$Grd := 19.0 \quad dBi$ — ReceiveAntenna Gain

$RIP := EIRP + LsdB + GrdB$

$RIP = -159.246 dBW$ — ReceivedIsotropic Power

$Ts := 552 \quad K$ — System Temperature

$R := 1000 \quad bps$ — Data Rate

$k := 13.8 \cdot 10^{-24}$ — Bolztmanns Constant

$Eb := P \cdot Ll \cdot Gt \cdot Ls \cdot Gr$ — Energy per Bit

$No := k \cdot Ts \cdot R$ — Noise Density

$$X := 10 \cdot \log\left(\frac{Eb}{No}\right) dB - Hz$$

$X = 13.936 \quad dB - Hz$ — Energy per Bit to Noise Density Ratio

$Y := 6.99 \quad dB - Hz$ — Required Energy per Bit to Noise Density Ratio

$FM = X - Y$

$FM = 6.946 \quad dB$ — Fade Margin

STDN Command Link Calculations

$f1 := 2106.4106 \cdot 10^6 MHz$ — Frequency

$c := 2.99792 \cdot 10^8 \frac{m}{s}$ — Speed of Light

$\eta := .55$ — Aperture Efficiency

$P := 1000W$ — Transmitted Power

$PdB := 10 \cdot \log(P)$

$PdB = 30dBW$

$D := 6 \quad m$ — Antenna Diameter

$Gt := \left(\frac{\pi \cdot D \cdot f1}{c}\right)^2 \cdot \eta$

$GtdB := 10 \cdot \log(Gt)$

$GtdB = 39.844 \ dBi$ — Antenna Gain

$LldB := -1 \ dB \qquad Ll := 1.25893$ — Line Loss

$EIRP := GtdB + PdB + LldB$

$EIRP = 68.844 \ dBW$ — Effective Isotropic Radiated Power

$S := 2100 \cdot 10^3 m$ — Path Length

$Ls := \left(\frac{c}{4 \cdot \pi \cdot S \cdot f1}\right)^2$

$LsdB := 10 \cdot \log(Ls)$

$LsdB = -165.363dB$ — Free Space Loss

$La := 0.89125$

$LadB := -0.5 \ dB$ — AtmosphericLoss

$Gr := 11.98dBi$ — ReceiveAntenna Gain

$RIP := EIRP + LsdB + Gr + LadB$

$RIP = -85.039dBW$ — ReceivedIsotropic Power

$Ts := 1295K$ — System Temperature

$R := 2000bps$ — Data Rate

$k := 13.8 \cdot 10^{-24}$ — Boltzmans Constant

$Eb := P \cdot Ll \cdot Gt \cdot Ls \cdot La \cdot Gr$ — Energy per Bit

$No := k \cdot Ts \cdot R$ — Noise Density

$X := 10 \cdot \log\left(\frac{Eb}{No}\right) dB - Hz$

$X = 80.234 \ dB - Hz$ — Energy per Bit to Noise Density Ratio

$Y = 21.99 \ dB - Hz$ — Required Energy per Bit to Noise Density Ratio

$FM := X - Y$

$FM = 58.244 \ dB$ — Fade Margin

STDN Telemetry Link Calculations

$f1 := 2287.5000 \cdot 10^6 MHz$ — Frequency

$c := 2.99792 \cdot 10^8 \frac{m}{s}$ — Speed of Light

$\eta := .55$ — Aperture Efficiency

$P := 5 \quad W$ — Transmitted Power

$PdB := 10 \cdot \log(P)$

$PdB = 6.99 dBW$

$GtdB := 13 dBi \qquad Gt := 20.2302$ — Transmit Antenna Gain

$LldB := -1 \, dB \qquad Ll := 1.25893$ — Line Loss

$EIRP := GtdB + PdB + LldB$

$EIRP = 19.05 \, dBW$ — Effective Isostropic Radiated Power

$S := 1200 \cdot 10^3 m$

$Ls := \left(\frac{c}{4 \cdot \pi \cdot S \cdot f1} \right)^2$

$LsdB := 10 \cdot \log(Ls)$

$LsdB = -166.079 dB$ — Free Space Loss

$La := 0.89125$

$LadB := -0.5 \, dB$ — Atmospheric Loss

$D := 26 \quad m$ — Diameter

$Gr := \left(\frac{\pi \cdot D \cdot f1}{c} \right)^2 \cdot \eta$

$Gr = 2.136 \cdot 10^5$

$GrdB := 10 \cdot \log(Gr)$

$GrdB = 53.297 \, dBi$ — ReceiveAntenna Gain

$RIP := EIRP + LsdB + GrdB$

$RIP = -93.733 dBW$ — ReceivedIsotropic Power

$Ts := 552 \quad K$ — System Temperature

$R := 20000 bps$ — Data Rate

$k := 13.8 \cdot 10^{-24}$ — Bolztmans Constant

$Eb := P \cdot Ll \cdot Gt \cdot Ls \cdot Gr$ — Energy per Bit

$No := k \cdot Ts \cdot R$ — Noise Density

$X := 10 \cdot \log\left(\frac{Eb}{No} \right) dB - Hz$

$X = 56.439 \, dB - Hz$ — Energy per Bit to Noise Density Ratio

$Y := 21.99 \, dB - Hz$ — Required Energy per Bit to Noise Density Ratio

$FM := X - Y$

$FM = 34.449 \, dB$ — Fade Margin

Beacon Link Calculations

$f := 12 \cdot 10^9\ GHz$ — Frequency

$Ta := 62K$ — Antenna Temperature
$To := 290K$ — Sky Temperature

$GtdB := 16.0\ dBi$ — Transmit Horn Gain
$PdB := 11.46\ dBW$
$Dr := 25m$ — RecieveAntenna Diameter

$\eta := 0.70$ — Aperture Efficiency

$c := 2.99792 \cdot 10^8 \frac{m}{s}$ — Speed of Propagation

$S := 1200 \cdot 10^3 m$ — MaximumPropagation Distance

$$LsdB := 10 \cdot \log\left[\left(\frac{c}{4 \cdot \pi \cdot S \cdot f}\right)^2\right]$$

$$GrdB := 10 \cdot \log\left[\left(\frac{\pi \cdot Dr \cdot f}{c}\right)^2 \cdot \eta\right]$$

$LsdB = -175.615 dB$ — Free Space Loss
$GrdB = 68.4\ dBi$ — ReceiveAntenna Gain

$$LadB := 10 \cdot \log\left(1 - \frac{Ta}{To}\right)$$

$LadB = -1.045\ dB$ — AtmosphericLoss

$XdB := GtdB + GrdB + LsdB + LadB + PdB$
$XdB = -80.8\ dB$ — Total CarrierGain

$k := 13.8 \cdot 10^{-24}$ — Boltzmans Constant

$B := 100 \cdot 10^3\ Hz$ — Bandwidth

$$Ts := Ta + \frac{1}{100 \cdot 10^3}$$

$NdB := 10 \cdot \log(k \cdot Ts \cdot B)$
$NdB = -160.677\ dB$ — Noise Strength

$YdB := -XdB + NdB$
$YdB = -79.878 \frac{dB}{Hz}$ — Ratio of XdB and NdB

$FMdB := 100 + YdB$
$FMdB = 20.122\ dB$ — Fade Margin

Table 5.6.3-1. Link budget summary.

Item	Symbol	Units	STDN Link		TDRSS Link	
			Command Link	Telemetry Link	Command Link	Telemetry Link
Frequency	f	MHz	2106.406	2287.5	2106.406	2287.5
Transmitter Power	P	Watts	1000	5	100	5
Transmitter Power	P	dBW	30	6.99	20	6.99
Transmitter Line Loss	L(t)	dB	-1	-1	-1	-1
Transmit Antenna Diameter	D(t)	m	6	N/A Helical	N/A Helical	N/A Helical
Transmit Antenna Gain	G(t)	dB	38.84	13.06	19	11.99
Equiv. Isotropic Radiated Power	EIRP	dBW	68.84	19.05	38	19.05
Propagation Path Length	S	km	2100	2100	35786	35786
Space Loss	L(s)	dB	-185.36	-186.06	-189.99	-190.91
Propagation & Polarization Loss	L(a)	dB	-0.5	-0.5	N/A	N/A
Receive Antenna Diameter	D(r)	m	N/A Helical	26	N/A Helical	N/A Helical
Receive Antenna Gain	G(r)	dB	11.99	53.3	13.06	19
Received Isotropic Power	RIP	dBW	-85.04	-93.73	-140.01	-168.85
System Noise Temperature	T(s)	K	1295	552	552	552
Data Rate	R	bps	2000	200000	1000	1000
Eb/No	Eb/No	dB	80.23	56.44	26.583	14.58
Required Eb/No	Req Eb/N	dB-Hz	21.99	21.99	21.99	8.99
Margin	-	dB	58.24	34.45	4.593	5.59

5.6.4 Summary

The communication design challenge was largely due to the system requirements necessitated by the WISPER mission. During the microwave beaming portion of the mission there will be a real time communications link during microwave power beaming experiments from the satellite to the ground station at the NOAA site near Fairbanks. Throughout the rest of the mission, including Phase II, the link with the satellite will be through the use of the TDRSS relay satellites. The system onboard the satellite includes the TDRSS standard user transponder, a diplexer, two antennas and all the necessary cables and interfaces needed so that the system will operate as needed.

The proposed system will theoretically operate sufficiently based on the supporting calculations. Although some values such as the TDRS satellite's antenna gain and required energy per bit to noise density ratio were estimated, the proposed system provides the groundwork for further design iterations.

5.7 Thermal Subsystem

5.7.1 Thermal Requirements

The thermal subsystems help to maintain the temperature of the satellite and its various components within acceptable limits during the mission lifetime. The primary objective of thermal management is to verify and maintain component operating temperatures within specified ranges.

5.7.2 Types of Thermal Control

Thermal control techniques are broadly divided into two classes, active and passive. The latter is preferred for smaller satellites due to its simplicity, reliability, and cost. The techniques employed for passive control include use of geometric coatings, insulation blankets, sun shields, radiating fins, and heat pipes. Another effective means of controlling temperature is by manipulation of the spacecraft configuration [14].

For passive control, different materials are used to perform specific functions. For instance, layers of aluminized Mylar, nylon, or Dacron mesh provide good thermal insulation against conductive heat transfer. Sunshields are used wherever solar heat influx must be minimized.

Simple heat transfer techniques are used to control temperatures in a passive system. Fins, because they have a relatively high surface area, radiate heat from within the satellite. One effective way of circulating heat within the structure is by means of heat pipes. Heat pipes are tubular devices containing a wick that runs along the length of a pipe. The pipe is partially filled with a gas such as ammonia. The pipe is connected between a hot portion of the satellite and the radiator. The fluid evaporates from the hot end and condenses at the radiator, removing the heat. The fluid is recirculated to the hot end by capillary action.

Active thermal control consists of devices that either require a constant input of power and/or require mechanical motion. Examples of the active systems include devices like louvers, shutters, heaters, and coolers.

5.7.3 Analysis Evolution

During the preliminary design, an approximate thermal model of the satellite was developed. The maximum and minimum temperatures were estimated within the satellite to develop a more detailed thermal design.

The first step in the thermal model was to determine key requirements and constraints. These include the temperature limits and power dissipation of all spacecraft components. Next, the spacecraft altitude and orientation relative to the earth and the sun for both

mission phases were used to determine the thermal boundary conditions. The diameter of a spherical spacecraft, with a surface area equal to that of WISPER, was calculated. This was then approximated to be an isothermal sphere, and first order estimates of the spacecraft's thermal performance were obtained. For this calculation the surface of the satellite was assumed to have a solar absorbtivity and emissivity of white paint. Later iterations were made with other coatings.

A thermal model was prepared to obtain a more accurate estimate of the component temperatures within the satellite. This model included the major heat sources and sinks, both external and internal. The heat sources included solar flux and radiation energy from the dish. The heat sinks were the sides of the satellite which conduct energy from within the satellite to deep space. Due to the sun-synchronous orbit and to the inflatable antenna virtually shadowing the satellite from earth, almost 85% of the input heat energy is from the sun. The solar heat influx heats one side of the satellite with the other sides being covered by either the solar panels or being on the "dark side". The problem was then defined as selecting suitable surface coatings for the various sides to keep the temperature within the operating limits of the components.

A radiation conduction model of the satellite was then constructed. The aim of this model was to find the temperature distribution in the external shell of the satellite. The satellite was modeled as being isothermal. Internal heat dissipation was neglected since it is just 12% of the total heat influx. A more accurate analysis would require a detailed model of each of the satellite components. The heat capacities of the radiative blankets are small and are assumed to be zero. It was impossible to consider heat conduction within the individual units due to a lack of information on the detailed design of the components. The steady state heat distribution can be determined by a variety of numerical and exact methods.

From this analysis, the side facing the sun should be coated with a layer that absorbs little solar radiation. For this reason white enamel with a solar absorptivity of 0.25 and an emissivity of 0.86 has been selected. Similarly the sides shadowed from the sun have to emit less energy to remain at moderate temperatures. The aluminum shell provides the necessary insulation due to low emissivity in the infrared region.

5.7.4 Finite Element Analysis

The radiator is divided into a finite number of areas. It is assumed that heat is conducted only by the evaporation and condensation of the spacecraft's working fluid [22]. The temperature distribution in each element is given by

$$T = N_1 T_1 + N_2 T_2 + N_3 T_3 + N_4 T_4 + T_5 N_5 \quad [K] \qquad (5.7.4\text{-}1)$$

where N_1, N_2, N_3, N_4, *and* N_5 are the non-linear shape factors.

Equation 5.7.4-1 is converted into a linear finite element problem by making the assumption that the temperature distribution in the fin is uniform. This assumption is justified considering that fluid condenses along the fin. Thus, maintaining the spacecraft at its condensation temperature and conduction plays a relatively small role in the heat transfer.

The solution of Equation 5.7.4-1 gives a radiator area for each of the components as shown in Table 5.7.4-1.

Table 5.7.4-1. Spacecraft component radiated area.

Part Name	Heat Dissipated (W)	Radiator Area (m^2)
Battery	20	0.07214
CPU	12	0.04329
TDRSS	40	0.14429
Power Circuits	20	0.07214
Science Payload	30	0.10822
TOTAL	122	0.44008

The calculations were based on an emissivity of 0.92 (white epoxy) in the infrared region.

5.7.5 Summary

The temperature distribution on the outside of the satellite varies as shown in Figure 5.7.5-1. Assuming an infinite conductance within the satellite, all components can be kept within their specific operating temperature ranges.

Dissipating heat from components that are heat intensive, like the CPU and the batteries, requires a suitable heat pipe. Also these components are placed on the side away from the sun to lower their temperatures. Table 5.7.5-1 summarizes the component operating temperatures.

Table 5.7.5-1. Component operating temperatures.

Component	Operating Temp. Range (K)	Achieved Temp. Range (K)
Electronics	273 to 313	290 to 275
Batteries	278 to 293	285 to 278
Solar Arrays	173 to 373	333 to 353
Structure	230 to 338	295 to 275

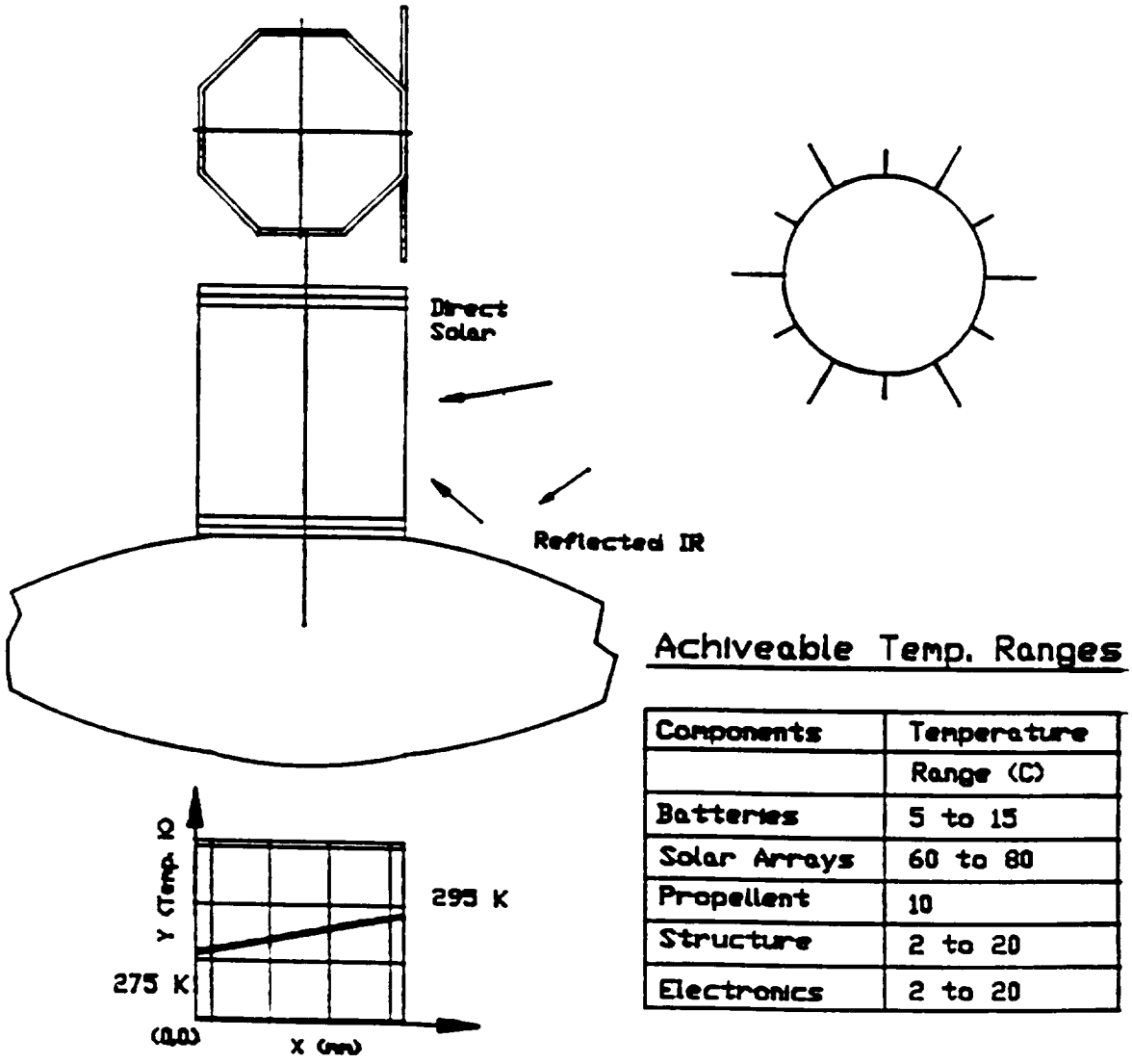

Figure 5.7.5-1. Temperature distribution within the satellite.

5.8 Mass and Volume Budget

5.8.1 Mass Budget

Satellite mass is transient throughout the life of the spacecraft, especially in the development stages. WISPER is a preliminary design study. As a result the masses are often estimates based on other designs, percentages of total mass, information from manufacturers, and best estimates.

Mass is a critical element of satellite design. There is a direct relationship between mass and launch costs which affect the mission. A spreadsheet was created to update and monitor the mass budget.

Total Mass: 560 lbm

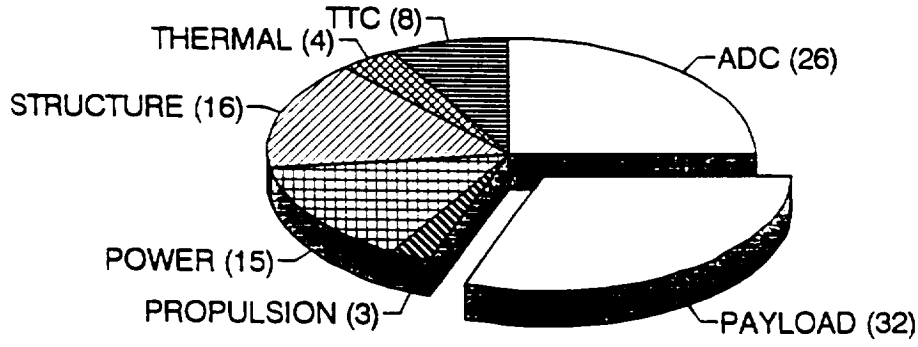

Figure 5.8.1-1. Mass budget.

Table 5.8.1-1. Mass budget.

SUBSYSTEMS/ COMPONENTS	QTY	UNIT MASS (LBM)	TOTAL MASS (KG)	TOTAL MASS (LBM)	% SUBSYSTEM MASS	% BOOSTED MASS TOTAL MASS BOOSTED 559.90 (LBM)	% INJECTED MASS M-B - PROPELLANT 552.95 (LBM)	% DRY MASS M-INJ - ADAPTER 537.95 (LBM)	% BOOSTER CAPABILITY BOOSTER: PEGASUS 614.00 (LBM)
ATTITUDE DETERMINATION & CONTROL						%M-B	%M-INJ	%M-DRY	%M-PPC
DIGITAL SUN SEN	3	0.88	1.20	2.65	1.88	0.47	0.48	0.49	0.43
ANALOG SUN SEN	1	0.88	0.40	0.88	0.63	0.16	0.16	0.16	0.14
MAGNETOMETER	1	1.10	0.50	1.10	0.78	0.20	0.20	0.20	0.18
TORQROD-ROLL	1	3.75	1.70	3.75	2.67	0.67	0.68	0.70	0.61
TORQROD-PITCH	1	3.75	1.70	3.75	2.67	0.67	0.68	0.70	0.61
TORQROD-YAW	1	0.88	0.40	0.88	0.63	0.16	0.16	0.16	0.14
MOM WHL	2	14.33	13.00	28.66	20.41	5.12	5.18	5.33	4.67
MOM WHL	2	37.48	34.00	74.96	53.38	13.39	13.56	13.93	12.21
MOM WHL ELEC	4	1.50	2.72	6.00	4.27	1.07	1.09	1.12	0.98
GPS MODULE	1	9.40	4.26	9.40	6.69	1.68	1.70	1.75	1.53
GPS ANT	2	2.00	1.81	4.00	2.85	0.71	0.72	0.74	0.65
INTERFEROMETER	1	4.41	2.00	4.41	3.14	0.79	0.80	0.82	0.72
SUBTOTALS:	**20**	**80.36**	**63.70**	**140.43**	**100.00**	**25.08**	**25.40**	**26.11**	**22.87**
PAYLOAD		(LBM)	(KG)	(LBM)	%M-SS	%M-B	%M-INJ	%M-DRY	%M-PPC
PWR SEN	6	0.30	0.82	1.80	1.06	0.32	0.33	0.33	0.29
14m MW ANT MOD	1	150.00	68.04	150.00	88.01	26.79	27.13	27.88	24.43
RECTENNA	1	2.20	1.00	2.20	1.29	0.39	0.40	0.41	0.36
LASER PV	1	6.61	3.00	6.61	3.88	1.18	1.20	1.23	1.08
MW ATTENUATOR	3	0.30	0.41	0.90	0.53	0.16	0.16	0.17	0.15
PWR METER	3	1.00	1.36	3.00	1.76	0.54	0.54	0.56	0.49
BEACON TWTA	1	1.54	0.70	1.54	0.91	0.28	0.28	0.29	0.25
BEACON PWR SUPPLY	1	4.08	1.85	4.08	2.39	0.73	0.74	0.76	0.66
PWR DEN GAIN HORN	3	0.10	0.14	0.30	0.18	0.05	0.05	0.06	0.05
SUBTOTALS:	**20**	**166.14**	**77.31**	**170.44**	**100.00**	**30.44**	**30.82**	**31.68**	**27.76**
PROPULSION		(LBM)	(KG)	(LBM)	%M-SS	%M-B	%M-INJ	%M-DRY	%M-PPC
0.2-LBF THRUSTER	4	0.73	1.32	2.91	33.67	0.52	0.53	0.54	0.47
TANKS	2	1.76	1.60	3.53	40.82	0.63	0.64	0.66	0.57
LINES & FITTINGS	1	2.20	1.00	2.20	25.51	0.39	0.40	0.41	0.36
SUBTOTALS:	**7**	**4.70**	**3.92**	**8.64**	**100.00**	**1.54**	**1.56**	**1.61**	**1.41**
PROPELLANT		(LBM)	(KG)	(LBM)	%M-SS	%M-B	%M-INJ	%M-DRY	%M-PPC
PROP-DELTA V/RESIDUAL	0	6.94	3.15	6.94	100.00	1.24	1.26	1.29	1.13
SUBTOTALS:	**0**	**6.94**	**3.15**	**6.94**	**100.00**	**1.24**	**1.26**	**1.29**	**1.13**
POWER		(LBM)	(KG)	(LBM)	%M-SS	%M-B	%M-INJ	%M-DRY	%M-PPC
BATTERIES	23	0.99	10.31	22.72	28.41	4.06	4.11	4.22	3.70
POWER CTRL UNIT	1	10.00	4.54	10.00	12.51	1.79	1.81	1.86	1.63
REG/CONVERTERS	1	12.50	5.67	12.50	15.63	2.23	2.26	2.32	2.04
WIRING	1	21.52	9.76	21.52	26.91	3.84	3.89	4.00	3.50
SOLAR PV	1	13.23	6.00	13.23	16.54	2.36	2.39	2.46	2.15
SUBTOTALS:	**27**	**58.24**	**36.27**	**79.97**	**100.00**	**14.28**	**14.46**	**14.87**	**13.02**
STRUCTURE		(LBM)	(KG)	(LBM)	%M-SS	%M-B	%M-INJ	%M-DRY	%M-PPC
BOOSTER ADAPTER	1	15.00	6.80	15.00	17.24	2.68	2.71	2.79	2.44
STRUCTURE	1	62.68	28.43	62.68	72.05	11.20	11.34	11.65	10.21
FASTENER/FITTING	1	7.77	3.52	7.77	8.93	1.39	1.40	1.44	1.27
MNTG HARDWARE	1	1.55	0.70	1.55	1.79	0.28	0.28	0.29	0.25
SUBTOTALS:	**4**	**87.00**	**39.46**	**87.00**	**100.00**	**15.54**	**15.73**	**16.17**	**14.17**
THERMAL		(LBM)	(KG)	(LBM)	%M-SS	%M-B	%M-INJ	%M-DRY	%M-PPC
THERMAL SYS	1	21.50	9.75	21.50	100.00	3.84	3.89	4.00	3.50
SUBTOTALS:	**1**	**21.50**	**9.75**	**21.50**	**100.00**	**3.84**	**3.89**	**4.00**	**3.50**
TELEMETRY/TRACKING/COMMAND			(KG)	(LBM)	%M-SS	%M-B	%M-INJ	%M-DRY	%M-PPC
COMM ANT	1	2.20	1.00	2.20	4.89	0.39	0.40	0.41	0.36
TDRSS	1	15.57	7.06	15.57	34.62	2.78	2.82	2.89	2.54
CPU MODULE	1	25.00	11.34	25.00	55.59	4.47	4.52	4.65	4.07
TDRSS ANT	1	2.20	1.00	2.20	4.89	0.39	0.40	0.41	0.36
SUBTOTALS:	**4**	**44.97**	**20.40**	**44.97**	**100.00**	**8.03**	**8.13**	**8.36**	**7.32**
TOTALS	**83**	**469.8**	**254.0**	**559.9**		**100.00**	**100.00**	**100.00**	**91.19**

5.8.2 Volume Budget

Volume is a critical element of satellite design. The total volume of a spacecraft is often dictated by the size of fairings available for a particular booster.

Although the volume budget does not directly provide packaging information for the various components, it does relate component volumes to total available volumes. Potential packaging problems can be identified and corrected early in the design process when iterations are the least expensive.

Total Internal Volume: 13.7 ft^3

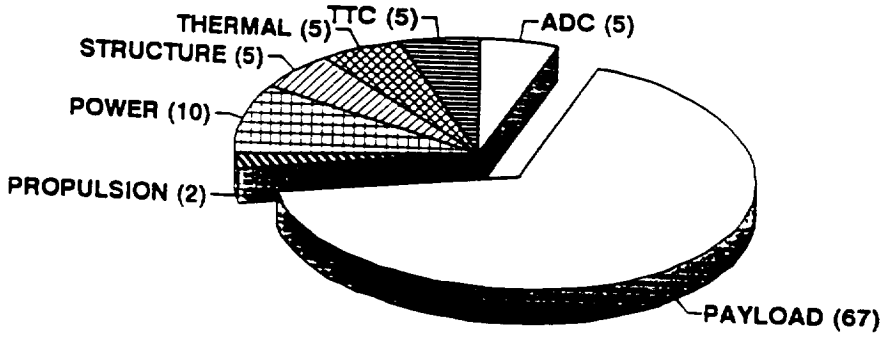

Figure 5.8.2-1. Volume budget.

Table 5.8.2-1. Volume budget.

SUBSYSTEMS/ COMPONENTS	QTY	(B)OX (C)YL (S)PH	(I)N (O)UT	DIMENSIONS								% INTERNAL COMPONENT VOLUME	% INTERNAL SATELLITE VOLUME	% BOOSTER FAIRING VOLUME
				METRIC UNITS				ENGLISH UNITS						
				L (CM)	W/D (CM)	H (CM)	VOL (CM^3)	L (IN)	W/D (IN)	H (IN)	VOL (IN^3)	18853 (IN^3)	23746 (IN^3)	75470 (IN^3)
ATTITUDE DETERMINATION & CONTROL														
DIGITAL SUN SEN	3	B	O	10.16	15.24	5.08	2359.74	4.00	6.00	2.00	144.00	EXTERNAL	EXTERNAL	0.19
ANALOG SUN SEN	1	B	O	10.16	15.24	5.08	786.58	4.00	6.00	2.00	48.00	EXTERNAL	EXTERNAL	0.06
MAGNETOMETER	1	B	I	10.16	10.16	15.24	1573.16	4.00	4.00	6.00	96.00	0.51	0.40	0.13
TORQROD-ROLL	1	C	I		2.60	64.00	339.79		1.02	25.20	20.74	0.11	0.09	0.03
TORQROD-PITCH	1	C	I		2.60	64.00	339.79		1.02	25.20	20.74	0.11	0.09	0.03
TORQROD-YAW	1	C	I		1.80	40.00	101.79		0.71	15.75	6.21	0.03	0.03	0.01
MOM WHL	2	C	I		30.00	3.18	4488.53		11.81	1.25	273.91	1.45	1.15	0.36
MOM WHL	2	C	I		21.20	3.18	2241.45		8.35	1.25	136.78	0.73	0.58	0.18
MOM WHL ELEC	4	B	I	17.78	15.24	3.18	3441.28	7.00	6.00	1.25	210.00	1.11	0.88	0.28
GPS MODULE	1	B	I	17.78	17.78	6.35	2007.42	7.00	7.00	2.50	122.50	0.65	0.52	0.16
GPS ANT	2	C	O	0.00	5.08	15.24	617.78		2.00	6.00	37.70	EXTERNAL	EXTERNAL	0.05
INTERFEROMETER	1	B	I	7.62	10.16	15.24	1179.87	3.00	4.00	6.00	72.00	0.38	0.30	0.10
SUBTOTALS:	**20**						**19477.2**				**1188.6**	**5.1**	**4.0**	**1.6**
PAYLOAD				L	W/D	H	VOL	L	W/D	H	VOL	%ICV	%ISV	%SFV
PWR SEN	6	C	I		3.81	9.40	642.87		1.50	3.70	39.23	0.21	0.17	0.05
14M M/W ANT MOD	1	C	I		96.52	25.40	185848.14		38.00	10.00	11341.15	60.16	47.76	15.03
RECTENNA	1	B	I	1.00	96.00	96.00	9215.98	0.39	37.80	37.80	562.39	2.98	2.37	0.75
LASER PV	1	B	O	326.60	3.00	55.88	54750.66	128.58	1.18	22.00	3341.09	EXTERNAL	EXTERNAL	4.43
MW ATTENUATOR	3	C	I		0.76	3.81	5.21		0.30	1.50	0.32	0.00	0.00	0.00
PWR METER	3	B	I	35.56	8.89	2.24	2119.83	14.00	3.50	0.88	129.36	0.69	0.54	0.17
BEACON TWTA	1	B	I	32.00	32.00	6.10	6243.86	12.60	12.60	2.40	381.02	2.02	1.60	0.50
BEACON PWR SUPPL	1	B	I	20.83	8.38	10.92	1906.77	8.20	3.30	4.30	116.36	0.62	0.49	0.15
PWR DEN GAIN HORN	3	B	I	4.45	2.54	2.03	68.83	1.75	1.00	0.80	4.20	0.02	0.02	0.01
SUBTOTALS:	**20**						**260802.2**				**15915.1**	**66.69**	**52.95**	21.09
PROPULSION				L	W/D	H	VOL	L	W/D	H	VOL	%ICV	%ISV	%SFV
.02-LBF THURSTER	4	C	I		5.84	14.68	1574.11		2.30	5.78	96.08	0.51	0.40	0.13
TANKS	2	S	I		16.60		4790.12		6.54		292.31	1.55	1.23	0.39
LINES & FITTINGS	1	C	I		0.16	304.80	6.03		0.06	120.00	0.37	0.00	0.00	0.00
SUBTOTALS:	**7**						**6370.3**				**388.7**	**2.06**	**1.64**	**0.52**
POWER				L	W/D	H	VOL	L	W/D	H	VOL	%ICV	%ISV	%SFV
BATTERIES	23	B	I	0.44	0.64	1.27	8.27	0.17	0.25	0.50	0.50	0.00	0.00	0.00
POWER CTRL UNIT	1	B	I	20.32	30.48	10.16	6292.63	8.00	12.00	4.00	384.00	2.04	1.62	0.51
REG/CONVERTERS	1	B	I	20.32	30.48	10.16	6292.63	8.00	12.00	4.00	384.00	2.04	1.62	0.51
WIRING	1	B	I	182.88	10.16	10.16	18877.90	72.00	4.00	4.00	1152.00	6.11	4.85	1.53
SOLAR PV	1	B	O	326.60	3.00	55.88	54750.66	128.58	1.18	22.00	3341.09	EXTERNAL	EXTERNAL	4.43
SUBTOTALS:	**27**						**86222.1**				**5261.6**	**10.19**	**8.09**	**6.97**
STRUCTURE				L	W/D	H	VOL	L	W/D	H	VOL	%ICV	%ISV	%SFV
BOOSTER ADAPTER	1	C	O		121.89	7.52	87737.30		47.99	2.96	5354.06	EXTERNAL	EXTERNAL	7.09
STRUCTURE	1	OCT	O	20.32	50.80	54.61	95665.61	8.00	20.00	21.50	24324.47	EXTERNAL	EXTERNAL	32.23
FASTENER/FITTING	1	B	O	15.24	15.24	15.24	3539.61	6.00	6.00	6.00	216.00	EXTERNAL	EXTERNAL	0.29
MNTG HARDWARE	1	B	I	25.40	25.40	25.40	16387.06	10.00	10.00	10.00	1000.00	5.30	4.21	1.33
SUBTOTALS:	**4**						**203329.6**				**30894.5**	**5.30**	**4.21**	**40.94**
THERMAL				L	W/D	H	VOL	L	W/D	H	VOL	%ICV	%ISV	%SFV
THERMAL SYS	1	B	I	25.40	25.40	25.40	16387.06	10.00	10.00	10.00	1000.00	5.30	4.21	1.33
SUBTOTALS:	**1**						**16387.1**				**1000.0**	**5.30**	**4.21**	**1.33**
TELEMETRY/TRACKING/COMMAND						H	VOL	L	W/D	H	VOL	%ICV	%ISV	%SFV
COMM ANT	1	C	O	0.00	3.30	39.50	337.81		1.30	15.55	20.61	EXTERNAL	EXTERNAL	0.03
TDRSS	1	B	I	33.07	14.05	13.97	6489.33	13.02	5.53	5.50	396.00	2.10	1.67	0.52
CPU MODULE	1	B	I	19.15	18.42	28.58	10077.74	7.54	7.25	11.25	614.98	3.26	2.59	0.81
TDRSS ANT	1	C	O		7.62	33.02	1505.83		3.00	13.00	91.89	EXTERNAL	EXTERNAL	0.12
SUBTOTALS:	**4**						**18410.7**				**1123.5**	**5.36**	**4.26**	**1.49**
TOTALS	**83**						**610999**				**55772**	**100.00**	**79.40**	**73.90**

5.9 Radiation Protection and Hardening

Every module and component that has been specified is space qualified. However, proper standard radiation hardening of custom components must be done prior to installation in the WISPER satellite. This experiment involves exposing the satellite to controlled high powered microwave energy. Without proper precautions, the performance of externally mounted components and electronic subsystems inside the satellite could be compromised.

The size of the inflatable antenna is large enough (14 m) to shield the satellite from the microwave energy beamed from earth. Components (helical communication antenna, power density horn antennas, monopulse beacon components, and interferometer system) placed on the focal point of the inflatable antenna facing the incoming microwave energy will not be affected due to the low power density (nominally 3 W/m^2).

The large size of the inflatable antenna will cause a potential difference between the ends of the antenna as it traverses space. Force is given by

$$\bar{F}=q(\bar{E}+\bar{v}x\bar{B}) \quad [N] \qquad (5.9\text{-}1)$$

where F is the force vector (N) and q is charge (C). At equilibrium the charge is zero leaving

$$\bar{E}=-\bar{v}x\bar{B} \quad [V/m] \qquad (5.9\text{-}2)$$

were v is the velocity vector (m/s) equal to 8000 m/s, B is the magnetic flux density (T) equal to 3×10^{-5} T. The electric field vector, E, is then equal to 0.24 V/m. Taking into account the 14 m over which the electric field exists yields a potential difference of 3.36 V from edge to edge of the inflatable antenna.

During laser power beaming experiments, the solar panels are sufficiently large to prevent the laser radiation from any direct contact with the satellite proper. However, the sun sensors mounted between the solar panels would have to be shielded due to their sensitivity to electromagnetic radiation.

Both the microwave and laser energies do not contain high energy particles that can penetrate the satellite hull or introduce any secondary processes such as Bremsstrahlung radiation (x rays), etc. The man-made radiation is small compared to the cosmic radiation.

The prevailing sources of penetrating radiation listing in order of significance are:

- Solar cosmic rays consisting chiefly of energetic protons, plus a small component

of alpha particles whose energy spectrum extends beyond 100 MeV during solar flares, as well as high Z ions including iron.

- Magnetically trapped protons with energies up to 40 MeV and electrons ranging from hundreds of keV to a few MeV. These protons are confined in the belts about the earth due to the interaction of the earth's magnetic field with the solar wind. These Van Allen belts corresponds to one or more of the naturally occurring charged particle belts extending from about 900 to 3000 km above the earth.

- Galactic cosmic rays whose energies range from about 10 MeV to 1 GeV which mainly consist of protons and heavy ions.

The satellite skin provides little attenuation to the above particles that might impinge on a space vehicle at altitudes above 200 km. For a relatively near earth mission the trapped radiation is the principle consideration. Electronics, including solar cells, pose the most critical requirements for radiation protection.

Heavy particles (e.g. the high energy ions from cosmic rays) including alpha particles can be assumed to be approximately incident isotropically on the spacecraft skin for shields of area density less than 100 g/cm^2. Heavy ion fluences for single-event upset is limited to alpha particles from the sun whose interactions are fundamentally the same as that for protons [23].

In the case of trapped electrons, their charge allows them to be stopped by relatively thin shields. Their range in material is approximately 0.5 g/cm^2/MeV of incident electron energy. However, they can produce bremsstrahlung x-rays whose fluence ultimately exceeds that of the electrons for sufficiently thick shields, because of the greater penetration of the x-rays.

In LEO energetic protons in the inner radiation belt contribute most to the total radiation dose. Radiation dose strongly depends on altitude; below 1000 km the dose increases approximately the fifth power of the altitude [11].

From Figure 5.9-1 and the altitudes of concern (500 to 600 km), the shield thickness of about 0.8 g/cm^2 is adequate for WISPER. Additional thickness does not provide significant protection.

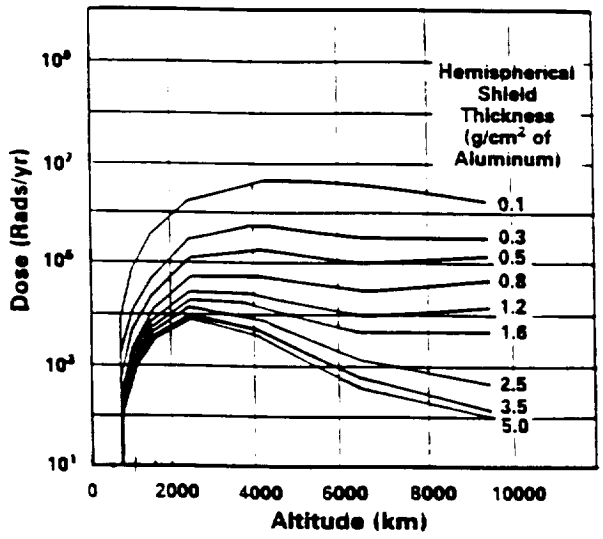

Figure 5.9-1. Satellite altitude versus dosage of radiation.

Figure 5.9-2 shows the radiation count versus energy level for selected earth orbits.

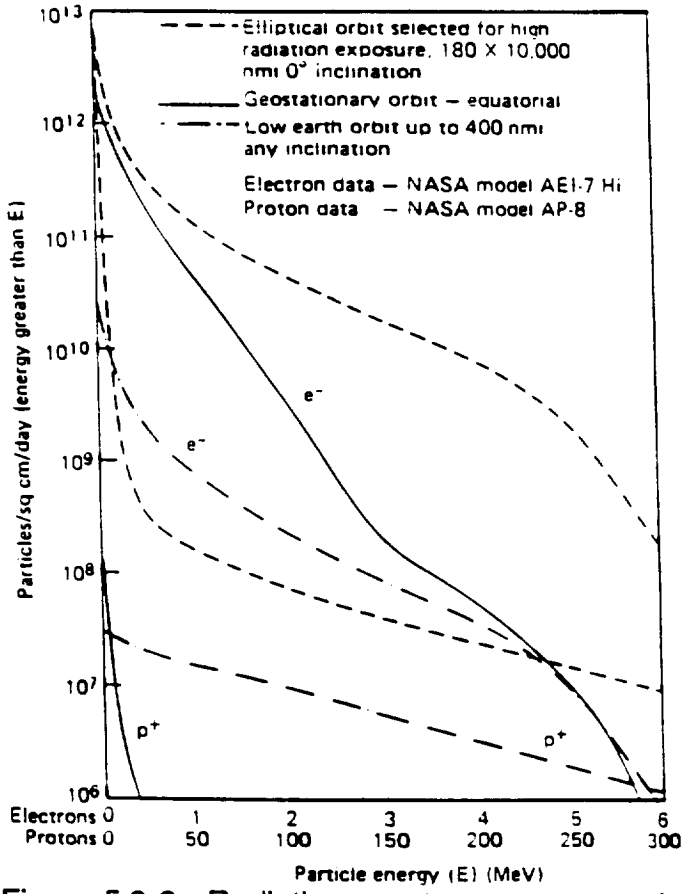

Figure 5.9-2. Radiation count versus energy level.

For LEO at any inclination, the proton density is less than that of the electrons. However, the protons have much higher energy. Shielding is only effective against electrons and does not provide much protection against the high energy protons.

Table 5.9-1 presents radiation hardness for various classes of electronic components. As this table shows, few components can sustain this much radiation and survive [14].

Table 5.9-1. Radiation hardness levels for semiconductor devices.

Technology	Total Dose, rads (Si)
CMOS (soft)	10^3-10^4
CMOS (hardened)	$5 \times 10^4-10^6$
CMOS/SOS (soft)	10^3-10^4
CMOS/SOS (hardened)	$> 10^5$
ECL	10^7
I^2L	$10^5-4 \times 10^6$
Linear IC^2s	$5 \times 10^3-10^7$
MNOS	10^3-10^5
MNOS (hardened)	$5 \times 10^5-10^6$
NMOS	$7 \times 10^2-7 \times 10^3$
PMOS	$4 \times 10^3-10^5$
TTL/STTL	$> 10^6$

Some applications of radiation hardness techniques include [23]:

- decreasing the intrinsic vulnerability of hardness-critical items by using different materials or components.

- optimizing the radiation protection provided by the satellite payload masses through radiation shadowing.

- reconfiguring the interior to provide maximum areal density (g/cm^2) for vulnerable subsystems.

- adding radiation shielding materials such as shield housings for individual piece parts.

UAF
NASA USRA ADP
Space Systems Engineering

WIreless Space Power ExpeRiment

Chapter 6
Mission Implementation

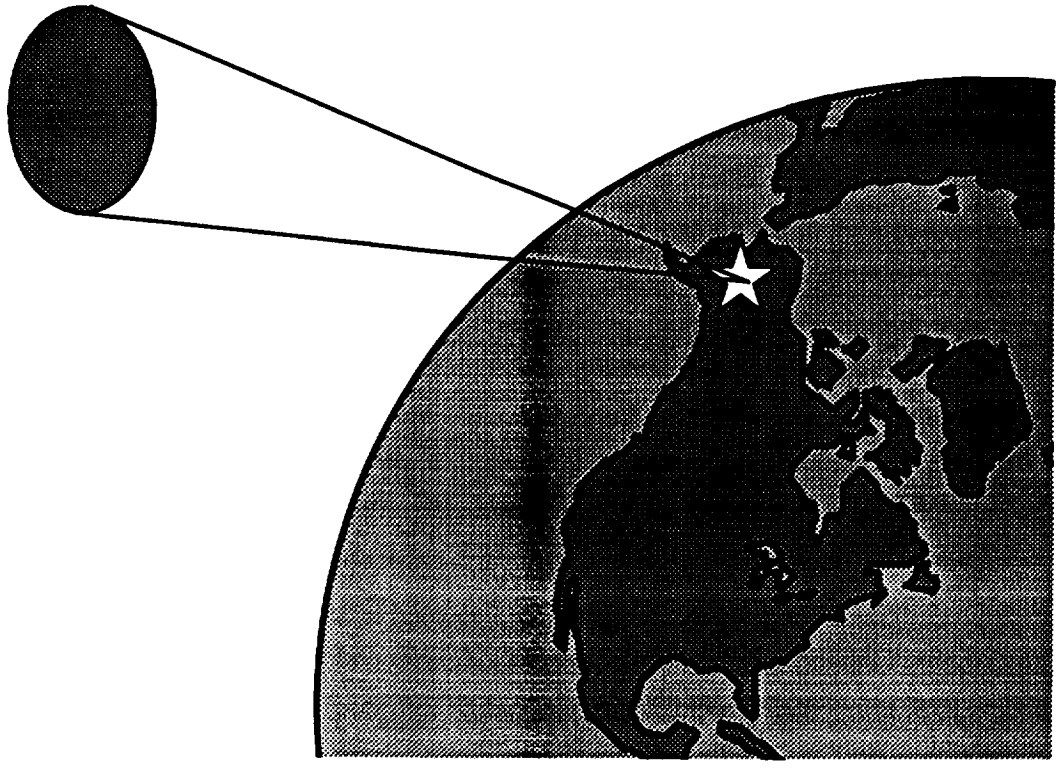

6.0 Mission Implementation

This chapter describes the phases of project development, then examines the cost estimations and the schedule considerations of each segment. Mission analysis defines the spacecraft, the mission, and what is logistically required to support it in very broad terms. The mission analysis provides component and materials lists that can be translated into material costs and their overhead. The tasks and spacecraft functions necessary to complete the mission are used to develop the schedule and to determine the labor costs.

This report is being considered as the preliminary mission analysis segment of the schedule. The rest of the segments that follow this report represent hypothetical ideas about what would be necessary to completely satisfy the Mission Success Criteria (section 7.1). In an ideal world, the next step would be a detailed mission analysis that would deepen the detail of the current design and attempt to resolve all conflicts. This step would allow the freezing of the budgets, component lists, and tasks to the degree that solid schedules and cost budgets could be written. This analysis would be given a year to occur from the end of this report. Fabrication of the spacecraft, ground equipment, and support hardware would be accomplished during the next 18 month segment. Testing of individual components can occur as needed during this time, but integration and testing will be placed in an ambitious 6 month segment. Launch would be in January of 1997. The 2 phases of on-orbit mission experimentation would each have a year to gather data during the operational phase. These times are estimates based on the complexity of the various phases. A mission success requirement is to have completed the mission before the passing of 5 years. This goal is important in terms of maintaining the momentum in wireless power transmission technology. There are other applications of power beaming in space that could use data gathered by this demonstration.

6.1 Cost Estimation

The cost estimation of the spacecraft relies on the experience of others. The estimation task has been done in industry for many years using a method called parametric analysis. This method can lead to a careful estimate that will fall within 10% of actual costs. After a number of components having the same function but with different capacities and costs have been launched, a plot can be generated of the relationship between their weight and their final cost. Regression analysis of these points can lead to equations that are used to find costs of components falling outside or between the plots of the original systems. Estimates can be made of a unit's cost even when all that is known is weight and state of development. Parameters other than weight can be used in the same manner, but weight is the most common and widely applied. These equations are called cost estimation relations (CER) and have been developed for most components that are common to spacecraft. An example is a thruster CER taken from the Satellite Cost Model software donated to the class [1]. The formulas from their software were

incorporated into a spreadsheet program that could be quickly updated as the mission analysis evolved. The example is shown below for thruster cost in thousands of 1974 dollars

$$C=(96.3W^{0.585}FE)+(T49.6W^{0.585}FT)+(14.6W^{0.585}) \quad (6.1\text{-}1)$$

where W is the weight (lbs). The superscript on W reflects how cost per pound plots curve downward as the total weight increases. The first term of the equation is used for those units which require design engineering. The FE term is an adjustment that accounts for variations in design costs based on the number of units being used in the spacecraft. Eighty-eight percent of design cost is fixed and eleven percent depends on the quantity used in the spacecraft, Q divided by 2.

$$FE=0.8875+0.1125(Q/2) \quad (6.1\text{-}2)$$

The second term is an estimation of testing and evaluation costs. T is a multiplier that reflects how thrust compared to weight affects complexity and consequently cost. If thrust is greater than weight, T=2.75. If thrust is less than weight, then T=1. FT is another fixed-cost, quantity-dependent cost percentage adjustment.

$$FT=0.3+0.7(Q/2) \quad (6.1\text{-}3)$$

The third term of Equation 6.1-1 is the production cost of the component (after units have been flight qualified). For thrusters there is no quantity benefit in this part of the analysis.

This CER has to be adjusted to 1993 or later constant year dollars by multiplying by an inflation factor. Commercially contracted and built units tend to run 20% less than those built on government contract. The assumption here is that these components will be government contracted.

The state of development of the components dictates the amount of time that must be devoted to test and qualify them before they are used on the mission. Hence, reliability is not the only motivation for using tested and flight qualified parts. The testing for new systems can increase the cost of including a component to 200% of what it costs to merely produce it. No learning curve adjustment is used to condition this spacecraft's components because the information to do that type of analysis won't be available until the design is finished. Ordinarily, a learning curve factor is used to reflect the fact that the more a fabricator makes a component, the better it will be made and in less time (hence, less costly).

There are items for which no CER exists. In this case, a price quote from the manufacturer is sought. Some components must be entirely created, and in that situation a manufacturer with experience in the field is asked to estimate a cost that includes the research and development costs. Some costs come from specification sheets and others from advertisements. The cost budget table shows the components list for WISPER, the associated weight in pounds (most CERs were written to require pounds), and the quantity. A column is given that reflects price quotes from industry for comparison. Mission equipment and some of the other items did not have corresponding CERs. In those cases, the manufacturer's estimate is used. Most equipment is standard and no "Research, Development, Testing, and Evaluation" costs are included. Only those components requiring development include the RDT&E costs. The sources of information are signified in the legend of Table 6.1-1.

The flight computer is estimated to need 251,400 words of memory (see Chapter 5). This translates into 3175 lines of source code (SLOC) in the C computer language. This parameter can be used to directly estimate the cost of the flight software using a SLOC-based CER. It can also be used to estimate the ground site costs. The flight software is a reliable indicator of the complexity of ground site support requirements. A CER is used to find those items that are typical ground site items, and manufacturer's estimates are used to find the atypical mission equipment costs for the ground site. Launch costs are estimated using a CER based on payload boosted weight that was provided in the Pegasus payload user's manual [2]. The totals are in 1993 constant year dollars. An expenditure schedule that would consider the spreading of development, fabrication and operations costs over their scheduled windows as well as the time value of money effects is left to those who would do a detailed design. The consideration of overhead depends on the award source and the eventual administrative unit that manages it. At this point in time these items are unknown. Table 6.1-1 shows the cost estimations and their respective sources for this project.

Table 6.1-1. Cost estimation table.

SYSTEM	QUANTITY	COMPONENT	WEIGHT (LB)	RDT&E	PRODUCTION	QUOTES/SOURCE
ATTITUDE DETERMINATION AND CONTROL SYSTEM						
	4	SUN SENSORS	0.9		$243,778	SCM
	1	MAGNETOMETER	1.1		$2,757	SCM
	3	TORQUE RODS	2.8		$81,469	SCM
	4	MOMENTUM WHLS	7.1		$206,925	SCM
	3	DIPOLE ANTENNAS	0.2		$17,008	SCM
	1	MIXER	2.2		$26,318	SCM
	1	GPS SYSTEM	11.4		$300,000	$20,000 SCM/SE
	1	INTERFEROMETER	2.2		$2,000,000	SE
					$2,878,254	

PAYLOAD SUBSYSTEMS						
6	POWER SENSOR	0.3		$55,178		SCM
1	MICROWAVE ANT.	150.0		$2,000,000		MQ
1	RECTENNA	2.2		$400,000		MQ
1	12 MHz BEACON	5.6		$2,000,000		MQ
1	LASER PV ARRAY	6.6		$300,000		SE
3	MCRWAVE SENSORS	0.3		$30,694	$30,000	SCM/SE
3	PWR DENSITY ANT.	0.1		$12,595	$20,000	SCM/SE
3	POWER METERS	1.0		$30,000		SE
				$4,828,467		
PROPULSION SYSTEM						
4	THRUSTERS	0.7		$124,600	$40,000	SCM/SE
2	TANKS, VALVES	2.9		$56,988		SCM
-	PROPELLANT	6.9		$1,000		SE
				$182,588		
POWER SYSTEM						
23	BATTERY CELLS	1.0		$448,799		SCM
1	POWER CONTROL	10.0		$190,267		SCM
1	POWER CONVERTER	12.5		$293,957		SCM
-	WIRING HARNESS	16.9		$108,412		SCM
-	SOLAR PV ARRAY	13.2		$96,618		SCM
				$1,138,053		
MECHANICAL SUBSYSTEMS						
1	BOOSTER ADAPTER	15.0	$77,895	$29,132		SCM
1	STRUCTURE	35.4	$2,276,525	$217,393		SCM
				$2,600,945		
THERMAL MANAGEMENT SYSTEM						
-	DISSIPATION SYSTEM	13.0		$104,865		SCM
				$104,865		
TELEMETRY , COMMAND AND COMMUNICATIONS						
1	COMM. ANTENNA	2.2		$29,325	$29,000	SCM/MQ
1	TDRSS	15.6		$2,890,150	$2,000,000	
1	CPU	25		$658,859	$660,000	
1	FLIGHT SOFTWARE	(3127 SLOC)		$1,172,625		
				$4,750,959		
BOOSTER						
1	PEGASUS VEHICLE AND SUPPORT			$16,883,856	MFR.CER	
				$16,883,856		

GROUND SUPPORT EQUIPMENT AND MISC.		
FACILITIES	$211,073	TXT
POWER BEAMING EQUIPMENT	$11,000,000	MQ
GROUND STATION SOFTWARE	$1,172,625	TXT
LOGISTICS	$175,625	TXT
MANAGEMENT	$211,073	TXT
SYSTEMS ENGINEERING	$351,788	TXT
QUALITY ASSURANCE	$175,894	TXT
INTEGRATION AND TESTING	$281,430	TXT
MAINTENANCE	$2,476,740	TXT
CONTRACTOR LABOR	$290,360	TXT
	$16,346,875	

LEGEND

SCM = SATELLITE COST MODEL SOFTWARE
SE = STUDENT ESTIMATE
MQ = MANUFACTURER'S QUOTES
TXT = CER FROM TEXT [3]

TOTALS

SPACECRAFT	$16,484,131
LAUNCH	$16,883,856
GSE	$16,346,875
GRAND TOTAL	$49,714,862

6.2 Project Schedule

The schedule necessary to complete the mission is derived from the tasks identified in the mission analysis. The level of detail that can be resolved in this initial report is limited. A practical schedule awaits a detailed design phase to fix the design for fabrication. Until then, there are many things that can cause great variations in schedule. Changes or revelations about the fundamental mission assumptions could greatly affect the design and, consequently, the schedule to complete the design. An example would be a medical study that revealed a direct connection between microwave energy and detrimental health affects. If the microwave experiment was discontinued, and only the laser segment were pursued, it would result in a different spacecraft and a different mission. Smaller changes can exert similar schedule effects as well.

The experience level of the designers involved in the mission analysis is low in comparison to those in industry who would build the spacecraft. The leaders of the various specialties in this class do not have an intuition of how long it would take to fabricate this spacecraft to NASA standards. At the time span of this report no written information, other than the text [3], or applicable software has been uncovered. Despite this, many things can still be defined. The constraints on the schedule are the "5 years to completion" goal, the funding available to intensify the manhours spent on fabrication, the mission equipment development (for the inflatable antenna, attitude control pointing system, microwave and laser power beaming equipment, and new boosters), testing facilities availability, the occurrence of the solar minimum, and the political environment.

The relationships of the identifiable tasks are shown in Figure 6.2-1.

- **MISSION ANALYSIS - 1/93 - 5/93**
- **DETAILED DESIGN - 9/93 - 9/94**
- **FABRICATION - 10/94 - 4/96**
- **TESTING - 5/96 - 11/96**
- **LAUNCH - 12/96**
- **OPERATION - 1/97 - 1/99**

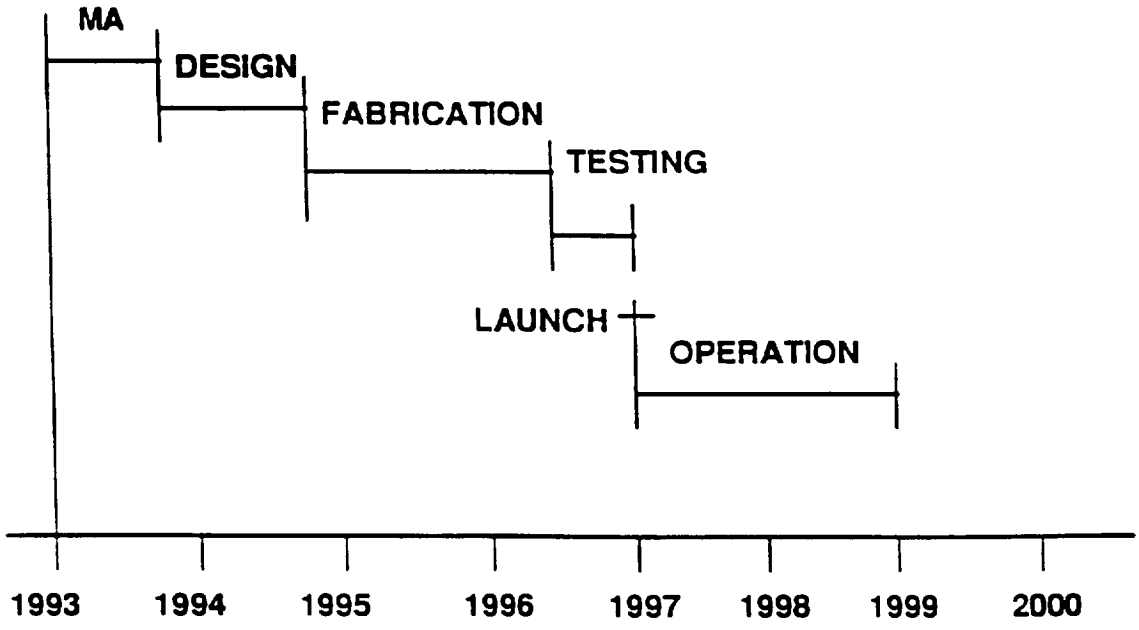

Figure 6.2-1 Proposed mission schedule.

The critical path will be the development of the mission equipment. The Strategic Defense Initiative has conducted most of the recent major research in the area of laser power beaming for use in their weapons systems. The extent of their progress is classified. The surface quality required for the surface of the receiving dish by the microwave system is yet to be demonstrated but is considered feasible by the manufacturer, L'Garde Inc., within the next two years. The pointing accuracy of 0.01 degrees for a spacecraft of this unique configuration will need to be proven in numerical simulation. The Scout II will be launched in 1993. If it is successful, it would be the best choice for the booster and there should be plenty of time to design the spacecraft to utilize it. If not, a development program to enhance the Pegasus to meet the altitude requirements will have to be pursued. The other concern is that there will be testing equipment available to complete testing in 6 months, as well as funds to intensify the manhours to accomplish the deadline. Another development consideration is the installation of the high power microwave transmitting equipment at the ground site. Safety studies will have to be done that could be time consuming. There have been predecessors to this demonstration that have used similar systems to beam power across the ground but not to space. Still, this reduces the number of the unknowns for installing the transmitter at the NOAA site.

UAF
NASA USRA ADP
Space Systems Engineering

WIreless Space Power ExpeRiment

Chapter 7
Conclusion

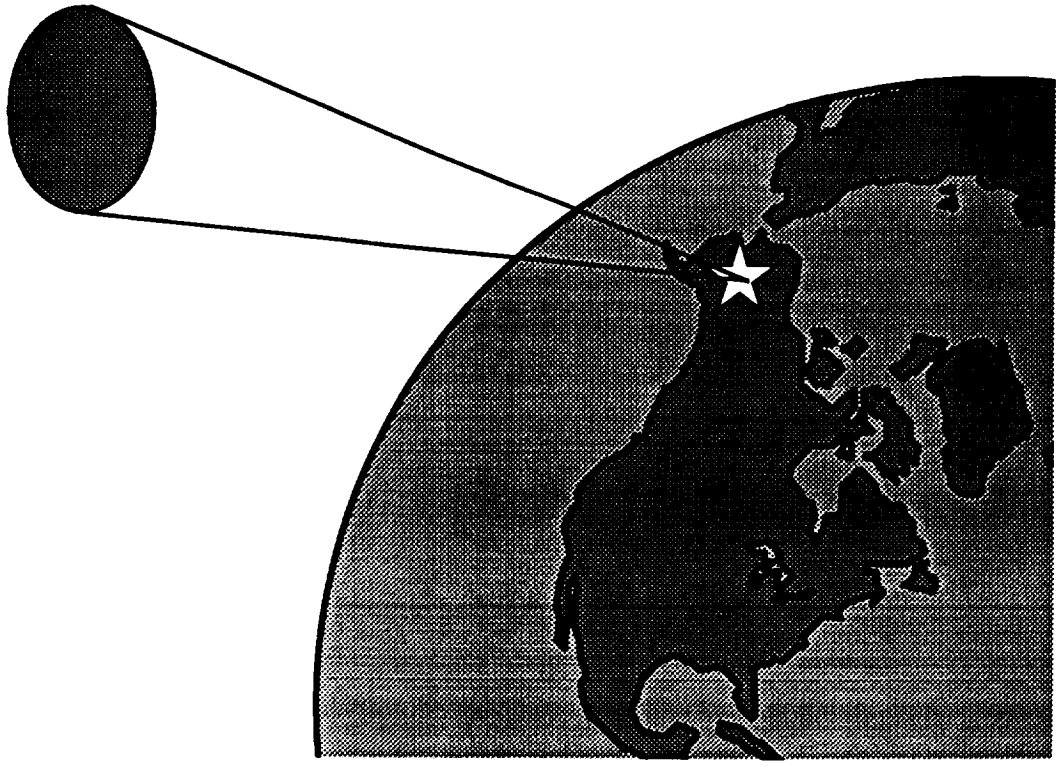

7.0 Conclusion

7.1 Mission Success Criteria

Several success criteria parameters have been selected by the PI. The first criteria will be the quantity of new information added to the fields of science and technology. Current models include microwave and laser power beam interaction with the earth's atmosphere. New discoveries about atmospheric interactions are quite possible. The second criteria is the effectiveness of the technology demonstration. If all the systems operate properly and the predicted power is received, WISPER will prove the earth to space power beaming concept. Gathering of experimental data to support the design of more advanced and larger scale systems is important. The third criteria is the quality and effectiveness of all the other supporting components of the mission. Booster, spacecraft, ground support systems, software, and personnel must all perform as required.

7.2 Alternative Approaches

Alternative designs to this project involve changes to the ground station and space platform. A large array of smaller microwave dishes would drastically reduce the stringent pointing requirements of the current configuration. With sufficient power transmitted from earth the inflatable dish could be eliminated. Due to the application dependent nature of WPT, WISPER advocates power transmission for space missions.

Microwave frequency selection is an issue that warrants further study. An analysis of microwave power beaming using an array of transmitting antennas may recommend a lower operating frequency.

7.3 Future

As a flight demonstration, project WISPER has a number of important features that are necessary to prove WPT in space. The experiment beams power over a longer distance than has been previously attempted. The distance between the transmitter on earth and power collection and conversion receivers on WISPER varies nominally between 500 km and 1000 km for both Phase I and Phase II. Three unique features of the satellite hardware include the inflatable antenna, the space qualified 35 GHz rectenna, and the Si 1.06 m photovoltaic array.

The microwave and laser power are transmitted through the atmosphere. Many proposed applications involve power transmitted from earth to space or space to earth. By transmitting through the atmosphere, WISPER allows experiments to examine how the high power microwave and laser beams interact with the atmosphere. These interactions can be compared with existing attenuation models. The high power levels involved in this experiment are limited by cost rather than available technology. Finally, the experiments

will last a minimum of two years. This period will provide ample time to conduct campaigns of experiments, study WPT in a variety of weather conditions, and examine the operation of unproven satellite components.

Most importantly, the Wireless Space Power Experiment takes the first delicate step of using WPT in space. Once operational, WISPER will provide a reference for WPT projects in space. Simultaneously, WISPER will act as a springboard for future applications.

As shown by the large number of NASA, academic, and industry WPT experts attending the critical design review for WISPER, the project has already generated interest and support for WPT. The next step after the demonstration is a space application that utilizes WPT. The technology is rapidly developing. The advent of higher power, lower maintenance, CW lasers will generate new interest in the WPT field. The present and near future requires sustained interest, research, and funding for WPT. The possibilities for the future show great promise.

UAF
NASA USRA ADP
Space Systems Engineering

WIreless Space Power ExpeRiment
References and Appendices

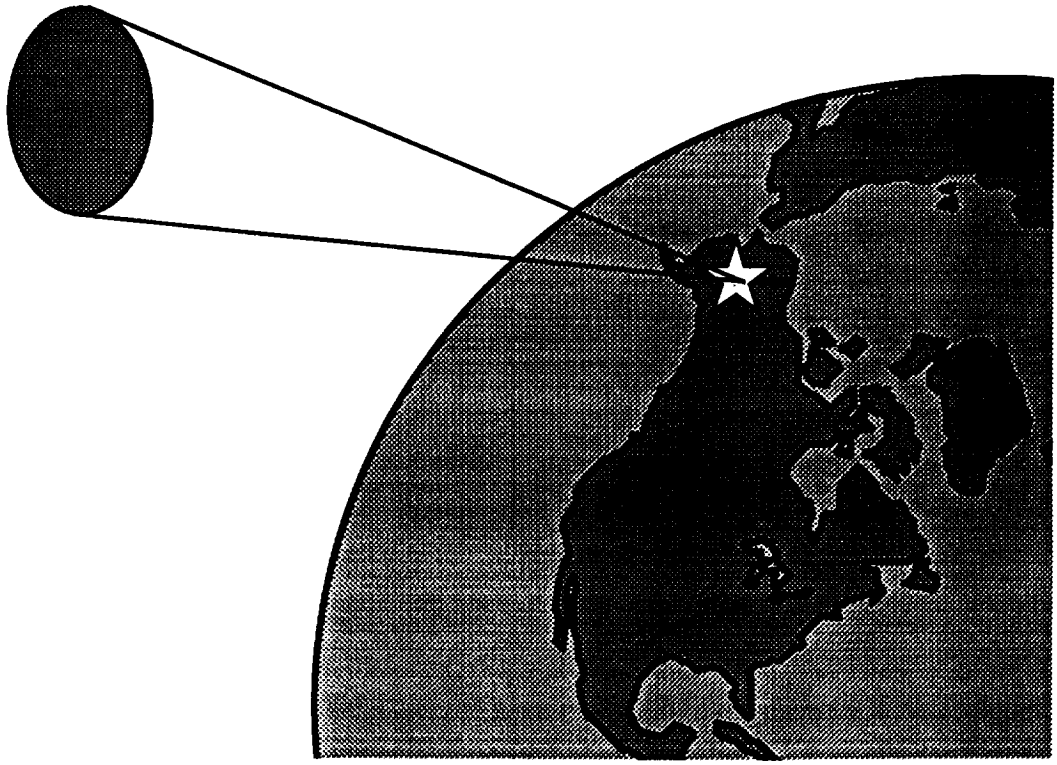

Chapter 1 References

[1] P.L. Haldane and B.W. Schupp, "Alaska '21: a terrestrial, point-to-point wireless power transmission system" in *Proceedings of the 1st Annual Wireless Power Transmission Conference*, 1993, pp. 191-198.

[2] W.C. Brown, "Design definition of a microwave power reception and conversion system for use on a high altitude powered platform," Raytheon Company, NASA CR 156866, 1980.

[3] M. Masse, "SHARP", Communications Canada, brochure, pp. 1-6.

[4] A. Fisher, "Secret of perpetual flight?: beam-power plane," *Popular Science*, pp. 62-107, Jan. 1988.

[5] Communications Research Center, "SHARP system characteristics," Ottawa, Canada, Nov. 1990, pp. 1-3.

[6] G. Jull and et. al., "SHARP (stationary high altitude relay platform): telecommunications and systems." in *IEEE Communications Society Global Telecommunications Conference*, pp. 955-959, Dec. 1985.

[7] J. DeLaurier and et. al., "Flying high with HALE: progress report," *Unmanned Systems*, vol. 5, no. 3, pp. 26-46, Winter 1987.

[8] NGL Consulting Ltd., "SHARP: supplementary information on the stationary high altitude relay platform (SHARP) system," Market Assessment Report, Sept. 1989.

[9] M. Rogers and K. Springen, "Can a plane fly forever?" *Newsweek*, pp. 42-47, Sept. 1987.

[10] ISU 1992, "Space solar power program; final report," International Space University, Kitakyushu, Japan, pp. 291-299, 1992.

[11] G. Landis, "A new space station power system," *Acta Astronautica*, vol. 17, no. 9, pp. 975-977, 1988.

[12] G. Arndt and E. Kerwin, "Applications of low-earth-orbit power transmission," *Space Power*, vol. 6, pp. 137-155, 1986.

[13] G.A. Landis, "Satellite eclipse power by laser illumination," *Acta Astronautica*, vol. 25, no. 4, pp. 229-233, 1991.

[14] P.E. Glaser, "Power from the sun; its future," *Science*, vol. 162, pp. 857-861, Nov. 1968.

[15] J.A. bamberger and E.P. Coomes, "Power beaming providing a space power infrastructure," *IEEE Aerospace and Electronic Systems*, vol. 7, no. 11, pp. 7-11, Nov. 1992.

[16] W.C. Brown, "A transportronic solution to the problem of interorbital transportation," Raytheon Company, Waltham, MA, NASA CR-PT-7452, July 1992.

[17] G.A. Landis and et. al., "Space transfer with ground based laser/electric propulsion," Sverdrup Technology and NASA Lewis Research Center, Cleveland, OH, NASA TM-106060, July 1992.

[18] G.A. Landis, "Space power by ground based laser illumination," in *Plasmadynamics & Lasers Conference*, 1992, AIAA-92-3024.

[19] S. Gill and et. al., "Laser power beaming systems for lunar surface applications," in *Proceedings of the IECEC '92*, 1992, pp. 2.289-2.292.

[20] E. Fay and R. Cull, "Lunar orbiting microwave power system," Sverdrup Technology and NASA Lewis Research Center, Cleveland, OH, NASA TM-103211, Aug. 1990.

[21] M. Stavens, "An analysis of power beaming for the moon and mars," in *Proceedings of the IECEC '92*, 1992, pp. 2.293-2.298.

[22] K. Long, "Analysis of a mars-stationary orbiting microwave power transmission system," NASA Lewis Research Center, Cleveland, OH, NASA TM-101344, July 1990.

[23] R. Cull and K. Faymon, "Orbit to surface beamed power for mars bases expansion, " in *Proceedings of the IECEC '89* , 1989, pp. 479-484.

[24] J. Christian, "Applicability of the beamed power concept to lunar rovers, construction, mining, explorers, and other mobile equipment," in *Second Beamed-Space Power Workshop*, 1989, pp. 343-356.

[25] W. Meador, "Laser-powered martian rover," in *Second Beamed-Space Power Workshop*, 1989, pp. 318-327.

[26] W.C. Brown, "Experiments involving a microwave beam to power and position a helicopter," *IEEE Trans. Aerospace Electronic Systems*, vol. AES-5, pp. 692-702, Sept. 1969.

[27] R.M. Dickinson and W.C. Brown, "Radiated microwave power transmission system efficiency measurements," Jet Propulsion Laboratory, California Institute of Technology, Pasadena, CA, Tech. Memorandum 33-727, May 1975.

[28] W.C. Brown, "Free-space microwave power transmission study, combined phase III and final report," Raytheon Company, Waltham, MA, Tech. Report No. PT-4601, NASA Contract No. NAS-8-25374, Sept. 1975.

[29] "Reception-conversion subsystem (RXCV) for microwave power transmission system, final report," Raytheon Company, Sudbury, MA, Tech. Report No. ER75-4386, JPL Contract No. 953968, NASA Contract No. NAS 7-100, Sept. 1975.

[30] R.M. Dickinson, "Evaluation of a microwave high-power reception-conversion array for wireless power transmission," Jet Propulsion Laboratory, California Institute of Technology, Pasadena, CA, Tech. Memorandum 33-741, Sept. 1975.

[31] R.M. Dickinson, "Performance of a high-power, 2.388 GHz receiving array in wireless power transmission over 1.54 km," in *1976 IEEE MTT-S International Microwave Symposium,* 1976, pp. 139-141.

[32] "Final Proc. of the Solar Power Satellite Program Review," Conf. Report 800491, Lincoln, NE, DOE/NASA Satellite Power System Concept Development and Evaluation Program, July, 1980.

[33] E.M Kerwin, D.J. Jezewski and G.D. Arndt, "Antenna optimization of single beam microwave systems for the solar power satellite," Space Solar Power Review, vol. 3, pp. 281-299, 1982.

[34] W.C. Brown and J. Triner, "Experimental thin-film, etched-circuit rectenna," *IEEE MTT-S Digest*, pp. 185-187, 1982.

[35] *The Proceedings of the Free-Space Power Transmission Workshop*, March 1988, NASA CP-10016.

[36] *The Proceedings of the Second Beamed Space-Power Workshop*, March 1989, NASA CP-3037.

[37] *Power Beaming Workshop Conference Proceeedings*, Battelle, Pacific Northwest Laboratory, May 1991.

[38] K. Schultz and et. al., "Ladar measurements of satellite vibration," in *Proceedings of the SPIE*, vol. 1633, Laser Radar VII, 1992, p. 172.

[39] "Space solar power program," Final Report of the International Space University, Kitakyushu, Japan, 1992.

[40] N. Kaya, H. Matsumoto, S. Miyatake, I. Kimura, M. Nagatomo and T. Obayashi, "Nonlinear interaction of strong microwave beam with the ionosphere MINEX rocket experiment," *Space Power*, vol. 6, pp. 181-186, 1986.

[41] N. Kaya, H. Matsumoto, H. Kojima, Y. Fujino and M. Fujita, "Test projects for microwave energy transmission," in *Proceedings of the 1st Wireless Power Transmission Conference*, 1993, pp. 245-253.

[42] *Proceedings of the 1st Annual Wireless Power Transmission Conference*, 1993.

Chapter 2 References

[1] J.D. Kraus, *Antennas*. 2nd ed. New York: McGraw-Hill, 1988, pp. 48-49.

[2] H. Matsumoto "Numerical estimation of SPS microwave impact on ionospheric environment," *Acta Astronautica*, vol. 9, no. 8, pp. 493-497, 1982.

[3] N. Kaya, H. Matsumoto, S. Miyatake, I. Kimura, M. Nagatomo and T. Obayashi, "Nonlinear interaction of strong microwave beam with the ionosphere MINIX rocket experiment," *Space Power*, vol. 6, pp. 181-186, 1986.

[4] H. Matsumoto and T. Kimura, "Nonlinear excitation of electron cyclotron waves by a monochromatic strong microwave, computer simulation analysis of the MINIX results," *Space Power*, vol. 6, pp. 187-191, 1986.

[5] W.E. Scharfman, W.C. Taylor and T. Morita, "Breakdown limitations on the transmission of microwave power through the atmosphere," *IEEE Transactions on Antennas and Propagation*, vol. AP-12, pp. 707-717, Nov. 1964.

[6] J.P. Quine, "Oversize Tubular Metallic Waveguides," in *Microwave Power Engineering*, vol. 1, E.C. Okress, Ed. New York: Academic Press, 1968, pp. 178-213.

[7] G. Goubau and F. Schwering, "Free Space Beam Transmission," in *Microwave Power Engineering*, vol. 1, E.C. Okress, Ed. New York: Academic Press, 1968, pp. 250-253.

[8] H. Weichel, *Laser Beam Propagation in the Atmosphere*, Bellingham, Washington: The International Society for Optical Engineering, 1990.

[9] R. K. Crane, *IEEE Transactions on Communications*, vol. COM-28, no. 9, pp. 1717-1732, Sept. 1980.

[10] L.J. Ippolito, "Propagation effects handbook for satellite systems design - a summary of propagation impairments on 10 to 100 GHz satellite links with techniques for system design," 4th ed., NASA Reference Publication 1082(04), 1989.

[11] R.L. Freeman, *Radio System Design for Telecommunications (1-100 GHz)*. New York: Wiley & Sons, 1987, p. 432.

[12] S.A. Hovanessian, "Microwave, millimeter-wave and electro-optical remote sensor systems," *Microwave Journal*, 1990 State of the Art Reference, pp. 109-129, 1990.

[13] W.C. Brown, "Electronic and mechanical improvement of the receiving terminal of a free-space microwave power transmission system," Raytheon Company, Wayland, MA, Tech. Report PT-4964, NASA Report No. CR-135194, NASA Contract No. NAS 3-19722, Aug. 1977.

[14] P. Koert and J.T. Cha, "Millimeter wave technology for space power beaming," IEEE Trans. Microwave Theory Tech., vol. 40, pp. 1251-1258, June 1992.

[15] National Radio Astronomy Observatory, "Very long baseline array project," Very Long Baseline Array Project Book, version 7, p. 5-9, Oct. 1988.

[16] T.W.R. East, "A self-steering array for the SHARP microwave-powered aircraft," *IEEE Trans. Antennas and Propagation*, vol. 40, pp. 1565-1567, Dec. 1992.

[17] Varian Microwave Power Tubes, Varian, Palo Alto, CA, pp. 19-20, Sept. 1989.

[18] T.A. Abele, D.A. Alsberg and P.T. Hutchinson, "A high-capacity digital communication system using TE_{01} transmission in circular waveguide," *IEEE Trans. Microwave Theory Tech.*, vol. MTT-23, pp. 326-333, April 1975.

[19] M. Thumm, V. Erckmann, W. Kasparek, H. Kumric, G.A. Muller, P.G. Schuller and R. Wilheim, "Very high power mm-wave components in oversized waveguides," *Microwave Journal*, pp. 103-121, Nov. 1986.

[20] D.M. Pozar, *Microwave Engineering*. Reading, MA: Addison-Wesley, 1990, pp. 200-201.

[21] N. Marcuvitz, *Waveguide Handbook*. London: Peter Peregrinus Ltd., 1986, p. 70.

[22] General Microwave, Pocket Guide to Non-Ionizing Radiation, General Microwave Corp., 1992.

[23] J. Coppola and D. Krautheimer, "Environmental monitoring for human safety part 1: compliance with ANSI standards," *RF Design*, pp. 41-45, March 1987.

[24] N.H. Steneck, H.J. Cook, A.J. Vander and G.L. Kane, "The origins of U.S. safety standards for microwave radiation," *Science*, vol. 208, pp. 1230-1237, June 1980.

[25] K.R. Foster and A.W. Guy, "The microwave problem," *Scientific American*, vol. 255, no. 3, pp. 32-39, 1986.

[26] J.D.G. Rather, "Project SELENE," in *Technology Workshop on Laser Beamed Power*, NASA Lewis Research Center, Feb. 1991.

[27] R.M. Dickinson, "The beamed power microwave transmitting antenna," *IEEE Trans. Microwave Theory Tech.*, vol. MTT-26, pp. 335-340, May 1978.

Chapter 3 References

[1] H. Weichel, *Laser Beam Propagation in the Atmosphere*, Bellingham, Washington: The International Society for Optical Engineering, 1990.

[2] G.A. Landis, "Receivers for laser power beaming," in *Space Photovoltaics Research and Technology Conference*, NASA Lewis Research Center, 1992.

[3] D.R. Ponikvar, "Independent assessment of laser power beaming options," in *Proc. SPIE*, vol. 1628, pp. 314-325, 1992.

[4] R.L. Lamb, "Free electron lasers for power beaming applications," presented at Power Beaming Workshop, Pasco, WA, 1991.

[5] J.M. Bozek. G.A. Landis, S.R. Oleson and M.A. Stavnes, "Comparison of selected laser beam power missions to conventionally powered mission," in *Proceedings of the 1st Annual Wireless Power Transmission Conference*, 1993, pp. 61-84.

[6] G.A. Landis, "Laser beamed power: satellite demonstrations applications," in *43rd Congress of the International Astronautical Federation*, Washington, DC, 1992.

[7] G.A. Landis, "The efficiency of photovoltaic cells exposed to pulsed laser light," in *11th Space Photovoltaic Research and Technology Conference*, NASA Lewis Research Center, Oct. 1992.

[8] G.A. Landis, "Photovoltaic receivers for laser beamed power in space," NASA Lewis Research Center, Dec. 1991.

[9] G.A. Landis, Intensity Curves, 1993.

[10] D.S. Abraham, B.E. Anspaugh, B.J Nesmith, P.A. Penzo and J.H. Smith, "A demonstration plan for laser-beamed power," Jet Propulsion Laboratory, California Institute of Tech., 1992.

[11] UDT Sensors, Optoelectronic Components Catalog, Hawthorne, CA, 1993.

[12] J.D.G. Rather, "Power beaming research at NASA," in *Proceedings of SPIE*, vol. 1628, pp. 276-298, 1992.

[13] D.P. Greenwood and C.A. Primmerman, "Adaptive optic research at Lincoln Laboratory," *Lincoln Laboratory Journal*, vol. 5, no. 1, pp. 3-22, Spring 1992.

[14] J.D.G. Rather, "Project SELENE," in *Technology Workshop on Laser Beamed Power*, NASA Lewis Research Center, Feb. 1991.

[15] R.R. Parenti, "Technology concept definition for a ground-based power-beaming system," *Lincoln Laboratory*, MIT, prepared for NASA under Air Force contract No. F19628-90-C-0002, 1992.

[16] US Army Corps of Engineers, "Final environmental impact statement of the proposed ground based free electron laser technology integration experiment, White Sands Missile Range, New Mexico," 1987.

Chapter 4 References

[1] W.J. Larson and J.R. Wertz, *Space Mission Analysis and Design*. 2nd ed. Torrance, CA: Microcosm, Inc., 1992, p.143.

[2] M.D. Griffin and J.R. French, *Space Vehicle Design*. Washington, DC: American Institute of Aeronautics and Astronautics, Inc., 1991, p. 117.

[3] D. Stodden, *PC SOAP* (software), Computer Graphics Sys. Dept., The Aerospace Corp., El Segundo, CA, 1990.

[4] Orbital Sciences Corp, *Pegasus Payload Users Guide*, Release 2.00, OSC Fairfax,VA, May 1991.

Chapter 5 References

[1] G.J. Friese and et. al., "Initial 1980's development of inflated antennas, final report," L'Garde Inc., Newport Beach, CA, NASA-CR-166060, Jan. 1983.

[2] ISU 1992, "Space solar power program; final report," International Space University, Kitakyushu, Japan, 1992, pp 291-299.

[3] Personal Correspondence with C. Cassapakis, L'Garde Inc., April 28, 1993.

[4] W.F. Hinson and L.S. Keafer, "Large inflated-antenna system," *In Step Experiment Requirements*, 1984, pp. 311-324.

[5] M. Thomas and G. Veal, "Highly accurate inflatable reflectors," L'Garde Inc., Newport Beach, CA, AFRPL TR-84-021, May 1984.

[6] J.D. Kraus, *Antennas*. 2nd ed. New York: McGraw-Hill, 1988, p. 569.

[7] M. Thomas, "Inflatable space structures," *IEEE Potentials*, pp. 29-32, Dec. 1992.

[8] M. Thomas and G. Williams, "Advances in large inflatable reflectors", in *Earth Science Geostationary Platform Technology*, NASA Conference Publication 3040, 1988, pp. 137-151.

[9] C.C. Osgood, *Spacecraft Structure.* Englewood Cliffs, NJ: Prentice-Hall, Inc. 1966.

[10] T.A. Wells, *Wells Manual of Aircraft Materials and Manufacturing Processes*: New York: Harper and Brothers, 1942.

[11] W.J. Larson and J.R. Wertz, *Space Mission Analysis and Design.* 2nd ed. Torrance, CA: Microcosm, Inc 1992.

[12] Orbital Sciences Corporation, *Pegasus Payload User's Guide*, Orbital Sciences Corp., Fairfax, VA , 1991.

[13] M.L. James, Smith, Worlford, and Whaley, *Vibrations of Mechanical and Structural Systems - With Microcomputer Applications.* New York: Harper & Row, Inc., 1989.

[14] M.D. Griffen and J.R. French, *Space Vehicle Design.* J.S. Przemieniecki, Ed., 3rd ed. Washington D.C.: AIAA, 1991, p. 404.

[15] SAFT, SAFT Space Department, DOC.N 12.90-1614.2, Pub. Communications Department.

[16] Schmidt and La Vean Editors, *Communication Satellite Development Technology*, AIAA and MIT Press, 1976.

[17] T. Yunck, *GPS.* Washington D.C.: AIAA, 1993 (to be published).

[18] W. Stallings, *Data and Computer Communications.* 3rd ed. New York: MacMillan, 1991.

[19] G.P. White, "Description of the NOAA/NEDSIS command and aquisition station Fairbanks, Alaska," U.S. Department of Ccommerce, National Oceanic and Atmospheric Administration, National Environmental Satellite Data and Information Service, Nov. 1987.

[20] D.J. Zillig, *Performance and Design Requirements and Specifications for the Second Generation TDRSS User Transponder.* NASA Goddard Space Flight Center, Greebelt, MD, Sept. 1987.

[21] W.L. Flock, *Propagation Effects on Satellite Systems at Frequencies Below 10 GHz.* NASA Reference Publication 1108, Dec. 1983.

[22] L.J. Segerlind, *Finite Element Analysis*, 2nd ed. New York: McGraw Hill, 1984.

[23] G. C. Messenger and M. S. Ash, *The Effects of Radiation on Electronic Systems.* New York: Van Nostrand Reinhold Company Inc., 1986.

Chapter 6 References

[1] H. Campbell and M.L. Newton, *Satellite Cost Model*, (software), The Aerospace Engineering Group, El Segundo, CA, 1990.

[2] Orbital Sciences Corp, *Pegasus Payload Users Manual.* OSC Fairfax, VA,1991.

[3] W.J. Larson and J.R. Wertz, *Space Mission Analysis and Design.* 2nd ed. Torrance, CA: Microcosm, Inc., 1992.

Appendix A - Project Personnel

Professor Joseph G. Hawkins - Director

Brian Chouinard - Project Manager, Teaching Assistant

Principal Investigation Team
Leader: James McSpadden
Sami Khouli
Eric Ruse
Christina M. Yearous
Tomas Zietlow

Mission Analysis Team
Leader: Mark Parrott
Jeffrey Alexander
Randy Meitner

Electrical Systems Design Team
Leader: Clifford L. Murray
Tom Clark
Millicent Jones
Monty Lawler
Richard T. Reimers
Kanwaljeet Singh

Mechanical Systems Design Team
Leader: R. Rajesh
Ted Hethcote
Shawn Houston
Afsar Khan
Jiong Shao

Appendix B - Glossary

AC	Attitude and Control
ADC	Atitude Determination and Control
A/S	Anti-Spoofing
BIT	Built-In Test
BOL	Beginning of Life
CCA	Circuit Card Assembly
CCIR	The International Radio Consultative Committee
CDH	Command and Data Handling
CER	Cost Estimation Relations
CG	Center of Gravity
CPU	Central Processing Unit
CW	Continuous Wave
DC	Direct Current
DOD	Depth of Discharge
EDAC	Error Detection and Correction
F/D	Focal length to Diameter ratio
FEL	Free Electron Laser
GaAs	Gallium Arsenide
GEO	Geosynchronous Orbit
GPS	Global Position System
HAPS	Hydrazine Auxiliary Propulsion System
IL-FEL	Induction Linac Free Electron Laser
ISM	Industrial Scientific and Medical
ISAS	Institute of Space and Aeronautical Science (Japan)
JPL	Jet Propulsion Laboratory
LACE	Low Power Atmospheric Compensation
LEO	Low Earth Orbit
LPB	Laser Power Beaming
METS	Microwave Energy Transmission in Space
MINEX	Microwave-Ionosphere Non-linear Interaction Experiment
MSIS	Mass Spectrometer Incoherent Scatter
NiCd	Nickel Cadmium
NiH_2	Nickel Hydrogen
NOAA	National Oceanic and Atmosphere Administration
NRZ-PSK	Not-Return-to-Zero Phase Shift Key
OTV	Orbit Transfer Vehicle
PAMELA	Phased Array Mirror, Expandable Large Aperture
PI	Principle Investigation
PMAD	Power Management and Distribution
RF-FEL	Radio Frequency Free Electron Laser
SEU	Single Event Upset
SHARP	Stationary High Altitude Relay Platform
Si	Silicon
SPRAT	Space Photovoltaic Research and Technology

SPS	Solar Power Satellite
SPS	Standard Positioning Service
STDN	Spacecraft Telemetry and Data Network
T&C	Telemetry and Command
TDRSS	Tracking and Data Relay Satellite System
TTC	Telemetry, Tracking and Control
TWT	Traveling-Wave Tube
TWTA	Traveling-Wave Tube Amplifier
VLBA	Very Long Baseline Array
WISPER	Wireless Space Power Experiment
WPT	Wireless Power Transmission

Appendix C - Ion Thrusters

While the concept of ion thruster propulsion has been around for decades, they have seen limited demonstrations in space. The principle behind the operation of the ion engine is relatively simple. In order to produce thrust, the engine uses an electric field to accelerate charged particles so that they exit the thruster at a high velocity. The reaction of the ion acceleration results in a thrust of the spacecraft in the opposite direction.

Figure 1 shows a cutaway diagram of a 30 cm laboratory model ring-cusp ion thruster [1]. The power systems required to operate this particular thruster are indicated in Figure 2 [2]. Since this 30 cm thruster seems to hold the most promise for future applications, and its design is relatively typical of the number of other thrusters presently developed, it specifically will be examined in detail.

This ion thruster incorporates a segmented-anode geometry consisting of aluminum and mild steel layers 0.76 mm thick. The xenon gas plenums are situated symmetrically around the back side of the anode to allow for an evenly injected propellant flow. Samarium-cobalt permanent magnets are used to create a cusped magnetic field boundary in the discharge chamber. The magnets are arranged in rings of alternating polarity along the steel chamber walls with the return flux carried by the steel. Conventional hollow cathodes are used in the discharge and neutralizer cathodes. The cathode tube consists of a molybdenum-rhenium alloy with a thoriated tungsten orifice plate. The orifice diameters for the discharge and neutralizer cathodes are 1.52 mm and 0.51 mm respectively. Porous tungsten inserts, impregnated with a low work function compound, are used as the emitters. The electrodes have a nominal thickness of 0.36 mm, with 1.91 mm and 1.14 mm diameter screen and accelerator apertures, and open-area-fractions of 0.67 and 0.24 [1].

Ion thrusters operate by ionizing a gas, commonly argon or xenon, and accelerating these ions through an electrical potential created by the accelerating grid. The performance advantage of the ion thrusters results from the high velocity with which they are capable of exhausting the propellant. This advantage is demonstrated by two simple equations which describe space propulsion [3]

$$N = \frac{dv}{dt} v \tag{1}$$

$$P_p = \frac{1}{2} \frac{dm}{dt} v^2 \tag{2}$$

where N is the thrust (N), m is the propellant mass (kg), d/dt is the time rate of propellant flow (kg/s), v is the propellant velocity (m/s) and P_p is the propulsion power (W).

Equation 1 indicates that the propellant consumption for a given level of thrust can be

reduced if the terminal velocity of the propellant is increased. With conventional chemical propellants, upper limit to the exhaust velocity exists. The highest practical velocity is developed with a mixture of oxygen and hydrogen, which is approximately 4000 m/s.

With the ion thrusters, higher propellant exhaust velocities can be reached over chemical propellants. Converting 10 kW of DC input power into 7 kW of ion beam power, the 30 cm described earlier has been tested to propel xenon ions at a velocity of 42,000 m/s, approximately 10.5 times faster than chemical propulsion. Consequently, the time rate of propellant consumption for the same propulsive force is reduced by the same factor of 10.5. Similarly for the same output power the time rate of propellant flow for the ion thruster using xenon gas is only 0.91% of that required by a conventional chemical engine.

In terms of the economical benefit available through electrical propulsion, a satellite transfer from low earth orbit to geostationary orbit and back can be analyzed. To accomplish this maneuver, a propulsive force must be applied to the vehicle to change its velocity by an amount known as ΔV. The one way ΔV associated with this orbital change is 4600 m/s, and for a round trip ΔV is 9200 m/s. The relationship between the velocity to which the propellant is accelerated, the change in velocity that the vehicle must undergo to complete the trip, and the ratio of the initial mass (propellant mass plus terminal mass) to the terminal mass is described by the expression [3]

$$\frac{M_i}{M_t} = e^{\frac{\Delta V}{v}} \tag{3}$$

where M_t is the terminal mass after trip completion (kg), M_i is the initial mass (M_t plus propellant mass, kg), ΔV is the required change in velocity (m/s) and v is the propellant velocity (m/s).

Applying this equation to a traditional chemical propulsion system with a propellant velocity of 4000 m/s and a ΔV of 9200 m/s, the ratio of initial mass to final mass is approximately 10. But when this same equation is applied to the xenon fueled ion thruster with its propellant velocity of 40,000 m/s, this ratio drops to 1.26. Accordingly, the amount of propellant required for the chemical system is 35 times greater than that required by the electric system.

To get an economically quantitative picture of this situation, assume that the terminal mass of the satellite and its payload is 10,000 kg. With a chemical propulsion system, the amount of propellant required for this orbital change would be 90,000 kg. The cost of transporting a chemical system's propellant from earth to LEO at the going rate of $5000/kg would be $450 million. By contrast, the transportation cost of the xenon propellant for the ion thruster system would only be $13 million, providing a savings of $437 million [3].

A number of presently operational ion thruster designs were considered for implementation on the WISPER satellite. Unfortunately, no systems were found to be suitable for the limited station keeping of this satellite. Instead, conventional hydrazine thrusters will be used for the minimal orbital maintenance.

The present systems are designed for the station keeping of large communication satellites or for complete orbital reboosting. A list of some of the more prominent ion thruster designs are briefly described below.

MELCO, IES, IPS: Expanding on the ion thruster results from Japan's Third Engineering Test Satellite (ETS-III), their National Space Development Agency (NASDA) has developed a 12 cm diameter xenon Ion Engine System (IES) with the cooperation of both the Mitsubishi Electric Corporation and Toshiba [4]. The IES is scheduled to perform the NSSK functions for the ETS-VI [5]. This ion thruster system is also proposed for the Ion Propulsion System (IPS) of INTELSAT VII [6].

RIT 10/15: The European Space Agency (ESA) has sponsored electric propulsion development resulting in two different xenon ion propulsion systems [7], [8]. Both systems use ion thrusters which are 10 cm in diameter. One known as the Radio Frequency Ion Thruster Assembly (RITA), has been selected as a flight experiment on the European Retrievable Carrier (EURECA-I) and proposed as an operational system for ESA's advanced communications technology satellite (SAT-2) [9]. The RIT ion thrusters is manufactured by Messerschmitt Bolkow Blohm and has an unique design by employing radio frequency power to ionize the xenon molecules.

UK 10/T5: ESA's other electrical propulsion system is designated the UK-10 Ion Propulsion System and has also been proposed for SAT-2 [8], [10]. The difference in this system is that the xenon ions are generated conventionally with a direct current discharge.

HRL, XIPS: Hughs Research Laboratories (HRL) has developed and endurance tested a working model Xenon Ion Propulsion Subsystem (XIPS) for the NSSK of large geosynchronous communication satellites. The ion thrusters for this subsystem are 25 cm in diameter. HRL has also proposed a propulsion system applying similar technology which utilizes a 13 cm diameter thruster [11]-[13].

DERATED 30 cm ION THRUSTER: NASA has tested the performance characteristics of this thruster which is operated at highly throttled conditions, appropriate for NSSK functions. The laboratory model has a mass of 10.7 kg, but based on preliminary testing, it is anticipated that this can be reduced to 7.0 kg through a structural redesign. For this thruster, and generally typical of the others, the propellant distribution system includes one low pressure propellant line flowing to a pair of latching valves at the thruster as shown in Figure 3 [2]. The line splits into three lines with each ending in a flow limiting impedance. The mass of the propellant distribution (MPD) hardware is estimated to be 7.3 kg. This particular system seems to exhibit the most promise for future development and smaller scale applications [1], [2].

Table 1 lists some of the nominal design and performance parameters and Table 2 lists the operating conditions for each of the thruster systems described [2].

Table 1. Design and performance parameters for several thrusters.

Thruster	Design Parameter		Performance Parameter		
	Bead Diameter (cm)	Mass (kg)	Input Power (W)	Thrust (mN)	Specific Impulse
MELCO	12.0	3.7	620	23.3	2906
UK 10/T5	10.0	1.0	644	25	3051
RIT 10	8.5	1.5	460	15	3435
RIT 15	13.5	2.5	680	20	3575
HRL	13.0	5.0	427	17.7	2718
DERATED	28.2	10.7	644	30	2285
DERATED	28.2	10.7	451	21	1961

Table 2. Operating parameters for several thrusters.

Thruster	Operating Parameter				
	Discharge Voltage (V)	Accelerated Voltage (V)	Beam Voltage (V)	Screen Grid Ion Trans.	Discharge Propellant Efficiency
MELCO	37.0	496	1000	0.8	0.81
UK 10/T5	47.0	800	1021	0.8	0.86
RIT 10	a	b	1500	b	b
RIT 15	a	b	1500	b	b
HRL	28.0	b	b	b	b
DERATED	27.9	141	556	0.8	0.84
DERATED	28.7	120	486	0.8	0.83

[a]Not applicable with RF discharge
[b]Data not available

Presently the power requirements of ion propulsion systems have limited their application to testing labs and large high power producing satellites. With the advent of successful and efficient power beaming systems, the emergence of electrical propulsion seems inevitable as an extremely cost effective replacement of the traditional chemical engines. Because of their economic advantage, electrical propulsion systems will play a dominant role as a motivational factor in the further commercial development of both microwave and laser power beaming.

REFERENCES

[1] M.J. Patterson and J.E. Foster, "Performance and optimization of a "derated" ion thruster for auxiliary propulsion," 27th Joint Propulsion Meeting, Sacramento, CA, NASA Technical Memorandum 105144, AIAA-91-2350, June 1991.

[2] V.K. Rawling and G.A. Majcher, "Mass comparisons of electric propulsion systems for NSSK of geosynchronous spacecraft," 27th Joint Propulsion Meeting, Sacramento, CA, NASA Technical Memorandum 105153, AIAA-91-2347, June 1991.

[3] W.C. Brown, "Beamed microwave power transmission and its application to space," *IEEE Trans. Microwave Theory and Techniques*, vol. 40. no. 6, pp. 1239-1249, June 1992.

[4] S. Kitamura, "ETS-III ion engine flight operations in the extended mission period," *J. Propulsion Power*, vol. 2, no. 6, pp. 513-520, Nov.-Dec. 1986.

[5] S. Shimada, "Ion engine system development of ETS-VI," AIAA Paper 89-2267, July 1989.

[6] M.L. Day, "INTELSAT VII ion propulsion subsystem implementation study," AIAA Paper 90-2550, July 1990.

[7] H. Bassner, "The design of RITA electric propulsion system for SAT 2," AIAA Paper 90-2539, July 1990.

[8] P. Smith, "Design and development of the UK-10 ion propulsion subsystem," in *20th International Electrical Propulsion Conference*, DGLR, AIAA Paper 88-2911, Oct. 1988.

[9] H. Bassner, C. Bartoli and A. Trippi, "Status of the RITA-experiment on EURECA," in *20th International Electrical Propulsion Conference*, DGLR, 1988.

[10] D.G. Fearn, "The proposed demonstration of the UK-10 ion propulsion system on ESA's SAT-2 spacecraft," in *20th International Electrical Propulsion Conference*, DGLR, 1988.

[11] J.R. Beattie, J.N. Matossian, and R.R. Robson, "Status of xenon ion propulsion technology," *J. Propulsion Power*, vol. 6, no. 2, pp. 145-150, Mar.-Apr. 1990.

[12] J.R. Beattie, "Xenon ion propulsion systems," AIAA Paper 85-2021, Sept. 1985.

[13] J.R. Beattie and J.P. Penn, "Electric propulsion - a national capability," AIAA Paper 89-2490, July 1989.

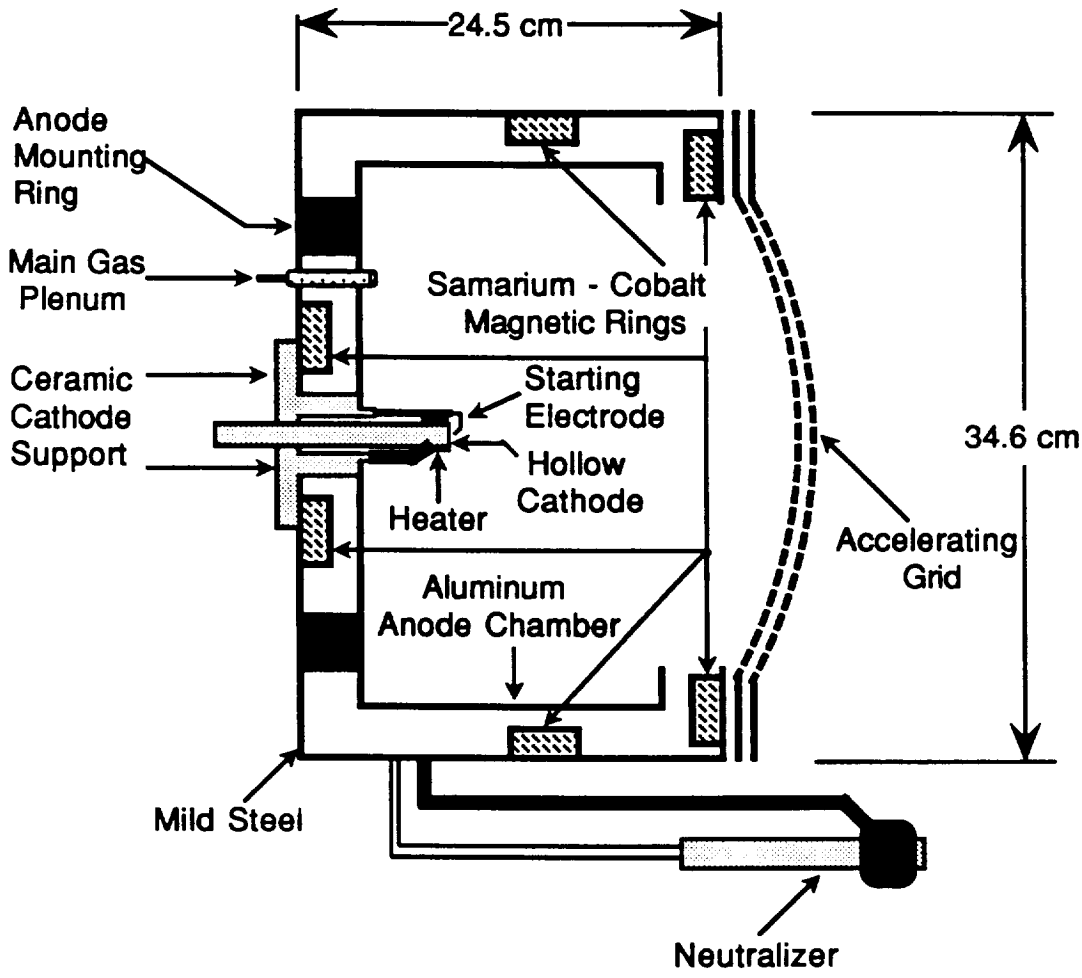

Figure 1. Cutaway drawing of a 30 cm ion thruster.

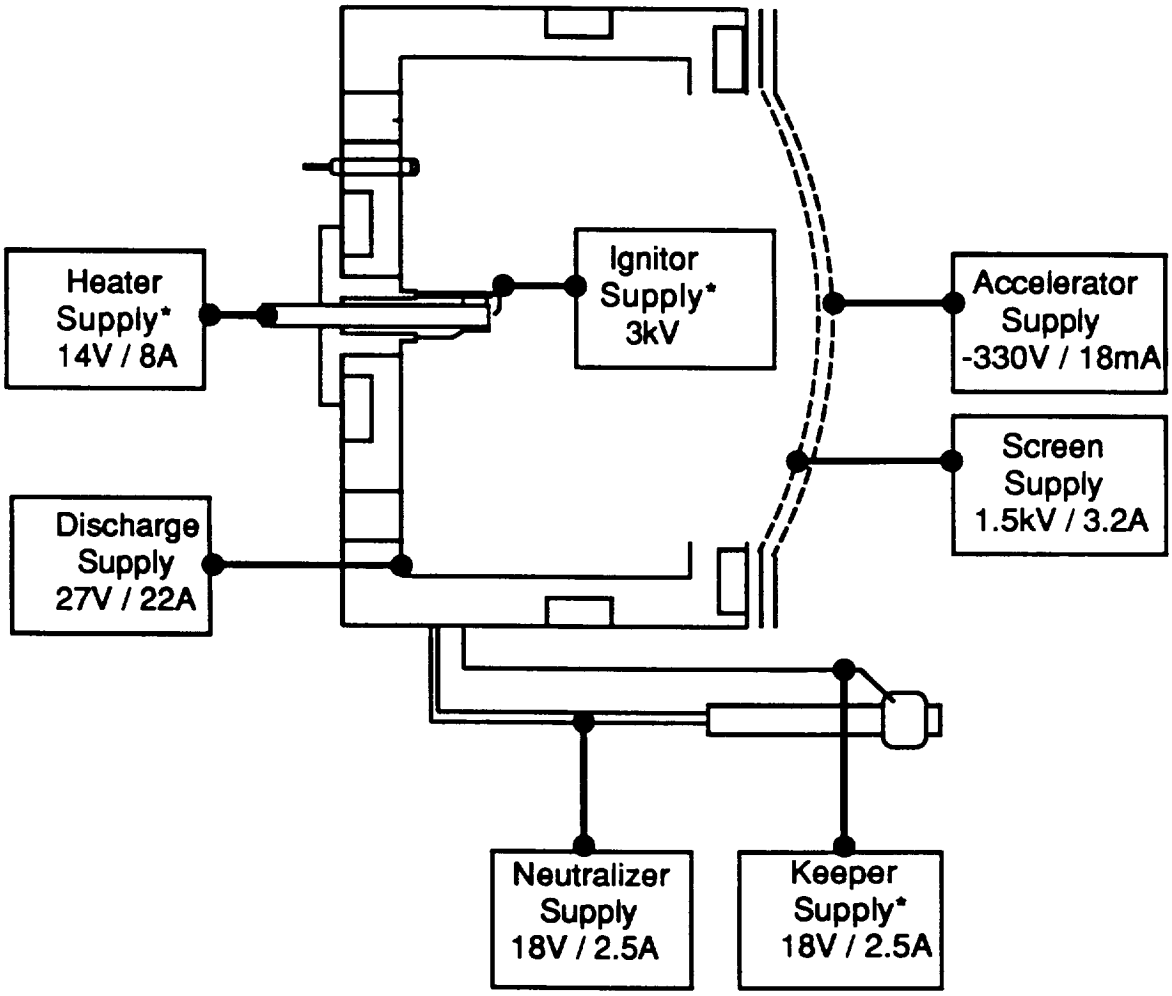

* Power supplies used on start-up only

Figure 2. Electrical block schematic for 30 cm ion thruster power system.

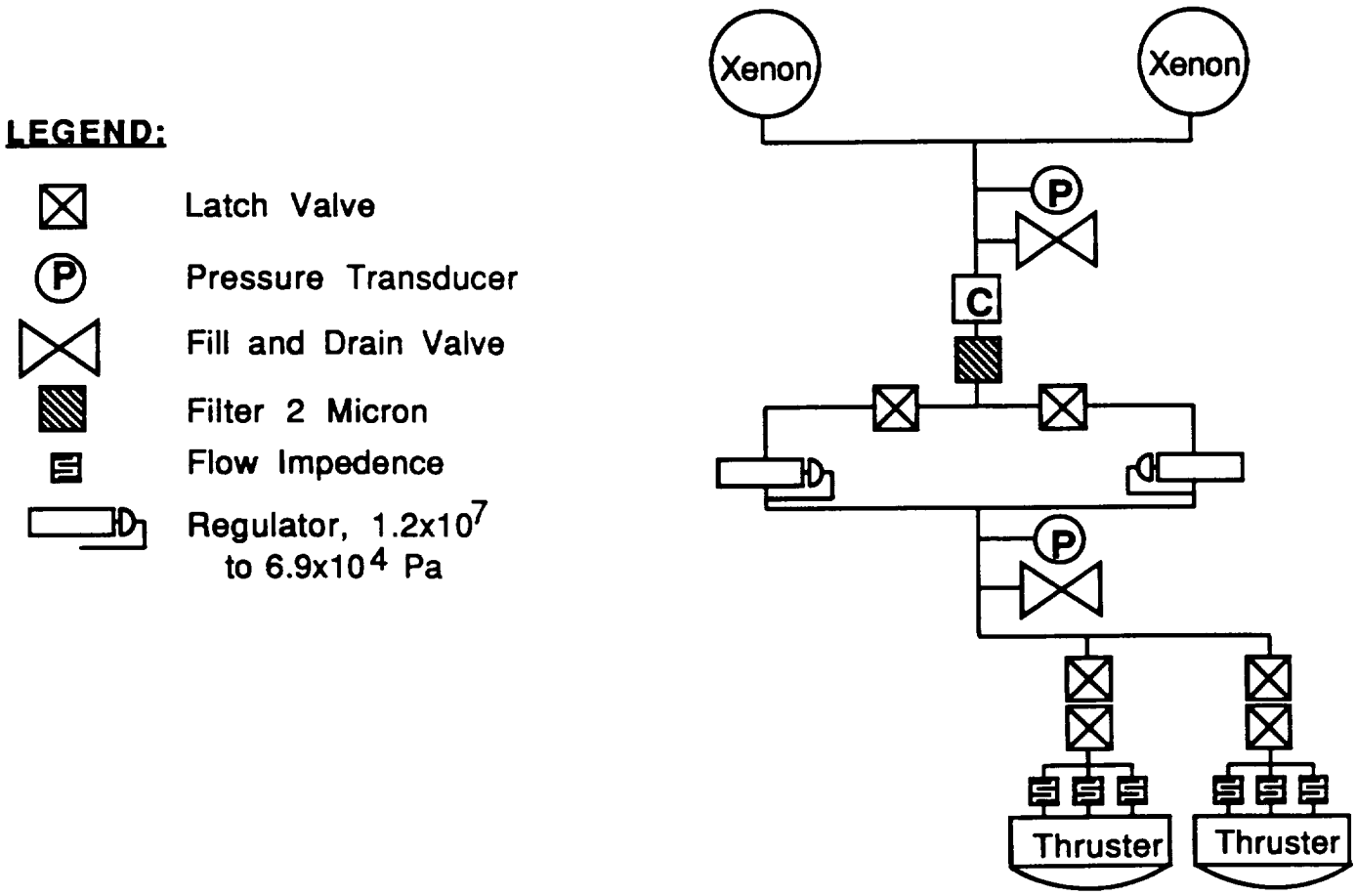

Figure 3. Propellant tankage and distribution system.

Appendix D - GPS Specifications

This appendix provides the system and interface specification for a packaged, 5-channel, standard positioning service (SPS) GPS receiver for use on low earth orbiting (LEO) satellites [1].

The GPS receiver is a multi-channel receiver that acquires and tracks five GPS signals from any number of GPS satellites seen within the receiver's antenna field of view. It continuously tracks four primary satellites on four channels and sequentially acquires and tracks all other visible and healthy satellites on the fifth channel. The four primary satellites are selected to provide minimum geometric dilution of precision (GDOP) to achieve a high navigation accuracy.

A block diagram of the receiver is shown in Figure 1. It consists of a receiver board with radio frequency (RF) and digital sections and a power supply board.

The RF section contains an RF and intermediate frequency (IF) translator implementing GaAs monolithic microwave integrated circuitry (MMIC). A temperature controlled crystal oscillator (TCXO) frequency reference is also included.

The digital section computes the receiver's position. Custom application specific integrated circuitry (ASIC) performs simultaneously the digital signal processing of five GPS signals. Rockwell's advanced architecture microprocessor (AAMP) implements the GPS measurements, navigation, and interface processing. Radiation hardened memory stores program instructions and temporary data. System recovery upset logic recovers single event upsets due to cosmic rays. Host vehicle interface circuitry is also included. The power supply board converts 28±6 VDC to regulated +5 VDC and -5 VDC.

The GPS receiver interfaces with the host vehicle for RF input, DC power input, and transfer of binary serial data. A host vehicle interface block diagram is shown in Figure 2. The serial data interface is accomplished through a 25-pin, D-type connector.

The RF input signal characteristics are summarized in Table 1. The input carrier frequencies are 1575.42 MHz for L1 and 1227.6 MHz for L2. The GPS signal bandwidth is 20.46 MHz.

Table 1. RF input signal characteristics.

RF Input Signal Levels (Signal and Noise)		VSWR	Impedance
Normal Operation	Survivability		
-101 to -46 dBm	+13 dBm CW	2.0:1	50 ohms

Assuming a 0 dBi antenna gain and 1.0 dB cable loss, the available carrier-to-noise (C/N_0) ratio at the receiver input, including a 4 dB margin, is shown in Table 2.

Table 2. Link Budget.

GPS Signal	Minimum Carrier Power at 0 dBi Antenna (dB-W)	Estimated Noise Spectral Density N_O (dB-W/Hz)	Availability C/N_O (dB-Hz)	Required C/N_O at Receiver Input (dB-Hz)	Link Margin (dB)
L1-C/A	-160	-200	40	36	4
L1-P	-163	-200	37	33	4
L2-P	-166	-200	34	30	4

The power input lines consists of a +28 VDC and ground lines. The total power consumption is less than 6.0 W. The input voltage range is 22 to 34 VDC. The receiver can recover from any surge overvoltage up to 70 VDC for a 10 ms period or up to 43 VDC for an indefinite period of time. The receiver can recover from any undervoltage down to 0 VDC.

The serial data interface port (IP) is electrically compatible with a RS232C serial data interface that provides asynchronous, bi-directional transfer of 16-bit data words as two 8-bit data bytes. The IP characteristics are:

Communication Parameters:
- 9600 baud
- Odd parity
- 8 data bits
- 1 start bit
- 1 stop bit

Signal Characteristics:
- 1 transmit signal
- 1 receive signal
- 1 ground signal
- 1 timemark signal

Electrical Characteristics:
- Compatible with RS232C driver signals
- Timemark frequency: 1 Hz nominal
- Timemark pulse width: 20 microseconds, active high

Commands and telemetry data between the receiver and the host vehicle are communicated over the IP in the form of individual messages of varying word length. Each message has a unique message identifier number and parameter set associated with it.

The GPS receiver will provide position, velocity and time (PVT) data at a 1 Hz rate. The accuracy will be as follows:

Position: < 15 m, spherical error probable (SEP)*
76 to 100 m SEP**

Velocity: < 0.08 m/s root mean square (rms) per axis*
< 0.5 m/s rms per axis**

Time: < 100 ns (1 sigma)*
< 1000 ns (1 sigma)**

* Select availability/anti-spoofing (SA/AS) not active
** Estimated values when SA/AS is active

REFERENCE

[1] "5 channel standard positioning system manual," Rockwell International, Autonetics Strategic Systems Division, Anaheim, CA, 1992.

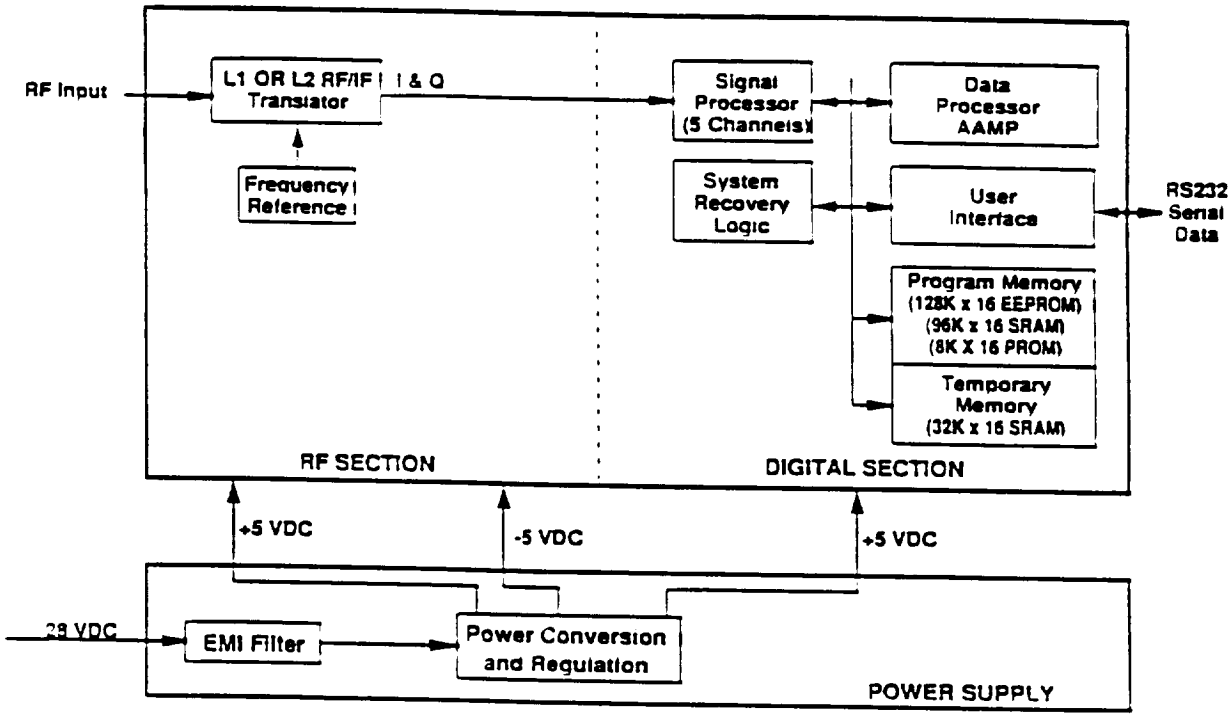

Figure 1. GPS receiver block diagram.

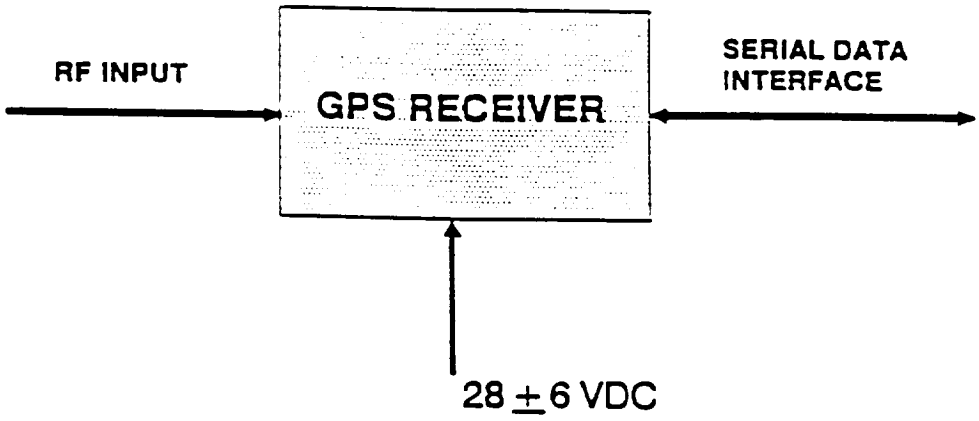

Figure 2. GPS receiver interface block diagram.

Appendix E - Mission Statement

The 1993 Advanced Design Project at UAF is to design a spacecraft as a technology demonstration of wireless power transmission (WPT). The objective is to devise a cost effective demonstration of WPT that will utilize existing technology in the present and near term.

Power beaming is not a new concept. Experimental work and major design and study efforts have continued since the 1960's. With the latest advances in transmitter and receiver technology, the next natural step is to beam power from earth to space. This flight demonstration will help to advance the science of power beaming and prove the viability of various applications of wireless power in space. The primary mission of this project is to demonstrate earth to space beamed power.

Two methods of power beaming will be examined: microwave and laser. Microwave power transmission is the state-of-the-art of advanced WPT technology. Laser power transmission is near term technology. In addition to demonstrating WPT, the mission will investigate the theory and models of high power microwave and laser transmission through the atmosphere.

There is considerable interest in WPT for space applications. By demonstrating power beaming from earth to space, the mission will provide the next step to future space applications. The design difficulties and tradeoffs analyzed within this study will lay the foundation for the understanding of WPT on a larger scale. Although the project is both conceptual and academic, a cost effective design which achieves the mission is the ultimate goal.

Appendix F - Mission Constraints

Mission constraints, along with the mission statement, are the drivers of the design. The constraints consist primarily of cost, schedule and availability of technology.

Cost is a fundamental limitation of most space missions. This is especially true during times of limited funds and program cut-backs. This primary constraint is one of the most limiting to the design. It is highly desirable to accomplish the demonstration as a microsatellite platform. This significantly reduces the investment necessary without compromising the mission. The financial budget should be within the guidelines for the NASA Small Explorer or University Explorer programs, 35 million dollars including launch costs and 60-80 million including launch costs, respectively.

The second constraint is schedule. To further promote WPT technology, a demonstration is needed. The two types of power beaming proposed are microwave and laser. All of the required technology for a microwave demonstration is readily available. No major component or systems development is required. The laser technology is near term. Within the next three years all systems will be available assuming continued funding. The project should begin immediately to ensure a 1997 launch. To prove the functionality of WPT and allow adequate experiment time, a mission life after launch is a minimum of two years. Another time constraint is the duration of the study. All analysis of mission options and design will be completed within one semester.

The third constraint involves technological availability. Since the primary mission is a demonstration, a high probability of success is required. Part of the demonstration is to show that WPT is feasible for space applications. Therefore, new technologies will only be considered when essential to the mission.

Other constraints include safety to personnel and environment, international law regarding allocation of frequencies and space debris, and level of NASA and international support and interest. An integral part of the mission is to examine the safety and environmental issues involved with beamed power. Safety of the employees at the transmitting site as well as residents around the facility will not be compromised. The impact of high power microwaves and lasers on the surrounding area of transmitting sites and on the atmosphere will be explored.

Appendix G - Manufacturer Sheets

VLBA 25 m Transmitting Antenna	Radiation Systems, Inc.
Monopulse Receiver, Model 133	Radiation Systems, Inc.
Ku-Band TWTA Beacon	Hughes Electron Dynamics Division
FS386	Fairchild Space
TDRSS Transponder	Motorola

Model 3250

Radiation Systems, Inc.

Universal Antennas Division

Very Long Baseline Array Antenna Radio Telescope

The Model 3250 25-meter elevation-over-azimuth antenna is designed for use by the scientific community as an astronomical instrument for radio telescope applications. Among the applications is the measurement of continental drift, observation of and the study of stars and assistance in determining the size and age of the universe and distant galaxies.

This highly-precisioned antenna is designed to provide full sky coverage with the elevation-driven bull gear and counterweights and the wheel and track concept to allow ±270 degrees travel in azimuth.

The main reflector employs 200 precisely manufactured AccuShape[1] aluminum panels which are field interchangeable in each tier. The panels are precision aligned using the adjustable panel support studs to achieve a main reflector surface accuracy of .018 inches rms.

The simplified steel structure design provides an ease of manufacturing benefit while offering a high stiffness to weight ratio. In addition, the utilization of standard, proven performance, state-of-the-art mechanical specialty hardware results in minimum use of heavy duty installation equipment during the erection and testing phase.

The structure is supplied with ample platforms and stairways to afford the customer ease of maintenance and ability to perform routine inspection of critical components.

The concrete tower/foundation design criteria is provided.

For antenna control, Universal Antennas offers a proven performance servo subsystem and encoder data package that have superior performance characteristics.

[1]AccuShape is a precision metal contouring process proprietary to Radiation Systems, Inc.

FEATURES:

- 25-meter solid surface reflector assembly
- Antenna subsystem design compatible with multiple feed systems
- Elevation-over-azimuth wheel and track pedestal assembly providing 0 to 125 degrees elevation coverage and ±270 degrees azimuth coverage
- Simplified steel structure design which provides ease of manufacture and a high stiffness to weight ratio
- Utilizes standard state-of-the-art mechanical specialty hardware

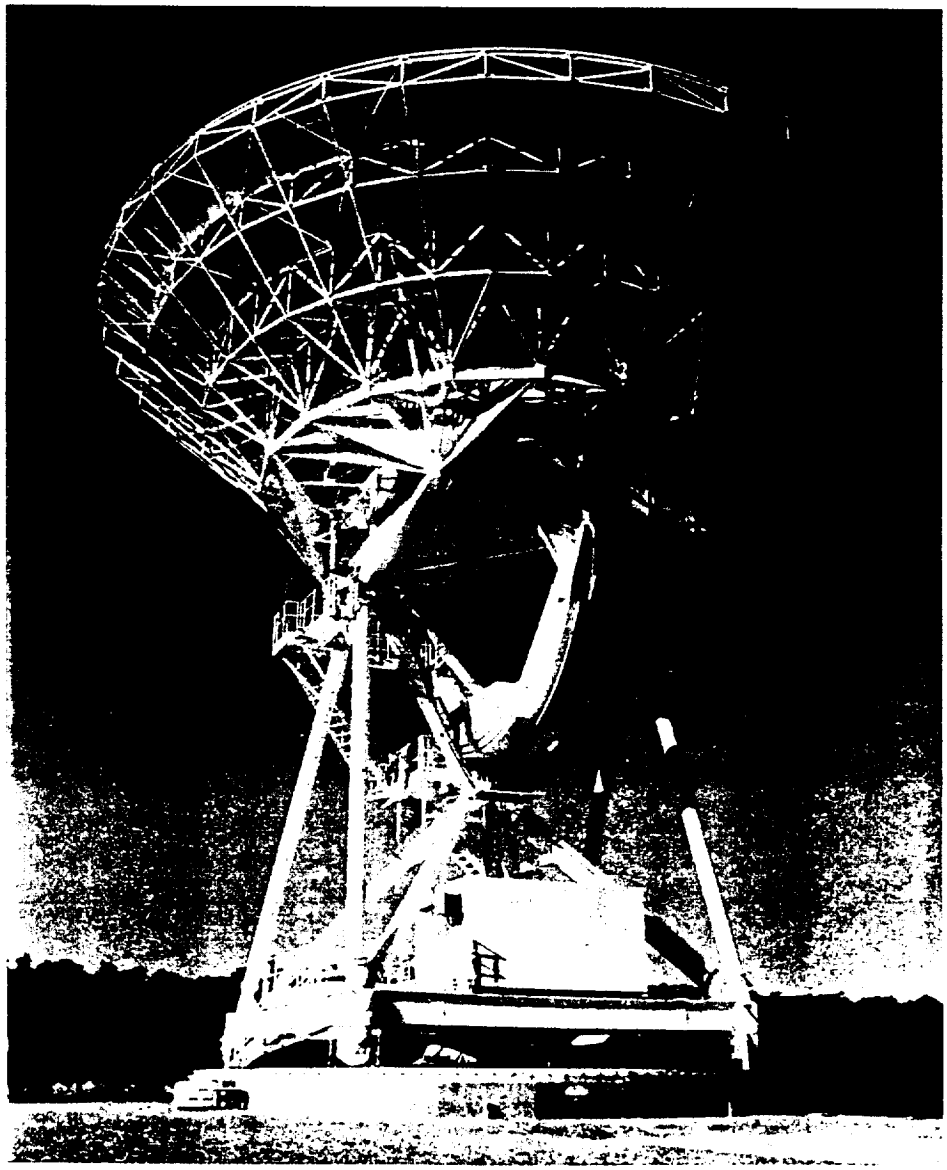

Radiation Systems, Inc.
Universal Antennas Division

900 Alpha Drive, Richardson, Texas 75081
Telephone (214) 690-8865 • Telex 79-1564 • Fax (214) 644-6322

Specifications — Model 3250

Electrical

Operational Receive Frequencies

Cassegrain Feed	43 GHz	10.7 GHz	5.0 GHz
	22 GHz	8.46 GHz	2.3 GHz
	15 GHz	6.1 GHz	1.4-1.7 GHz
Prime Focus	611 MHz		
	325 MHz		
Gain (dBi) (55% efficiency)	78.3 dB at 43 GHz		
	69.3 dB at 15 GHz		
	59.7 dB at 5 GHz		

Mechanical

Antenna Type	Elevation-over-Azimuth
Antenna Diameter	25-meter (82 feet)
Reflector Construction	200 AccuShape Panels
Reflector Surface Tolerance	
15.6 mph wind and dead weight	.011" rss
Panel Manufacturing Tolerance	.005" rms
Focal Length	8.85 meters (29.035 feet)
F/D	0.354
Antenna Travel	
Elevation	0° to 125°
Azimuth	±270°
Drive System	
Elevation	Bull Gear-Counterweight
Azimuth	Wheel/Track
Total Weight	568,000 lbs.
Slew Velocity	
Elevation	0.5°/sec.
Azimuth	1.5°/sec.
Slew Acceleration	
Elevation	.75°/sec.^{2}
Azimuth	.25°/sec.^{2}
Foundation-Reinforced Concrete	
Azimuth Track	50 feet diameter
Concrete	392 cubic yards
Reinforcement Steel	44,816 lbs.
Anchors	3,225 lbs.

Environmental

Wind Loading	
Precision Operating Conditions	13.4 mph gusting to 15.6 mph
Normal Operating Conditions	40.0 mph gusting to 45.6 mph
Survival at Zenith	110 mph
Pointing Accuracy and Tracking Error	
Normal	14 arc seconds peak
Repeatable	3 arc minutes
Non-repeatable (no temperature effect)	8 arc seconds
Seismic Accelerations	
Horizontal	.30 G
Vertical	.15 G

Radiation Systems, Inc.
1501 Moran Road, Sterling, Virginia 22170 Telephone (703) 450-5680

DIVISIONS

ELECTROMECHANICAL SYSTEMS (813) 541-6681
SATCOM TECHNOLOGIES (404) 497-8800
MARK ANTENNAS (312) 298-9420
TECHNICAL PRODUCTS (703) 450-5680
UNIVERSAL ANTENNAS (214) 690-8865

Model 100 and 133

Radiation Systems, Inc.

Precision Controls Division

Tracking and Pointing Control System

The RSi distributed tasking, microprocessor based control system executes multiple axis tracking, pointing and acquisition via a complement of proprietary algorithms. A full product line of integrated system components provides a range of capability and accuracy to address virtually any antenna aperture and beamwidth requirement for *satellite tracking, telemetry & control, radar, radio & optical telescope applications.*

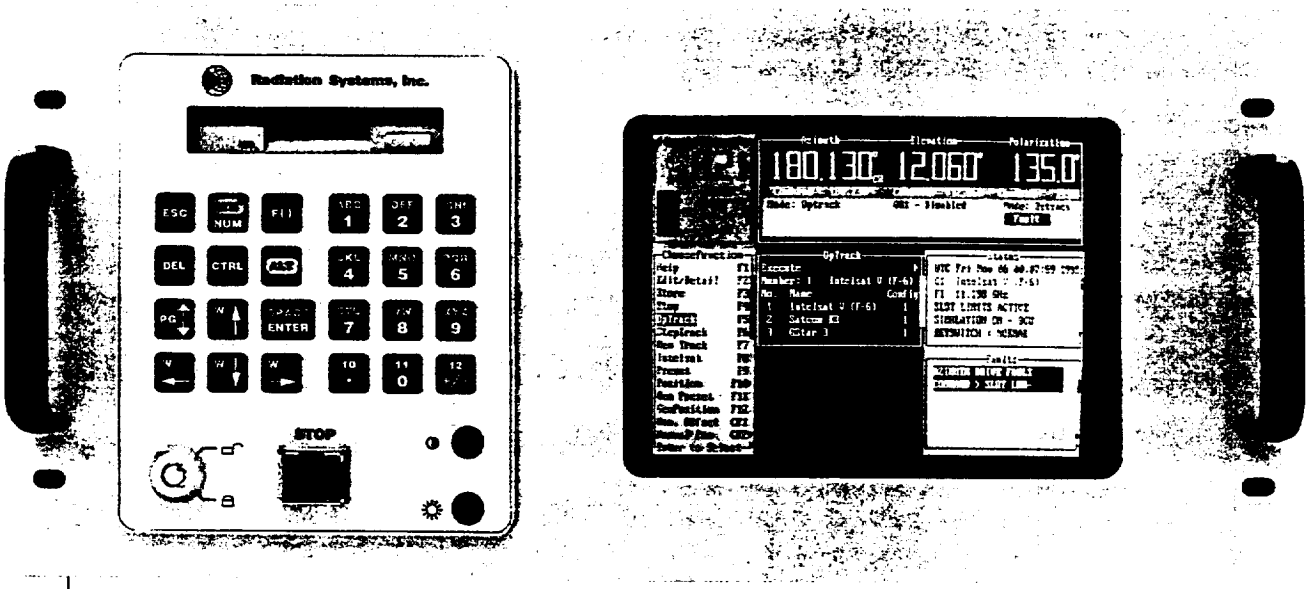

The Operation Control Unit is a PC based unit, providing a complete control and monitoring point via an innovative, menu-driven, windowing interface. The Model 100 and 133 implement the same operator interface to provide commonality of intuitive operation.

The system computing platform is based on the 80X86 processor family. This cost effective, high performance industry standard allows the *distribution of dedicated processors to key system components* such as the Operation Control Unit, Tracking Receiver and position loop closure electronics in the Power Drive Unit. This architecture permits *unprecedented features and capabilities to autonomously reside in these key components.* The computer based design also allows key system connections via serial links instead of numerous, multi-conductor cables. The resultant *insensitivity to equipment separation distance* differentiates the RSi system by providing the utmost configuration flexibility with immunity to electrical ground transients.

The modular, well defined interfaces of the control system hardware and software components assure *efficient overall integration for both new and upgrade programs.* The Model 100 system addresses mid-performance applications that typically require a single AC motor-per-axis drive system and nominal accuracy position transducers. The Model 133 system addresses high performance applications that typically require a single or multiple DC motor(s)-per-axis drive system and high accuracy position transducers.

Radiation Systems, Inc.
Precision Controls Division

1219 Digital Drive, Richardson, Texas 75081
Telephone (214)907-9599 • Fax (214)907-0027

Product Support and Services

Analysis Work Station

Quality

Continuous effort to maintain a superior level of quality is always the top priority at RSi. To achieve this, internal configuration management policies govern development, documentation, manufacturing and testing of both hardware and software. The standard quality assurance program is in accordance with MIL-I-45208. All RSi drawings are CAD generated and based on DOD-D-1000 and DOD-STD-100.

Testing

All equipment undergoes thorough testing prior to shipment. Antenna and satellite motion simulators provide realistic feedback to verify both the static and dynamic performance of each control loop. Test switch panels demonstrate correct safety interlocking and fault reporting. RSi procedures document the testing sequence and associated results.

Capability

RSi has the in-house capability to support all of the control system aspects for a new antenna, or upgrade program:

Site Survey

•

Specification and Requirement Definition

•

Pointing and Tracking Analysis

•

Linear and Non-linear Modeling and Simulation

•

Program Management

•

System Design, Support and Customization

•

Integrated Factory Acceptance Testing

•

Worldwide Site Installation, Testing and Training

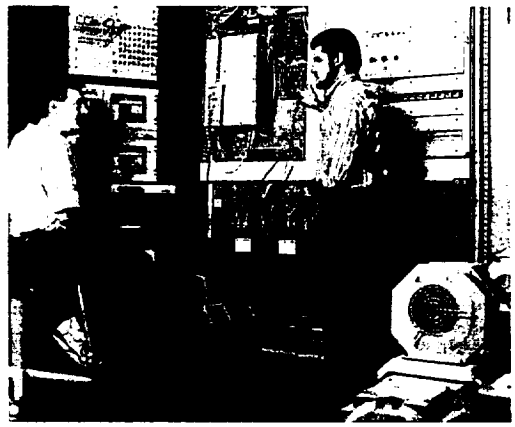

Integrated Factory Testing

Key Component Characteristics

Component	Size (inches) H x W x D	Mounting Style	Weight (lbs.)	Single Phase Power	Location
OCU	8.75 x 19 x 24	Rack mount with slides, 5 U	55	120/220 VAC, 350 VA	Indoor
OCU Keyboard	1.75 x 19 x 22	Rack mount with slides, 1 U	5	Powered by OCU	Indoor
MRU or MSU	1.75 x 19 x 8	Rack mount, 1 U	5	Powered by PDU	Indoor
PMU	10 x 3.5 x 2.5	Hand held	5	Powered by PDU	Outdoor
Tracking Receiver	3.5 x 19 x 22	Rack mount with slides, 2 U	15	90-264 VAC, 350 VA	Indoor
PDU, Multi DC	81 x 71 x 20	Free standing with lift bolts	1000	120/220 VAC, 300 VA	Indoor
PDU, Single DC	71 x 32 x 16	Free standing with lift bolts	400	120/220 VAC, 300 VA	Indoor (standard)
PDU, Single AC	31 x 31 x 10	Wall / Pedestal mount	120	120/220 VAC, 300 VA	Outdoor
PDU, Slew AC	21 x 21 x 10	Wall / Pedestal mount	60	Powered by Single AC PDU	Outdoor
PTU, Electrical	4 x 3.5 x 3.5	3" circular face inset with clamps	5	Powered by PDU	Outdoor
PTU, Mechanical	6 x 4.6 x 4.6	Face mount with bolts	5	Powered by PDU	Outdoor

- Depth of rack mount assemblies and PTUs does not include a recommended 6" for cable connectors and bend radius.
- PDUs may be placed in a vertical or horizontal position for shipment.
- Single phase power tolerances: Voltage ±10%. Frequency (50/60 Hz) ±3%.
- PDUs normally require three phase power for drive system. Amount of power primarily determined by motor size. Consult factory.
- Indoor location environment: Temperature 0° to 50°C, Humidity 0 to 95% non-condensing.
- Outdoor location environment: Temperature -20° to 50°C, Humidity 0 to 100% condensing.
- Storage environment: Temperature -40° to 70°C, Humidity 0 to 95% non-condensing.
- All equipment meets FCC Class A EMI specifications.

Capabilities and Specifications

	Model 100	Model 133	Capability (● : Standard ○ : Optional)	Description
MODES		○	Monopulse	Continuous nulling of RF tracking errors, accuracy typically better than 3% of receive 3 dB beamwidth (RMS) in moderate winds.
	●	●	Steptrack	Intermittent maximizing of RF tracking signal strength, accuracy typically better than 10% of receive 3 dB beamwidth (RMS) in moderate winds and target inclinations less than 2°.
	●	●	Optrack	Continuously executing trajectory derived from intermittent Steptrack and internal ephemeris model, ideal for inclined targets and/or scintillation, accuracy typically better than 5% of receive 3 dB beamwidth (RMS) in moderate winds and target inclinations less than 15°.
		○	NORAD	Generates and executes trajectories based on SDP4 and SGP4 models from two line elements (120 sets).
	●	●	Intelsat	Generates and executes trajectories from Intelsat 11 parameters (10 sets).
	●	●	Memtrack	Executes interpolated trajectory from data stored while autotracking.
	○	●	Table Track	Executes interpolated trajectories from time-tagged tables each with 144 points per axis (10 tables).
	○	●	Star Track	Generates and executes selected star trajectory for G/T and calibration testing (10 preset stars, others programmable).
	●	●	Preset Position	Simultaneously drives all axes to selected stored coordinate sets, enterable in azimuth/elevation (40 sets) or latitude/longitude (10 sets).
	●	●	Position Designate	Simultaneously drives all axes to commanded coordinates, enterable in azimuth/elevation or latitude/longitude.
	●	●	Manual Offset	Incremental operator commanded position offsets, convenient OCU observation and control window provided.
	○	●	Box Scan	Drives in outwardly growing, adjustable azimuth/elevation box for target acquisition.
		○	Spiral Scan	Drives in outwardly growing, adjustable spiral pattern for target acquisition.
	○	●	Geo Scan	Drives in adjustable latitude/longitude raster pattern along geosynchronous arc for target acquisition.
	○	●	Raster Scan	Drives in adjustable azimuth/elevation raster pattern for target acquisition.
		○	Automatic Stow	Automatically and sequentially executes a drive to alignment position and operation of the axis stow mechanism.
	●	●	Maintenance	Direct, microprocessor independent axis control of the drive system via PMU.
	○	●	Manual Rate	Direct, microprocessor independent axis control of the drive system via MRU.
	●	●	Stop	Individual axis or system drive disable via any control point.
	○	○	Polarization Control	Various mode control of polarization rotation axis, Model 100 AC drive (up to 8A @ 480 VAC), Model 133 AC or DC drive.
	●	●	Computer	Full supervisory monitor and control via RS232/422 link with customer computer. Other formats available, contact factory.
	●	●	Simulator	OCU executes antenna simulator software for operator training and computer interface link testing.
OCU	○	○	Redundancy	Two fully capable OCUs with manual and automatic switchover.
	●	●	Monitor	OCU Model 100 with monochrome monitor, Model 133 with color monitor.
	○	●	Keyboard	Rackmounted keyboard provided for OCU operator interaction.
	○	○	Trackball	Trackball provided for OCU operator interaction.
	○	○	Data Logger	Printer port output for providing hard copy of time-tagged status and faults.
	○	○	Reference Signals	IRIG-B time reference, GPS, and other interfaces available, contact factory.
PDU		●	Multiple DC Drive	Two axis drive, dual DC motors-per-axis, consult factory for alternate configurations and power.
	○	○	Single DC Drive	Two axis drive, single DC motor-per-axis, consult factory for alternate configurations and power.
	●		AC Drive - One Speed	Two axis drive, one single speed AC motor per axis, up to 25A @ 480 VAC power per motor.
	○		AC Drive - Two Speed	Upgrade single speed PDU with additional box to drive two axes of high speed motor windings, up to 48A @ 480 VAC for high power version and up to 11A @ 480 VAC for low power version.
PTU	○	●	Electrical Resolver	Electrical multispeed resolver assembly, .001° readout, .0003° resolution, .0026° RMS accuracy.
	●		Mechanical Resolver	Mechanical multispeed resolver assembly, .01° readout, .0014° resolution, .03° RMS accuracy.
		○	Optical Encoder	Optical encoders, consult factory for type required and specifications.
RF	○	○	Steptrack Receiver	Frequency agile tracking receiver for steptrack: Standard Bands (GHz): 3.625-4.225, 7.250-7.750, 10.95-11.45, 11.198-11.80, 11.70-12.20, 12.20-12.75 Input VSWR: 2.2 Input Impedance: 50Ω Input Beacon Power(dBm): -55 to -100 Freq. Steps: 12.5 kHz Predetection BW (kHz): 2.5, 6.7 or 280 Signal Strength Linearity: 20% CW, PM (<1.2 radians) Modulation with 43dB/Hz Acq. C/N Ratio BPSK (800Hz) Modulation with 46dB/Hz Acq. C/N Ratio Sweep Width: +/- 120 kHz Acq. Time: 710 msec.
		○	Monopulse Receiver	Upgrades steptrack tracking receiver for monopulse operation and also includes electronic scanner, summing coupler and error channel LNA to be located in feed area.
		○	Autophase	OCU algorithm that automatically phases monopulse error and sum tracking signals when required.
OTHER	●	●	Port. Maint. Unit (PMU)	Hand held portable maintenance unit (PMU) with 50' cable for microprocessor independent drive control at the antenna.
	○	○	PMU with Readout	Upgrades standard PMU to include display of axis positions, tracking signal level indication and scrolling status messages.
	○	●	Manual Rate Unit (MRU)	Rack mount unit for microprocessor independent drive control.
		○	Manual Stow Unit (MSU)	Rack mount unit for microprocessor independent manual control and monitoring of axis stowing mechanism.
	●	●	Cabling	System cabling and connectors for OCU/PDU 50' separation, no RF interconnections provided.
	○	○	Spares	Full sparing for all units.
	●	●	Documentation	Test procedures and O&M manuals. Model 100 one set, Model 133 five sets.
	○	○	Training	On-site or factory, operator and maintenance staff courses available.
	○	○	Installation	Technical services available from turnkey to supervisory.
	●	●	Warranty	Full one year warranty standard, extended period available.

Corporate Headquarters:

Radiation Systems, Inc.
1501 Moran Road
Sterling, Virginia 20166
Phone (703) 450-5680
Fax (703) 450-4706

Other Divisions

Electromechanical Systems
6200 118th Avenue North
Largo, Florida 34643
Phone (813) 541-6681
Fax (813) 544-4944

Mark Antennas
1757 South Winthrop Drive
Des Plaines, Illinois 60018
Phone (708) 298-9420
Fax (708) 635-7946

Mexia Fabricators
1604 North Avenue A
Wortham, Texas 76693
Phone (817) 765-3304
Fax (817) 765-3528

CSA Antenna Systems
Knight Road, Rochester
Kent ME2 2AX England
Phone 0634-715544
Fax 0634-715742

SatCom Technologies
4825 River Green Parkway
Duluth, Georgia 30136
Phone (404) 497-6800
Fax (404) 497-1009

Satellite Networks
1501 Moran Road
Sterling, Virginia 20166
Phone (703) 450-5680
Fax (703) 450-4694

Technical Products
1501 Moran Road
Sterling, Virginia 20166
Phone (703) 450-5680
Fax (703) 450-4706

Universal Antennas
900 Alpha Drive
Richardson, Texas 75081
Phone (214) 690-8865
Fax (214) 644-6322

PG Technology
Milnham Junction
Surrey, GR4 4TX, England
Phone 081-648 9461
Fax 081-685 9638

10/92, REV —

21 April 1993

HUGHES

ELECTRON DYNAMICS DIVISION
Industrial Electronics Group

In Reply Refer To:
MAM-93-116

University of Alaska, Fairbanks
P.O. Box 901121
Fairbanks Alaska 99775

Dear Mr. J. McSpadden;

As discussed, the attached 14 Watt Ku-Band TWTA information is provided. The approximate EPC and TWT physical characteristics will be as follows:

EPC Size (In)	8.0 x 3.2 x 3.8 (Cardwell Design)
EPC Weight	1850
EPC Efficiency	>90%
EPC Size (In)	14.14 x 3.3 x 4.5
EPC Weight	2550
EPC Efficiency	>85%
TWT Size (In)	12.7 x 2.6 x 2.4
TWT Weight	700 gms
TWT Efficiency	55-58%

The information provided is contingent upon your specific requirements such as input bus voltage, auxiliary supplies etc.

Please contact me at (310) 517-6463 should you have any questions.

Regards,

M. A. Matsuoka
Marketing and Sales
Space Products

MAM/vg

Attachment

3100 West Lomita Boulevard, P.O. Box 2999, Torrance, CA 90509-2999
(310) 517-6000

FS386

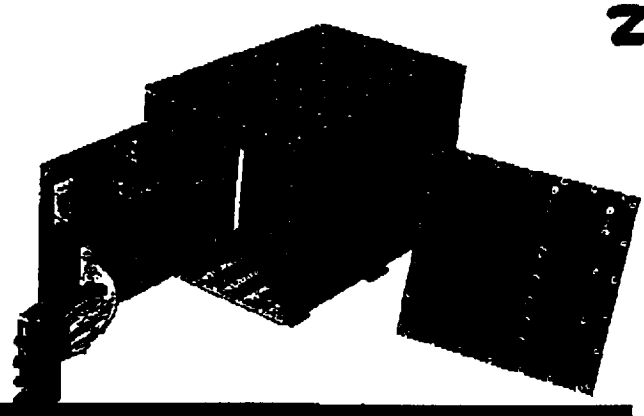

Abstract

The present and future aerospace systems demand effective, compact, lightweight, and power efficient general purpose stand-alone flight computers, supporting data handling and control functions. These computers must be highly reliable, support full redundancy, be radiation hard, and have extensive processing capability and throughput. The innovative design techniques used in the FS386 offer a unique and comprehensive solution to this quandary.

Introduction

The FS386 system is a modular general purpose, I/O intensive, information management and command processing control subsystem, designed primarily for use on small spacecraft. Through the selection of appropriate card types the FS386 system can be configured to provide a multitude of configurations ranging from a simple data gathering system to a full up distributed fully intelligent network capable of data handling, command processing, and high speed number crunching. The system supports analog, discrete, and serial inputs and outputs. In addition, the bus arbitration scheme employed can be adapted to support multiple bus masters allowing for increased computational throughput. Using power management techniques, the standby power dissipation is only a few watts. All interfaces remain free of all unwanted transients during all operating mode changes including power cycling.

System Architecture

The system is very modular and easily reconfigurable, allowing for a diversity of I/O configurations. The architecture provides for high computing throughput while supporting both fault tolerance and fault recovery. All I/O cards (T&C and Transponder CCAs) are cross-strappable. The established methodology consists of an internal parallel backplane bus and multiple external serial buses which affords flexibility of system configurability and operation. A block diagram of the non-redundant FS386 is shown below. Note the multiple Memory and T&C CCAs.

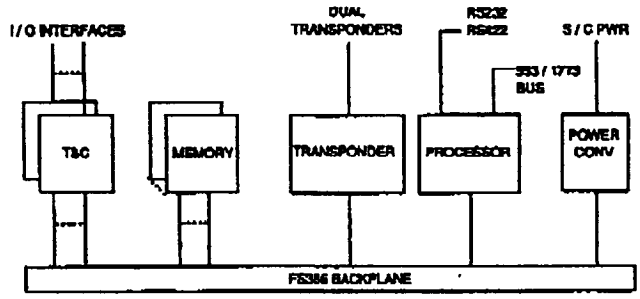

FS386 Block Diagram

System Components

The basic configuration consists of a number of different types of CCAs that have been selected to meet the most rigid of system requirements. They are outlined as follows:

- Processor
- Memory
- Telemetry & Command (T&C)
- Transponder
- Power Converter
- Backplane

The basic non-redundant configuration consists of Processor, Transponder, Power Converter, and T&C CCAs interconnected via the Backplane CCA.

FAIRCHILD SPACE

PROCESSOR CCA

The Processor CCA is the heart of the FS386 system providing for high speed data processing and the controlling of the total system. Multiple processors can be installed for redundancy and to increase the computational rates. The CCA consists of two (2) Printed Wiring Boards (PWB) on opposite sides of the aluminum heat sink core. The major characteristics of this module are:

- 80386 processor
- 80387 math coprocessor
- 82380 DMA controller
- 512K bytes SRAM (SEU Immune) - executing application code, work space (8K X 8 chips)
- 384K bytes EEPROM - program, boot purposes
- RS-232 port - testing, external interface
- High speed serial port - 4 Mhz max data rate
- MIL-STD-1553 or MIL-STD-1773 data bus interface
- Processing capability - >1 MIPS using Gibson mix
- Clock rate - 32 mHz
- Fault recovery - watchdog timer forces rebooting
- Keeps spacecraft time

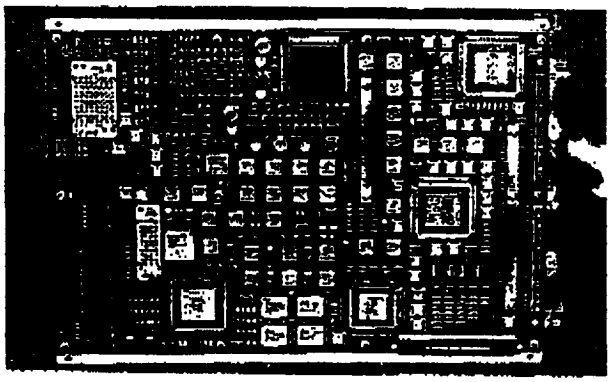

Processor CCA

Memory CCA

The Memory CCA provides the primary bulk mass data storage medium of the system on a double sided totally surface mount packaged card. The card's surface mount design and construction is based on Fairchild's successful Solid State Recorder (SSR) program of which many are flying flawlessly today. Multiple CCAs can be installed to increase the available mass memory capacity or for redundancy. The major characteristics of this assembly are:

- 6.6 megabytes user space of SRAM (32K X 8 chips)
- Single correct, double detect 7 bit Error Detection And Correction (EDAC)

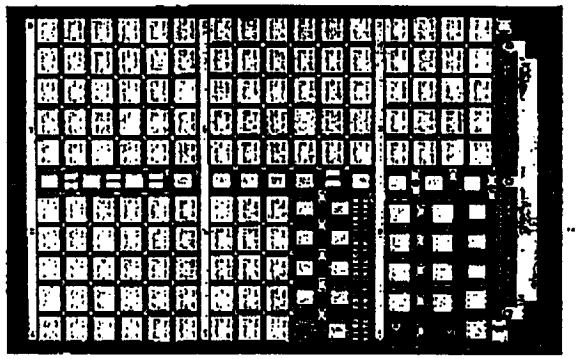

Memory CCA

Telemetry and Command (T&C) CCA

THE T&C CCA is a double sided surface mount and "through hole" packaged card which serves as the primary data gathering and command generation interface element between the user equipment and the controlling FS386 processor. Input/output (I/O) types and quantities have been determined from extensive studies of past, present, and future spacecraft systems and are more than adequate to meet even the most rigid user requirements. Multiple modules can be installed to increase the I/O interface capacity or for redundancy purposes. All outputs are designed for cross strapping capability. The major characteristics are shown below.

- One (1) differential analog command
- Sixty-four (64) discrete commands - 32 logic and 32 relay drivers
- Sixteen (16) serial digital command channels
- Sixty-four (64) telemetry channels
  - 64 active analog or
  - 64 bi-level or
  - 16 passive analog using 1 ma constant current or
  - 16 serial digital channels with pro-grammable lengths of 8, 16, or 40 bits
- One (1) 28 volt pulse with programmable duration
- Programmable analog telemetry gain control
- In-flight reprogramming capability
- Programmable backplane bus control

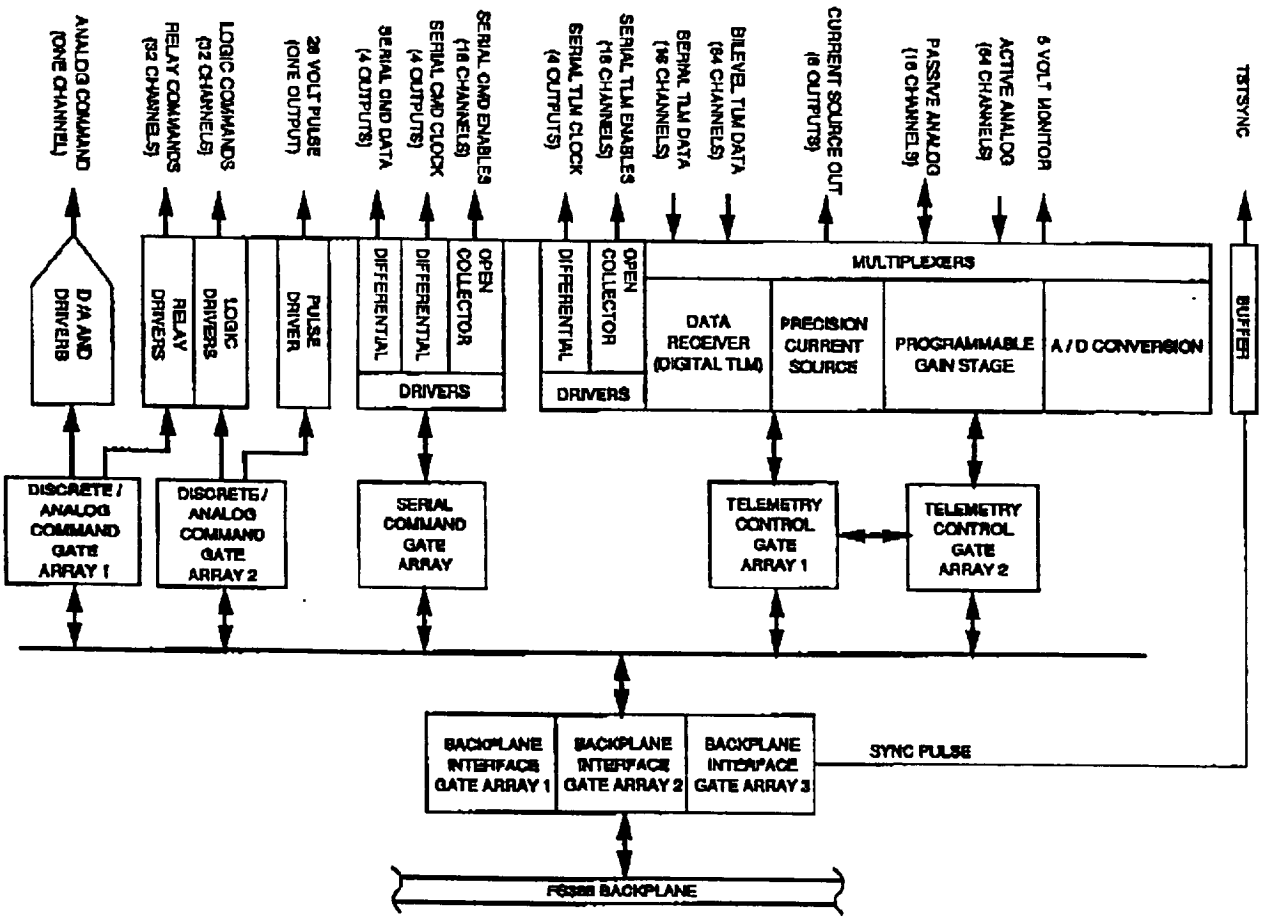

T&C CCA Block Diagram

Transponder CCA

The Transponder CCA provides cross-strappable uplink and downlink interfaces to two redundant transponders. The design includes the following characteristics:

For the Uplink portion:

- Dual redundant transponder I/F (TDRSS or SGLS)
- Command authentication
- Command decryption supported
- CCSDS or NASA STD 56 bit accommodation
- Command bypass detection for critical commands
- Rate from 100 BPS to 200 KBPS

For the Downlink portion:

- CCSDS AOS protocol or TDM frames
- Reed Solomon data encoding Convolutional encoding with interleave
- TDRSS, SGLS, DSN, STDN/GSTDN compatibility
- Dual channel, 6 megaBPS aggregate data rate

Power Converter

The Power Converter CCA provides the power to the FS386 system from the spacecraft power bus. The module consists of "through hole" component packaging on a single-sided PWB. The major characteristics of the CCA are:

- Input voltage - 21 to 35 volts
- Output voltage/current
  - +5 volts @ 5 amperes (regular CCA power)
  - +5 volts @ 1 ampere (standby power to memory CCAs)
  - +/- 15 volts @ 500 milliamperes for T&C CCAs
- Input to output isolation ->10 megohms
- Efficiency ->70% at full load
- Soft start capability
- Power On Reset - active at <4.5 volts, 50 milliseconds power on delay
- Overcurrent protection - 125% of maximum primary current

25 lbs

SPECIFICATIONS

5

Features

- All solid state
- Semiconductor reliability
- Low power
- Configurability through modularity
- Memory EDAC

Environmental:

- *Operating Temperature:* -25°C to 80°C (baseplate)
- *Storage Temperature:* -55°V to 125°C (ambient)
- *Vibration:* 14 gRMS random 20Hz to 2000 Hz

Physical Characteristics:

- *Box Size:* Configuration dependent 8 CCA system:
  - footprint - 8 X 11.25 inches
  - height - 7.6 inches
- *Box Weight:*
  - 8 CCA system - 19 pound
  - *CCA Size:* 10 X 7.35 inches
  - *CCA Power:* 0.25 (Memory) to 8.6 (Processor) watts
  - CCA Weight: 1 to 2.85 (Processor) pounds

FAIRCHILD SPACE

FAIRCHILD SPACE • 20301 CENTURY BOULEVARD • GERMANTOWN, MARYLAND 20874-1181

PHONE: (301) 428-6620 FAX: (301) 428-6641

USER	UAF USRA/ADP	RFQ. OR REFERENCE NO.	
DIVISION/LOCATION	MOTOROLA	PROGRAM NAME	

CONFIGURATION OPTION TABLE
NASA STANDARD TDRSS USER TRANSPONDER

1	TRANSPONDER S-BAND FREQUENCY (MEGAHERTZ)	A	TRANSMIT (RETURN LINK) 2106.4106 MHz			B	RECEIVE (FORWARD LINK) 2287.5000 MHz		
2	CLASS OF SERVICE	A	MULTIPLE ACCESS X			B	S-BAND SINGLE ACCESS		
3	TRANSMITTER RF POWER OUTPUT LEVEL (WATTS)	A	1 WATT	B	2.5 WATTS	C	5.0 WATTS X		
4	DIPLEXER/OUTPUT FILTER MOUNTING	A	TOGETHER AT TRANSPONDER X	B	DIPLEXER ONLY REMOTE	C	BOTH REMOTE		
5	STDN FORWARD LINK COMMAND DATA BIT RATE (BITS PER SECOND)	A	125	B	250	C	500	D	1000	E	2000 X
6	TDRSS FORWARD LINK COMMAND LOW DATA BIT RATE (BITS PER SECOND)	A	125	B	250	C	500	D	1000 X		
7	TDRSS FORWARD LINK COMMAND HIGH DATA BIT RATE (BITS PER SECOND)	A	125	B	250	C	500	D	1000 X		
8	STDN RANGING CHANNEL BANDWIDTH (KILOHERTZ)	A	160	B	800						
9	STDN RETURN LINK TELEMETRY COMMANDABLE MODULATION SENSITIVITY (BETWEEN 0.5 AND 5.0 RAD. PEAK/VOLT. PEAK	A	LOW X	B	HIGH (SEE TABLE 3.4-1)						
10	STDN RETURN LINK TONE RANGING MODULATION INDEX (BETWEEN 0.35 AND 1.5 RAD. PEAK)	(SINGLE TONE SINE WAVE) X									
11	TDRSS TLM Q:I CHANNEL POWER RATIO	A	1:1 X	B	2:1	C	4:1				
12	TDRSS TRANSPONDER ADDRESS (RESPONDS TO B_0 OF COMMAND WORD)	A	"A" X	B	"B"						
13	TDRSS PN CODE (SEE SECTION 3.5.2 FOR CODE NUMBER)	ONE NUMBER OUT OF 85 POSSIBLE.									
14	TDRSS TLM CHANNEL INPUT IMPEDANCE (BOTH CHANNELS THE SAME)	A	50 OHMS X	B	5000 OHMS						
15	TEMPERATURE TRANSDUCER (USER SUPPLIED) (MANUFACTURER AND MODEL NUMBER)	A	TCXO	B	POWER AMPLIFIER						

CONFIGURATION PART NUMBER ASSIGNED: 01-P06700J	DATE:

4630-11